Optical Space Division Multiplexing in Short Reach Multi-Mode Fiber Systems

Dissertation

zur Erlangung des akademischen Grades
Doktor der Ingenieurwissenschaften
(Dr.-Ing.)
der Technischen Fakultät
der Christian-Albrechts-Universität zu Kiel

André Sandmann

Kiel
2021

1. Gutachter: Prof. Dr.-Ing. Stephan Pachnicke

2. Gutachter: Prof. Dr.-Ing. habil. Steffen Lochmann

Datum der mündlichen Prüfung: 22.02.2022

Acknowledgment

I would like to cordially thank Prof. Andreas Ahrens and Prof. Steffen Lochmann for the opportunity to work on this very interesting topic and for the invaluable support they have provided throughout my work.

Furthermore, I would like to thank Prof. Stephan Pachnicke for the great opportunity to carry out my doctoral studies in cooperation with the Christian-Albrechts-Universität zu Kiel, and I am grateful for the fruitful discussions. His feedback in the development of different publications and during the finalization of this thesis is very much appreciated.

I also want to thank Prof. Werner Rosenkranz for providing the multi-segment detector devices and for the productive discussions. Moreover, I would like to express my thanks to Prof. Christian-Alexander Bunge for his valuable feedback on the system model for optical MIMO with intensity modulation and direct detection.

I wish also to thank my colleague Marek Götten for proofreading my thesis and for the valuable exchange of ideas.

Finally, I would like to thank my family and especially my parents for their unlimited support.

André Sandmann

Abstract

The application of space division multiplexing (SDM) to fiber-optic communications is a promising approach to further increase the channel capacity of optical waveguides. In this work, short reach and low-cost optical SDM systems with intensity modulation and direct detection (IM/DD) are in the focus of interest. Herein, different modes are utilized to generate spatial diversity in a multi-mode fiber (MMF).

In such IM/DD systems, the process of square-law detection is inherently non-linear. In order to obtain an understanding of the channel characteristics, a system model is developed, which is able to show under which conditions the system can be considered linear in baseband. It is shown that linearity applies in scenarios with low mode cross-talk. This enables the use of linear multiple-input multiple-output (MIMO) signal processing strategies for equalization purposes. In conditions with high mode cross-talk, significant interference occurs, and the transmitted information cannot be extracted at the receiver. Consider a system with single-mode fiber (SMF) to MMF launches with different radial offsets for mode-selective excitation and OM4-grade MMFs. This work indicates that such a system is limited to a MIMO configuration with two inputs. A corresponding system with three MIMO inputs is impaired by its low mode-orthogonality, which leads to mode cross-talk, and hence it results in substantial interference.

Furthermore, a method to determine the power coupling coefficients between mode groups is presented that does not require the excitation of individual modes, and hence it can be realized with inexpensive components. It is based on multiple impulse response measurements. The coupling matrices of different coupler types are determined, and it is shown that custom manufactured fusion couplers are well-suited for mode separation. In addition, the obtained coupling matrix of an MMF of 1 km length confirms that coupling between distant mode groups does not occur, and only a small portion is coupled into neighboring groups. This practically enables the use of each mode group as a separate transmission channel. A time variance analysis is performed, and it shows that, even under significant vibration stress, a MIMO system can be considered time-invariant for at least three seconds, if the MIMO data streams are transferred on separate mode groups.

In addition, different optical components are analyzed with respect for their suitability in MIMO setups with IM/DD. The conventional approach with SMF to MMF offset launches and optical couplers as well as a configuration that utilizes multi-segment detection are feasible options for a (2×2) setup. It is further shown that conventional photonic lanterns are not suited for MIMO with IM/DD due to their low mode orthogonality during the multiplexing process. In order to enable higher order MIMO configurations, devices for mode multiplexing and demultiplexing need to be developed, which exhibit a high mode orthogonality on one hand and are low-cost on the other hand.

Kurzzusammenfassung

Die Anwendung von Raummultiplex in der Glasfaser-basierten Telekommunikation ist ein vielversprechender Ansatz, um die Kanalkapazität von Lichtwellenleitern weiter zu erhöhen. In dieser Arbeit stehen kostengünstige Raummultiplexsysteme für Kurzstreckenübertragungen mit Intensitätsmodulation und Direktdetektion (IM/DD) im Fokus. Hierbei werden unterschiedliche Moden zur Erzeugung von räumlicher Diversität in Multimode Fasern (MMF) genutzt.

In solchen IM/DD Systemen ist deren quadratischer Detektionsprozess von Natur aus nicht linear. Um ein Verständnis für die Kanal-Charakteristika zu erlangen, wird ein Systemmodell entwickelt, welches zeigt, unter welchen Bedingungen das System als linear im Basisband angesehen werden kann. Es wird dargelegt, dass Linearität in Szenarien mit geringem Modenübersprechen zutrifft. Dies ermöglicht die Nutzung von linearen Multiple-Input Multiple-Output (MIMO) Signalverarbeitungsstrategien zum Zwecke der Entzerrung. Unter Bedingungen mit hohen Modenübersprechen treten signifikante Interferenzen auf und die übertragene Information kann nicht am Empfänger zurückgewonnen werden. Nehmen wir nun ein System an, dass auf Singlemode Faser (SMF) zu MMF Einkopplungen mit verschiedenen radialen Versätzen für die modenselektive Anregung basiert und eine MMF der Kategorie OM4 verwendet. In dieser Arbeit wird gezeigt, dass ein solches System auf eine MIMO Konfiguration mit zwei Eingängen limitiert ist. Ein gleichartiges System mit drei MIMO Eingängen ist durch seine geringe Modenorthogonalität beeinträchtigt. Dies führt zu Modenübersprechen und resultiert daher in erheblicher Interferenz.

Weiterhin wird eine Methode zur Bestimmung der Leistungskoppelkoeffizienten zwischen Modengruppen präsentiert. Diese benötigt keine Anregung einzelner Moden und kann daher mit kostengünstigen Komponenten realisiert werden. Die Methode basiert auf mehrfacher Messung der Gewichtsfunktion. Die Koppelmatrizen verschiedener Kopplertypen wurden damit bestimmt, und es wurde gezeigt, dass speziell hergestellte Schmelzkoppler für die Separation von Moden gut geeignet sind. Zudem wird die Koppelmatrix einer 1 km langen MMF bestimmt. Diese bestätigt, dass Leistungskopplungen zwischen entfernten Modengruppen nicht stattfinden und nur ein kleiner Teil in die benachbarten Gruppen gekoppelt wird. In der Praxis ermöglicht dies die Nutzung von Modengruppen als separate Übertragungskanäle. Eine Zeitvarianzanalyse wird durchgeführt, welche hervorhebt, dass selbst unter erheblichem Einfluss von Vibrationen ein MIMO System als zeitinvariant für mindestens drei Sekunden angesehen werden kann, wenn die MIMO Datenströme auf separaten Modengruppen übertragen werden.

Zusätzlich werden verschiedene optische Bauteile in Hinblick auf deren Eignung für einen Einsatz in einem MIMO Setup mit IM/DD untersucht. Der konventionelle Ansatz, der SMF zu MMF Einkopplungen mit verschiedenen Versätzen und optische Koppler nutzt, sowie eine Konfiguration mit Multisegmentdetektoren sind geeignet für einen (2×2) Aufbau. Es

wird ferner gezeigt, dass herkömmliche Photonische Laternen für MIMO mit IM/DD nicht geeignet sind, da diese nur eine geringe Modenorthogonalität beim Multiplex Prozess haben. Um MIMO Konfigurationen höherer Ordnung zu ermöglichen, müssen Komponenten für den Moden-Multiplex und Demultiplex entwickelt werden, welche zum einen eine hohe Modenorthogonalität aufweisen und zum anderen kostengünstig sind.

Contents

List of frequently used Abbreviations and Symbols 11

1 Introduction 15
- 1.1 Historical Development and State of the Art 17
- 1.2 Novel Contributions 20
- 1.3 Published Material 21
- 1.4 Structure of this Thesis 22

2 Fundamentals of Multi-Mode Fiber Systems with IM/DD for MIMO 23
- 2.1 Modal Analysis in Graded-Index Optical Waveguides 23
  - 2.1.1 Mode Excitation – SMF to MMF Launch 26
  - 2.1.2 MMF Direct Detection and Modal Noise 27
- 2.2 Modeling of non-ideal Lasers 30
  - 2.2.1 Influence of Laser Phase Noise on the Carrier Signal's PSD 31
  - 2.2.2 Coherence Time and Length 33
- 2.3 MIMO Signal Processing for Frequency-selective Channels 36
  - 2.3.1 Broadband MMSE-DFE System Model 36
  - 2.3.2 Mean Square Error Minimization 42
  - 2.3.3 Backward Filter Coefficients 43
  - 2.3.4 Special Cases 43
  - 2.3.5 Performance Evaluation 44

3 Square-law Detection in Fiber-Optic Transmission 47
- 3.1 Equivalent Linear Baseband Representation for Square-law Detected Systems 47
- 3.2 Single-Mode Fiber SISO System Model 48
  - 3.2.1 Analytic versus Real-valued Bandpass Signal Representation 50
  - 3.2.2 SMF Channel Impulse Response 51
- 3.3 Multi-Mode Fiber SISO System Model 58
  - 3.3.1 Baseband Linearity of the Desired Signal 61
  - 3.3.2 Properties of the Interference Signal 62
  - 3.3.3 MMF Channel Impulse Response 63
- 3.4 Multi-Mode Fiber MIMO System Model 68
  - 3.4.1 System Model 68
  - 3.4.2 Simulation Results 74
  - 3.4.3 Measurement Results 76
  - 3.4.4 MUX Interference 78

4 Multi-Mode Fiber MIMO Channel Description 83
- 4.1 Mode Group Power Coupling Analysis 83
  - 4.1.1 Measurement Procedure 84
  - 4.1.2 Determining the Power Coupling Coefficients 85
  - 4.1.3 Mode Group Power Coupling Results 88
  - 4.1.4 Coupling Analysis at 1508 nm 92
  - 4.1.5 BER Performance Evaluation 94

4.2 Fiber Channel Time-Variance Characterization 97
    4.2.1 Intensity Profile Analysis 98
    4.2.2 Input Delay Spread Function Measurement 100
    4.2.3 Signal Processing Considerations 105

5 Testbed Results **107**
5.1 Multi-Mode Setup with Offset SMF to MMF Splices and Fiber Optical Couplers 107
    5.1.1 Multi-Mode Coupler-Types 108
    5.1.2 Analysis of a (4x4) Configuration 111
    5.1.3 BER Performance of a (2x2) Configuration 117
5.2 Multi-Segment Detection 120
    5.2.1 Chip Characterization 120
    5.2.2 Packaging and MIMO Impulse Responses 122
    5.2.3 BER Performance Analysis 124
5.3 Few-Mode Setup with Photonic Lanterns 127
5.4 Hardware Component Discussion for MIMO Systems with IM/DD 131

6 Closing Remarks **135**

Appendices **137**

A Derivations **137**
A.1 MMSE-DFE Backward Filter Coefficients Optimization 137
A.2 Equivalence of the Analytic and Real-valued Bandpass Signal 139
A.3 Inverse Fourier Transform of a Complex Exponential Function with Quadratic Argument 140
A.4 Inverse Fourier Transform of the Heaviside Step Function 141
A.5 Hilbert Transform of a Sine Function with Quadratic Argument 142

Bibliography **145**

Liste der Veröffentlichungen des Autors **155**

Erklärung zur Arbeit **161**

List of frequently used Abbreviations and Symbols

List of Abbreviations

AC	Alternating component
ACF	Auto-correlation function
AFC	Asymmetric fusion coupler
BER	Bit-error rate
CDF	Cumulative distribution function
CFC	Customized fusion coupler
DC	Direct component
DFB	Distributed feedback (laser)
DFE	Decision feedback equalizer
DSO	Digital storage oscilloscope
DUT	Device under test
EDFA	Erbium-doped fiber amplifier
FFE	Feed forward equalizer
FMF	Few-mode fiber
FP	Fabry-Pérot
FWHM	Full width at half maximum
HOM	High-order mode
IM/DD	Intensity modulation and direct detection
ISI	Inter-symbol interference
LOM	Low-order mode
MC	Mirror coupler
MIMO	Multiple-input multiple-output
MMF	Multi-mode fiber
MMSE	Minimum mean square error
MPLC	Multi-plane light conversion
MSE	Mean square error
MUX, DEMUX	Multiplex, demultiplex
NMAE	Normalized mean absolute error
O/E	Optical to electrical conversion
OOK	On-off keying
PC	Polished coupler
PDP	Power delay profile

PL	Photonic lantern
PRBS	Pseudo random binary sequence
PSD	Power spectral density
RMS	Root mean square
Rx	Receiver
SDM	Space division multiplexing
SFC	Symmetric fusion coupler
SINR	Signal-to-interference-plus-noise ratio
SIR	Signal-to-interference ratio
SISO	Single-input single-output
SMF	Single-mode fiber
SNR	Signal-to-noise ratio
Tx	Transmitter
ZF	Zero forcing

Notation

$\boldsymbol{a}$	Vector notation
$\boldsymbol{A}$	Matrix notation
$\mathrm{tr}(\boldsymbol{A})$	Trace of matrix $\boldsymbol{A}$
$(\,\cdot\,)^{\mathsf{T}}$	Transpose operator
$(\,\cdot\,)^{\mathsf{H}}$	Transpose and complex conjugate operator (Hermitian)
$(\,\cdot\,)^{*}$	Complex conjugate operator
$\underline{s}(t)$	Complex-valued signal
$s^{+}(t)$	Analytic signal with $^{+}$ indicating that it has only components at positive frequencies
$\mathcal{F}\{\,\cdot\,\}$	Fourier transform
$\mathcal{H}\{\,\cdot\,\}$	Hilbert transform
$\mathrm{Im}\{\,\cdot\,\}$	Imaginary part
$\mathrm{Re}\{\,\cdot\,\}$	Real part
$\mathrm{E}\{\,\cdot\,\}$	Expectation functional
$s_k = s[k]$	kth sample of the discrete-time signal s
$s(k)$	All samples of the discrete-time signal s
$*$	Signal convolution operator
$\propto$	Proportional to

List of Symbols

c	Speed of light in vacuum
j	Imaginary unit $\mathrm{j}^2 = -1$
N_0	Power spectral density of white Gaussian noise
P_s	Transmit signal power referenced to $1\,\Omega$
P_n	Noise power
$\mathbf{0}_n$	$(n \times n)$ sized zero matrix
$\boldsymbol{I}_{n\times m}$	$(n \times m)$ sized identity matrix
T_s	Symbol duration
f_T	Symbol frequency $f_\mathrm{T} = 1/T_\mathrm{s}$
t	Continuous-time
f	Frequency
ω	Angular frequency
ω_c	Center angular frequency
λ	Wavelength
δ	Alignment offset/ eccentricity between SMF and MMF
n_T	Number of MIMO inputs
n_R	Number of MIMO outputs
μ	MIMO input index, $\mu = 1, \ldots, n_\mathrm{T}$
ν	MIMO output index, $\nu = 1, \ldots, n_\mathrm{R}$
$1(t)$	Heaviside step function
$\delta(t)$	Dirac delta function
$\mathrm{rect}(t)$	Rectangular function
$g_\mathrm{s}(t)$	Transmit filter for pulse shaping
$g(t)$	Baseband channel impulse response
$g_\mathrm{ef}(t)$	Receive filter
$h(t)$	Cumulative channel impulse response $h(t) = g_\mathrm{s}(t) * g(t) * g_\mathrm{ef}(t)$

1 Introduction

In the telecommunications sector the demand for solutions to increase the data throughput at the same cost is ever-rising. It includes the aim to reduce the energy 'used' per transmitted bit. This demand is driven by a growth of users with access to the internet, a higher number of connected devices and an increased use of services that require high data throughput, such as high resolution video streaming and video conferencing services [ITU20; Cisc20]. The latter became a necessity for many people during the COVID-19 pandemic. Fiber-optic systems are the backbone of today's telecommunications infrastructure since they offer significantly higher bandwidth-distance products compared to copper-based solutions, and optical waveguides are resistant to electromagnetic interference [Agra10; Rao20].

In the recent decades, the following physical dimensions have been used to better exploit the available channel capacity of optical waveguides, i.e. the theoretical maximum bit-rate that can be reliably transmitted: time, frequency, polarization, quadrature and space [Winz18; Will20, pp. 341–343]. An overview of these dimensions is illustrated in Fig. 1.1. The dimension time includes the symbol-rate and its shape. Frequency is utilized in massively parallelized dense wavelength division multiplexed systems that fully exploit the available optical spectrum. In addition, the use of specific zero water peak fibers increases the available spectrum. By using the two linear polarization directions as separate transmission channels, the channel capacity is nearly doubled [Will20, pp. 347–348]. The dimension quadrature is exploited with the deployment of coherent systems that make use of higher-order and complex modulation schemes. These four multiplexing dimensions are well-researched. In order to avoid the upcoming "capacity crunch" [Elli16], new scaling methods need to be investigated to further increase the fiber capacity. It has been stated that "[…] parallelism in space is the only option to significantly scale system capacities by appreciable factors in the long run" [Winz18]. Thus, the dimension space is in the focus of interest in this work.

As the name *space division multiplexing* (SDM) suggests, its idea is to use spatially diverse channels to transmit parallel data. In wireless communications, this technique is well established, and spatial diversity is generated by using multiple antennas at the transmitter and receiver, which are arranged at different locations. This leads to a MIMO system, and the occurring channel cross-talk is eliminated by using MIMO equalization at the transmitter and/or receiver. In optical fiber systems, one way to generate spatial diversity is the use of multi-core fibers. However, the manufacturing costs of such fibers are high

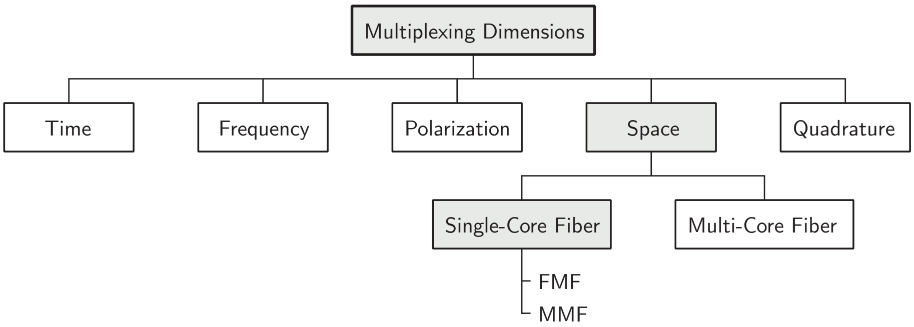

Figure 1.1: Multiplexing dimensions in fiber-optic transmission systems

compared to conventional MMFs, and it can be seen as an integration of multiple fiber strands into a single piece of silica glass. Thus, in this work the focus is on exploiting different modes in a conventional MMF or few-mode fiber (FMF) as separate transmission channels.

Considering an OM4-grade MMF with a core diameter of 50 µm and an operating wavelength of 1550 nm, 55 modes per polarization can propagate. This shows the massive potential for parallelization, if each mode could be used for a separate channel. However, effects like mode cross-talk, different mode delays (i.e. modal dispersion), mode specific losses and the phase of each mode need to be considered, and therefore these effects make this quite a difficult task. In the early days of optical communications these effects were seen as disturbance, which lead to the advent of SMFs. In contrast, with SDM modes are used as carriers of information.

Coherent optical MIMO systems are heavily researched and their required hardware is costly since the implemented state of the art multiplexing devices contain free-space components. Laboratory results have highlighted that SDM enables record-breaking transmission speeds through a single fiber strand with one core [Ryf18; Rade20]. However, the high costs have not yet lead to a wide-spread adoption in commercial products.

This thesis focuses on low-cost fiber-optic SDM systems for short transmission distances up to 2 km. Thus, IM/DD is considered and mainly conventional MMFs are utilized. Furthermore, this work solely concentrates on the dimension space (and time) in terms of the presented multiplexing opportunities. Such systems could be used in in-house communication applications, specifically in scenarios with a link distance beyond 100 meters. In this distance region copper-based transmission media are not feasible due to their bandwidth-distance limitation and the impact of cross-talk [Coom14]. Even below 100 m fiber length low-cost IM/DD solutions with SDM for e.g. rack-to-rack optical interconnects are an option to further increase data rates [Zou20]. In environments where MMFs are already deployed, SDM techniques can be applied to multiply the link's bit-rate. This requires the exchange of just the transceiver units. In addition, the focus of this work is the physical layer transmission. Channel coding is not taken into consideration since it can be formally separated from the physical transmission aspect.

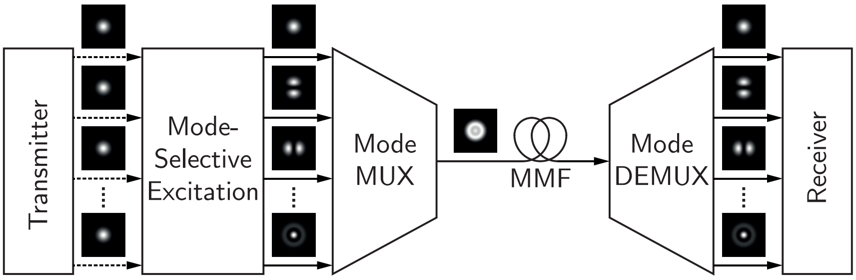

Figure 1.2: Ideal multi-mode SDM system displaying the intensity distributions in the fiber cores (dashed line: SMF, solid line: MMF)

In an optical spatial multiplexing system numerous data streams are transmitted on different modes through a fiber in conditions that support the propagation of multiple modes. These conditions comprise the fiber geometry, its numerical aperture and the operating wavelength. The maximum theoretical transmission capacity is achieved, if each mode is utilized to carry a separate data stream as shown in the concept in Fig. 1.2. In this idealized model, the parallel data streams, which are carried on the fundamental mode (i.e. LP_{01}), are converted to individual spatial modes in a parallel set of MMFs (e.g. LP_{01}, LP_{11a}, LP_{11b}). Subsequently, these modes are multiplexed (MUX) into one MMF. The processes of mode-selective excitation and mode MUX can either be carried out by individual devices or they can be performed by a single device. During the transmission through the MMF channel, mode-mixing occurs. At the receiver-side the individual modes are separated by the mode demultiplexer (DEMUX) and they are individually detected. It is worth noting that in IM/DD systems, the output of the mode DEMUX can be an MMF. Considering coherent detection strategies, they require that the modes at the DEMUX output are transferred to fundamental modes in SMFs, enabling the subsequent superposition of a local oscillator with the received data signals. A simple MMF to SMF splice is not suitable for this task due to modal noise. In practice, the excitation of just one individual mode and its separation at the receiver requires complex and costly opto-mechanical constructions, e.g. with phase plates, spatial light modulators or multi-plane light conversion [Wild15; Koeb11; Labr14]. Since low-cost IM/DD systems are in the focus of interest in this work, other multiplexing devices are considered.

1.1 Historical Development and State of the Art

The concept of exploiting fiber modes to carry different data streams is known since the 1980s [Berd82]. Throughout the development process, different optical components were used to realize and further optimize SDM. Early concepts used conventional multi-mode couplers to combine and split the data streams [Stua00]. Furthermore, the use of SMF to MMF transitions at the transmitter, each being aligned with a different radial offset, enables a mode-selective excitation [Rame81; Schoe06]. Multi-segment photo detectors that are able to perform the DEMUX process and optical to electrical conversion in a single process were suggested [Pate01]. The first testbed results (with IM/DD) that exploit multi-plane light conversion (MPLC) emerged in 2015 [Labr15].

Table 1.1 gives a historical list of SDM transmission experiments with IM/DD and their reported data rates. Please note, results based on coherent detection are not included in this list. The data rates are normalized by the number of used polarization directions and the number of used wavelengths (Gbps/pol/λ) to solely focus on the spatial multiplicity. In addition to the table, the resulting normalized rates in dependency on the fiber length for the different transmission experiments are compared in Fig. 1.3. It is evident that results based on optical couplers for MUX and DEMUX are practically limited to a (2×2) configuration. Fully operational (3×3) configurations using a fiber with 50 µm core diameter have not been reported. In this work it is shown that the coupler setup in combination with SMF to MMF offset launch is limited by its low mode orthogonality, which leads to interference. The introduction of MPLC improved the mode orthogonality since this technology enables the excitation of individual modes. This lead to higher order MIMO configurations, e.g. a (4×4) setup [Simo16]. However, MPLC is based on a costly free-space setup, and thus its suitability for low-cost IM/DD configurations needs to be questioned. It is worth noting that operational setups with photonic lanterns, which use similar fiber cores in the capillary, in combination with IM/DD do not exist. The reason is that each input of these photonic lanterns excites multiple modes at the output, leading to cross-talk between the data streams, and thus it results in significant interference. Approaches to increase the mode-selectivity of photonic lanterns by using dissimilar fiber cores in the capillary exist [Sai17]. However, the overall MIMO setup based on such mode-selective photonic lanterns is still impaired by mode cross-talk, and the manufacturing process seems to require low tolerances in order to get the exact geometries [Liu17].

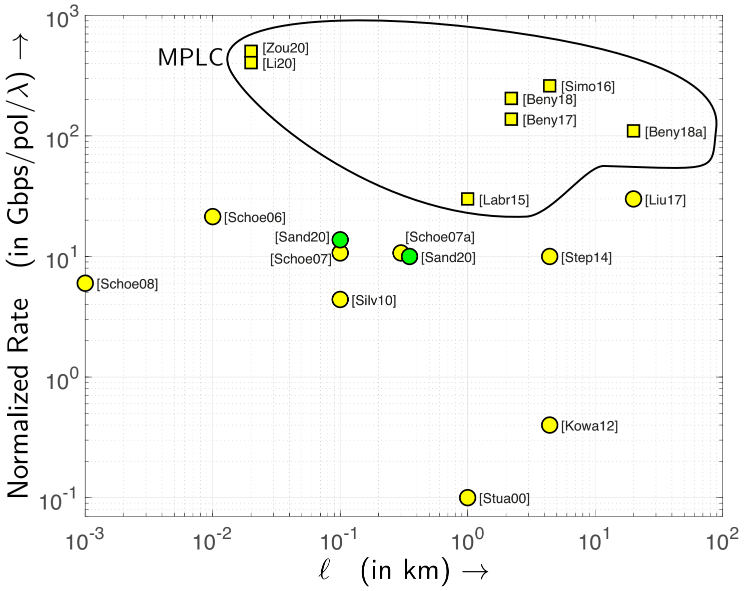

Figure 1.3: Documented gross bit-rates per polarization and wavelength in dependency on the fiber length in MIMO configurations with IM/DD

Table 1.1: Selection of optical MIMO transmission experiments with IM/DD

Reference	Date	ℓ/km	n_L	f_T/GHz	Modulation	Normalized Rate Gbps/pol/λ	SDM Device, Fiber	Comments
[Stua00]	07/2000	1	2	0.05	BPSK	0.1	Coupler	1
[Schoe06]	2006	0.01	2	10.7	OOK	21.4	Coupler, POF	2
[Schoe07a]	03/2007	0.3	2	5.35	OOK	10.7	Coupler	2
[Schoe07]	09/2007	0.1	2	5.35	OOK	10.7	Coupler	2
[Schoe08]	02/2008	0.001	3	2.0	OOK	6.0	Coupler, ∅ 62.5 µm	2
[Silv10]	03/2010	0.1	2	2.2	OOK	4.4	Segmented-Photo-Det.	
[Kowa12]	05/2012	4.4	2	0.2	OOK	0.4	Coupler	
[Step14]	04/2014	4.4	2	5.0	OOK	10.0	Coupler	
[Labr15]	09/2015	1	3	10.0	OOK	30.0	MPLC	
[Simo16]	03/2016	4.4	4	32.5	PAM-4	260.0	MPLC	
[Liu17]	03/2017	20	3	10	OOK	30	DCF-PL	
[Beny17]	03/2017	2.2	2	*	DMT	137.6	MPLC	3
[Beny18]	09/2018	2.2	2	*	DMT	204.5	MPLC	3
[Beny18a]	09/2018	20	2	*	DMT	110.0	MPLC	3
[Zou20]	03/2020	0.02	3	67	PAM-6	502.5	MPLC	
[Li20]	07/2020	0.02	3	*	DMT	405	MPLC	
[Sand20]	12/2020	0.1	2	6.875	OOK	13.75	Coupler	
[Sand20]	12/2020	0.35	2	5.0	OOK	10.0	Coupler	
In this thesis	2021	0.5	2	1.25	OOK	2.5	Segmented-Photo-Det.	

Comments

[1] Additional electrical carrier is used

[2] (n_L×1) setup, no DEMUX (e.g. Coupler) included

[3] Only 2 mode groups operate on the same wavelength

Legend

ℓ	… Fiber length	PAM	… Pulse-amplitude modulation
n_L	… Number of MIMO layers	DMT	… Discrete multitone
f_T	… Symbol frequency	POF	… Plastic optical fiber
BPSK	… Binary phase shift keying	DCF-PL	… Photonic lantern with dissimilar core fibers
OOK	… On-off keying		

1.2 Novel Contributions

Within the framework of my doctoral studies the following novel contributions have been developed:

A system model has been presented that shows under which conditions an optical MIMO system with IM/DD can be considered linear in baseband. The main focus is the reduction of mode cross-talk in order to minimize interference. In conditions with high mode cross-talk, the system is majorly distorted by an interference term that cannot be linearly equalized. The theoretic analysis is supported by simulations and measurements. In addition, the interference that occurs in the multiplexing process has been quantified. It has been shown that in a MIMO setup with three inputs and conventional SMF to MMF offset excitation, significant interference (more than 50% normalized interference) occurs when considering an OM4-grade MMF, regardless of the chosen eccentricities. Thus, with this type of mode excitation and fiber a MIMO system is limited to a (2×2) configuration.

A method has been developed, which is able to calculate power coupling coefficients between mode groups of an arbitrary device under test based on impulse response measurements. The algorithm does not require the excitation of individual modes. Instead, it combines multiple measurements to obtain these coefficients through a linear system of equations. This algorithm enables the measurement of these coefficients with inexpensive hardware that do not require free-space components such as phase plates, spatial light modulators or an MPLC device. With this algorithm, the coupling coefficients of an OM4-grade MMF of 1 km length and different multi-mode coupler types are determined, and the algorithm has been confirmed to work in the spectral regions of 1300 nm and 1550 nm.

In the time-variance analysis, the measured input delay spread functions and intensity profiles show, that no coupling between mode groups occurs under considerable vibration stress. From the single-input single-output (SISO) results it is concluded that a corresponding MIMO channel can be considered as time-invariant in a time window of at least three seconds, if the MIMO setup is designed to transmit the data streams on separate mode groups (i.e. fully orthogonal system).

Transmission results in a (2×2) MIMO configuration of 13.75 Gbps over 100 m of OM4-grade MMF, 10 Gbps over 350 m and 2.5 Gbps over 1 km with a bit-error rate (BER) of less than 10^{-3} are achieved. It is further shown that the mode orthogonality of the overall system needs to be improved to significantly scale the MIMO approach to higher-order systems beyond a (2×2) configuration when using IM/DD. Thus, new devices need to be found that increase the mode orthogonality in the excitation, MUX and DEMUX processes on one hand and are inexpensive on the other hand. Multi-segment photo detectors have proven to be an alternative component that enables efficient mode separation and optical to electrical conversion in a single device. However, the limited bandwidth of the segments and the required operating wavelength in the 850 nm optical window due to the silicon detector material are bottlenecks. It has also been shown that the analyzed photonic lanterns (they are not optimized for high mode-selectivity) are not suited for MIMO with IM/DD since they exhibit high mode cross-talk in the multiplexing process, which leads to significant interference.

1.3 Published Material

Parts of the thesis have already been published in different conference and journal papers. This list describes, which sections have been reused and gives the corresponding citation.

Chapter 3:

- Parts of Section 3.4 have been published in [Sand20].

Chapter 4:

- Parts of Section 4.1 have been published in [Sand18] and [Sand19].
- Parts of Section 4.2 have been published in [Sand19a][*].

Chapter 5:

- Parts of Section 5.1 have been published in [Sand14] and [Sand16].
- Parts of Section 5.1.1 have been published in [Sand14].
- Parts of Section 5.1.2 have been published in [Sand16] and [Sand17c][†].
- Parts of Section 5.1.3 have been published in [Sand20].
- Parts of Section 5.2 have been published in [Sand17].
- Parts of Section 5.3 have been published in [Sand16a].

---

[*] For reuse permission: A. Sandmann, A. Ahrens and S. Lochmann, Characterization of Mechanically Stressed Multi-Mode Fiber Channels, 2019 International Interdisciplinary PhD Workshop, ©2019 IEEE

[†] For reuse permission: A. Sandmann, A. Ahrens and S. Lochmann, Evaluation of Polynomial Matrix SVD-based Broadband MIMO Equalization in an Optical Multi-Mode Testbed, 2017 Advances in Wireless and Optical Communications, ©2017 IEEE

1.4 Structure of this Thesis

This thesis is divided into 6 chapters, the first being the present introduction. Chapter 2 describes the fundamentals of optical MIMO in terms of fiber mode theory in graded-index fibers and presents a strategy for MIMO signal processing in frequency-selective channel conditions. A transmission system model for optical MIMO with IM/DD is derived in Chapter 3, where it is shown under which conditions the channel can be considered linear in baseband. Chapter 4 characterizes the optical MIMO channel with respect to its power coupling between mode groups and its time-variance properties. Further testbed experiments and end-to-end transmission results, analyzing different hardware components for SDM, are presented in Chapter 5. Chapter 6 provides the closing remarks.

2 Fundamentals of Multi-Mode Fiber Systems with IM/DD for MIMO

In multi-mode fiber transmission, the propagation of different modes can be seen as a challenge to handle the interactions between modes as well as different group delays, and it can also be seen as an opportunity to generate spatial diversity. This chapter describes the fundamental concepts of multi-mode fiber transmission systems with IM/DD. It includes the description of fiber modes, how they can be excited and how modal noise can be avoided. Furthermore, laser source properties are evaluated to understand how they affect the modal phase. Finally, a frequency-selective MIMO signal processing strategy is presented to highlight that a MIMO channel can be transferred into parallel non-interfering transmission layers.

2.1 Modal Analysis in Graded-Index Optical Waveguides

In order to model the propagation of light in a fiber, different concepts exist. They reach from a simple ray optical model over a particle model to one that is based on wave propagation. The latter model is ideal to describe different modes, and hence it is more closely described in this section. In the testbed configurations that are analyzed in this work, mainly graded-index MMFs are used. Thus, the following derivations are focused on graded-index waveguides. In such waveguides the refractive index profile $n(r)$ changes slowly over the radius r. Based on Maxwell's equations, the scalar wave equation can be derived, which applies for such weakly guided fibers [Unge93, p. 198]. Considering the in x-direction linearly polarized electrical field component $\underline{E}_{\mathrm{x}}$, the scalar wave equation is given by

$$\nabla^2 \, \underline{E}_{\mathrm{x}} + n^2(r) \, k^2 \, \underline{E}_{\mathrm{x}} = 0 \ , \tag{2.1}$$

where k is the wave number. Throughout this work underlined variables are complex-valued. A solution of the scalar wave equation is formulated in cylindrical coordinates as follows

$$\underline{E}_{\mathrm{x}}(r, \varphi, z) = \underbrace{\Psi_{mp}(r) \cdot \left\{ \begin{array}{c} \cos(m\varphi) \\ \sin(m\varphi) \end{array} \right\}}_{E_{\mathrm{x}}(r, \varphi)} \cdot \exp(-\mathrm{j}\beta_{mp} z) \ , \tag{2.2}$$

where φ is the angle in the transversal plane, and z is in direction of the fiber length. Variable β_{mp} is the phase constant of the wave propagating in z-direction along the fiber.

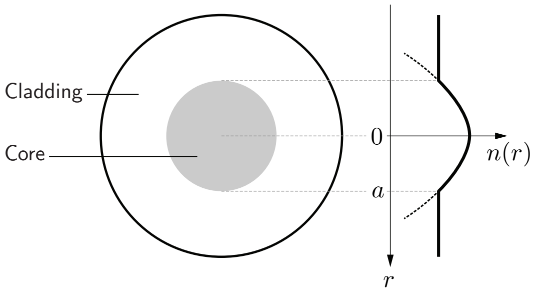

Figure 2.1: Parabolic refractive index profile of a multi-mode fiber

The integer $m = 0, 1, 2, \dots$ denotes the azimuthal order, and $p = 1, 2, 3 \dots$ denotes the radial order. Each combination of these two orders represents a unique solution of the scalar wave equation. These unique solutions are termed fiber modes, and each mode has a distinct electrical field pattern. In the fiber the electrical fields of all modes are superimposed. The cosine and sine factors describe the periodic azimuthal dependency, and the radial field dependency is denoted by $\Psi_{mp}(r)$. Thus, for all m and p so-called cosine and sine modes are present (except for $m = 0$ no sine modes exist). These in x-direction linearly polarized modes are abbreviated as LP modes. Here, $\mathrm{LP}_{mp,\mathrm{a}}$ describes the cosine modes, and $\mathrm{LP}_{mp,\mathrm{b}}$ refer to the sine modes.

A multi-mode fiber with an infinite parabolic refractive index profile is used to obtain an expression for the radial component of the electrical field $\Psi_{mp}(r)$. The fiber cross-section and the refractive index profile are illustrated in Fig. 2.1. In practice, the refractive index of the cladding is constant. However, the continuation of the parabolic refractive index into the cladding is often used as an approximation. Its profile is given by

$$n^2(r) = n^2(0) \left[1 - 2\Delta \left(\frac{r}{a} \right)^2 \right] \quad . \tag{2.3}$$

Parameter a denotes the core radius, and Δ describes the relative difference between the refractive index of the core $n_{\mathrm{co}} = n(0)$ and the refractive index of the cladding $n_{\mathrm{cl}} = n(a)$ as follows

$$\Delta \approx \frac{n_{\mathrm{co}} - n_{\mathrm{cl}}}{n_{\mathrm{co}}} \quad . \tag{2.4}$$

The radial distribution of the electrical field in such a fiber results in [Unge93; Grim89]

$$\Psi_{mp}(r) = \left(\sqrt{2} \frac{r}{\omega_0} \right)^m L_{p-1}^{(m)} \left(\frac{2r^2}{\omega_0^2} \right) \exp \left(-\frac{r^2}{\omega_0^2} \right) \quad , \tag{2.5}$$

with ω_0 denoting the mode field radius when considering the LP_{01} mode, and the generalized Laguerre polynomial is defined by

$$L_q^{(m)}(x) = \sum_{\nu=0}^{q} \binom{q+m}{q-\nu} \frac{(-x)^\nu}{\nu!} \quad . \tag{2.6}$$

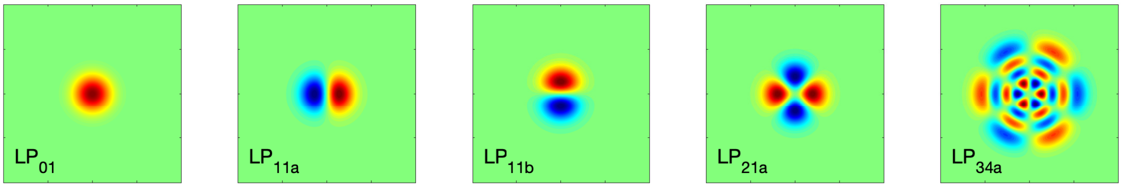

Figure 2.2: Electrical field patterns of different modes in a graded-index fiber (blue: negative amplitudes or 180° phase shift, green: zero, red: positive amplitudes)

The corresponding electrical field of the LP$_{01}$ mode yields

$$\underline{E}_{\mathrm{x}}(r,z) = \exp\left(\frac{-r^2}{\omega_0^2}\right) \cdot \exp(-\mathrm{j}\beta_{01}z) \ , \tag{2.7}$$

being independent on the azimuthal angle φ and having the magnitude 1/e at the mode field radius ω_0. Accordingly, the power at the mode field radius is reduced by 1/e^2 with respect to the maximum intensity. The mode field diameter in a graded-index fiber can be approximated by [Unge93, p. 199]

$$2\omega_0 \approx 2a\sqrt{2/V} \ , \tag{2.8}$$

where V is the V-number. A selection of electrical field patterns of different modes is shown in Fig. 2.2. The power of the LP$_{01}$ mode is concentrated in the core center, whereas higher order modes have a higher portion concentrated at the edge of the fiber core. Modes can be summarized in groups, wherein modes of the same group have a similar propagation delay. The group number can be calculated as follows [Grim89, p. 70]

$$\text{Mode Group Number} = m + 2p - 1 \ . \tag{2.9}$$

A list of modes and their respective groups is given in Tab. 2.1. When considering a continuous wave laser source, the time parameter is added to the spatial distribution as

Table 2.1: Individual modes and their respective groups

Mode group	Individual modes
1	LP$_{01}$
2	LP$_{11\mathrm{a}}$ LP$_{11\mathrm{b}}$
3	LP$_{21\mathrm{a}}$ LP$_{21\mathrm{b}}$ LP$_{02}$
4	LP$_{31\mathrm{a}}$ LP$_{31\mathrm{b}}$ LP$_{12\mathrm{a}}$ LP$_{12\mathrm{b}}$
5	LP$_{41\mathrm{a}}$ LP$_{41\mathrm{b}}$ LP$_{22\mathrm{a}}$ LP$_{22\mathrm{b}}$ LP$_{03}$
6	LP$_{51\mathrm{a}}$ LP$_{51\mathrm{b}}$ LP$_{32\mathrm{a}}$ LP$_{32\mathrm{b}}$ LP$_{13\mathrm{a}}$ LP$_{13\mathrm{b}}$
⋮	⋮

follows

$$\underline{E}_{\mathrm{x}}(r,\varphi,z,t) = \underline{E}_{\mathrm{x}}(r,\varphi,z) \cdot \exp\Big[\mathrm{j}\Big(\omega_{\mathrm{c}} t + \phi(t)\Big)\Big] \ , \tag{2.10}$$

where ω_{c} is the center angular frequency of the laser source, and $\phi(t)$ is the laser phase noise. Therefore, the spatial distribution and time-dependent terms can be clearly separated and independently analyzed.

Modes are the basis to generate spatial diversity in a fiber, enabling the transmission of parallel data streams at the same time and on the same frequency. In theory, each single mode could be used to carry an individual data stream. Considering that at 1550 nm in an OM4-grade MMF 55 modes per polarization can propagate, shows the huge potential of MIMO to multiply the fiber capacity compared to a conventional single-mode fiber SISO transmission. However, the excitation of individual modes is difficult, modes interact with each other in the fiber, and the different mode delays make this not an easy task.

2.1.1 Mode Excitation – SMF to MMF Launch

Consider a transfer from an SMF to MMF with different radial offsets δ, see Fig. 2.3. In this scenario, the power coupling efficiency at the cross-sectional area between the incident mode and a specific mode guided in the MMF can be calculated by taking the overlap of the respective electrical fields as follows [Rame81]

$$c_{mp}(z_0) = \frac{\left| \iint\limits_{-\infty}^{+\infty} \underline{E}_{\mathrm{in}}(x,y,z_0)\, \underline{E}^{*}_{mp}(x,y,z_0)\,\mathrm{d}x\,\mathrm{d}y \right|^2}{\iint\limits_{-\infty}^{+\infty} \underline{E}_{\mathrm{in}}(x,y,z_0)\, \underline{E}^{*}_{\mathrm{in}}(x,y,z_0)\,\mathrm{d}x\,\mathrm{d}y \iint\limits_{-\infty}^{+\infty} \underline{E}_{mp}(x,y,z_0)\, \underline{E}^{*}_{mp}(x,y,z_0)\,\mathrm{d}x\,\mathrm{d}y} \ , \tag{2.11}$$

where $\underline{E}_{\mathrm{in}}(x,y,z_0)$ is the incident electrical field, $\underline{E}_{mp}(x,y,z_0)$ is the field of the specific mode in the MMF, z_0 is the location of the transfer, and $(\,\cdot\,)^*$ denotes the complex conjugate. Since the exact phase relations of the fields in an MMF are not available, an SMF is chosen as the incident fiber type for a theoretical analysis. The calculated power coupling efficiencies for a selection of individual modes and mode groups are depicted in

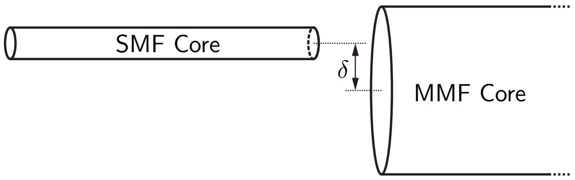

Figure 2.3: Fiber core alignment of an SMF to MMF splice with a certain offset δ for mode-selective excitation

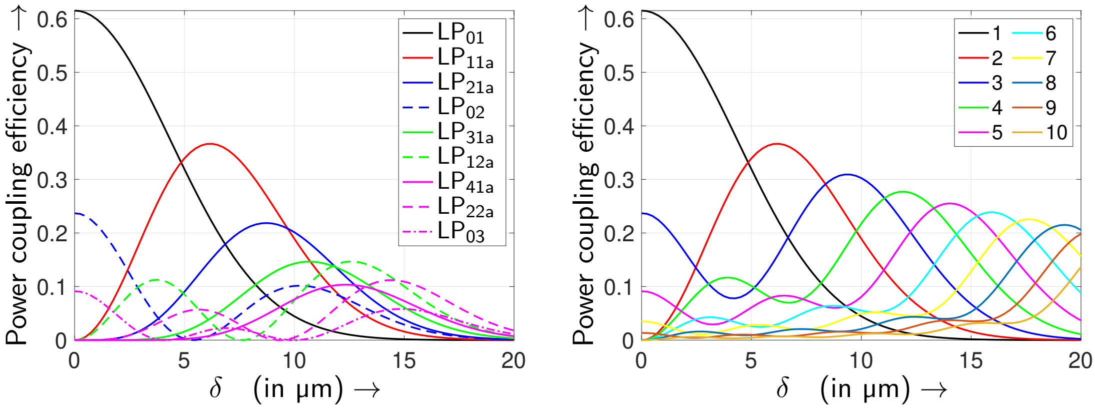

(a) Selected modes

(b) Mode groups
[Legend shows respective group]

Figure 2.4: Power coupling efficiency of a standard SMF to MMF transfer in dependency on the launch offset δ

Fig. 2.4. Here, the wavelength is chosen to be $\lambda = 1550$ nm, and the fiber core radius as well as numerical aperture (NA) are chosen as follows:

$$\text{SMF:} \quad a = 4.1 \text{ µm, NA} = 0.14 \qquad\qquad \text{MMF:} \quad a = 25 \text{ µm, NA} = 0.2 \quad .$$

Please note that the alignment δ is shifted in x-direction, and therefore only cosine modes are excited. The results show that with a centric alignment (i.e. $\delta = 0$ µm) mainly low order modes are excited, and a high offset leads to the excitation of mainly high order modes. Considering mode group number 5 (magenta graph in Fig. 2.4b), it is shown that this group is present over the complete offset band from 0 to 20 µm. In addition, modes within the same group are likely to couple with each other [Carp13]. This already highlights that having a full orthogonal set of modes at the receiver-end is not possible with this excitation method. An early experimental study that demonstrates the excitation of different modes for MIMO applications is presented in [Berd82], and an extension of the theoretic analysis for different spot sizes of the incident electrical field is performed in [Mori13].

Such an SMF to MMF transfer is an easy and low-cost method to excite different modes in the fiber. The overlap integral can also be applied to any kind of transfer where the input and output electrical fields do not match, such as transfers between different fiber types or in cases of fiber misalignment. Therefore, each connector between two MMFs introduces mode coupling due to the core concentricity error. This needs to be avoided in MIMO systems by minimizing the number of MMF connectors.

2.1.2 MMF Direct Detection and Modal Noise

In general, the current produced by a photo diode at the receiver is proportional to the incident optical power, and hence it is proportional to the square of the incident electrical field. By additionally taking the spatial distribution and the phase of the electrical field into account, the detection can be modeled as a square-law process as follows

$$u = F \iint\limits_{A} \left|\underline{E}_\mathrm{x}(x, y, z_1)\right|^2 \mathrm{d}x\,\mathrm{d}y \quad . \tag{2.12}$$

Herein, the detector surface area is A, and F is a conversion factor that includes the responsivity and transimpedance such that u is a voltage.

Modal noise is introduced at transitions (e.g. connectors or at the detector) where just parts of the electrical field are covered. This is caused by changes of the modal phases that lead to a varying speckle pattern. Specifically, when considering narrow-linewidth lasers, these speckle patterns are pronounced. When a detector covers the whole MMF surface area, no modal noise occurs since the modes are orthogonal to each other. Hereinafter, let us revise this fact and analyze what happens, if the detector consists of a radial symmetric segment that does not cover the whole fiber end-face area. This case is of interest when considering multi-segment detection in multi-mode MIMO systems. The subsequent derivation and notation is inspired by [Schoe09, pp. 34–37]. The superposition of multiple modes at the detector can be written as follows

$$\underline{E}_\mathrm{x}(r, \varphi, z_1) = \sum_{m,p} A_{mp} \cdot \Psi_{mp}(r) \cdot \left\{ \begin{array}{c} \cos(m\varphi) \\ \sin(m\varphi) \end{array} \right\} \cdot \exp(\mathrm{j}\zeta_{mp}) \quad . \tag{2.13}$$

The phase variable ζ_{mp} subsumes the modal phase change, the carrier and laser phase noise. Thus, it can be considered as a time-variant variable, and hence the expression is a superposition of electrical fields with changing phases. This results in changing speckle patterns and is the origin of modal noise. Let us summarize the orders m and p into a single index i for simplification purposes. Combining the products into a single variable $\underline{G}_i$ we can write

$$\underline{E}_\mathrm{x}(r, \varphi, z_1) = \sum_{i} \underline{G}_i \quad . \tag{2.14}$$

Considering the detection of just two superimposed modes, then the direct detection is given by

$$\begin{aligned} u &= F \iint\limits_{A} \left|\underline{G}_1 + \underline{G}_2\right|^2 \mathrm{d}x\,\mathrm{d}y = \iint\limits_{A} (\underline{G}_1 + \underline{G}_2) \cdot (\underline{G}_1 + \underline{G}_2)^* \,\mathrm{d}x\,\mathrm{d}y \\ &= F \iint\limits_{A} \left(\underline{G}_1\,\underline{G}_1^* + \underline{G}_1\,\underline{G}_2^* + \underline{G}_2\,\underline{G}_1^* + \underline{G}_2\,\underline{G}_2^*\right) \mathrm{d}x\,\mathrm{d}y \quad . \end{aligned} \tag{2.15}$$

In $\underline{G}_1\,\underline{G}_1^*$ and $\underline{G}_2\,\underline{G}_2^*$ the phase is eliminated, and hence no modal noise originates from these terms. Therefore, the focus is on the mixed products where $\underline{G}_1\,\underline{G}_2^*$ is representatively analyzed. Assuming an infinitely large detection area, the integral of this product is expressed by

$$\int_{-\infty}^{+\infty}\int_{-\infty}^{+\infty} \underline{G}_1\, \underline{G}_2^*\, \mathrm{d}x\, \mathrm{d}y = A_{m_1p_1} A_{m_2p_2}\, \exp\Big(\mathrm{j}\left(\zeta_{m_1p_1} - \zeta_{m_2p_2}\right)\Big) \cdot \ldots$$
$$\ldots \int_0^\infty \Psi_{m_1p_1}(r)\, \Psi_{m_2p_2}(r)\, r \int_0^{2\pi} \left\{ \begin{array}{c} \cos(m_1\varphi) \\ \sin(m_1\varphi) \end{array} \right\} \left\{ \begin{array}{c} \cos(m_2\varphi) \\ \sin(m_2\varphi) \end{array} \right\} \mathrm{d}\varphi\, \mathrm{d}r \ . \tag{2.16}$$

Please note that $\mathrm{d}x\, \mathrm{d}y = r\, \mathrm{d}\varphi\, \mathrm{d}r$ when converting from Cartesian into polar coordinates. Let us consider the detection of the whole fiber end-face area. Since the azimuthal order of both modes $m_1, m_2 \in \mathbb{Z}$ it follows

$$\int_0^{2\pi} \cos(m_1\varphi)\, \sin(m_2\varphi)\, \mathrm{d}\varphi = 0 \ . \tag{2.17}$$

Thus, cosine and sine modes are fully orthogonal. Furthermore, the following applies

$$\int_0^{2\pi} \cos(m_1\varphi)\, \cos(m_2\varphi)\, \mathrm{d}\varphi = \begin{cases} 0 & : \quad m_1 \neq m_2 \\ \pi & : \quad m_1 = m_2 \neq 0 \\ 2\pi & : \quad m_1 = m_2 = 0 \end{cases} \tag{2.18}$$

and

$$\int_0^{2\pi} \sin(m_1\varphi)\, \sin(m_2\varphi)\, \mathrm{d}\varphi = \begin{cases} 0 & : \quad m_1 \neq m_2 \\ \pi & : \quad m_1 = m_2 \neq 0 \\ 0 & : \quad m_1 = m_2 = 0 \ . \end{cases} \tag{2.19}$$

Please note that no sine modes with $m = 0$ exist. If the azimuthal orders are different (i.e. $m_1 \neq m_2$), no modal noise exists when two sine or cosine modes overlap. Otherwise, if $m_1 = m_2 = m$ the focus needs to be on the integral over the radial field distribution consisting of the generalized Laguerre polynomial:

$$\int_0^\infty \Psi_{mp_1}(r)\, \Psi_{mp_2}(r)\, r\, \mathrm{d}r = \ldots$$
$$\ldots = \int_0^\infty \left(\sqrt{2}\frac{r}{\omega_0}\right)^{2m} L_{p_1-1}^{(m)}\!\left(\frac{2r^2}{\omega_0^2}\right) L_{p_2-1}^{(m)}\!\left(\frac{2r^2}{\omega_0^2}\right) \exp\!\left(-\frac{2r^2}{\omega_0^2}\right) r\, \mathrm{d}r \ . \tag{2.20}$$

Substituting $v = 2\, r^2/\omega_0^2$ and using

$$r\, \mathrm{d}r = \frac{\omega_0^2}{4}\, \mathrm{d}v \ , \tag{2.21}$$

we get [Bron05, p. 531]

$$\begin{aligned}\int\limits_0^\infty \Psi_{mp_1}(r)\,\Psi_{mp_2}(r)\,r\,\mathrm{d}r &= \frac{\omega_0^2}{4}\int\limits_0^\infty v^m\,L_{p_1-1}^{(m)}(v)\,L_{p_2-1}^{(m)}(v)\ \exp(-v)\,\mathrm{d}v \\ &= \frac{\omega_0^2}{4}\binom{p_2+m-1}{p_2-1}\Gamma(1+m)\,\delta_{p_1,p_2}\ ,\end{aligned} \tag{2.22}$$

where $\Gamma(\,\cdot\,)$ is the gamma function, and δ_{p_1,p_2} denotes the Kronecker delta. Thus, the integral is zero, if the radial orders are different (i.e. $p_1 \neq p_2$).

Overall, the surface integral over the mixed product can be summarized as follows

$$\begin{aligned}&\int\limits_{-\infty}^{+\infty}\int\limits_{-\infty}^{+\infty} \underline{G}_1\,\underline{G}_2^*\,\mathrm{d}x\,\mathrm{d}y = \int\limits_{-\infty}^{+\infty}\int\limits_{-\infty}^{+\infty} \underline{G}_2\,\underline{G}_1^*\,\mathrm{d}x\,\mathrm{d}y \dots \\ &\dots \propto \begin{cases} 0 & : \text{ sine AND cosine modes overlap} \\ 0 & : m_1 \neq m_2 \text{ OR } p_2 \neq p_2 \\ \dfrac{\omega_0^2}{4}\dbinom{p_2+m-1}{p_2-1}\Gamma(1+m)\,\delta_{p_1,p_2} & : m_1 = m_2 \text{ AND } p_1 = p_2\ ,\end{cases}\end{aligned} \tag{2.23}$$

where symbol $\propto$ denotes 'proportional to'. Therefore, the modes are orthogonal in the direct detection process, and no modal noise occurs, if the whole fiber end-face area is detected. Considering a multi-segment detector setup, the use of a radial symmetric geometry reduces, but not fully eliminates the modal noise since the integral over the azimuthal angle is zero in cases where the azimuthal orders differ (i.e. $m_1 \neq m_2$). In other words, if there is no symmetry in the detector surface area when not the complete electrical field is detected, the integration over the azimuthal angle would not be zero for different orders of m, leading to additional modal noise compared to a radial symmetric geometry.

2.2 Modeling of non-ideal Lasers

The phase of each fiber mode is fundamental to understand the origin of interference effects in multi-mode fiber MIMO systems, and the laser source has a major impact on the phase and phase changes. In addition, the laser choice plays an important role when considering chromatic dispersion. This type of dispersion depends on the operating conditions (such as the fiber profile) and the spectral content of the transmitted signal. In general, two factors that contribute to the total spectral width of the modulated optical signal are differentiated. Firstly, spectral broadening occurs when a data signal is modulated with an ideal carrier, i.e. monochromatic light. Secondly, the carrier is never ideal and is usually characterized by its spectral width $\Delta\lambda$ (in nm) or Δf (in Hz). This spectral width or linewidth of the laser's power spectral density (PSD) $\Phi_{\mathrm{AA}}(f)$ can be equally described in time-domain by a harmonic carrier with phase noise $\phi(t)$. The laser phase noise can be modeled as a Wiener process having the variance σ_p^2. Other equivalent descriptions are the coherence time τ_coh, coherence length L_coh and the temporal auto-correlation function (ACF) of the carrier signal.

Hereinafter, the relations between the equivalent description methods as shown in Figure 2.5 are presented with respect to the temporal properties of lasers. Spatial coherence properties are not considered.

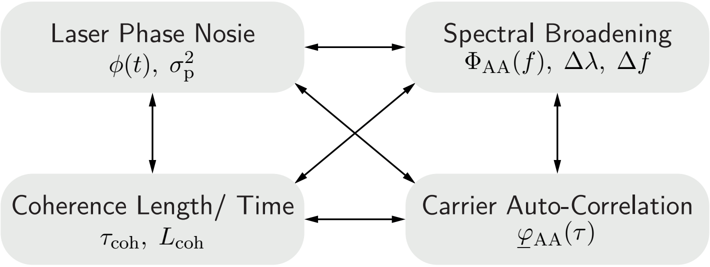

Figure 2.5: Interchangeable terminology for a non-ideal laser

2.2.1 Influence of Laser Phase Noise on the Carrier Signal's PSD

Real world semiconductor lasers have amplitude and phase noise, which mainly originate from spontaneous emissions of photons [Yari89, pp. 577–591]. Focusing on phase noise, a carrier signal is given by

$$\underline{A}(t) = A_0 \exp\Big[\mathrm{j}\Big(\omega_\mathrm{c} t + \phi(t)\Big)\Big] \quad . \tag{2.24}$$

The laser phase noise $\phi(t)$ can be described as a Wiener process in which the phase increments between two time instances t and $t+\tau$ are independent as well as normal distributed with zero mean and variance σ_p^2 as given by [Stee13]:

$$\Delta\phi = \phi(t+\tau) - \phi(t) \quad \propto \mathcal{N}(0, \sigma_\mathrm{p}^2) \enspace . \tag{2.25}$$

This phase noise description can be directly translated into spectral broadening of the carrier signal's PSD. Therefore, let us define the ACF of the carrier signal as follows

$$\underline{\varphi}_\mathrm{AA}(\tau) = \mathrm{E}\{\underline{A}(t+\tau)\,\underline{A}^*(t)\} = A_0^2 \exp(\mathrm{j}\omega_\mathrm{c}\tau) \cdot \mathrm{E}\{\exp(\mathrm{j}\Delta\phi)\} \enspace , \tag{2.26}$$

with $\mathrm{E}\{\,\cdot\,\}$ denoting the expectation functional. The probability density function of the phase increment is Gaussian-distributed as defined by

$$g(\Delta\phi) = \frac{1}{\sigma_\mathrm{p}\sqrt{2\pi}} \exp\left(-\frac{\Delta\phi^2}{2\sigma_\mathrm{p}^2}\right) \enspace . \tag{2.27}$$

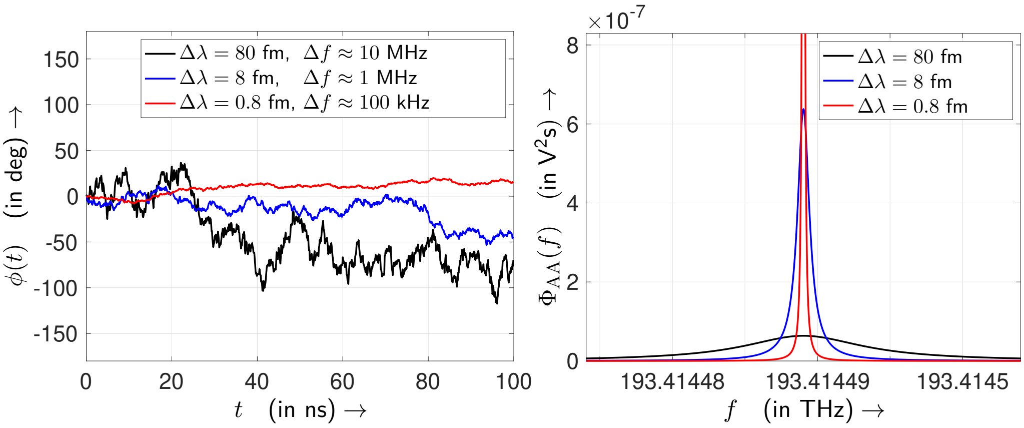

Figure 2.6: Realization of the phase evolution as a Wiener process (left) and their corresponding PSD (right) using laser sources of different spectral FWHM $\Delta\lambda$ at 1550 nm

Here, the variance is proportional to the delay between two phase samples as given by $\sigma_{\mathrm{p}}^2 = b\,|\tau|$. It has been shown in [Stee13] that the ACF results in

$$\underline{\varphi}_{\mathrm{AA}}(\tau) = A_0^2 \exp(\mathrm{j}\omega_{\mathrm{c}}\tau) \exp\left(-\frac{b\,|\tau|}{2}\right) \,. \tag{2.28}$$

With the ACF, the PSD of the carrier signal is calculated by using the Wiener–Khinchin theorem, which is essentially the application of the Fourier transform. The resulting PSD is given by

$$\Phi_{\mathrm{AA}}(\omega) = \frac{A_0^2\,b}{\dfrac{b^2}{4} + (\omega - \omega_{\mathrm{c}})^2} \,, \tag{2.29}$$

which is a frequency shifted Lorentzian function. Herein, the proportionality factor b is the full width at half maximum (FWHM) $\Delta\omega$ of the Lorentzian function such that

$$\underline{\varphi}_{\mathrm{AA}}(\tau) = A_0^2 \exp(\mathrm{j}\omega_{\mathrm{c}}\tau) \exp\left(-\frac{\Delta\omega\,|\tau|}{2}\right) \quad \circ\!\!-\!\!\bullet \quad \Phi_{\mathrm{AA}}(\omega) = \frac{A_0^2\,\Delta\omega}{\dfrac{\Delta\omega^2}{4} + (\omega - \omega_{\mathrm{c}})^2} \,. \tag{2.30}$$

Please note that $\Delta\omega = 2\pi\,\Delta f$, and hence the variance of the phase noise increments is given by

$$\sigma_{\mathrm{p}}^2 = 2\pi\,\Delta f\,|\tau| \,. \tag{2.31}$$

The FWHM Δf in the unit Hz is termed laser linewidth. An example of the phase evolution and their corresponding PSDs is shown in Fig. 2.6.

Spectral Broadening by Modulation When modulating a baseband signal $s(t)$ with an ideal monochromatic laser, see Fig. 2.7, the modulated signal $\underline{s}_{\mathrm{o}}^{+}(t)$ has a spectral width according to the transmit signal. Its spectral width depends on the data rate and the

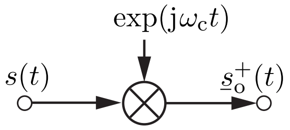

Figure 2.7: Modulation scheme

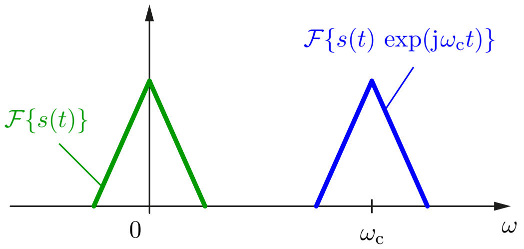

Figure 2.8: Spectrum of the baseband and modulated bandpass transmit signal

pulse shaping form. A simplified example for the corresponding spectrum is illustrated in Fig. 2.8.

2.2.2 Coherence Time and Length

In the previous section, the relation between laser phase noise and spectral width has been presented. In this part, it is shown how these terms connect to coherence length and coherence time.

Joint light waves of the same frequency are considered coherent, if they are in phase with each other. A suitable measure of the degree of coherence is the ACF of the carrier signal, which compares the carrier $\underline{A}(t)$ with its delayed version $\underline{A}(t+\tau)$ as defined by

$$\underline{\varphi}_\mathrm{AA}(\tau) = \mathrm{E}\{\underline{A}(t+\tau)\,\underline{A}^*(t)\} \ . \tag{2.32}$$

With the normalized ACF

$$\underline{g}(\tau) = \frac{\underline{\varphi}_\mathrm{AA}(\tau)}{\underline{\varphi}_\mathrm{AA}(0)} \ , \tag{2.33}$$

the coherence time is defined as the width of $|\underline{g}(\tau)|$, which is the absolute normalized ACF. Since the definition of the width varies in the literature, e.g. taking the FWHM where the value decays to 1/2 or using the 1/e value, we take the power equivalent width as it is proposed in [Sale91, pp. 346–349] as follows

$$\tau_\mathrm{coh} = \int\limits_{-\infty}^{+\infty} |\underline{g}(\tau)|^2 \mathrm{d}\tau \ . \tag{2.34}$$

An ideal monochromatic carrier $\underline{A}(t) = A_0 \exp\{\mathrm{j}\omega_\mathrm{c}t\}$ has the corresponding normalized ACF $\underline{g}(\tau) = \exp\{\mathrm{j}\omega_\mathrm{c}\tau\}$, resulting in $|\underline{g}(\tau)| = 1$. In this case the coherence time is infinite. For a non-ideal laser with a Lorentzian shaped PSD, see Eq. 2.30, the ACF is given by

$$\underline{\varphi}_\mathrm{AA}(\tau) = A_0^2 \exp(\mathrm{j}\omega_\mathrm{c}\tau)\ \exp\left(-\frac{\Delta\omega\,|\tau|}{2}\right) \ , \tag{2.35}$$

and therefore the absolute normalized ACF results in

$$|\underline{g}(\tau)| = \exp\left(-\frac{\Delta\omega\,|\tau|}{2}\right) \ . \tag{2.36}$$

This function is illustrated in Fig. 2.9. By calculating the power equivalent width (compare Eq. 2.34), the coherence time results in

$$\tau_{\mathrm{coh}} = \frac{2}{\Delta\omega} = \frac{1}{\pi\,\Delta f} \approx \frac{\lambda^2}{\pi \cdot \Delta\lambda \cdot c} \ , \tag{2.37}$$

with c being the speed of light. This coherence time definition deviates from other definitions in various literature by the factor $1/\pi$ [Grim89, p. 66]. In these sources, it is assumed that the PSD is rectangularly shaped as given by

$$\Phi_{\sqcap}(\omega) = C \cdot \mathrm{rect}\left(\frac{\omega - \omega_{\mathrm{c}}}{\Delta\omega}\right) \ , \tag{2.38}$$

where $\mathrm{rect}(\,\cdot\,)$ is the rectangular function. With this shape, the normalized ACF results in

$$\underline{g}_{\sqcap}(\tau) = \mathrm{si}\left(\Delta\omega\frac{\tau}{2}\right)\ \exp(\mathrm{j}\omega_{\mathrm{c}}\tau) \ , \tag{2.39}$$

and the coherence time can be easily calculated by using Parseval's theorem as follows

$$\tau_{\mathrm{coh},\sqcap} = \int_{-\infty}^{\infty} |\underline{g}_{\sqcap}(\tau)|^2 \mathrm{d}\tau = \frac{1}{2\pi}\int_{-\infty}^{\infty} |G_{\sqcap}(\omega)|^2 \mathrm{d}\omega = \frac{2\pi}{\Delta\omega} = \frac{1}{\Delta f} \ . \tag{2.40}$$

Since a measured PSD is more similar to a Lorentzian than a rectangular shape, Eq. 2.37 is used for calculating the coherence time.

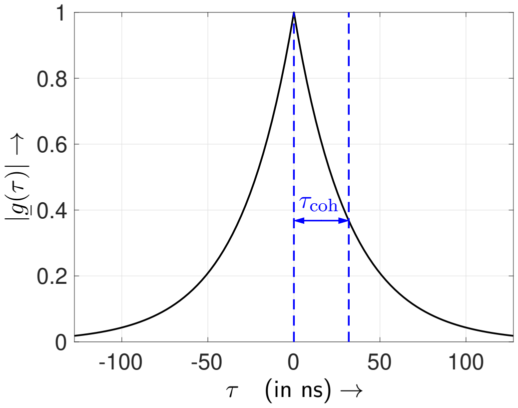

Figure 2.9: Absolute normalized ACF of a laser source with $\Delta\lambda = 80$ fm and a center wavelength of 1550 nm

In order to obtain the relation between spectral width in frequency and wavelength units, consider the wavelength-frequency relation in vacuum as expressed by

$$\lambda = \frac{c}{f} \ . \tag{2.41}$$

The derivative of λ with respect to f is used to obtain the difference quotient as follows

$$\frac{\mathrm{d}\lambda}{\mathrm{d}f} = -\frac{c}{f^2} \ , \qquad \text{and hence} \qquad \frac{\Delta\lambda}{\Delta f} \approx \frac{c}{f^2} \ . \tag{2.42}$$

Therefore, the relation between the spectral width in frequency and wavelength units is given by

$$\Delta\lambda \approx \Delta f \cdot \frac{\lambda^2}{c} \ , \qquad \text{and} \qquad \Delta f \approx \Delta\lambda \cdot \frac{c}{\lambda^2} \ . \tag{2.43}$$

Please note that the center wavelength and the spectral width in the data-sheet of lasers are defined in vacuum. Thus, the refractive index is neglected. The coherence length in a medium with an effective refractive index n is defined by

$$L_{\text{coh}} = \frac{c}{n} \cdot \tau_{\text{coh}} \ . \tag{2.44}$$

Table 2.2 lists the coherence times and lengths for light sources, which are common in telecommunications. Considering a light-emitting diode (LED) or a Fabry-Pérot laser, the coherence length is in the range of a few micrometers. A distributed feedback (DFB) laser has a coherence length of a few decimeters to a few meters. The properties of a signal reflected by a fiber Bragg grating (FBG) are listed as well.

Besides the laser phase noise, originating from spontaneous emissions of photons and leading to a Lorentzian PSD profile, the laser current is not ideal. The $1/f$ electronic noise of the laser current leads to a Gaussian PSD profile. Thus, the overall laser spectrum is described as the convolution of a Lorentzian and Gaussian PSD profile, which is named Voigt profile [Nguy10].

Table 2.2: Coherence times and lengths for light sources with different spectral FWHM $\Delta\lambda$ at a center wavelength of $\lambda = 1550$ nm

Device	Typical $\Delta\lambda$ [Agil01] in vacuum	Coherence time	Coherence length in fiber ($n = 1.5$)
LED	30 . . . 100 nm	85 fs . . . 26 fs	17 µm . . . 5.1 µm
Fabry-Pérot Laser	3 . . . 20 nm	850 fs . . . 128 fs	170 µm . . . 25 µm
DFB Laser	80 . . . 800 fm	31.9 ns . . . 3.19 ns	6.37 m . . . 637 mm
100 kHz Laser	0.8 fm	3.19 µs	637 m
Reflected FBG Spectrum	100 pm	26 ps	5.1 mm

2.3 MIMO Signal Processing for Frequency-selective Channels

In addition to chromatic dispersion and attenuation, which are the main impairment factors in single-mode SISO transmission systems, multi-mode MIMO systems need to account for modal dispersion, different modal attenuation, mode mixing and interference effects due to the different modal phases. In Section 3.4 it is shown that under certain conditions a MIMO system with IM/DD can be considered linear in baseband. Therefore, equalization techniques that are well-known from wireless MIMO systems can be applied to optical MIMO systems with IM/DD as well. At a high symbol rate and a sufficiently long transmission distance, these systems exhibit a frequency-selective characteristic. This means that interferences between neighboring symbols occur, i.e. inter-symbol interference (ISI). The additional mode cross-talk leads to inter-channel interference (ICI), and in combination they demand for a combined spatial and temporal MIMO equalization approach. Since in this work the focus is on low-cost MIMO systems, transmitter-side equalization strategies that require a feedback channel to obtain the channel-state information at the transmitter, are not reasonable. Thus, the focus is on receiver-side and electronic equalization strategies. At the receiver, the channel-state information can be obtained by using a pilot-based least-squares estimator as it is described in [Weik07]. This type of estimator is used in all testbed configurations of this work. The following list is a non-comprehensive overview of equalization techniques that match the requirements of low-cost MIMO systems with IM/DD:

- Feed-forward equalizers: Zero forcing, minimum mean square error (MMSE) [Ette75]
- Decision feedback equalizer (DFE) [Al-D00]
- Adaptive equalization strategies: Least mean squares, recursive least squares [Male99]
- QR-decomposition-based approach with subsequent successive-interference cancellation; For frequency-selective channels, polynomial matrix QR decomposition can be used [Davi09; Fost10].
- Strategies that prevent ICI with fully orthogonal multiplexing and remove the remaining ISI with SISO signal processing, e.g. with discrete multi-tone [Gatt19].

Singular-value decomposition-based equalization strategies are not feasible since they require transmitter-side pre-processing. In this work, feed-forward and decision feedback strategies are applied due to their simplicity. Therefore, the MMSE-DFE is derived hereinafter to give an introduction to MIMO equalization.

2.3.1 Broadband MMSE-DFE System Model

The presented DFE, which is suited for broadband MIMO channels, is a well-known concept and is derived with reference to [Al-D00]. The beauty of the subsequent derivation for the MMSE-DFE is that different linear equalizer types can be obtained as special cases. This includes the zero forcing (ZF) feed forward equalizer (FFE) and the MMSE-FFE. The included forward and backward filters have a finite impulse response characteristic, and hence they are stable.

A general broadband MIMO channel model is illustrated in Fig. 2.10. Herein, $\underline{s}_\mu[k]$ denotes the k-th transmit symbol at MIMO input $\mu = 1, \ldots, n_{\mathrm{T}}$, signal $\underline{r}_\nu[k]$ denotes the corresponding receive symbol at MIMO output $\nu = 1, \ldots, n_{\mathrm{R}}$, and $\underline{n}_\nu[k]$ is the noise signal. Matrix $\boldsymbol{H}(z)$ represents the frequency-selective MIMO channel, with z^{-1} denoting the unit delay in this section.

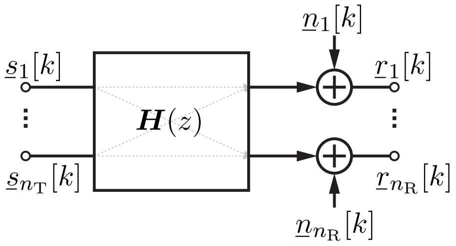

Figure 2.10: Broadband MIMO channel

An MMSE-DFE consists of an FFE $\boldsymbol{F}(z)$ and a backward equalizer $\boldsymbol{B}(z)$, which is visible in the corresponding system model in Fig. 2.11. The general idea of this equalization concept is to compare the MIMO transmit symbols in vector $\boldsymbol{s}_k$ with the equalized MIMO receive symbols in vector $\boldsymbol{z}_k$ and minimize the mean square error of the resulting error vector $\boldsymbol{e}_k$. Since the channel can introduce a delay, vectors $\boldsymbol{s}_k$ and $\boldsymbol{z}_k$ need to be synchronized by introducing a delay of κ symbols, compare path with dashed lines. The number of parallel channel input streams is n_{T}, the number of channel output streams is n_{R}, and the number of forward equalizer output streams is n_{T}. Vector $\boldsymbol{n}_k$ includes the MIMO noise samples, vector $\boldsymbol{r}_k$ contains the MIMO receive symbols, $\boldsymbol{y}_k$ represents the output vector of the FFE, and $\hat{\boldsymbol{s}}_{k-\kappa}$ is the estimated transmit symbol vector. The dimensions and exact structures of these vectors are derived hereinafter. Please note that a hard-decision block is included in the model, and the decided symbols are used for the feedback. Approaches with soft-decision exist that adjust the weights of the feedback coefficients according to the likelihood of a correct decision [Bala00].

Subsequently, the system model is described in matrix notation, and the MMSE-DFE is derived, assuming that the frequency-selective MIMO channel $\boldsymbol{H}(z)$, the FFE $\boldsymbol{F}(z)$ and the backward equalizer $\boldsymbol{B}(z)$ are finite impulse response filters, see [Al-D00]. The received symbol at MIMO output ν is given by

$$\underline{r}_\nu[k] = \sum_{\mu=1}^{n_{\mathrm{T}}} \sum_{i=0}^{L_{\mathrm{h}}-1} \underline{h}_{\nu\mu}[i]\, \underline{s}_\mu[k-i] + \underline{n}_\nu[k] \ , \tag{2.45}$$

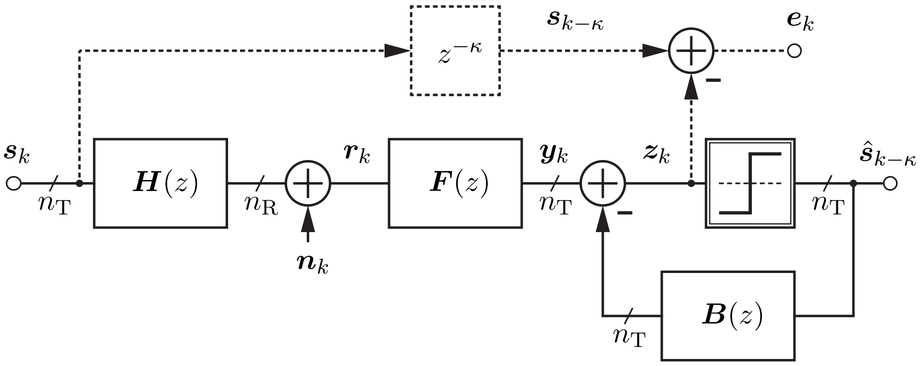

Figure 2.11: MIMO channel and DFE signal model

where the i-th channel coefficient between MIMO input μ and output ν is given by $\underline{h}_{\nu\mu}[i]$. The number of channel taps is L_h. Summarizing all n_R received signals in matrix notation results in

$$\begin{pmatrix} \underline{r}_1[k] \\ \vdots \\ \underline{r}_{n_\mathrm{R}}[k] \end{pmatrix} = \sum_{i=0}^{L_\mathrm{h}-1} \begin{pmatrix} \underline{h}_{11}[i] & \cdots & \underline{h}_{1n_\mathrm{T}}[i] \\ \vdots & \ddots & \vdots \\ \underline{h}_{n_\mathrm{R}1}[i] & \cdots & \underline{h}_{n_\mathrm{R}n_\mathrm{T}}[i] \end{pmatrix} \cdot \begin{pmatrix} \underline{s}_1[k-i] \\ \vdots \\ \underline{s}_{n_\mathrm{T}}[k-i] \end{pmatrix} + \begin{pmatrix} \underline{n}_1[k] \\ \vdots \\ \underline{n}_{n_\mathrm{R}}[k] \end{pmatrix} \tag{2.46}$$

and is shortened as follows

$$\underset{(n_\mathrm{R}\times 1)}{\boldsymbol{r}_k} = \sum_{i=0}^{L_\mathrm{h}-1} \underset{(n_\mathrm{R}\times n_\mathrm{T})}{\boldsymbol{H}_i} \cdot \underset{(n_\mathrm{T}\times 1)}{\boldsymbol{s}_{k-i}} + \underset{(n_\mathrm{R}\times 1)}{\boldsymbol{n}_k} \quad . \tag{2.47}$$

Throughout this work bold upper case symbols denote matrices and bold lower case symbols are vectors. Rewriting the summation as a matrix multiplication leads to

$$\boldsymbol{r}_k = \begin{pmatrix} \boldsymbol{H}_0 & \boldsymbol{H}_1 & \cdots & \boldsymbol{H}_{L_\mathrm{h}-1} \end{pmatrix} \cdot \begin{pmatrix} \boldsymbol{s}_k \\ \boldsymbol{s}_{k-1} \\ \vdots \\ \boldsymbol{s}_{k-L_\mathrm{h}+1} \end{pmatrix} + \boldsymbol{n}_k \quad . \tag{2.48}$$

For the system description the receive vectors of previous time instances are needed in the range from

$$\boldsymbol{r}_{k-1} = \begin{pmatrix} \boldsymbol{H}_0 & \boldsymbol{H}_1 & \cdots & \boldsymbol{H}_{L_\mathrm{h}-1} \end{pmatrix} \cdot \begin{pmatrix} \boldsymbol{s}_{k-1} \\ \boldsymbol{s}_{k-2} \\ \vdots \\ \boldsymbol{s}_{k-L_\mathrm{h}} \end{pmatrix} + \boldsymbol{n}_{k-1} \tag{2.49}$$

to

$$\boldsymbol{r}_{k-L_\mathrm{f}+1} = \begin{pmatrix} \boldsymbol{H}_0 & \boldsymbol{H}_1 & \cdots & \boldsymbol{H}_{L_\mathrm{h}-1} \end{pmatrix} \cdot \begin{pmatrix} \boldsymbol{s}_{k-L_\mathrm{f}+1} \\ \boldsymbol{s}_{k-L_\mathrm{f}} \\ \vdots \\ \boldsymbol{s}_{k-L_\mathrm{f}-L_\mathrm{h}+2} \end{pmatrix} + \boldsymbol{n}_{k-L_\mathrm{f}+1} \ , \tag{2.50}$$

where L_f is the number of FFE coefficients. These equations are summarized by using the matrix $\boldsymbol{H}_\mathrm{M}$ as follows

$$\begin{pmatrix} \boldsymbol{r}_k \\ \boldsymbol{r}_{k-1} \\ \vdots \\ \boldsymbol{r}_{k-L_\mathrm{f}+1} \end{pmatrix} = \boldsymbol{H}_\mathrm{M} \cdot \begin{pmatrix} \boldsymbol{s}_k \\ \boldsymbol{s}_{k-1} \\ \boldsymbol{s}_{k-2} \\ \vdots \\ \boldsymbol{s}_{k-L_\mathrm{f}-L_\mathrm{h}+2} \end{pmatrix} + \begin{pmatrix} \boldsymbol{n}_k \\ \boldsymbol{n}_{k-1} \\ \vdots \\ \boldsymbol{n}_{k-L_\mathrm{f}+1} \end{pmatrix} \ , \tag{2.51}$$

with

$$\boldsymbol{H}_\mathrm{M} = \begin{pmatrix} \boldsymbol{H}_0 & \boldsymbol{H}_1 & \boldsymbol{H}_2 & \cdots & \boldsymbol{H}_{L_\mathrm{h}-1} & \mathbf{0} & \cdots & \mathbf{0} \\ \mathbf{0} & \boldsymbol{H}_0 & \boldsymbol{H}_1 & \cdots & \boldsymbol{H}_{L_\mathrm{h}-2} & \boldsymbol{H}_{L_\mathrm{h}-1} & \cdots & \mathbf{0} \\ \mathbf{0} & \mathbf{0} & \boldsymbol{H}_0 & \cdots & \boldsymbol{H}_{L_\mathrm{h}-3} & \boldsymbol{H}_{L_\mathrm{h}-2} & \cdots & \mathbf{0} \\ \vdots & \vdots & \vdots & \ddots & & & \ddots & \vdots \\ \mathbf{0} & \mathbf{0} & \mathbf{0} & \cdots & & & \cdots & \boldsymbol{H}_{L_\mathrm{h}-1} \end{pmatrix} \ , \tag{2.52}$$

where $\mathbf{0}$ denotes a zero matrix. Equation 2.51 is summarized as follows

$$\underset{(n_\mathrm{R}\,L_\mathrm{f}\times 1)}{\boldsymbol{r}_\mathrm{V}} = \underset{(n_\mathrm{R}\,L_\mathrm{f}\times n_\mathrm{T}\,(L_\mathrm{f}+L_\mathrm{h}-1))}{\boldsymbol{H}_\mathrm{M}} \cdot \underset{(n_\mathrm{T}\,(L_\mathrm{f}+L_\mathrm{h}-1)\times 1)}{\boldsymbol{s}_\mathrm{V}} + \underset{(n_\mathrm{R}\,L_\mathrm{f}\times 1)}{\boldsymbol{n}_\mathrm{V}} \ . \tag{2.53}$$

By defining the input auto-correlation matrix

$$\boldsymbol{R}_{ss} = \mathrm{E}\{\boldsymbol{s}_\mathrm{V}\,\boldsymbol{s}_\mathrm{V}^\mathsf{H}\} \quad \in \mathbb{C}^{(n_\mathrm{T}\,(L_\mathrm{f}+L_\mathrm{h}-1)\times n_\mathrm{T}\,(L_\mathrm{f}+L_\mathrm{h}-1))} \tag{2.54}$$

and the noise auto-correlation matrix

$$\boldsymbol{R}_{nn} = \mathrm{E}\{\boldsymbol{n}_\mathrm{V}\,\boldsymbol{n}_\mathrm{V}^\mathsf{H}\} \quad \in \mathbb{C}^{(n_\mathrm{R}\,L_\mathrm{f}\times n_\mathrm{R}\,L_\mathrm{f})} \ , \tag{2.55}$$

the input-output cross-correlation matrix is given by

$$\begin{aligned} \boldsymbol{R}_{sr} &= \mathrm{E}\{\boldsymbol{s}_\mathrm{V}\,\boldsymbol{r}_\mathrm{V}^\mathsf{H}\} = \mathrm{E}\{\boldsymbol{s}_\mathrm{V}\,(\boldsymbol{H}_\mathrm{M}\,\boldsymbol{s}_\mathrm{V} + \boldsymbol{n}_\mathrm{V})^\mathsf{H}\} \\ &= \boldsymbol{R}_{ss}\,\boldsymbol{H}_\mathrm{M}^\mathsf{H} \quad \in \mathbb{C}^{(n_\mathrm{T}\,(L_\mathrm{f}+L_\mathrm{h}-1)\times n_\mathrm{R}\,L_\mathrm{f})} \ . \end{aligned} \tag{2.56}$$

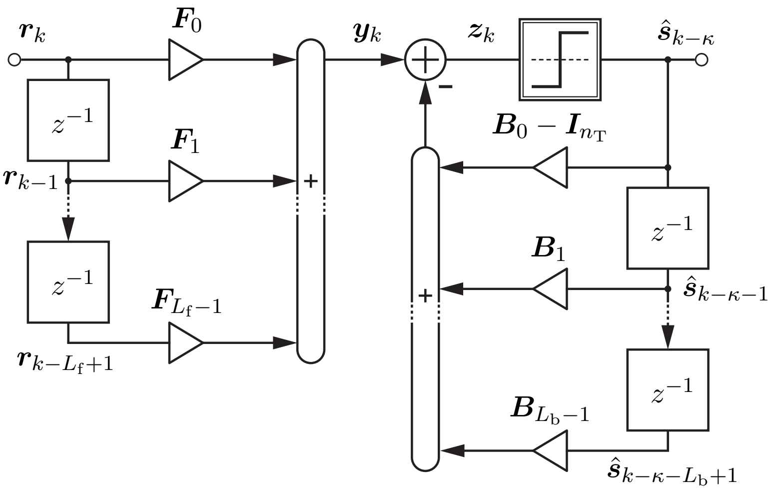

Figure 2.12: Broadband MIMO DFE finite impulse response filter structure

Notation $(\cdot)^\mathsf{H}$ refers to a transpose and complex conjugate matrix, i.e. Hermitian matrix. The output auto-correlation matrix results in

$$\boldsymbol{R}_{rr} = \mathrm{E}\{\boldsymbol{r}_\mathrm{V}\,\boldsymbol{r}_\mathrm{V}^\mathsf{H}\} = \boldsymbol{H}_\mathrm{M}\,\boldsymbol{R}_{ss}\,\boldsymbol{H}_\mathrm{M}^\mathsf{H} + \boldsymbol{R}_{nn} \quad \in \mathbb{C}^{(n_\mathrm{R}\,L_\mathrm{f} \times n_\mathrm{R}\,L_\mathrm{f})} \ . \tag{2.57}$$

In the case of uncorrelated transmit symbols and noise samples we get

$$\boldsymbol{R}_{ss} = P_\mathrm{s} \cdot \boldsymbol{I}_{n_\mathrm{T}\,(L_\mathrm{f}+L_\mathrm{h}-1)} \quad \text{and} \quad \boldsymbol{R}_{nn} = P_\mathrm{n} \cdot \boldsymbol{I}_{n_\mathrm{R} L_\mathrm{f}} \ , \tag{2.58}$$

with P_s and P_n denoting the transmit and noise power, respectively.

The equalization structure, being applied at the receiver-side, is shown in Fig. 2.12. Firstly, a feed forward equalizer with each coefficient being described by the $(n_\mathrm{T} \times n_\mathrm{R})$ matrix

$$\boldsymbol{F}_k = \begin{pmatrix} \underline{f}_{11}[k] & \cdots & \underline{f}_{1n_\mathrm{R}}[k] \\ \vdots & \ddots & \vdots \\ \underline{f}_{n_\mathrm{T}1}[k] & \cdots & \underline{f}_{n_\mathrm{T}n_\mathrm{R}}[k] \end{pmatrix} \tag{2.59}$$

is applied to the receive vector, and thus the $(n_\mathrm{T} \times 1)$ FFE output vector results in

$$\boldsymbol{y}_k = \sum_{m=0}^{L_\mathrm{f}-1} \boldsymbol{F}_m \cdot \boldsymbol{r}_{k-m} = \begin{pmatrix} \boldsymbol{F}_0 & \boldsymbol{F}_1 & \cdots & \boldsymbol{F}_{L_\mathrm{f}-1} \end{pmatrix} \cdot \begin{pmatrix} \boldsymbol{r}_k \\ \boldsymbol{r}_{k-1} \\ \vdots \\ \boldsymbol{r}_{k-L_\mathrm{f}+1} \end{pmatrix} = \boldsymbol{F}_\mathrm{M}\,\boldsymbol{r}_\mathrm{V} \ . \tag{2.60}$$

Substituting $\boldsymbol{r}_\mathrm{V}$ from Eq. 2.53 leads to

$$\boldsymbol{y}_k = \boldsymbol{F}_\mathrm{M} \cdot \boldsymbol{H}_\mathrm{M} \cdot \boldsymbol{s}_\mathrm{V} + \boldsymbol{F}_\mathrm{M} \cdot \boldsymbol{n}_\mathrm{V} \ . \tag{2.61}$$

Secondly, interference from previous symbols is subtracted via the backward equalizer, which has L_b taps. Therefore, the hard-decision block input signal results in

$$\boldsymbol{z}_k = \boldsymbol{y}_k - \left(\sum_{i=0}^{L_\mathrm{b}-1} \boldsymbol{B}_i \, \hat{\boldsymbol{s}}_{k-\kappa-i} - \hat{\boldsymbol{s}}_{k-\kappa} \right) , \tag{2.62}$$

with κ being the delay introduced by the channel as well as the feed forward equalizer. Note that the zeroth coefficient of the backward equalizer is different to the others, confer Fig. 2.12. This trick produces the additional summand $\hat{\boldsymbol{s}}_{k-\kappa}$, which simplifies the error vector later on. The $(n_\mathrm{T} \times n_\mathrm{T})$ sized matrices $\boldsymbol{B}_i$ are given by

$$\boldsymbol{B}_i = \begin{pmatrix} \underline{b}_{11}[i] & \dots & \underline{b}_{1n_\mathrm{T}}[i] \\ \vdots & \ddots & \vdots \\ \underline{b}_{n_\mathrm{T}1}[i] & \dots & \underline{b}_{n_\mathrm{T}n_\mathrm{T}}[i] \end{pmatrix} . \tag{2.63}$$

Rewriting the summation as a matrix multiplication leads to

$$\boldsymbol{z}_k = \boldsymbol{y}_k - \underbrace{\begin{pmatrix} \boldsymbol{0}_{n_\mathrm{T}} & \dots & \boldsymbol{0}_{n_\mathrm{T}} & \boldsymbol{B}_0 & \boldsymbol{B}_1 & \dots & \boldsymbol{B}_{L_\mathrm{b}-1} \end{pmatrix}}_{\boldsymbol{B}_\mathrm{M}} \begin{pmatrix} \hat{\boldsymbol{s}}_k \\ \vdots \\ \hat{\boldsymbol{s}}_{k-\kappa+1} \\ \hat{\boldsymbol{s}}_{k-\kappa} \\ \hat{\boldsymbol{s}}_{k-\kappa-1} \\ \vdots \\ \hat{\boldsymbol{s}}_{k-\kappa-L_\mathrm{b}+1} \end{pmatrix} + \hat{\boldsymbol{s}}_{k-\kappa} . \tag{2.64}$$

Matrix $\boldsymbol{B}_\mathrm{M}$ is of size $(n_\mathrm{T} \times n_\mathrm{T}\,(\kappa + L_\mathrm{b}))$. Choosing $k - \kappa - L_\mathrm{b} + 1 = k - L_\mathrm{f} - L_\mathrm{h} + 2$ and assuming that all decisions are correct, then the equation can be rewritten as follows

$$\boldsymbol{z}_k = \boldsymbol{y}_k - \boldsymbol{B}_\mathrm{M}\, \boldsymbol{s}_\mathrm{V} + \boldsymbol{s}_{k-\kappa} . \tag{2.65}$$

Based on this choice, the equalizer design parameters can be selected with the following strategy:

1^st: Choose FFE length $L_\mathrm{f} \geq 1$

2^nd: Delay is optimized in range $0 \leq \iota \leq L_\mathrm{f} + L_\mathrm{h} - 1$ according to $\kappa = \arg\min_{\iota} \left(\mathrm{tr}(\boldsymbol{R}_{ee}) \right)$

3^rd: Backward equalizer length calculates to $L_\mathrm{b} = L_\mathrm{f} + L_\mathrm{h} - \kappa - 1$

Expression $\mathrm{tr}(\boldsymbol{R}_{ee})$ calculates the trace of the error auto-correlation matrix, see next part.

2.3.2 Mean Square Error Minimization

Considering the system model in Fig. 2.11, the error vector at time instance k is given by

$$\begin{aligned} \boldsymbol{e}_k &= \boldsymbol{s}_{k-\kappa} - \boldsymbol{z}_k = \begin{pmatrix} \underline{e}_1[k] & \cdots & \underline{e}_\mu[k] & \cdots & \underline{e}_{n_\mathrm{T}}[k] \end{pmatrix}^\mathsf{T} \\ \boldsymbol{e}_k &= \boldsymbol{s}_{k-\kappa} - (\boldsymbol{y}_k - \boldsymbol{B}_\mathrm{M}\, \boldsymbol{s}_\mathrm{V} + \boldsymbol{s}_{k-\kappa}) = \boldsymbol{B}_\mathrm{M}\, \boldsymbol{s}_\mathrm{V} - \boldsymbol{F}_\mathrm{M}\, \boldsymbol{r}_\mathrm{V} \;\; , \end{aligned} \tag{2.66}$$

assuming all decisions to be correct. Symbol $(\,\cdot\,)^\mathsf{T}$ is the transpose operator. Thus, the error auto-correlation matrix is defined by

$$\begin{aligned} \boldsymbol{R}_{ee} &= \mathrm{E}\{\boldsymbol{e}_k\, \boldsymbol{e}_k^\mathsf{H}\} = \mathrm{E}\{(\boldsymbol{B}_\mathrm{M}\boldsymbol{s}_\mathrm{V} - \boldsymbol{F}_\mathrm{M}\boldsymbol{r}_\mathrm{V}) \cdot (\boldsymbol{s}_\mathrm{V}^\mathsf{H}\boldsymbol{B}_\mathrm{M}^\mathsf{H} - \boldsymbol{r}_\mathrm{V}^\mathsf{H}\boldsymbol{F}_\mathrm{M}^\mathsf{H})\} \\ &= \boldsymbol{B}_\mathrm{M}\, \boldsymbol{R}_{ss}\, \boldsymbol{B}_\mathrm{M}^\mathsf{H} - \boldsymbol{B}_\mathrm{M}\, \boldsymbol{R}_{sr}\, \boldsymbol{F}_\mathrm{M}^\mathsf{H} - \boldsymbol{F}_\mathrm{M}\, \boldsymbol{R}_{rs}\, \boldsymbol{B}_\mathrm{M}^\mathsf{H} + \boldsymbol{F}_\mathrm{M}\, \boldsymbol{R}_{rr}\, \boldsymbol{F}_\mathrm{M}^\mathsf{H} \;\; . \end{aligned} \tag{2.67}$$

After some rearranging and expanding we get the expression, compare [Al-D00]

$$\begin{aligned} \boldsymbol{R}_{ee} &= \boldsymbol{B}_\mathrm{M}\, (\boldsymbol{R}_{ss} - \boldsymbol{R}_{sr}\, \boldsymbol{R}_{rr}^{-1}\, \boldsymbol{R}_{rs})\, \boldsymbol{B}_\mathrm{M}^\mathsf{H} \\ &\quad + (\boldsymbol{F}_\mathrm{M} - \boldsymbol{B}_\mathrm{M}\, \boldsymbol{R}_{sr}\, \boldsymbol{R}_{rr}^{-1})\, \boldsymbol{R}_{rr}\, (\boldsymbol{F}_\mathrm{M} - \boldsymbol{B}_\mathrm{M}\, \boldsymbol{R}_{sr}\, \boldsymbol{R}_{rr}^{-1})^\mathsf{H} \;\; . \end{aligned} \tag{2.68}$$

In order to obtain the optimal filter coefficients, the mean square error (MSE) of vector $\boldsymbol{e}_k$ needs to be minimized as follows

$$\mathrm{MSE}(\boldsymbol{F}_\mathrm{M}, \boldsymbol{B}_\mathrm{M}, L_\mathrm{f}, \kappa) = \frac{1}{n_\mathrm{T}}\, \mathrm{tr}\,\{\boldsymbol{R}_{ee}\} = \frac{1}{n_\mathrm{T}} \sum_{\mu=1}^{n_\mathrm{T}} \mathrm{E}\{\underline{e}_\mu[k]\, \underline{e}_\mu^*[k]\} \longrightarrow \min\,. \tag{2.69}$$

Here, $\mathrm{tr}\{\,\cdot\,\}$ calculates the trace of a matrix. Since only the second summand in Eq. 2.68 depends on the forward equalizer matrix $\boldsymbol{F}_\mathrm{M}$, the trace of $\boldsymbol{R}_{ee}$ is minimized, if $\boldsymbol{F}_\mathrm{M}$ is chosen such that the second summand gets zero. Therefore, the optimal forward equalizer matrix yields

$$\boldsymbol{F}_{\mathrm{M,opt}} = \boldsymbol{B}_{\mathrm{M,opt}}\, \boldsymbol{R}_{sr}\, \boldsymbol{R}_{rr}^{-1} \;\; . \tag{2.70}$$

The remaining error auto-correlation matrix is described by

$$\boldsymbol{R}_{ee}\Big|_{\boldsymbol{F}_\mathrm{M} = \boldsymbol{F}_{\mathrm{M,opt}}} = \boldsymbol{B}_\mathrm{M}\, (\boldsymbol{R}_{ss} - \boldsymbol{R}_{sr}\, \boldsymbol{R}_{rr}^{-1}\, \boldsymbol{R}_{rs})\, \boldsymbol{B}_\mathrm{M}^\mathsf{H} \;\; . \tag{2.71}$$

With using the Woodbury matrix identity [Pete12, p. 18], the remaining error auto-correlation matrix is expressed with the input and noise auto-correlation matrices as follows

$$\boldsymbol{R}_{ee}\Big|_{\boldsymbol{F}_\mathrm{M} = \boldsymbol{F}_{\mathrm{M,opt}}} = \boldsymbol{B}_\mathrm{M}\, (\boldsymbol{R}_{ss}^{-1} + \boldsymbol{H}_\mathrm{M}^\mathsf{H}\, \boldsymbol{R}_{nn}^{-1}\, \boldsymbol{H}_\mathrm{M})^{-1}\, \boldsymbol{B}_\mathrm{M}^\mathsf{H} = \boldsymbol{B}_\mathrm{M}\, \boldsymbol{R}^{-1}\, \boldsymbol{B}_\mathrm{M}^\mathsf{H} \;\; . \tag{2.72}$$

2.3.3 Backward Filter Coefficients

In order to find the optimal backward filter coefficients, the trace of the error auto-correlation matrix needs to be minimized as follows

$$\min_{\boldsymbol{B}_{\mathrm{M}},\kappa} \mathrm{tr}(\boldsymbol{R}_{ee}) \ . \tag{2.73}$$

It is assumed that only previous decisions are used for the feedback, i.e. $\boldsymbol{B}_0 = \boldsymbol{I}_{n_\mathrm{T}}$. For the minimization the backward filter matrix is partitioned as defined by

$$\boldsymbol{B}_{\mathrm{M}} = \Big(\underbrace{\boldsymbol{0}_{n_\mathrm{T} \times n_\mathrm{T}\,\kappa} \quad \boldsymbol{I}_{n_\mathrm{T}}}_{\boldsymbol{X}^{\mathsf{H}}} \quad \underbrace{\boldsymbol{B}_1 \quad \ldots \quad \boldsymbol{B}_{L_\mathrm{b}-1}}_{\boldsymbol{Y}} \Big) \ , \tag{2.74}$$

where $\boldsymbol{X}^{\mathsf{H}}$ of size $n_\mathrm{T} \times n_\mathrm{T}\,(\kappa+1)$ describes the delay κ as well as the zeroth backward filter matrix, and matrix $\boldsymbol{Y}$ of size $n_\mathrm{T} \times n_\mathrm{T}\,(L_\mathrm{b}-1)$ includes the backward filter coefficients that need to be optimized. Accordingly, matrix $\boldsymbol{R}$ (compare Eq. 2.72) is also partitioned into sub-matrices and yields

$$\boldsymbol{R} = \begin{pmatrix} \boldsymbol{R}_{11} & \boldsymbol{R}_{12} \\ \boldsymbol{R}_{21} & \boldsymbol{R}_{22} \end{pmatrix} \ , \tag{2.75}$$

with $\boldsymbol{R}_{11}$ is of size $n_\mathrm{T}\,(\kappa+1) \times n_\mathrm{T}\,(\kappa+1)$, and matrix $\boldsymbol{R}_{12}$ is of size $n_\mathrm{T}\,(\kappa+1) \times n_\mathrm{T}\,(L_\mathrm{b}-1)$. With this partitioning, the optimal backward filter matrix is derived in Appendix A.1 and results in

$$\boldsymbol{B}_{\mathrm{M,opt}} = \boldsymbol{X}^{\mathsf{H}} \cdot \Big(\boldsymbol{I}_{n_\mathrm{T}\,(\kappa+1)} \, , \quad \boldsymbol{R}_{11}^{-1}\, \boldsymbol{R}_{12} \Big) \ . \tag{2.76}$$

The remaining error auto-correlation matrix is described by

$$\boldsymbol{R}_{ee,\mathrm{min}} = \boldsymbol{X}^{\mathsf{H}}\, \boldsymbol{R}_{11}^{-1}\, \boldsymbol{X} \ . \tag{2.77}$$

2.3.4 Special Cases

Considering only the FFE and eliminating the feedback path by setting $\boldsymbol{B}_0 = \boldsymbol{I}_{n_\mathrm{T}}$ and $\boldsymbol{B}_i = \boldsymbol{0}$ for $i > 0$, see Fig. 2.12, the MMSE solution of the FFE results in

$$\begin{aligned} \boldsymbol{F}_{\mathrm{M,MMSE}} &= \boldsymbol{B}_{\mathrm{M,FFE}}\, \boldsymbol{R}_{sr}\, \boldsymbol{R}_{rr}^{-1} \\ &= \boldsymbol{B}_{\mathrm{M,FFE}}\, \boldsymbol{R}_{ss}\, \boldsymbol{H}_{\mathrm{M}}^{\mathsf{H}} \cdot (\boldsymbol{H}_{\mathrm{M}}\, \boldsymbol{R}_{ss}\, \boldsymbol{H}_{\mathrm{M}}^{\mathsf{H}} + \boldsymbol{R}_{nn})^{-1} \ . \end{aligned} \tag{2.78}$$

The $(n_\mathrm{T} \times n_\mathrm{T}\,(L_\mathrm{f} + L_\mathrm{h} - 1))$ sized matrix containing the Nyquist conditions is given by

$$\boldsymbol{B}_{\mathrm{M,FFE}} = \Big(\boldsymbol{0}_{n_\mathrm{T} \times n_\mathrm{T}\,\kappa} \quad \boldsymbol{I}_{n_\mathrm{T}} \quad \boldsymbol{0}_{n_\mathrm{T} \times n_\mathrm{T}\,(L_\mathrm{f}+L_\mathrm{h}-\kappa-2)} \Big) \ . \tag{2.79}$$

Table 2.3: Derived equalizer types as special cases of the MMSE-DFE

Equalizer type	Design constraints	Remarks
MIMO MMSE-DFE	—	Only past decision are used
MIMO MMSE-FFE	$\boldsymbol{B}_i = \boldsymbol{0}_{n_\mathrm{T}}$ for $i > 0$	No backward filter
MIMO ZF-FFE	$\boldsymbol{B}_i = \boldsymbol{0}_{n_\mathrm{T}}$ for $i > 0,\ P_\mathrm{n} = 0$	No backward filter and noise is neglected
SISO <all types>	$n_\mathrm{T} = n_\mathrm{R} = 1$	Only one in- and output is considered

Assuming uncorrelated transmit symbols and noise samples leads to

$$\boldsymbol{F}_{\mathrm{M,MMSE}} = P_\mathrm{s}\,\boldsymbol{B}_{\mathrm{M,FFE}}\,\boldsymbol{H}_\mathrm{M}^\mathsf{H} \cdot (\boldsymbol{H}_\mathrm{M}\,P_\mathrm{s}\,\boldsymbol{H}_\mathrm{M}^\mathsf{H} + P_\mathrm{n}\,\boldsymbol{I}_{n_\mathrm{R}\,L_\mathrm{f}})^{-1} \ . \tag{2.80}$$

Since $P_\mathrm{s} = (P_\mathrm{s}^{-1})^{-1}$ and $b^{-1}\,\boldsymbol{A}^{-1} = (b\,\boldsymbol{A})^{-1}$ it follows that

$$\boldsymbol{F}_{\mathrm{M,MMSE}} = \boldsymbol{B}_{\mathrm{M,FFE}}\,\boldsymbol{H}_\mathrm{M}^\mathsf{H} \cdot \left(\boldsymbol{H}_\mathrm{M}\,\boldsymbol{H}_\mathrm{M}^\mathsf{H} + d\,\frac{P_\mathrm{n}}{P_\mathrm{s}}\,\boldsymbol{I}_{n_\mathrm{R}\,L_\mathrm{f}}\right)^{-1} \quad \text{with} \quad d = 1 \ . \tag{2.81}$$

By changing $d = 0$, the noise dependent term is neglected, resulting in the ZF solution. An overview of the derived equalizer types is given in Tab. 2.3. The ZF-FFE is the simplest equalization strategy with no feedback loop, where noise is not considered in the equalizer design. This choice leads to a lower signal-to-noise ratio (SNR) of the received symbols compared to the other equalization strategies, which impairs the BER performance. In contrast, the MMSE-FFE accounts for noise in the design process, leading to an improved SNR. With the MMSE-DFE, parts of the equalization are done by the backward filter, which uses already decided symbols. This majorly improves the SNR of the received symbols since the decided symbols are not affected by noise. However, error propagation due to wrong decisions needs to be taken into account.

2.3.5 Performance Evaluation

A bit-level simulation of a (2×2) MIMO system with two channel taps is performed in order to conduct a performance analysis of the presented equalizer types. The channel coefficients are chosen as follows

$$\boldsymbol{H}_0 = \frac{4}{5} \cdot \begin{pmatrix} 1 & 0.6 \\ 0.5 & 0.8 \end{pmatrix} \ , \text{and} \quad \boldsymbol{H}_1 = \frac{\boldsymbol{H}_0}{2} \ , \tag{2.82}$$

compare Eqs. 2.46 and 2.47. The factor 4/5 is chosen to guarantee that the MIMO channel is not amplifying, the transmitted 2-ary pulse amplitude modulation signals are pseudo random binary sequences with different primitive polynomials, and the number of FFE coefficients is $L_\mathrm{f} = 30$. Figure 2.13 shows the simulated BER and MSE with respect to the SNR. Here, $P_\mathrm{s}T_\mathrm{s}$ represents the transmit power multiplied by the symbol period, and N_0 is the noise power spectral density of the additive white Gaussian noise. As expected,

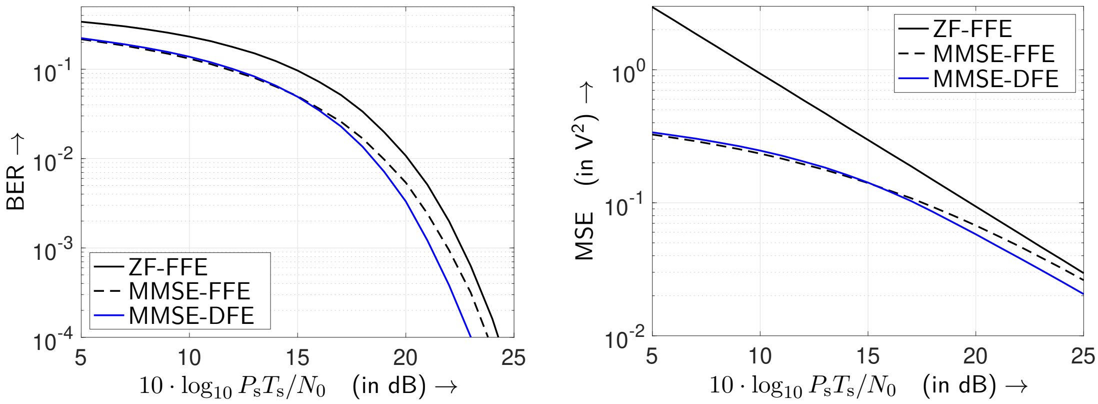

(a) Bit-error rate **(b)** Mean square error

Figure 2.13: Simulated BER and MSE versus SNR comparing different equalizer types in a (2×2) MIMO configuration with two channel taps

the ZF-FFE exhibits the highest BER and MSE of the studied equalizer types. The MMSE-FFE significantly improves the BER and MSE, especially in the low SNR region. In the high SNR region the MMSE-FFE performance approaches the ZF-FFE results since the factor $P_\mathrm{n}/P_\mathrm{s}$ in Eq. 2.81 gets negligibly small. In contrast to the theoretical results, the MMSE-DFE has a higher MSE in the low SNR region (below 15 dB) compared to the MMSE-FFE, leading to a lower BER performance. This is caused by error propagation, which is not taken into consideration in the theoretical design of the MMSE-DFE.

3 Square-law Detection in Fiber-Optic Transmission

Square-law detection is inherently a non-linear process. However, in MIMO systems with IM/DD, linear signal processing approaches have often been used in literature, e.g. frequency-flat signal processing in [Schoe07] and frequency-selective signal processing in [Step14]. This contradiction is resolved hereinafter, and it is explained under which conditions the equivalent baseband model can be considered as linear. Therefore, this chapter is structured as follows: Firstly, the equivalent linear baseband representation of a general square-law detected system is revised. Secondly, this representation is applied to single-mode and multi-mode fiber SISO systems in order to introduce the terminology. Finally, the analysis is extended to a multi-mode fiber MIMO system, and it is described in which conditions baseband linearity applies.

3.1 Equivalent Linear Baseband Representation for Square-law Detected Systems

A square-law detected communication system can be linearly represented under certain conditions [Paul09; Fisc15]. Figure 3.1 depicts the corresponding system model, which includes modulation, bandpass transmission and square-law detection as well as its corresponding equivalent baseband representation. The nomenclature of this model is designed to suit a fiber-optic transmission with IM/DD. Signals $\tilde{s}(t)$ and $\tilde{r}(t)$ denote the bipolar baseband transmit and receive signals, respectively. The equivalent baseband channel impulse response is described by $g(t)$ and the equivalent baseband noise by $n(t)$. All signals with subscript 'o' denote the optical bandpass versions of these signals around the

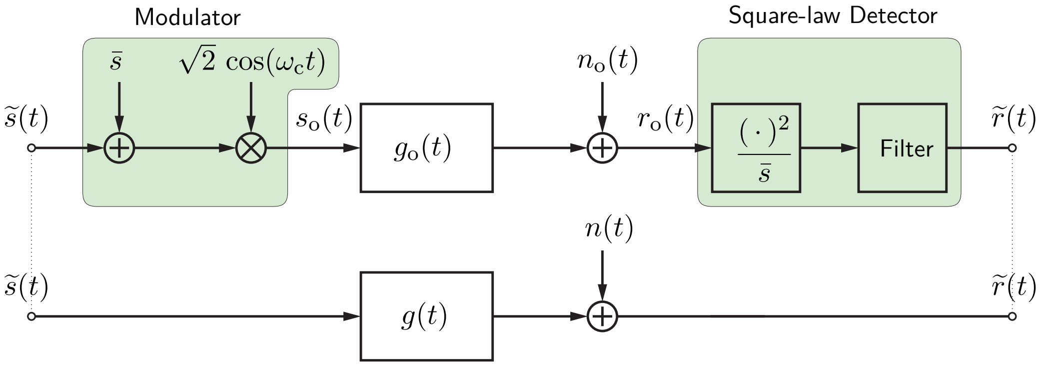

Figure 3.1: Bandpass transmission system with IM/DD (top) and equivalent baseband representation (bottom), compare [Fisc15]

carrier angular frequencies ω_{c} and $-\omega_{\mathrm{c}}$. The filter at the detector is modeled as a lowpass filter with direct component (DC) suppression. Finally, $\bar{s}$ represents the carrier amplitude. Please note: In the bandpass domain a two-sided and real-valued representation is used in correspondence with [Paul09]. When considering a strong carrier $\bar{s}$ and neglecting the signal-signal beat interference, the equivalent baseband channel impulse response is given by

$$g(t) = 2\,\mathrm{Re}\Big\{g_{\mathrm{o}}(t)\,\mathrm{e}^{-\mathrm{j}\omega_{\mathrm{c}}t}\Big\} \quad . \tag{3.1}$$

Since intensity modulation is considered, all signals are real-valued such that

$$g(t) = 2\,g_{\mathrm{o}}(t)\,\cos(\omega_{\mathrm{c}}t) \quad . \tag{3.2}$$

This key relation is used to evaluate the baseband linearity of the system models that are described hereinafter. Table 3.1 gives an overview of the signal notation, taking the channel impulse response as an example.

Table 3.1: Signal notation

Signal notation	Description
$\underline{g}_{\mathrm{o}}^{+}(t)$	Analytic bandpass channel (complex-valued)
$g_{\mathrm{o}}(t)$	Real-valued bandpass channel
$g(t)$	Equivalent baseband channel

3.2 Single-Mode Fiber SISO System Model

Consider a standard SISO transmission through an SMF channel as shown in Fig. 3.2. Herein, the bit pattern is modulated onto the optical carrier, which originates from a continuous wave laser source. Subsequently, the optical signal is transmitted through the SMF channel and is directly detected at the receiver (Rx). The corresponding system model is depicted in Fig. 3.3. Similar to the description in Section 3.1, signal $\tilde{s}(t)$ denotes the bipolar transmit pattern, $\bar{s}$ is the DC offset or carrier amplitude, $E_1(x, y)$ describes the transversal electrical field of the LP_{01} mode, the filter is a lowpass with DC suppression and $\tilde{r}(t)$ is the alternating component (AC)-only receive signal. Complex-valued signals

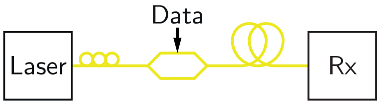

Figure 3.2: SMF SISO system configuration

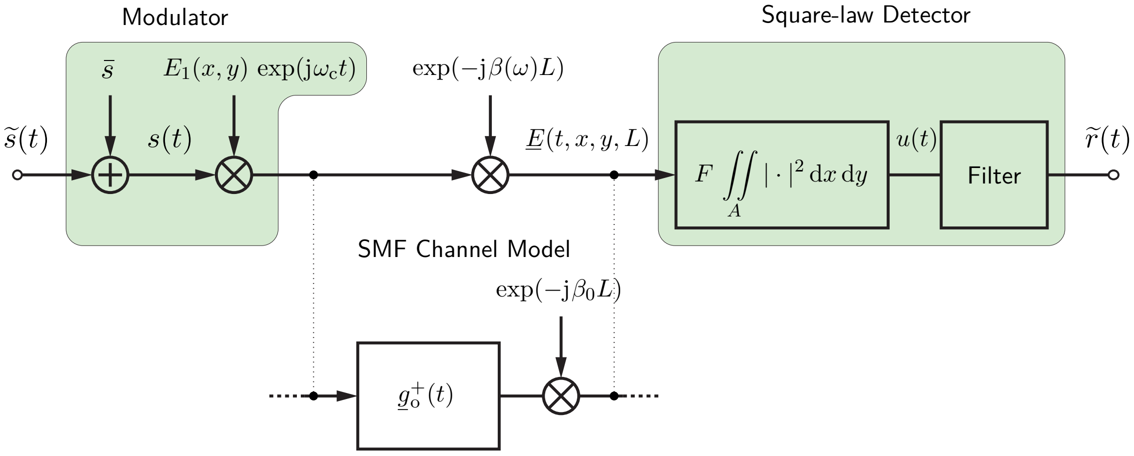

Figure 3.3: SMF SISO system model

are underlined and symbol L denotes the fiber length. Please note that a monochromatic laser source is assumed for simplicity. The electrical field at the detector is given by

$$\underline{E}(t,x,y,L) = s(t)\,E_1(x,y)\,\exp(\mathrm{j}\omega_\mathrm{c}t)\,\exp(-\mathrm{j}\beta(\omega)L)\ . \tag{3.3}$$

Herein, the term with the phase constant $\beta(\omega)$ can be separated into a phase shift and a frequency-selective bandpass channel $\underline{g}_\mathrm{o}^+(t)$ as follows

$$\underline{E}(t,x,y,L) = \Big[\big(s(t)\,\exp(\mathrm{j}\omega_\mathrm{c}t)\big) * \underline{g}_\mathrm{o}^+(t)\Big]\cdot E_1(x,y)\,\exp(-\mathrm{j}\beta_0 L)\ . \tag{3.4}$$

Symbol $(\,\cdot\,)^+$ represents an analytic bandpass signal and $*$ denotes the signal convolution operator. The electrical output voltage is obtained by integrating over the fiber end-face area A as follows

$$u(t) = F\iint_A \left|\underline{E}(t,x,y,L)\right|^2 \mathrm{d}x\,\mathrm{d}y\ . \tag{3.5}$$

Conversion factor F includes the photo diode's responsivity as well as the transimpedance of the receiver's circuitry such that $u(t)$ is a voltage signal. Inserting Eq. 3.4 gives

$$u(t) = F\left|\big(s(t)\,\exp(\mathrm{j}\omega_\mathrm{c}t)\big) * \underline{g}_\mathrm{o}^+(t)\right|^2 \cdot \underbrace{\iint_A \left|E_1(x,y)\right|^2 \mathrm{d}x\,\mathrm{d}y}_{=P_\mathrm{opt}} \cdot \underbrace{\left|\exp(-\mathrm{j}\beta_0 L)\right|^2}_{=1}\ , \tag{3.6}$$

simplifying to

$$u(t) = F\,P_\mathrm{opt}\left|\big(s(t)\,\exp(\mathrm{j}\omega_\mathrm{c}t)\big) * \underline{g}_\mathrm{o}^+(t)\right|^2\ . \tag{3.7}$$

This expression signifies that the received phase has no influence on the detection result, and the integral over the absolute squared transversal field of the LP_{01} mode contributes as the optical power P_opt. Therefore, in this SMF transmission model only the time dependent components are of interest. At the end of the signal processing chain, a lowpass filter with DC suppression is applied to remove the components at twice the carrier frequency that appear due to the squaring operation. With this filter, the bipolar baseband receive signal $\widetilde{r}(t)$ is obtained.

3.2.1 Analytic versus Real-valued Bandpass Signal Representation

Equation 3.7 is the analytic bandpass representation. As shown in Fig. 3.4a, the transmit signal $s(t)$ is shifted in the bandpass region to $+f_\mathrm{c}$ (with $\omega_\mathrm{c} = 2\pi f_\mathrm{c}$) and is then transferred through the complex-valued analytic bandpass channel $\underline{g}_\mathrm{o}^+(t)$. Symbol $\mathcal{F}\{\,\cdot\,\}$ denotes the Fourier transform. Since the absolute value of the channel spectrum is constant (compare Section 3.2.2), only the quadratic phase of the channel transfer function $\angle\underline{G}_\mathrm{o}^+(f)$ is plotted. Therein, symbol $\angle$ denotes the angle.

As derived in Appendix A.2, the real-valued bandpass representation corresponding to Eq. 3.7 is expressed as follows

$$u(t) = F\,P_\mathrm{opt}\left(\underbrace{s(t)\,\sqrt{2}\,\cos(\omega_\mathrm{c}t)}_{s_\mathrm{o}(t)} * g_\mathrm{o}(t)\right)^2 . \tag{3.8}$$

Here, the single-sided modulation $\exp(\mathrm{j}\omega_\mathrm{c}t)$ is replaced with the two-sided $\sqrt{2}\,\cos(\omega_\mathrm{c}t)$ such that the modulated signal is real-valued. Factor $\sqrt{2}$ is introduced in order to guarantee that the signal power before and after modulation is identical. Please note that all signals are real-valued, and hence the absolute value is omitted. The resulting two-sided spectral representation is illustrated in Fig. 3.4b. With Eq. 3.8 an equivalent linear baseband model can be formed according to Section 3.1.

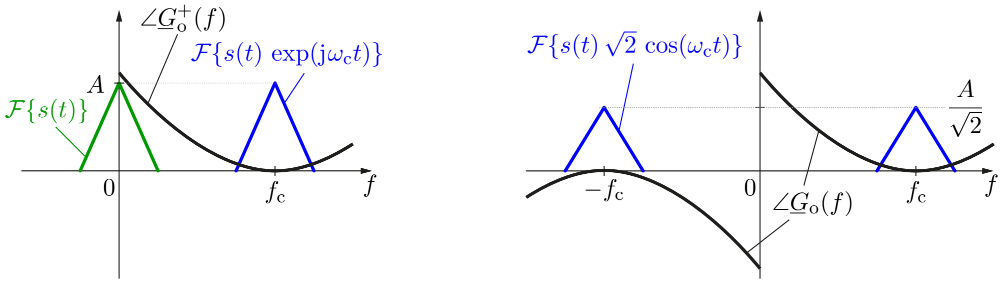

(a) Analytic transmit signal's spectrum **(b)** Real-valued transmit signal's spectrum

Figure 3.4: Modulated signal spectrum and channel phase

The transformation of an analytic bandpass signal $\underline{x}^{+}(t)$ to a real-valued representation $x(t)$ is defined by [Kamm04, p. 24]

$$\begin{array}{l} \underline{X}^{+}(\omega) = 2\,\underline{X}(\omega)\cdot 1(\omega) \\ \quad\begin{array}{c} \bullet \\ | \\ \circ \end{array} \\ \quad\underline{x}^{+}(t) = x(t) + \mathrm{j}\,\mathcal{H}\{x(t)\} \;\; , \end{array} \tag{3.9}$$

with $\mathcal{H}\{\,\cdot\,\}$ denoting the Hilbert transform, and $1(\omega)$ is the Heaviside step function. Therefore, the real-valued bandpass representation can be obtained as follows

$$x(t) = \mathrm{Re}\Big\{\underline{x}^{+}(t)\Big\} \;\; . \tag{3.10}$$

All real-valued signals have a Hermitian symmetric spectrum as defined by

$$\underline{X}(\omega) = \underline{X}^{*}(-\omega) \;\; , \tag{3.11}$$

where $(\,\cdot\,)^{*}$ denotes the complex conjugate. This means the real part of the spectrum is even and the imaginary part is odd.

3.2.2 SMF Channel Impulse Response

The missing link of the system model is the knowledge of the SMF impulse response. It is evaluated in this section to determine the equivalent baseband channel description.

Analytic Bandpass Channel

The channel impulse response includes attenuation, phase shift, delay, chromatic dispersion and nonlinear effects. It is modeled in the frequency domain by

$$\underline{\widetilde{G}}^{+}_{\mathrm{o,SMF}}(\omega) = \exp\!\big[-(\alpha + \mathrm{j}\beta(\omega))\,L\big]\cdot 1(\omega) \;\; , \tag{3.12}$$

where L is the fiber length, and α is the loss coefficient per unit length (e.g. in Neper/km) [Wang92; Agra01]. Please note that the Heaviside step function $1(\omega)$ is included since the analytic channel needs to be limited to positive frequency components. The frequency dependent phase coefficient $\beta(\omega)$ is commonly approximated with a Taylor series at the carrier angular frequency ω_{c} as follows

$$\begin{aligned} \beta(\omega) = n(\omega)\,\frac{\omega}{c} &\approx \sum_{n=0}^{\infty}\frac{\beta_n}{n!}\cdot(\omega-\omega_{\mathrm{c}})^n \\ &\approx \beta_0 + \beta_1\,(\omega-\omega_{\mathrm{c}}) + \frac{\beta_2}{2}\,(\omega-\omega_{\mathrm{c}})^2 + \frac{\beta_3}{6}\,(\omega-\omega_{\mathrm{c}})^3 + \ldots \;\; , \end{aligned} \tag{3.13}$$

with

$$\beta_n = \left[\frac{\mathrm{d}^n \beta(\omega)}{\mathrm{d}\,\omega^n}\right]_{\omega=\omega_\mathrm{c}} \quad . \tag{3.14}$$

The dependency of the refractive index $n(\omega)$ on the wavelength or frequency is described by the Sellmeier equation, compare [Agra01, p. 8], and constant c is the speed of light in vacuum. Coefficient β_0 denotes a phase change per unit length, β_1 is the delay per unit length, and the quadratic phase constant β_2 is the first derivative of the latter with respect to the angular frequency, and hence it describes chromatic dispersion. Higher-order terms describe nonlinear effects. With all linear effects considered, the transfer function is approximated by

$$\begin{aligned}\underline{\widetilde{G}}^{+}_{\mathrm{o,SMF}}(\omega) =& \exp(-\alpha L)\, \exp[-\mathrm{j}(\beta_0 L - \beta_1 L \omega_\mathrm{c})]\, \exp(-\mathrm{j}\beta_1 L\omega)\ldots \\ &\ldots \exp\left(-\mathrm{j}\, L\,\frac{\beta_2}{2}(\omega-\omega_\mathrm{c})^2\right) \cdot 1(\omega) \quad ,\end{aligned} \tag{3.15}$$

which is relatively accurate around the evaluation point ω_c. In order to obtain the corresponding analytic channel impulse response, the inverse Fourier transform of the quadratic exponential term, see Appendix A.3, and of the Heaviside step function, see Appendix A.4, are used

$$\begin{aligned}\exp\left(-\mathrm{j}\, L\,\frac{\beta_2}{2}(\omega-\omega_\mathrm{c})^2\right) \quad &\bullet\!\!-\!\!\circ \quad \frac{1}{\sqrt{-2\pi L\beta_2}} \cdot \exp\left(\mathrm{j}\left(\frac{t^2}{2L\beta_2} + \omega_\mathrm{c} t + \frac{\pi}{4}\right)\right) \quad \text{if } \beta_2 < 0 \\ 1(\omega) \quad &\bullet\!\!-\!\!\circ \quad \frac{1}{2}\left(\frac{\mathrm{j}}{\pi t} + \delta(t)\right) \quad .\end{aligned} \tag{3.16}$$

Thus, the analytic channel impulse response can be structured as follows

$$\begin{aligned}\underline{\widetilde{g}}^{+}_{\mathrm{o,SMF}}(t) =& \exp(-\alpha L) && \text{(modal) attenuation} \\ & \exp[-\mathrm{j}(\beta_0 L - \beta_1 L\omega_\mathrm{c})] && \text{phase shift} \\ & \Bigg[\delta(t-\beta_1 L) && \text{(modal) delay} \\ & * \frac{1}{\sqrt{-2\pi L\beta_2}} \cdot \exp\left(\mathrm{j}\left(\frac{t^2}{2L\beta_2} + \omega_\mathrm{c} t + \frac{\pi}{4}\right)\right) && \text{chromatic dispersion} \\ & * \frac{1}{2}\left(\frac{\mathrm{j}}{\pi t} + \delta(t)\right)\Bigg] \quad . && \text{analytic representation}\end{aligned}$$

Signal $\delta(t)$ denotes the Dirac delta function. It is worth noting that the convolution of a signal with $1/(\pi t)$ is equivalent to the Hilbert transform:

$$\underline{a}(t) * \frac{1}{\pi t} = \mathcal{H}\{\underline{a}(t)\} \quad . \tag{3.17}$$

Hereinafter, only the quadratic component β_2 is considered since the absolute delay is not of interest for BER performance evaluation, and the phase shift term vanishes in the detection process. Furthermore, a lossless fiber is assumed, and therefore the analytic SMF transfer function simplifies to

$$\underline{G}^{+}_{\mathrm{o,SMF}}(\omega) = \exp\left(-\mathrm{j}\, L\, \frac{\beta_2}{2}(\omega-\omega_{\mathrm{c}})^2\right) \cdot 1(\omega) \ . \tag{3.18}$$

The resulting analytic bandpass channel impulse response yields

$$\begin{aligned} \underline{g}^{+}_{\mathrm{o,SMF}}(t) = \frac{1}{2}\frac{1}{\sqrt{-2\pi L\beta_2}} \cdot \Bigg[&\exp\left(\mathrm{j}\left(\frac{t^2}{2L\beta_2} + \omega_{\mathrm{c}} t + \frac{\pi}{4}\right)\right) \\ &+ \mathrm{j}\,\mathcal{H}\left\{\exp\left(\mathrm{j}\left(\frac{t^2}{2L\beta_2} + \omega_{\mathrm{c}} t + \frac{\pi}{4}\right)\right)\right\}\Bigg] \quad \text{if } \beta_2 < 0 \ . \end{aligned} \tag{3.19}$$

The quadratic phase constant is expressed as follows

$$\beta_2 = -\frac{D}{2\pi c}\lambda_{\mathrm{c}}^2 \ , \tag{3.20}$$

where D denotes the chromatic dispersion in unit ps/nm/km, λ_{c} describes the center wavelength and β_2 has unit s^2/m. In a standard SMF at 1550 nm the chromatic dispersion D is positive, and hence $\beta_2 < 0$. At 850 nm D is negative, and therefore $\beta_2 > 0$. At 1300 nm the chromatic dispersion is practically zero, see Fig. 3.5. Please note that subsequently the quadratic phase constant is assumed to be negative to simplify the derivation. This case encompasses the most used 1550 nm operating wavelength in a standard fiber. An expression of the analytic channel impulse response for all β_2 values is provided in Eq. A.31, see Appendix A.3.

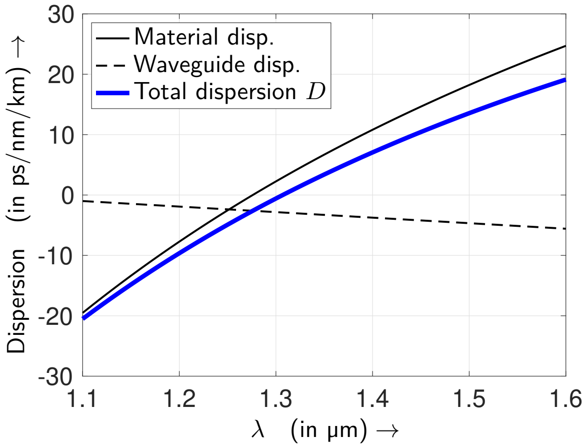

Figure 3.5: Chromatic dispersion and its contributors in a standard SMF, see [Agra02, pp. 39-42]

Real-valued Bandpass Channel

In order to obtain the corresponding real-valued SMF channel impulse response, being suited for two-sided modulation with a cosine carrier, simply the real part of the analytic channel is taken as follows

$$g_{\mathrm{o,SMF}}(t) = 2 \cdot \mathrm{Re}\Big\{ \underline{g}^{+}_{\mathrm{o,SMF}}(t) \Big\} \ , \tag{3.21}$$

compare Eq. A.22 in Appendix A.2. The real-valued bandpass channel impulse response yields

$$g_{\mathrm{o,SMF}}(t) = \frac{1}{\sqrt{-2\pi L\beta_2}} \left[\cos\left(\frac{t^2}{2L\beta_2} + \omega_{\mathrm{c}} t + \frac{\pi}{4} \right) - \mathcal{H}\left\{ \sin\left(\frac{t^2}{2L\beta_2} + \omega_{\mathrm{c}} t + \frac{\pi}{4} \right) \right\} \right] \ . \tag{3.22}$$

Since the Hilbert transform of the sine function with quadratic argument is given by

$$\mathcal{H}\left\{ \sin\left(\frac{t^2}{2L\beta_2} + \omega_{\mathrm{c}} t + \frac{\pi}{4} \right) \right\} = \begin{cases} -\cos\left(\frac{t^2}{2L\beta_2} + \omega_{\mathrm{c}} t + \frac{\pi}{4} \right) \ , & \text{if} \quad t < \omega_{\mathrm{c}} L(-\beta_2) \\ +\cos\left(\frac{t^2}{2L\beta_2} + \omega_{\mathrm{c}} t + \frac{\pi}{4} \right) \ , & \text{if} \quad t \geq \omega_{\mathrm{c}} L(-\beta_2) \ , \end{cases} \tag{3.23}$$

compare Appendix A.5, the real-valued bandpass channel for two-sided modulation is described as follows

$$g_{\mathrm{o,SMF}}(t) = \begin{cases} \dfrac{2}{\sqrt{-2\pi L\beta_2}} \cos\left(\dfrac{t^2}{2L\beta_2} + \omega_{\mathrm{c}} t + \dfrac{\pi}{4} \right) \ , & \text{if} \quad t < t_0 \\ 0 \ , & \text{if} \quad t \geq t_0 \ , \end{cases} \tag{3.24}$$

with $t_0 = \omega_{\mathrm{c}} L(-\beta_2) = LD\lambda_{\mathrm{c}}$ and considering that $\beta_2 < 0$. Summarizing the two cases with a mirrored and shifted Heaviside step function results in

$$g_{\mathrm{o,SMF}}(t) = \frac{2}{\sqrt{-2\pi L\beta_2}} \cos\left(\frac{t^2}{2L\beta_2} + \omega_{\mathrm{c}} t + \frac{\pi}{4} \right) \cdot 1(t_0 - t) \quad \text{if } \beta_2 < 0 \ . \tag{3.25}$$

Choosing a standard SMF with $D = 17$ ps/nm/km of length $L = 120$ km, and operating at a wavelength of $\lambda_{\mathrm{c}} = 1550$ nm, the discontinuity is located at $t_0 = 3.162$ µs.

Equivalent Baseband Channel

The equivalent linear baseband channel impulse response considering IM/DD is given by

$$g_{\mathrm{SMF}}(t) = 2\, g_{\mathrm{o,SMF}}(t)\, \cos(\omega_{\mathrm{c}} t) \ , \tag{3.26}$$

see Section 3.1. Using a trigonometric identity and neglecting the parts at twice the carrier frequency, which are filtered at the detector, the equivalent baseband channel impulse response results in

$$g_{\text{SMF}}(t) = \frac{2}{\sqrt{-2\pi L\beta_2}} \cos\left(\frac{t^2}{2L\beta_2} + \frac{\pi}{4}\right) \cdot 1(t_0 - t) \quad , \quad \text{if} \quad \beta_2 < 0 \ . \tag{3.27}$$

This channel impulse response has a chirp characteristic. Convolving the channel with a shaping filter $g_\text{s}(t)$ and receive filter $g_\text{ef}(t)$ to obtain the overall channel impulse response

$$h(t) = g_\text{s}(t) * g_{\text{SMF}}(t) * g_\text{ef}(t) \ , \tag{3.28}$$

a peak appears at the location of the lowest frequency, i.e. $t = 0$, due to the phase shift by $\pi/4$. At locations with high frequencies the convolution result is zero since the negative and positive parts cancel each other, compare Fig. 3.6 (left). At the location of the discontinuity t_0, the resulting peak height is much smaller than the peak height at $t = 0$, compare Fig. 3.6. Therefore, the discontinuity is neglected hereinafter and the equivalent baseband impulse response for an SMF channel is defined by

$$g_{\text{SMF}}(t) = \frac{2}{\sqrt{-2\pi L\beta_2}} \cos\left(\frac{t^2}{2L\beta_2} + \frac{\pi}{4}\right) \quad , \quad \text{if} \quad \beta_2 < 0 \ . \tag{3.29}$$

The corresponding transfer function is given by, compare [Fisc15]

$$G_{\text{SMF}}(\omega) = 2\cos\left(L\frac{\beta_2}{2}\omega^2\right) \ . \tag{3.30}$$

This can be verified by expressing the cosine with exponential functions and using the transformation pairs of Eq. A.27 in the appendix. Please note that this SMF channel model assumes a monochromatic laser source with the angular carrier frequency ω_c, compare

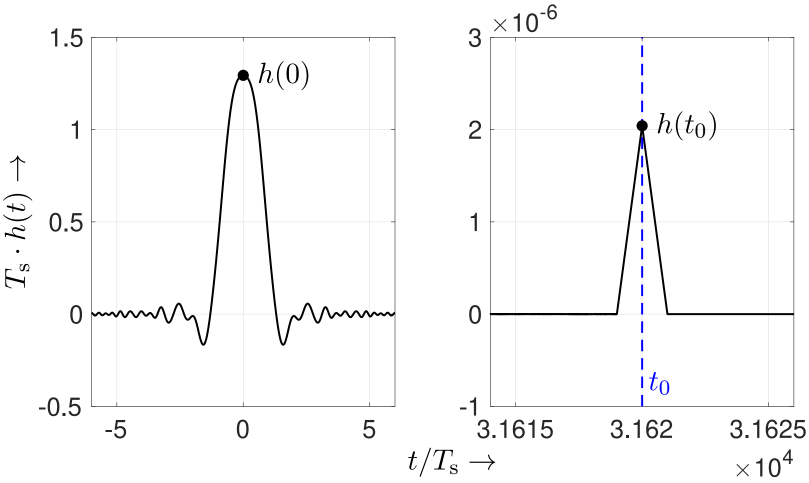

Figure 3.6: Overall channel impulse response around $t = 0$ (left) and around the discontinuity t_0 (right) when considering a 120 km standard SMF at 1550 nm with rectangular pulse shaping and receive filtering at $1/T_\text{s} = 10$ GHz symbol rate

Fig. 3.3. Thus, chromatic dispersion is only in effect since the monochromatic carrier is spectrally broadened during modulation with the transmit signal.

Standard Single-Mode Fiber Example

Consider a standard SMF complying to the ITU-T G.652 recommendation [G652] with the following parameters:

$$\begin{aligned} L &= 120 \text{ km} \\ \beta_2 &= -21.683 \text{ ps}^2/\text{km} \quad (D = 17 \text{ ps/nm/km}, \quad \lambda_\text{c} = 1550 \text{ nm}) \end{aligned} \tag{3.31}$$

The equivalent baseband transfer function and channel impulse response are depicted in Fig. 3.7.

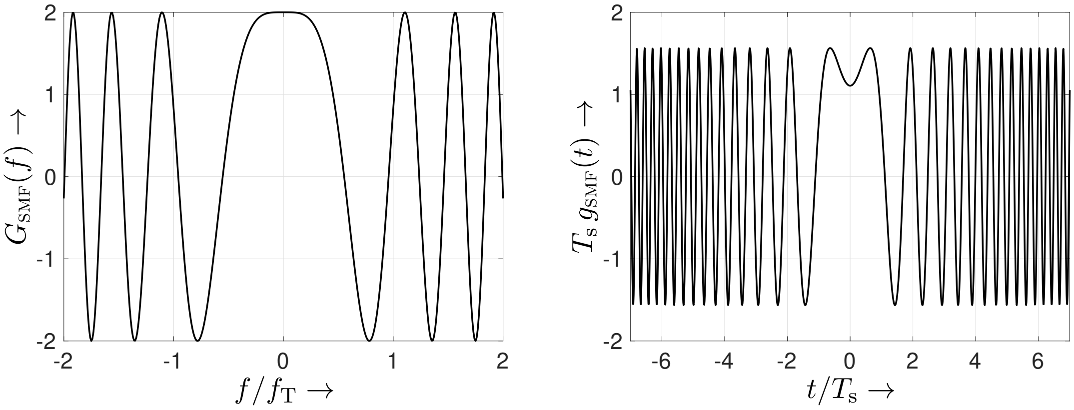

(a) Transfer function **(b)** Channel impulse response

Figure 3.7: Equivalent baseband standard SMF channel with $f_\text{T} = 1/T_\text{s} = 10$ GHz

Despite the squaring operation at the detector, the equivalent baseband channel impulse response has negative values. This is a result of the DC suppression of the detection filter. Subsequently, pulse shaping and receive filtering are included as shown in Fig. 3.8. The non-causal representations of the rectangular transmit and receive filter are given by

$$g_\text{s}(t) = \frac{1}{T_\text{s}} \cdot \text{rect}\left(\frac{t}{T_\text{s}}\right) \qquad \text{and} \qquad g_\text{ef}(t) = g_\text{s}(-t) \ . \tag{3.32}$$

Therefore, the overall channel impulse response is given by

$$h(t) = g_\text{s}(t) * g(t) * g_\text{s}(-t) = \phi_{g_\text{s}}(t) * g(t) \ , \tag{3.33}$$

with $\phi_{g_\text{s}}(t)$ denoting the auto-correlation function of $g_\text{s}(t)$. The application of a matched receive filter maximizes the SNR. It is adapted to the transmit filter and the channel as follows

$$g_\text{ef,match}(t) = g_\text{s}(-t) * g(-t) \ , \tag{3.34}$$

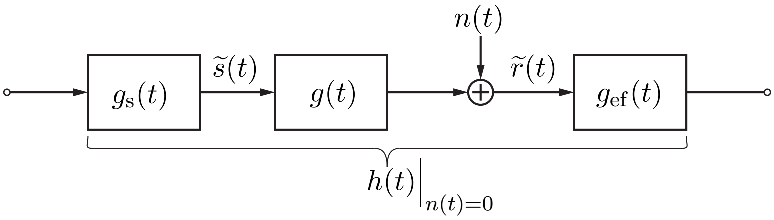

Figure 3.8: Equivalent baseband system with pulse shaping and receive filtering

and therefore the overall matched filter channel impulse response is defined by

$$h_\mathrm{match}(t) = g_\mathrm{s}(t) * g(t) * g_\mathrm{s}(-t) * g(-t) = \phi_{g_\mathrm{s}}(t) * \phi_g(t) \ . \tag{3.35}$$

Signal $\phi_g(t)$ describes the auto-correlation function of $g(t)$. With matched receive filtering, the noise coloring needs to be taken into account since the matched receive filter has no Nyquist edge. In this case, a decorrelation filter is required for some detection methods to achieve optimal results, e.g. maximum-likelihood detection. In correspondence to the channel depicted in Fig. 3.7, the rectangular and matched-receive filtered impulse responses are depicted in Fig. 3.9. Herein, the continuous and symbol-spaced sampled versions are shown. Based on these impulse responses, further studies could be performed, e.g. to analyze different linear equalization concepts [Teic16; Rath17].

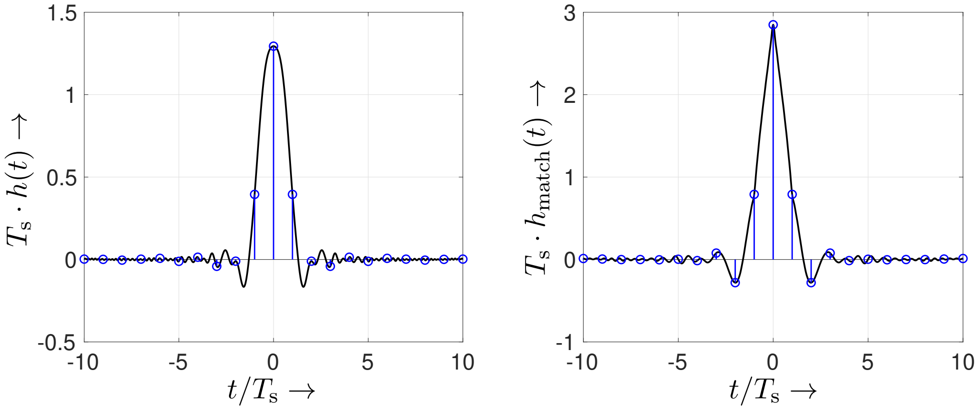

(a) Rectangular Rx-Filter (b) Matched Rx-Filter

Figure 3.9: Overall standard SMF channel impulse responses comparing different receive filters when transmitting with a rate of $f_\mathrm{T} = 1/T_\mathrm{s} = 10$ GHz

3.3 Multi-Mode Fiber SISO System Model

In this section, the transmission through an MMF channel is investigated by extending the SMF model of the previous section. The corresponding setup in Fig. 3.10 includes an SMF to MMF splice with adjustable radial offset and an MMF channel. Instead of the splice, any SMF to MMF transition or a laser directly coupled to the MMF could be used. The corresponding system model is depicted in Fig. 3.11, where only two propagating modes are shown for simplicity. Herein, the input SMF's length is assumed to be very short. The input mode of the MMF has index $j = 1, \dots, M$, the output mode index $i = 1, \dots, M$, and M is the number of supported fiber modes. Variable c_j is the factor by which the LP$_{01}$ mode excites the jth mode in the MMF. The electrical field with its time and z-direction component is denoted by $\underline{E}_j(t,z)$ and the transversal field distribution by $E_i(x,y)$. Please note that the transversal electrical field changes when mode coupling occurs. Therefore, it is considered just before the detection process. Furthermore, $\underline{g}^{+}_{\mathrm{o},ij}(t)$ describes the chromatic and modal dispersion in the bandpass region, and φ_{ij} is the resulting phase. The analytic channel $\underline{g}^{+}_{\mathrm{o},ij}(t)$ also includes mode dependent losses. Combining all parts, the electrical field of the ith mode at the detector is described by

$$\underline{E}_i(t,x,y,L) = E_i(x,y) \cdot \sum_{j=1}^{M} \left(\left[(s(t)\ \exp(\mathrm{j}\omega_{\mathrm{c}} t)) * c_j\, \underline{g}^{+}_{\mathrm{o},ij}(t) \right] \cdot \exp(-\mathrm{j}\varphi_{ij}) \right) \ . \tag{3.36}$$

All M modes are superimposed at the detector as follows

$$\begin{aligned} \underline{E}(t,x,y,L) &= \sum_{i=1}^{M} \underline{E}_i(t,x,y,L) \\ &= \sum_{i} \left\{ E_i(x,y) \cdot \sum_{j} \left[(s(t)\ \exp(\mathrm{j}\omega_{\mathrm{c}} t)) * c_j\, \underline{g}^{+}_{\mathrm{o},ij}(t) \right] \cdot \exp(-\mathrm{j}\varphi_{ij}) \right\} \ . \end{aligned} \tag{3.37}$$

Substituting the time dependent signals by $\underline{b}_{ij}(t)$ gives

$$\underline{E}(t,x,y,L) = \sum_{i} \left\{ E_i(x,y) \cdot \sum_{j} \underline{b}_{ij}(t) \cdot \exp(-\mathrm{j}\varphi_{ij}) \right\} \ . \tag{3.38}$$

Moreover, the summation is substituted by $\underline{f}_i(t)$ resulting in

$$\underline{E}(t,x,y,L) = \sum_{i} \quad E_i(x,y) \cdot \underline{f}_i(t) \ . \tag{3.39}$$

Figure 3.10: MMF SISO measurement configuration

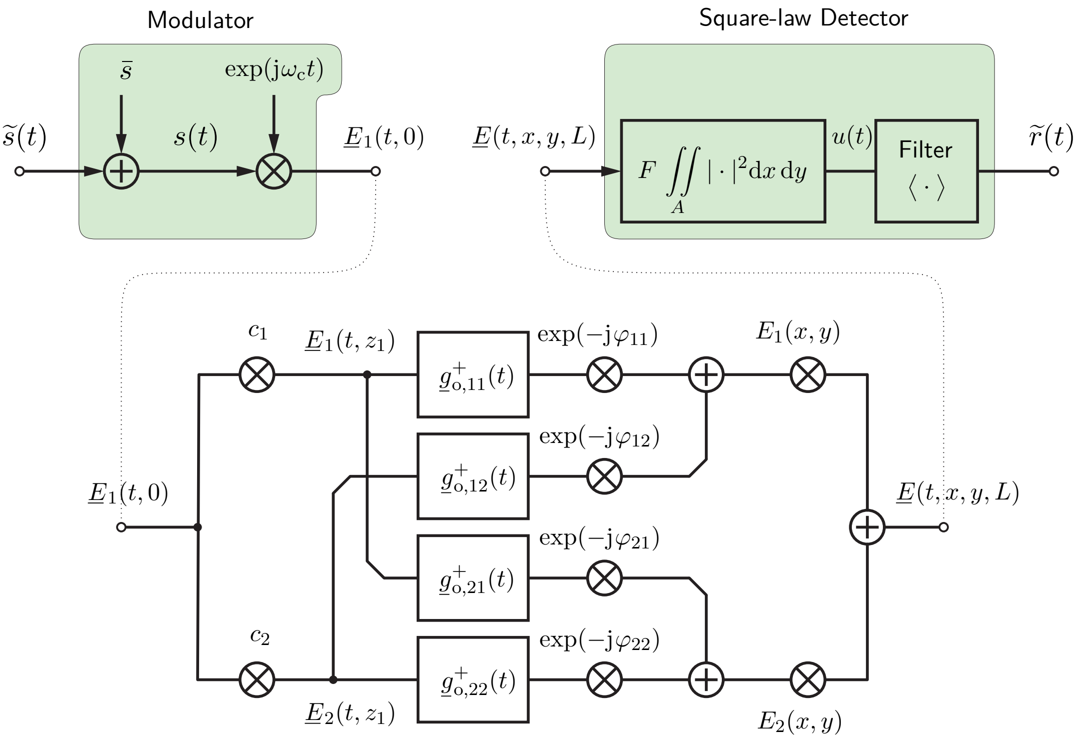

Figure 3.11: IM/DD system model for a 2-mode fiber SISO transmission

The application of the detector yields

$$\begin{aligned} u(t) &= F \iint\limits_A \left|\underline{E}(t,x,y,L)\right|^2 \mathrm{d}x\,\mathrm{d}y \\ &= F \iint\limits_A \Big(\sum_i E_i(x,y)\cdot \underline{f}_i(t)\Big)\cdot\Big(\sum_k E_k(x,y)\cdot \underline{f}_k(t)\Big)^* \mathrm{d}x\,\mathrm{d}y \quad . \end{aligned} \tag{3.40}$$

Expanding the sums and splitting the resulting term into a sum with identical indices as well as into a double sum with mixed indices results in

$$\begin{aligned} u(t) = F \iint\limits_A \Big[&\Big(\sum_i E_i(x,y)\,E_i(x,y)\,\underline{f}_i(t)\,\underline{f}_i^*(t)\Big) \\ &+\Big(\underbrace{\sum_i\sum_k}_{i\neq k} E_i(x,y)\,E_k(x,y)\,\underline{f}_i(t)\,\underline{f}_k^*(t)\Big)\Big]\,\mathrm{d}x\,\mathrm{d}y \quad . \end{aligned} \tag{3.41}$$

The integral over the mixed term with $i \neq k$ is zero since the transversal fields of different modes are orthogonal as given by

$$\iint\limits_A E_i(x,y)\,E_k(x,y)\,\mathrm{d}x\,\mathrm{d}y = \begin{cases} P_i & : i = k \\ 0 & : i \neq k \end{cases} , \tag{3.42}$$

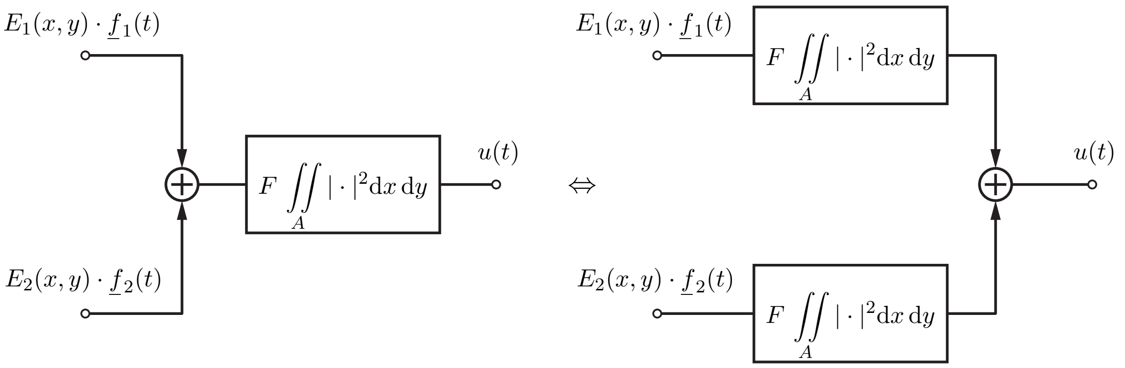

Figure 3.12: Equivalent parallel detection considering orthogonal modes

compare Section 2.1.2. With this orthogonality, the detection can be performed in parallel for each mode separately as shown in Fig. 3.12. Using the mode orthogonality and interchanging the integral with the summation we get

$$u(t) = F\sum_i \underline{f}_i(t)\,\underline{f}_i^*(t)\underbrace{\iint_A E_i(x,y)\,E_i(x,y)\,\mathrm{d}x\,\mathrm{d}y}_{P_i} \ , \tag{3.43}$$

where P_i denotes the optical power of the respective mode. The back-substitution of $\underline{f}_i(t)$ leads to

$$u(t) = F\sum_i P_i\left(\sum_j \underline{b}_{ij}(t)\cdot\exp(-\mathrm{j}\varphi_{ij})\right)\left(\sum_{j'} \underline{b}_{ij'}^*(t)\cdot\exp(+\mathrm{j}\varphi_{ij'})\right) \ . \tag{3.44}$$

By expanding the sums, two cases can be differentiated, i.e. $j = j'$ and $j \neq j'$:

$$\begin{aligned} u(t) =& F\sum_i P_i\left(\sum_j \left|\underline{b}_{ij}(t)\right|^2\right) \\ &+F\sum_i P_i\left(\underbrace{\sum_j\sum_{j'}}_{j\neq j'} \underline{b}_{ij}(t)\,\underline{b}_{ij'}^*(t)\,\exp\Big(-\mathrm{j}\left(\varphi_{ij}-\varphi_{ij'}\right)\Big)\right) \ . \end{aligned} \tag{3.45}$$

The short notation is given by

$$u(t) = u_{\mathrm{sig}}(t) + u_{\mathrm{int}}(t) \ . \tag{3.46}$$

In $u_{\mathrm{sig}}(t)$ the phase cancels such that the signals add constructively. Term $u_{\mathrm{int}}(t)$ is a phase dependent superposition, which is interpreted as interference. The application of the detection filter $\langle\cdot\rangle$ leads to

$$\begin{aligned} \tilde{r}(t) = \Big\langle\ u(t)\ \Big\rangle &= \Big\langle u_{\mathrm{sig}}(t)\Big\rangle + \Big\langle u_{\mathrm{int}}(t)\Big\rangle \\ &= \quad \tilde{r}_{\mathrm{sig}}(t) \quad + \quad \tilde{r}_{\mathrm{int}}(t) \ . \end{aligned} \tag{3.47}$$

Signal $\widetilde{r}_{\text{sig}}(t)$ denotes the desired and $\widetilde{r}_{\text{int}}(t)$ the interference signal.

3.3.1 Baseband Linearity of the Desired Signal

In this part, it is shown that the desired signal can be considered as linear in baseband. By back-substituting the time dependent signal $\underline{b}_{ij}(t)$, the desired signal in its full form is written by

$$\widetilde{r}_{\text{sig}}(t) = F \sum_i P_i \left(\sum_j \left\langle \left| (s(t)\, \exp(\mathrm{j}\omega_{\mathrm{c}} t)) * c_j\, \underline{g}^{+}_{\mathrm{o},ij}(t) \right|^2 \right\rangle \right) \quad . \tag{3.48}$$

Replacing the complex modulation with a real-valued two-sided modulation, and converting the analytic bandpass channel $\underline{g}^{+}_{\mathrm{o},ij}(t)$ into the corresponding real-valued channel $g_{\mathrm{o},ij}(t)$ (compare Section 3.2.1 and Appendix A.2), the overall transmission is described by

$$\begin{aligned} \widetilde{r}_{\text{sig}}(t) &= \sum_i \sum_j F\, P_i \left\langle \left[(s(t)\, \sqrt{2}\, \cos(\omega_{\mathrm{c}} t)) * g_{\mathrm{o},ij}(t) \right]^2 \right\rangle \\ &= \sum_i \sum_j \widetilde{r}_{ij}(t) \quad . \end{aligned} \tag{3.49}$$

Signal $\widetilde{r}_{ij}(t)$ is the contribution from the jth transmitted mode received at the ith mode. Please note the variable c_j is merged into $g_{\mathrm{o},ij}(t)$. The desired signal is a superposition of SMF-like transmissions between the input and output modes. For each $\widetilde{r}_{ij}(t)$ an equivalent linear baseband model can be formed according to Section 3.1 as follows

$$\widetilde{r}_{ij}(t) = \widetilde{s}(t) * g_{ij}(t) + n'(t) \quad , \tag{3.50}$$

with $g_{ij}(t)$ being the equivalent baseband channel impulse response given by

$$g_{ij}(t) = 2\, g_{\mathrm{o},ij}(t) \cos(\omega_{\mathrm{c}} t) \quad . \tag{3.51}$$

The equivalent baseband description of the desired signal results in

$$\widetilde{r}_{\text{sig}}(t) = \sum_i \sum_j \left(\widetilde{s}(t) * g_{ij}(t) + n'(t) \right) = \widetilde{s}(t) * \sum_i \sum_j g_{ij}(t) + n(t) \quad . \tag{3.52}$$

Without mode coupling the interference signal vanishes, and hence the overall receive signal is solely represented by the desired signal as given by

$$\widetilde{r}(t) = \widetilde{s}(t) * \underbrace{\sum_i g_i(t)}_{g_{\text{MMF}}(t)} + n(t) \quad , \tag{3.53}$$

where $i = j$ such that $g_i(t)$ is the short notation of $g_{ii}(t)$. Signal $g_{\text{MMF}}(t)$ denotes the equivalent baseband impulse response of the MMF.

3.3.2 Properties of the Interference Signal

The interference signal is denoted by

$$\tilde{r}_{\mathrm{int}}(t) = F \sum_i P_i \left(\underbrace{\sum_j \sum_{j'}}_{j\neq j'} \left\langle \underline{b}_{ij}(t)\, \underline{b}^*_{ij'}(t)\, \exp\Big(-\mathrm{j}\,(\varphi_{ij} - \varphi_{ij'})\Big) \right\rangle \right) . \tag{3.54}$$

For each summand a complementary complex conjugate summand exists. Therefore, the relation $\underline{X} + \underline{X}^* = 2\,\mathrm{Re}\{\underline{X}\}$ is used to rewrite the interference signal as follows

$$\tilde{r}_{\mathrm{int}}(t) = 2\,F \sum_i P_i \left(\sum_{j=1}^{J-1} \sum_{j'=j+1}^{J} \left\langle \mathrm{Re}\Big\{ \underline{b}_{ij}(t)\, \underline{b}^*_{ij'}(t)\, \exp\Big(-\mathrm{j}\,(\varphi_{ij} - \varphi_{ij'})\Big) \Big\} \right\rangle \right) . \tag{3.55}$$

Please note the change in the running indices. This proves that the interference signal is real-valued. If no mode coupling in the MMF is present, the product $\underline{b}_{ij}(t)\,\underline{b}^*_{ij'}(t)$ is zero, if $j \neq j'$. In this case the interference signal vanishes. If mode coupling is present, signals of different and unknown phases are superimposed. Therefore, the interference signal cannot be transferred into an equivalent linear baseband representation.

Figures 3.13 and 3.14 show a simulated example of the received signal components for two laser types when transmitting through a 6-mode fiber, where only coupling between modes of the same group is allowed. The simulated symbol rate is $f_{\mathrm{T}} = 1/T_{\mathrm{s}} = 5$ GHz, and a zero chromatic dispersion operating wavelength is chosen. Differential mode delays between mode groups 1 and 2 of 150 ps and between groups 1 and 3 of 160 ps are used. The phase is chosen as a uniformly distributed random variable in the interval $[0, 2\pi]$, where the same seed of the random number generator is used to ensure comparability between the simulated signals. Furthermore, laser phase noise is used in order to model the different laser types, compare Section 2.2.1. The graphs show that with a broad-linewidth laser

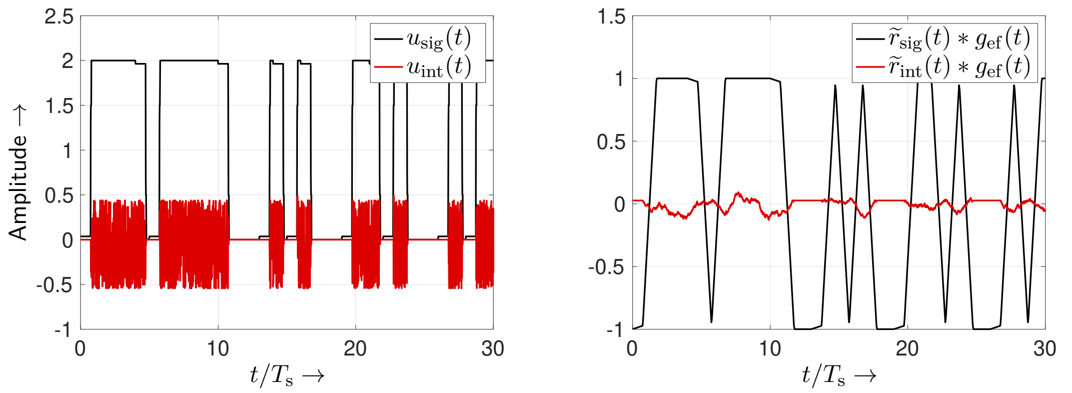

(a) Unfiltered signal **(b)** Receive filtered signal incl. DC suppression

Figure 3.13: Simulated desired and interference signals for a 6-mode fiber transmission with a broad-linewidth laser ($\Delta\lambda = 5$ nm, e.g. Fabry-Pérot laser)

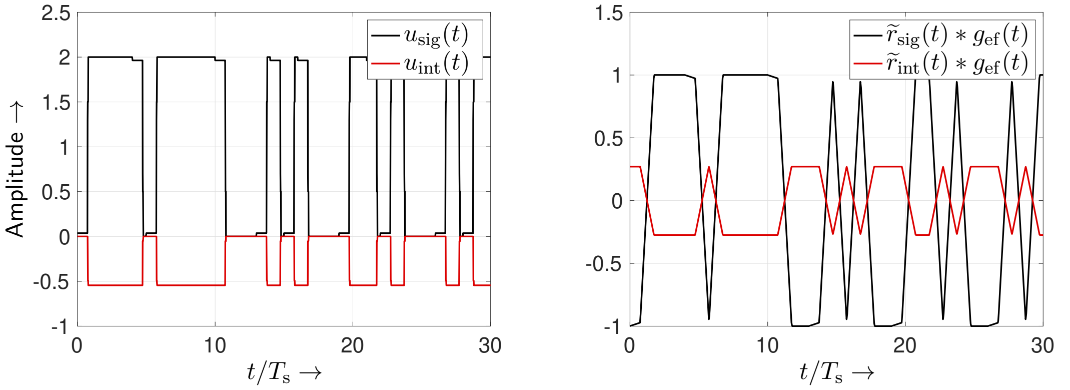

(a) Unfiltered signal **(b)** Receive filtered signal incl. DC suppression

Figure 3.14: Simulated desired and interference signals for a 6-mode fiber transmission with a narrow-linewidth laser ($\Delta\lambda = 0.8$ fm, e.g. DFB laser)

the interference signal is a noise-like signal with zero mean. Its variance depends on the amplitude of the superimposed bit values and the magnitude of mode cross-talk. If one or both bits in $\underline{b}_{ij}(t)$ and $\underline{b}^*_{ij'}(t)$ are zero, the interference signal is zero as well. The applied rectangular receive filter $g_\mathrm{ef}(t)$ significantly reduces the noise-like interference. In contrast, the narrow-linewidth interference signal appears to be a normal bit-pattern. However, in this iteration the phase has a destructive influence since the interference signal is practically inverted to the desired signal. In addition to the description above, the different linear and non-linear signal contributions in IM/DD multi-mode systems with mode coupling are elaborated in [Sale85].

3.3.3 MMF Channel Impulse Response

In SMF transmission only the LP_{01} mode needs to be taken into account. Since multiple modes propagate in an MMF, the corresponding channel model needs to consider the following parameter set:

- Mode excitation efficiency c_i
- Mode specific attenuation $\alpha_i L$
- Mode specific delay (modal dispersion) $\beta_{1,i} L$
- Chromatic dispersion for each mode (quadratic phase constant $\beta_{2,i}$)
- Mode coupling model

The system parameters (e.g. transmit power) are chosen such that an operation in the linear region is ensured. Different mode coupling models exist. In this work, the focus is on the model without considering mode coupling for simplicity. In practice, mode coupling occurs distributed along the fiber length, specifically between modes of the same group [Carp13]. An interesting approach is the matrix propagation model presented in [Ho13]. It considers that mode coupling is distributed along the fiber length by dividing the MMF into a finite number of short length segments.

Analytic Bandpass Channel

Assuming that no modal coupling occurs along the MMF channel, the input mode is received at the same output. Therefore, the mode indices are equal, i.e. $i = j$. With this assumption, the analytic channel transfer function of the MMF is given by

$$\underline{G}^{+}_{\mathrm{o},i}(\omega) = c_i \, \exp\{-\alpha_i \, L\} \cdot \exp\Big\{ -\mathrm{j}\,[\beta_{1,i}(\omega-\omega_{\mathrm{c}}) + \frac{\beta_{2,i}}{2}(\omega-\omega_{\mathrm{c}})^2]L \Big\} \cdot 1(\omega) \ . \tag{3.56}$$

It should be pointed out that the attenuation $\alpha_i L$, the delay $\beta_{1,i}L$ and the quadratic phase constant $\beta_{2,i}$ are different for each mode [Carp12; Chen12]. The differences in delay between modes of the same mode group are minor, whereas the delay between modes of different groups is significant. Instead of including the phase constant $\beta_{0,i}$ in the channel description, it is used in the system model directly with parameter φ_{ij}. Without modal coupling the phase constant has no influence. The derivation of the analytic channel impulse response is carried out by calculating the inverse Fourier transform similarly to the SMF case, see Appendix A.3, and results in

$$\begin{aligned}\underline{g}^{+}_{\mathrm{o},i}(t) = \frac{1}{2}\,\frac{c_i \, \exp(-\alpha_i L)}{\sqrt{-2\pi L\beta_{2,i}}} \Bigg[&\exp\Bigg(\mathrm{j}\Bigg[\frac{(t-L\beta_{1,i})^2}{2L\beta_{2,i}} + \omega_{\mathrm{c}}t + \frac{\pi}{4}\Bigg]\Bigg) \\ &+\mathrm{j}\,\mathcal{H}\Bigg\{\exp\Bigg(\mathrm{j}\Bigg[\frac{(t-L\beta_{1,i})^2}{2L\beta_{2,i}} + \omega_{\mathrm{c}}t + \frac{\pi}{4}\Bigg]\Bigg)\Bigg\}\Bigg] \ , \quad \text{if} \quad \beta_{2,i} < 0 \ .\end{aligned} \tag{3.57}$$

Real-valued Bandpass Channel

In order to obtain the corresponding real-valued MMF channel impulse response, two times the real part of the analytic channel is taken, see Eq. 3.21. The result is as follows

$$\begin{aligned}g_{\mathrm{o},i}(t) = \frac{c_i \, \exp(-\alpha_i L)}{\sqrt{-2\pi L\beta_{2,i}}} \Bigg[&\cos\Bigg(\frac{(t-L\beta_{1,i})^2}{2L\beta_{2,i}} + \omega_{\mathrm{c}}t + \frac{\pi}{4}\Bigg) \\ &-\mathcal{H}\Bigg\{\sin\Bigg(\frac{(t-L\beta_{1,i})^2}{2L\beta_{2,i}} + \omega_{\mathrm{c}}t + \frac{\pi}{4}\Bigg)\Bigg\}\Bigg] \ , \qquad \text{if} \quad \beta_{2,i} < 0 \ .\end{aligned} \tag{3.58}$$

Solving the Hilbert transform, similar to the SMF case, leads to

$$g_{\mathrm{o},i}(t) = \frac{2\,c_i \, \exp(-\alpha_i L)}{\sqrt{-2\pi L\beta_{2,i}}} \cos\Bigg(\frac{(t-L\beta_{1,i})^2}{2L\beta_{2,i}} + \omega_{\mathrm{c}}t + \frac{\pi}{4}\Bigg) \cdot 1(t_0 - t) \ . \tag{3.59}$$

Equivalent Baseband Channel

The equivalent linear baseband channel representation is calculated according to Eq. 3.2 and results in

$$g_i(t) = \frac{2\, c_i\ \exp(-\alpha_i L)}{\sqrt{-2\pi L \beta_{2,i}}} \cos\left(\frac{(t - L\beta_{1,i})^2}{2L\beta_{2,i}} + \frac{\pi}{4} \right) \cdot 1(t_0 - t) \ . \tag{3.60}$$

As shown for the SMF case, the Heaviside step function can be neglected under certain conditions. Rewriting the expression as a convolution with a time shift yields

$$g_i(t) = \frac{2\, c_i\ \exp(-\alpha_i L)}{\sqrt{-2\pi L \beta_{2,i}}} \left[\cos\left(\frac{t^2}{2L\beta_{2,i}} + \frac{\pi}{4} \right) * \delta(t - L\beta_{1,i}) \right] \ , \qquad \text{if} \quad \beta_{2,i} < 0 \ . \tag{3.61}$$

Considering the superposition of all modes, similar to the equivalent linear transmission system in Eq. 3.53, and assuming identical chromatic dispersion parameter for all modes (i.e. $\beta_{2,i} = \beta_2$) leads to a frequently used description of an MMF channel

$$\begin{aligned} g_{\text{MMF}}(t) &= \sum_i g_i(t) \\ &= \underbrace{\frac{2}{\sqrt{-2\pi L\beta_2}} \cos\left(\frac{t^2}{2L\beta_2} + \frac{\pi}{4} \right)} * \underbrace{\sum_i c_i\ \exp(-\alpha_i L)\, \delta(t - L\beta_{1,i})} \\ &= \qquad\qquad g_{\text{SMF}}(t) \qquad\qquad * \qquad\qquad g_{\text{MD}}(t) \ , \end{aligned} \tag{3.62}$$

where $g_{\text{SMF}}(t)$ is the equivalent baseband channel impulse response of an SMF, similar to Eq. 3.29, and $g_{\text{MD}}(t)$ models the modal dispersion with mode excitation efficiency and mode attenuation. The corresponding transfer function of the modal dispersion impulse response is given by

$$g_{\text{MD}}(t) = \sum_i A_i \cdot \delta(t - \tau_i) \quad \circ\!\!-\!\!\!-\!\!\bullet \quad \underline{G}_{\text{MD}}(\omega) = \sum_i A_i \cdot \exp(-\mathrm{j}\omega\tau_i) \ , \tag{3.63}$$

with $L\beta_{1,i} = \tau_i$ representing the mode specific delay and $c_i\ \exp(-\alpha_i L) = A_i$ denoting the amplitude for each mode as exemplarily illustrated in Fig. 3.15.

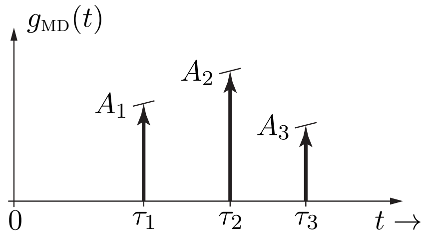

Figure 3.15: Modal dispersion impulse response for a 3-mode fiber

Few-Mode Fiber Example

Consider an FMF of 1.01 km length and a wavelength of 1550 nm with the mode specific parameters listed in Tab. 3.2. These parameters relate to the few-mode fiber implemented in the testbed. Based on the dispersion parameter D_i, the quadratic phase constant $\beta_{2,i}$ is calculated according to Eq. 3.20, and based on the differential mode delays (DMD) the absolute delays are evaluated as follows

$$\tau_i = \mathrm{DMD}_i \cdot L \ . \tag{3.64}$$

The summands $g_i(t)$ are shown in Fig. 3.16, where the blue line marks the modal delays τ_i, and $1/T_\mathrm{s} = 10$ GHz is the symbol rate. Figure 3.17 highlights the overall FMF channel impulse response. The transmission of a Gaussian pulse with an FWHM of 25 ps through the FMF channel is used to simulate an impulse response measurement with a picosecond impulse, see the result in Fig. 3.18. Extending this result to a multi-mode fiber with 10 propagating mode groups, the convolution of the baseband channel impulse response $g_\mathrm{MMF}(t)$ with the same Gaussian pulse $p(t)$ is expected to exhibit up to 10 visible peaks (e.g. compare Fig. 4.2).

The results show that approximating the MMF channel impulse response with multiple Gaussian pulses, which are located at their respective mode delay, and choosing the pulse width according to the chromatic dispersion, is a valid modeling approach in case that no mode cross-talk exists. If modal dispersion is much greater than chromatic dispersion, a model that solely relies on Dirac delta pulses is feasible.

Table 3.2: Mode dependent parameters (only cosine modes)

Mode	Index i	A_i	D_i in ps/nm/km	DMD_i in ps/m
LP_{01}	1	1	18.5	0
$\mathrm{LP}_{11\mathrm{a}}$	2	0.2	18.9	0.15
$\mathrm{LP}_{21\mathrm{a}}$	3	0.1	17.9	0.16
LP_{02}	4	0.4	16.6	0.16

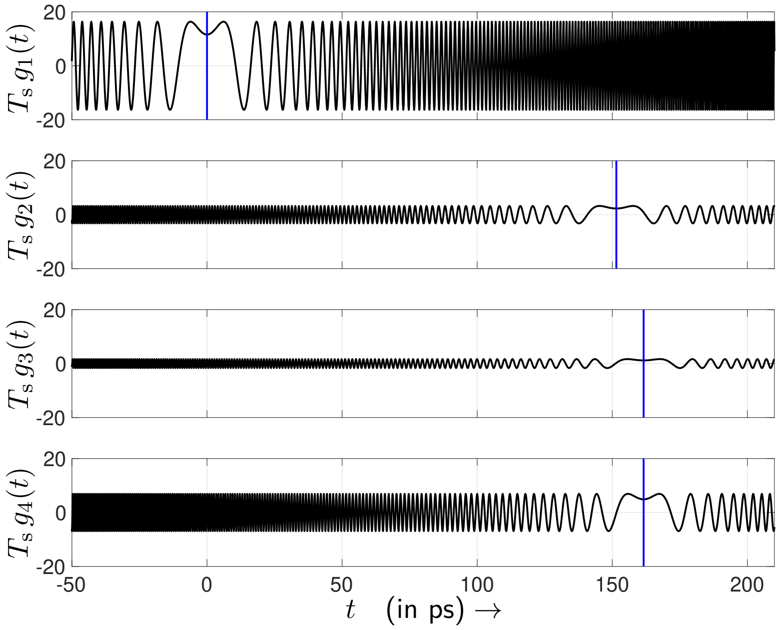

Figure 3.16: Summands $g_i(t)$ of the equivalent baseband FMF channel impulse response

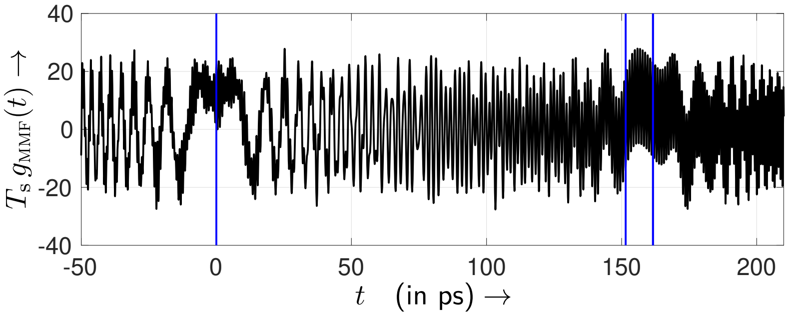

Figure 3.17: Equivalent baseband FMF channel impulse response

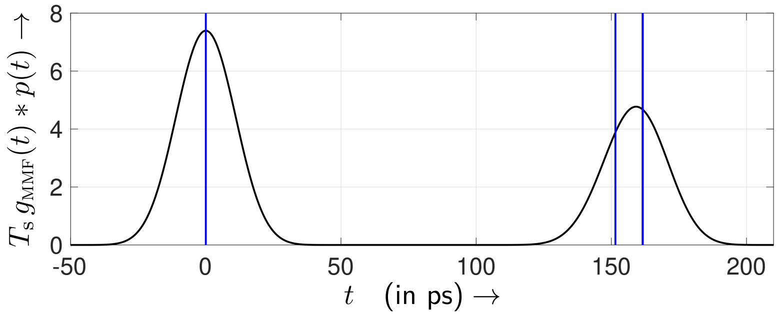

Figure 3.18: Convolution of the equivalent baseband FMF channel impulse response with a Gaussian pulse $p(t)$ of 25 ps FWHM

3.4 Multi-Mode Fiber MIMO System Model

In this section, the system model is extended to the MIMO case. Different modeling concepts for optical MIMO exist [Gree07; Bikh09]. However, it has not been shown under which conditions the MIMO system can be considered as linear in baseband when applying IM/DD. The analysis presented hereinafter focus on exactly these conditions that need to apply for a baseband linearity. The motivation for this analysis has a practical background. In testbed experiments it turned out that in some configurations linear signal processing allows to eliminate MIMO cross-talk and in others it does not. The unknown cause for this was impetus to fundamentally review the system model concept. With simulations and measurements the presented theoretic results are validated.

3.4.1 System Model

The system model presented in this section can be applied to any multi- or few-mode fiber MIMO testbed concept that implements IM/DD. As an example Fig. 3.19 shows a (2x2) configuration that is based on different SMF to MMF alignments for mode-selective excitation and MMF couplers for MUX and DEMUX. Let us consider the corresponding communication system model with $\mu = 1, \dots, n_\mathrm{T}$ inputs and $\nu = 1, \dots, n_\mathrm{R}$ outputs as depicted in Fig. 3.20. The presented model integrates the phase state of each fiber mode, mode coupling, mode orthogonality at the square-law detector and different spectral properties of the laser source. All of this information is required in order to determine under which conditions the system can be considered linear in baseband.

The electrical field at the νth MIMO output is given by

$$\underline{E}_\nu(t,x,y) = \sum_{i=1}^{M} E_i(x,y) \sum_{j=1}^{M} \sum_{\mu=1}^{n_\mathrm{T}} \underline{b}^{+}_{\mathrm{o},\nu i j \mu}(t) \, \exp\{-\mathrm{j}\varphi_{\nu i j \mu}\} \,, \tag{3.65}$$

where $E_i(x,y)$ is the transversal field of the ith linearly polarized mode at the detector. This field is simplified to a single polarization direction. Signal $\underline{b}^{+}_{\mathrm{o},\nu i j \mu}(t)$ contains all time dependent signals, and it integrates all possible paths through the system from the MIMO input μ with input mode $j = 1, \dots, M$ to the output mode $i = 1, \dots, M$ at the νth MIMO output. Signal $\exp\{-\mathrm{j}\varphi_{\nu i j \mu}\}$ describes the resulting phase of each path. The time

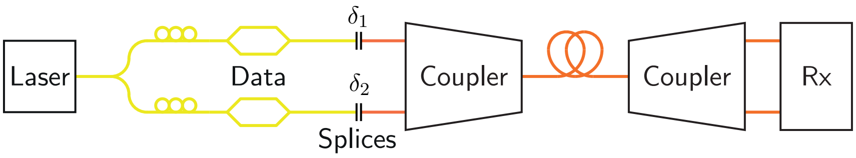

Figure 3.19: 2x2 MIMO testbed example

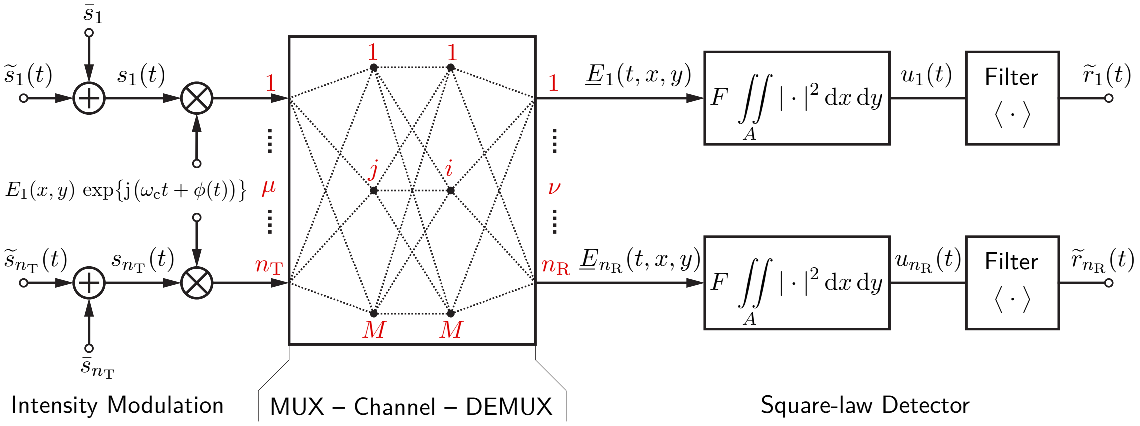

Figure 3.20: Multi-mode MIMO system model with IM/DD with the following index notation: MIMO input μ, input mode j, output mode i and MIMO output ν

dependent signal is defined as follows

$$\underline{b}^{+}_{\mathrm{o},\nu ij\mu}(t) = k_{\nu ij\mu}\left[\left(s_\mu(t)\;\exp\{\mathrm{j}\,(\omega_\mathrm{c}t+\phi(t))\}\right) * \underline{g}^{+}_{\mathrm{o},\nu ij\mu}(t)\right] . \tag{3.66}$$

Here, the electrical input signal $s_\mu(t)$, consisting of an AC signal $\tilde{s}_\mu(t)$ and a DC or carrier component $\bar{s}_\mu$, is modulated onto the optical carrier with angular center frequency ω_c and laser phase noise $\phi(t)$. The modulated signals are transferred through different paths denoted by the analytic channel $\underline{g}^{+}_{\mathrm{o},\nu ij\mu}(t)$. In addition, these signals are weighted by the constant $k_{\nu ij\mu}$, containing all sorts of mode coupling factors. This constant also maps the mode dependent losses [Ho13]. With substitution, Eq. 3.65 is simplified yielding

$$\underline{E}_\nu(t,x,y) = \sum_i E_i(x,y)\,\underline{f}_{\nu i}(t) \quad . \tag{3.67}$$

The square-law detection process is carried out as follows

$$\begin{aligned} u_\nu(t) &= F \iint_A \left|\underline{E}_\nu(t,x,y)\right|^2 \mathrm{d}x\,\mathrm{d}y \\ &= F \iint_A \Big[\sum_i E_i(x,y)\,\underline{f}_{\nu i}(t)\Big] \cdot \Big[\sum_i E_i(x,y)\,\underline{f}_{\nu i}(t)\Big]^* \mathrm{d}x\,\mathrm{d}y \quad , \end{aligned} \tag{3.68}$$

where A is the detector surface area, and F is a conversion factor, which includes the detector's responsivity as well as the amplifier's transimpedance. Please be advised, receiver noise is not considered in this system model for the sake of simplicity. Expanding the sums into one with identical indices i and into a double sum with mixed indices $i \neq i'$ leads to

$$\begin{aligned} u_\nu(t) = F \iint\limits_A \Bigg[& \sum_i E_i(x,y)\, E_i(x,y)\, \underline{f}_{\nu i}(t)\, \underline{f}^*_{\nu i}(t) \\ & + \underbrace{\sum_i \sum_{i'}}_{\text{if } i\neq i'} E_i(x,y)\, E_{i'}(x,y)\, \underline{f}_{\nu i}(t)\, \underline{f}^*_{\nu i'}(t) \Bigg] \mathrm{d}x\, \mathrm{d}y \quad . \end{aligned} \tag{3.69}$$

Assuming a large detector surface area, the integration over the product of transversal fields of different modes is zero due to mode orthogonality as given by Eq. 3.42. Considering the mode orthogonality and interchanging the integral with the summation we get

$$\begin{aligned} u_\nu(t) &= F \sum_i \underline{f}_{\nu i}(t)\, \underline{f}^*_{\nu i}(t) \iint\limits_A E_i(x,y)\, E_i(x,y)\, \mathrm{d}x\, \mathrm{d}y \\ &= F \sum_i P_i\, \underline{f}_{\nu i}(t)\, \underline{f}^*_{\nu i}(t) \quad . \end{aligned} \tag{3.70}$$

Back-substitution leads to

$$\begin{aligned} u_\nu(t) = F \sum_i P_i & \left(\sum_j \sum_\mu \underline{b}^+_{\mathrm{o},\nu i j \mu}(t)\, \exp\{-\mathrm{j}\varphi_{\nu i j \mu}\} \right) \\ & \left(\sum_{j'} \sum_{\mu'} \left[\underline{b}^+_{\mathrm{o},\nu i j' \mu'}(t)\right]^* \exp\{+\mathrm{j}\varphi_{\nu i j' \mu'}\} \right) . \end{aligned} \tag{3.71}$$

Expanding the expression and grouping the summands with respect to the similarity and dissimilarity of the indices yields to

$$\begin{aligned} u_\nu(t) = {} & F \sum_i P_i \left(\sum_j \sum_\mu \left|\underline{b}^+_{\mathrm{o},\nu i j \mu}(t)\right|^2 \right) \\ & + F \sum_i P_i \left(\underbrace{\sum_j \sum_\mu \sum_{j'} \sum_{\mu'}}_{\text{if } j\neq j' \text{ or } \mu\neq\mu'} \underline{b}^+_{\mathrm{o},\nu i j \mu}(t) \left[\underline{b}^+_{\mathrm{o},\nu i j' \mu'}(t)\right]^* \cdot \exp\Big\{-\mathrm{j}\, (\varphi_{\nu i j \mu} - \varphi_{\nu i j' \mu'})\Big\} \right) \end{aligned} \tag{3.72}$$

and in short form

$$u_\nu(t) = u^{(\nu)}_{\text{sig}}(t) + u^{(\nu)}_{\text{int}}(t) \quad . \tag{3.73}$$

The phase cancels in term $u^{(\nu)}_{\text{sig}}(t)$, and therefore the signals add constructively. In contrast, in $u^{(\nu)}_{\text{int}}(t)$ the phase remains, which results in interference. Please note that signal $u^{(\nu)}_{\text{int}}(t)$ is real-valued since each summand has a complementary one where the signal is the complex conjugate. The last step in the detection process is modeled by a lowpass filter with DC suppression denoted by $\langle \cdot \rangle$. This detection filter is applied to formally remove the signal components around twice the carrier frequency. Thus, the measurable output of the MIMO system decomposes to

$$\begin{aligned}\widetilde{r}_\nu(t) = \left\langle u_\nu(t) \right\rangle &= \left\langle u_{\text{sig}}^{(\nu)}(t) \right\rangle + \left\langle u_{\text{int}}^{(\nu)}(t) \right\rangle \\ &= \widetilde{r}_{\text{sig}}^{(\nu)}(t) \quad + \quad \widetilde{r}_{\text{int}}^{(\nu)}(t) \;\; ,\end{aligned} \tag{3.74}$$

where $\widetilde{r}_{\text{sig}}^{(\nu)}(t)$ denotes the desired and $\widetilde{r}_{\text{int}}^{(\nu)}(t)$ the interference signal.

Baseband Linearity of the Desired Signal

Hereinafter, it is shown that the desired signal $\widetilde{r}_{\text{sig}}^{(\nu)}(t)$ can be considered as linear in baseband. It is given by

$$\widetilde{r}_{\text{sig}}^{(\nu)}(t) = F \sum_i P_i \left(\sum_j \sum_\mu \left\langle \left| \underline{b}_{\text{o},\nu i j \mu}^{+}(t) \right|^2 \right\rangle \right) \;\; . \tag{3.75}$$

Let us focus on the summands and omit the indices for simplicity. Each summand contains analytic signals and is described with the back-substitution of Eq. 3.66 as follows

$$\left\langle \left| \underline{b}_{\text{o}}^{+}(t) \right|^2 \right\rangle = \left\langle \left| k \left[\left(s(t) \, \exp(\text{j}\omega_\text{c} t) \right) * \underline{g}_{\text{o}}^{+}(t) \right] \right|^2 \right\rangle \;\; , \tag{3.76}$$

assuming a monochromatic laser. Applying the relation between an analytic and real-valued representation, compare Section 3.2.1, yields

$$\left\langle b_{\text{o}}^2(t) \right\rangle = k^2 \left\langle \left[\left(s(t) \, \sqrt{2} \, \cos(\omega_\text{c} t) \right) * g_{\text{o}}(t) \right]^2 \right\rangle \;\; . \tag{3.77}$$

In accordance with Section 3.1, the equivalent linear representation results in

$$\left\langle \left[\left([\widetilde{s}(t) + \bar{s}] \, \sqrt{2} \, \cos(\omega_\text{c} t) \right) * g_{\text{o}}(t) \right]^2 \right\rangle = \widetilde{s}(t) * g(t) \;\; , \tag{3.78}$$

with the equivalent baseband channel impulse response being defined by

$$g(t) = 2 \, g_{\text{o}}(t) \, \cos(\omega_\text{c} t) \;\; . \tag{3.79}$$

Therefore, each summand in $\widetilde{r}_{\text{sig}}^{(\nu)}(t)$ is linear in baseband, and hence their summation is linear as well.

Properties of the Interference Signal

The interference signal is given by

$$\widetilde{r}_{\text{int}}^{(\nu)}(t) = F \sum_i P_i \left(\underbrace{\sum_j \sum_\mu \sum_{j'} \sum_{\mu'}}_{\text{if } j \neq j' \text{ or } \mu \neq \mu'} \left\langle \underline{b}^{+}_{\text{o},\nu ij\mu}(t) \left[\underline{b}^{+}_{\text{o},\nu ij'\mu'}(t)\right]^* \right\rangle \cdot \exp\left\{ -\mathrm{j} \left(\varphi_{\nu ij\mu} - \varphi_{\nu ij'\mu'} \right) \right\} \right) \quad . \tag{3.80}$$

It is worth noting that the use of a high mode count M does not remove the interference in terms of an averaging effect. However, the interference signal is completely eliminated, if no modal cross-talk exists, i.e. the overall system is composed of parallel SISO systems. Such systems have been realized in literature [Labr15; Beny17]. Here, different mode groups are used as separate transmission channels since in short reach systems coupling between mode groups is negligibly small [Carp13; Sand19]. This technique is known as mode group multiplexing. However, in order to exclusively excite modes of one group, phase plates or spatial light modulator type devices are required. They have the disadvantage of being free-space components, and therefore they have a high cost.

By means of illustration, the analytic channel $\underline{g}^{+}_{\text{o},\nu ij\mu}(t)$ in $\underline{b}^{+}_{\text{o},\nu ij\mu}(t)$, see Eq. 3.66, is assumed to be an ideal Dirac delta pulse. In this case the time dependent signal is proportional to the MIMO input signal, and hence we can write

$$\underline{b}^{+}_{\text{o},\nu ij\mu}(t) \left[\underline{b}^{+}_{\text{o},\nu ij'\mu'}(t)\right]^* \propto s_\mu(t) \cdot s_{\mu'}(t) \quad . \tag{3.81}$$

Considering an ordinary on-off keying constellation, a ’0’ bit is represented by $s_\mu(t) = 0$. Thus, in case of all MIMO inputs transmitting a ’0’ bit no interference can occur. In contrast, if at all inputs a ’1’ bit is transmitted, the interference term is non-negligible. In mixed conditions, if at least one MIMO input transmits a ’1’ bit, it can self-interfere. This happens when mode coupling occurs in combination with mode dispersion, i.e. the analytic channel $\underline{g}^{+}_{\text{o},\nu ij\mu}(t)$ is non-ideal. The latter is a prime example for interference in MMF SISO links. Such links can be considered as a special case of the presented system model when choosing $n_\text{T} = n_\text{R} = 1$.

Simulations have shown that with a broad-linewidth laser the interference signal before filtering, i.e. $u_{\text{int}}^{(\nu)}(t)$, is a noise-like signal with its variance being weighted by the amplitudes of the time dependent signals product. Since this noise-like signal has high frequency components, the application of the detection filter reduces the power of the interference signal. With a narrow-linewidth laser the interference signal before filtering appears to be a normal bit pattern. However, it is a result of phase dependent superpositions, and hence the signal cannot be linearly predicted since the phase information is lost in the detection process.

As shown in Eq. 3.74 the measured output signal consists of the desired and interference signals. When considering a sufficient number of realizations of the same data being transmitted over the same channel, the ensemble average of the interference signal is zero. This is a result of the laser phase noise $\phi(t)$ for broad- as well as narrow-linewidth lasers and changes in the output phase $\varphi_{\nu i j \mu}$. Therefore, with an ensemble average measurement the desired signal $\widetilde{r}_{\mathrm{sig}}^{(\nu)}(t)$ can be extracted for research purposes.

Quality Criterion

In order to evaluate the influence of the interference term, the signal-to-interference-plus-noise ratio (SINR) is defined at each MIMO output as follows

$$\mathrm{SINR}_\nu = \lim_{T\to\infty} \frac{\displaystyle\int\limits_T \left[\widetilde{r}_{\mathrm{sig}}^{(\nu)}(t)\right]^2 \mathrm{d}t}{\displaystyle\int\limits_T \left[\widetilde{r}_{\mathrm{int}}^{(\nu)}(t) + \widetilde{n}_\nu(t)\right]^2 \mathrm{d}t} \quad . \tag{3.82}$$

Here, the receiver noise $\widetilde{n}_\nu(t)$ that has been neglected up to this point is taken into consideration. It affects the receive signal as given by

$$\widetilde{r}_\nu(t) = \widetilde{r}_{\mathrm{sig}}^{(\nu)}(t) + \widetilde{r}_{\mathrm{int}}^{(\nu)}(t) + \widetilde{n}_\nu(t) \quad . \tag{3.83}$$

The SINR metric is needed in the measurement section, whereas in the simulation section an isolated view on the interference effect is possible. Therefore, the signal-to-interference ratio (SIR) without noise influence is additionally implemented:

$$\mathrm{SIR}_\nu = \mathrm{SINR}_\nu \Big|_{\widetilde{n}_\nu(t)=0} \quad . \tag{3.84}$$

The constant mode coupling parameter is defined to satisfy the conservation of energy as follows

$$\sum_{\nu,i,j} k_{\nu i j \mu}^2 = 1 \quad \forall \mu \quad . \tag{3.85}$$

Finally, a mode cross-talk parameter is defined by

$$k_{\mathrm{x-talk}} = \left(\frac{1}{n_\mathrm{T}} \underbrace{\sum_\nu \sum_i \sum_j \sum_\mu}_{\nu\neq i \text{ or } i\neq j \text{ or } j\neq\mu} k_{\nu i j \mu}^2 \right)^{1/2} \in [0,1] \quad , \tag{3.86}$$

measuring the degree of cross-talk between fiber modes in the system.

3.4.2 Simulation Results

In the previous section, the theoretic results have shown that considering mode coupling, the interference term is non-negligible, and hence the SIR needs to be analyzed. This section shall answer how mode coupling affects the SIR and how it influences the BER when linear signal processing is applied. Therefore, a bit-level simulation of essentially Eqs. 3.72 and 3.74 is implemented for evaluating a (2×2) MIMO transmission through a 3-mode fiber using on-off keying and a symbol rate of 5 GHz. Herein, pseudo-random binary sequences of length $2^{11} - 1$ trailed by a zero bit are repeatedly transmitted. The center wavelength is assumed such that no chromatic dispersion is in effect and the maximum mode delay with reference to the LP_{01} mode is chosen to be 200 ps. Two laser sources are compared: The first is referred to as the narrow-linewidth laser having a full width at half maximum spectral width of $\Delta\lambda = 0.8$ fm and the second is referred to as the broad-linewidth laser with $\Delta\lambda = 5$ nm. Laser phase noise modeled by a Wiener process is used to consider the laser's Lorentzian shaped spectrum [Gall84]. Receiver noise is not considered in the simulation. The phase $\varphi_{\nu i j \mu}$ is chosen as a uniformly distributed variable in the interval $[0, 2\pi]$, and the mode coupling parameter $k_{\nu i j \mu}$ is randomly chosen in each realization as follows

$$k_{\nu i j \mu} = \begin{cases} S(|a| + 1) & : \nu = i = j = \mu \\ S\ |a| & : \text{else} \end{cases} , \tag{3.87}$$

where a is normally distributed with zero mean and adjustable variance. Factor S is a scaling factor to satisfy the conservation of energy, compare Eq. 3.85. Considering the extreme case $a = 0$ represents a fully orthogonal MIMO transmission. In contrast, the non-ideal case with active mode coupling (i.e. $a \neq 0$) is accompanied by mode dependent losses. These losses lead to a different weighting of the received signals, and hence they affect the quality of the MIMO layers in terms of the SIR. Receiver-side linear signal processing includes a least squares channel estimator, evaluating 9 taps per MIMO sub-channel, and a MIMO zero forcing equalizer with a finite impulse response having 80 taps per sub-channel.

In Figure 3.21 the dependency of the SIR on the mode cross-talk parameter is analyzed. Each marker represents a realization of the simulation. Since the MIMO output with the lower SIR decisively determines the overall BER performance, the worst case scenario is analyzed by taking the MIMO output with the minimum SIR. The results show that with increasing mode cross-talk the SIR decreases. Without mode coupling, i.e. $k_{\mathrm{x-talk}} = 0$, no interference is present leading to an infinite SIR. Considering weak mode coupling with $k_{\mathrm{x-talk}} < 0.2$, the worst case SIR is approximately 6 dB, highlighting that the overall transmission is predominantly linear in baseband. With higher mode coupling the influence of interference is significant, and the overall transmission is not linear. Comparing the two laser types shows that the variation of the SIR is higher in the narrow-linewidth case

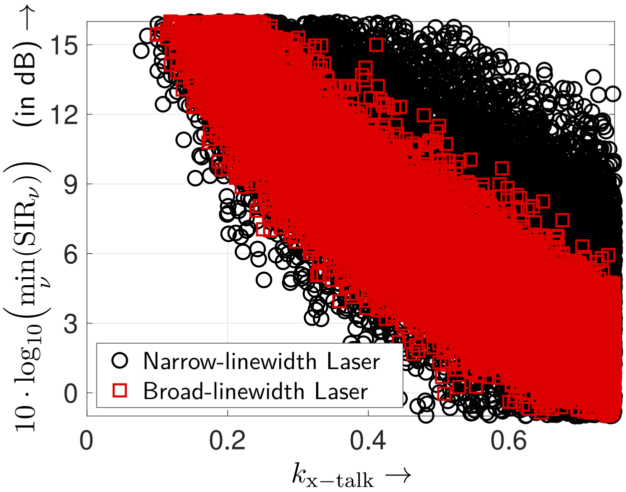

Figure 3.21: Minimum SIR depending on the cross-talk between fiber modes

when choosing the same mode cross-talk value. This is a result of the different signal properties of the interference signal when comparing the two laser types. In fact, the worst-case scenario, i.e. the lowest SIR value for a given mode cross-talk value, is the critical parameter and here the differences are just minor. Table 3.3 summarizes the dependency of the baseband linearity on the mode coupling magnitude. It shows, that in weak mode coupling conditions linear frequency-selective equalization strategies can be applied to eliminate MIMO cross-talk and time-dispersion impairments.

Since it is known that coupling between modes of the same group is high, the use of all 55 modes (per polarization) as separate transmission channels in a 50/125 parabolic index MMF with a numerical aperture of 0.2 at 1550 nm is not viable in IM/DD systems [Carp13]. In contrast, coupling between mode groups is quite low in short reach MMF systems, and hence at best all 10 mode groups could be used as separate transmission channels. Indeed, this requires orthogonal mode group multiplexing and demultiplexing, which is complex and to date demands for costly and bulky free space components.

The influence of the minimum SIR on the BER for different channel realizations is shown by means of an empirical cumulative distribution function (CDF) in Fig. 3.22. Let us consider an extreme example for clarification purposes: In 100% of the channel realization cases the BER is lower than 0.5, compare diamond shaped marker. In 99.9% of the cases the BER is lower than 10^{-3} for a broad-linewidth laser with an SIR of 6 dB, see star marker. Using a narrow-linewidth laser this probability reduces to 91%, compare cross marker. This

Table 3.3: MIMO baseband linearity for different mode coupling conditions

Mode coupling	$k_{\mathrm{x-talk}}$	Baseband linearity
no coupling	0	linear conditions
weak	< 0.2	predominantly linear
strong	> 0.2	not linear

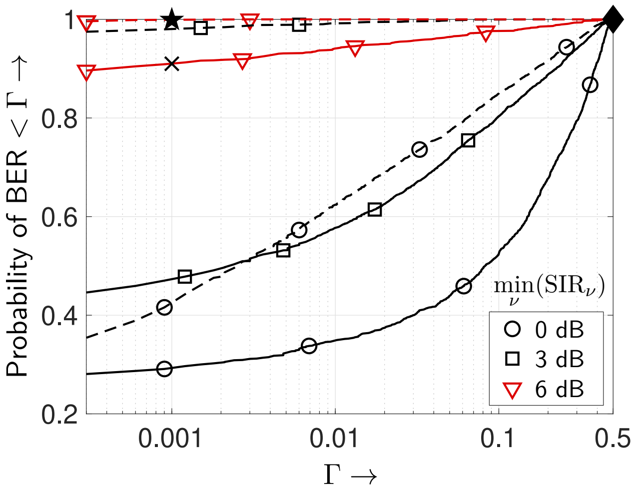

Figure 3.22: Empirical CDFs showing the BER distribution for a multitude of channel realizations at fixed SIRs (solid lines: narrow-linewidth laser, dashed lines: broad-linewidth laser)

signifies that a broad-linewidth laser is advantageous in terms of the BER performance, which is a result of this laser producing a noise-like interference signal whose power is significantly reduced by the receive filter (compare Section 3.4.1). Also, the CDF clearly shows that with a low minimum SIR of 0 dB a high BER is very likely, making a reliable transmission unfeasible. For practical applications the results imply that a broad-linewidth laser is beneficial. In fact, this advantage might be consumed by its higher chromatic dispersion in practice compared to narrow-linewidth lasers since chromatic dispersion is not considered in this simulation.

3.4.3 Measurement Results

In order to visualize the interference and to evaluate its impact on the BER performance two MIMO testbed setups are analyzed as shown in Fig. 3.23. The first setup uses two (6×1) port photonic lanterns (PL) and a 1 km 6-mode fiber channel to realize a (2×2) MIMO configuration. Since not all ports of the PLs are used, the selection of the input and output

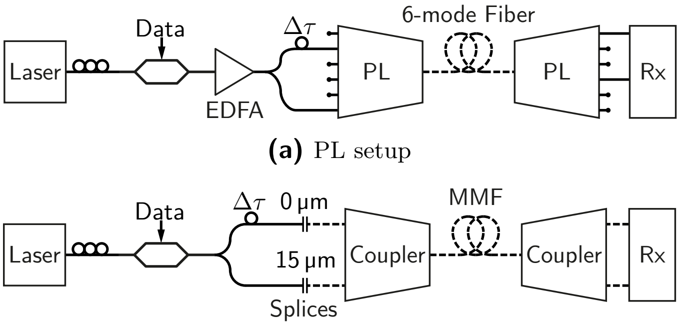

(a) PL setup

(b) Coupler setup

Figure 3.23: MIMO testbed configurations (solid line: SMF, dashed line: 6-mode fiber or MMF)

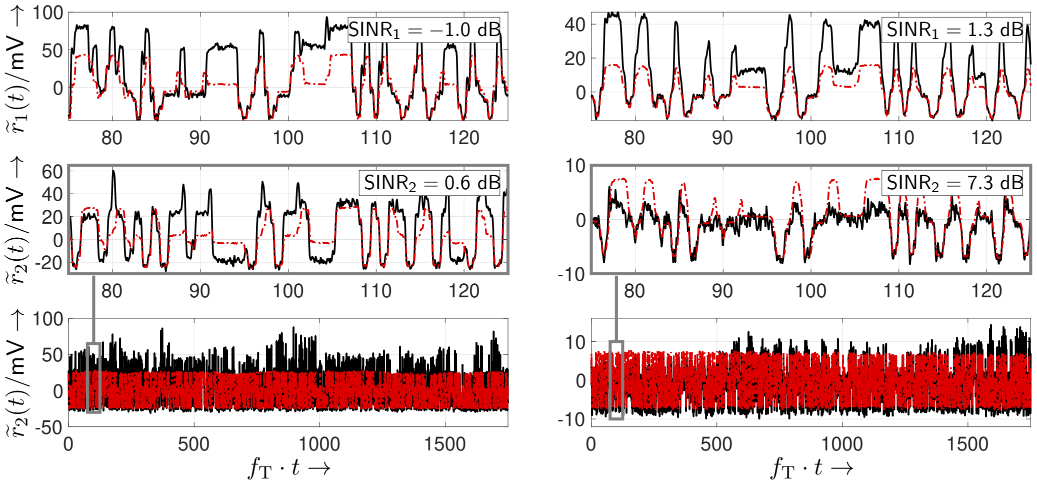

(a) PL setup and DFB laser (b) PL setup and FP laser

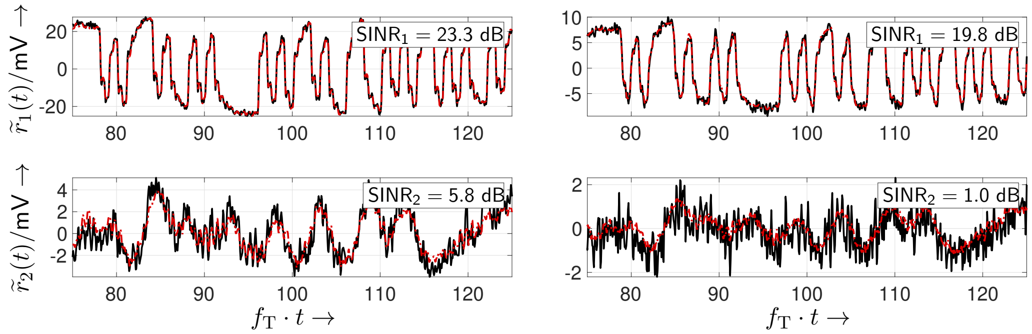

(c) Coupler setup and DFB laser (d) Coupler setup and FP laser

Figure 3.24: Measured MIMO receive signals comparing different (2×2) configurations at $f_T = 2.5$ GHz (red dashed lines: ensemble average, black solid lines: without ensemble averaging)

ports is important to optimize the channel capacity, compare section "under-addressed channel" in [Winz13]. For instance, in the worst case scenario a MIMO output port could be chosen, which extracts a set of modes that do not contain any of the transmitted data information. Therefore, different combinations of PL inputs and outputs have been tested, and the option with the best BER performance is chosen. It is worth noting, that the high insertion loss of the PL setup requires the use of an Erbium-doped fiber amplifier (EDFA), which is deployed after the modulator. Secondly, a setup based on SMF to MMF splices with different radial offsets for mode-selective excitation, fusion couplers for mode MUX and DEMUX and a 1 km 50/125 graded-index fiber channel is studied. Both setups use on-off keying signaling at an operating wavelength of 1550 nm. Furthermore, the signal at one MIMO input is delayed by $\Delta\tau = 819.2$ ns in order to guarantee independent and uncorrelated bit patterns. In both testbed configurations the mode dependent losses in the fiber channel are negligibly small due to their short length. In contrast, the loss characteristics of the MUX and DEMUX components are highly mode dependent.

Figure 3.24 shows the measured receive data of both testbed configurations when transmitting at a symbol rate of $f_\mathrm{T} = 2.5$ GHz. For each configuration two laser types are studied, namely a DFB and a Fabry-Pérot laser. Each figure compares the signal measured without averaging to the ensemble averaged one. The latter consists of the desired signal $\widetilde{r}_\mathrm{sig}^{(\nu)}(t)$ only since the interference and noise terms are removed during the averaging process.

Photonic Lantern Setup Considering the PL setup, significant interference can be observed in the high level envelope of the signal measured without averaging. In contrast, the low level envelope does not show interference since here no light is transmitted at either MIMO input, and hence no interference can occur. It is worth noting that the high level envelope of the ensemble averaged signal is constant showing the situation without interference. In subfigure (a) mainly constructive interference occurs, whereas in subfigure (b) also destructive interference is visible. It can also be observed that the interference strongly varies with time, which is a result of the changing phase relations between the fiber modes at the receiver. The low SINR values are mainly a result of the high interference due to significant mode coupling in the photonic lantern configuration. The noise influence is relatively low since an EDFA is used. These findings are representative for other input and output port choices. As a result, a reliable MIMO transmission with the implemented PL setup is not feasible due to the high interference. Thus, the focus is on the coupler setup in the remaining part.

Coupler Setup In subfigures (c) and (d) the signal waveforms overlap quite well. This indicates that the interference term is relatively small, and hence we can assume baseband linearity. However, a high noise influence can be observed in signal $\widetilde{r}_2(t)$, leading to low SINR values. This signal originates from the path with the 15 µm offset launch, which has a higher insertion loss than the path with the centric launch. It is also worth noting that the transmit power of the DFB laser is higher compared to the Fabry-Pérot (FP) laser, which explains the differences in the signal amplitudes and consequently the SINR values. Fortunately, the high noise values are not critical since the signal-to-noise ratio is optimized with the application of the receive filter. The BER performance analysis of the coupler setup is carried out in Section 5.1.3.

3.4.4 MUX Interference

Let us focus on the coupler setup and just take the mode-selective excitation and multiplexing process into account. Figure 3.25 shows the corresponding testbed setup. In this configuration the amount of interference in the measured signal with respect to the launch offset δ is of interest. The measurement approach is based on oscilloscope persistence screenshots. A measured example is shown in Fig. 3.26. By slightly delaying one of the two MIMO inputs by half a symbol duration with utilizing fibers of different lengths, all

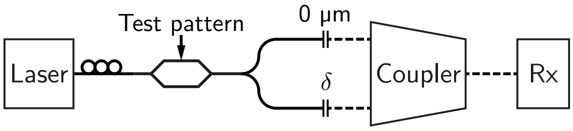

Figure 3.25: Measurement setup for evaluating the interference for varying launch offsets δ (solid line: SMF, dashed line: MMF)

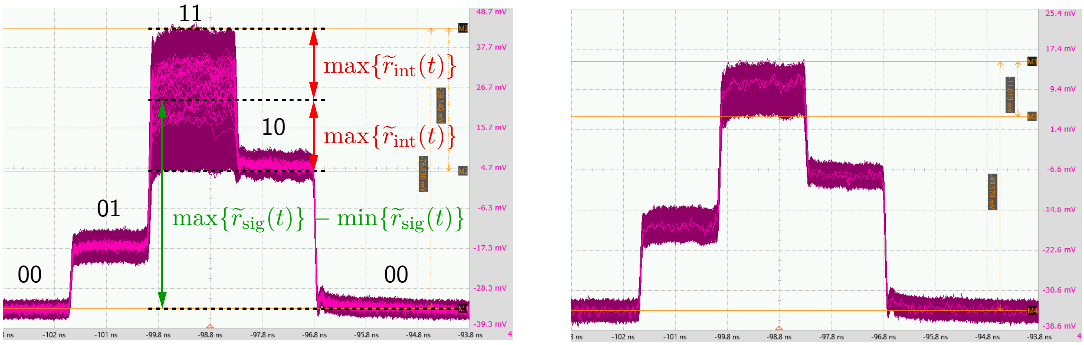

(a) $\delta = 0$ µm **(b)** $\delta = 16$ µm

Figure 3.26: Persistence measurement screenshots for the 2x1 configuration using coupler type C

bit combinations (i.e. '00', '01', '11' and '10') can be observed. The figure highlights the occurring interference when both MIMO inputs transmit a '1' bit, specifically when multiplexing the same set of modes, i.e. $\delta = 0$ µm. At $\delta = 16$ µm the interference is significantly reduced. Figure 3.26a also highlights the signal components of the received signal. Please note that the implemented receiver is DC-coupled. Since this approach is based on persistence screenshots it differs from previous measurements, and hence requires a new interference metric. This metric is defined as follows

$$\zeta_{\text{rel}} = \frac{\max\{\widetilde{r}_{\text{int}}(t)\}}{\max\{\widetilde{r}_{\text{sig}}(t)\} - \min\{\widetilde{r}_{\text{sig}}(t)\} + \max\{\widetilde{r}_{\text{int}}(t)\}} \ . \tag{3.88}$$

It evaluates the percentage of the measured signal amplitude, which results from interference. A value $\zeta_{\text{rel}} = 1/2$ states that the interference signal amplitude is identical to the one of the desired signal. In the worst case scenario when both signals destructively interfere, the measured signal completely vanishes. In order to cover the range between full destructive and constructive interference during measurements, the fibers are shaken before the multiplexing process. Please note that complete destructive interference only occurs, if the interfering signals have the same power. In order to make the measured data independent of the power of individual signals, the following normalization is applied

$$\zeta_{\text{norm}} = \frac{\zeta_{\text{rel}}}{\left(\sum_\mu P_\mu - \max\{P_\mu\}\right) / \left(\sum_\mu P_\mu\right)} \in [0,1] \ , \tag{3.89}$$

with P_μ being the optical signal power originating from the μth input. Normalizing a ratio of electrical amplitudes with a ratio of optical powers is valid since they are linearly related via the responsivity and this scaling factor is removed in the quotient. An excerpt of the

Table 3.4: Measured data excerpt for the 2x1 configuration using coupler type C

δ/µm	$\max\{\widetilde{r}_{\mathrm{int}}(t)\}$	$(\max\{\widetilde{r}_{\mathrm{sig}}(t)\} - \min\{\widetilde{r}_{\mathrm{sig}}(t)\})$	ζ_{rel}	P_1/µW	P_2/µW	ζ_{norm}
0	18.07 mV	57.26 mV	0.24	17.51	38.33	0.77
8	9.83 mV	51.40 mV	0.16	16.54	33.83	0.49
16	4.01 mV	44.07 mV	0.08	16.51	26.07	0.21

measured data is listed in Tab. 3.4. Herein, it is noteworthy that the measured receive power P_2 of the eccentric path decreases with increasing offset δ, signifying the need for the normalization. Furthermore, the noise influence is subtracted from the measured electrical amplitudes by identifying the maximum noise amplitudes that appeared in the persistence measurement with the help of a noise histogram.

The measured dependency of the normalized interference metric on the launch offset δ is depicted in Fig. 3.27, comparing different coupler types. Coupler types A and B are mode-selective couplers with a low degree of fusion, and type C is a standard 50:50 coupler. The simulated results are based on the calculated coupling efficiency when launching from the SMF into the MMF with a defined offset and assuming that no mode coupling occurs in the MUX process, see Section 2.1.1. Considering $\delta = 0$ µm then both MIMO inputs launch the same set of modes and without further mode coupling this leads to 100% interference in the worst-case scenario. With increasing launch offset δ the interference decreases. The lowest interference values are observed in the range from 16 to 20 µm. The results highlight that the excitation of a fully orthogonal set of modes is not possible with an SMF to MMF splice with radial offset.

Envisioning a (3×1) setup based on the same type of components, the simulated interference results are shown in Fig. 3.28 for the three launch offsets δ_1 to δ_3. They show that a configuration of 0, 10 and 20 µm exhibits the lowest interference values. However, these

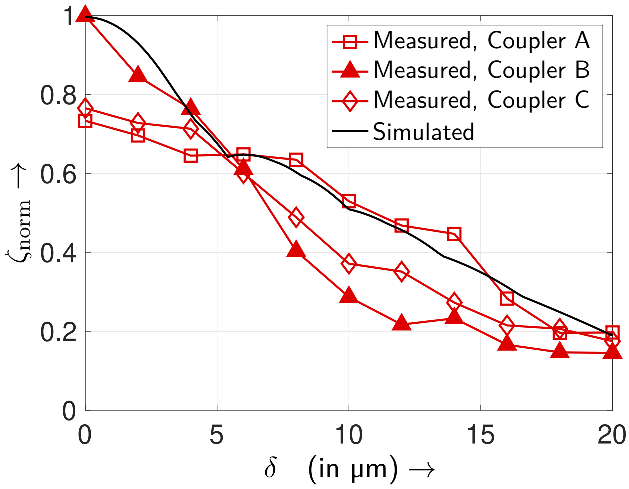

Figure 3.27: Normalized interference metric as a result of the 2x1 multiplexing process in dependency on the launch offset δ

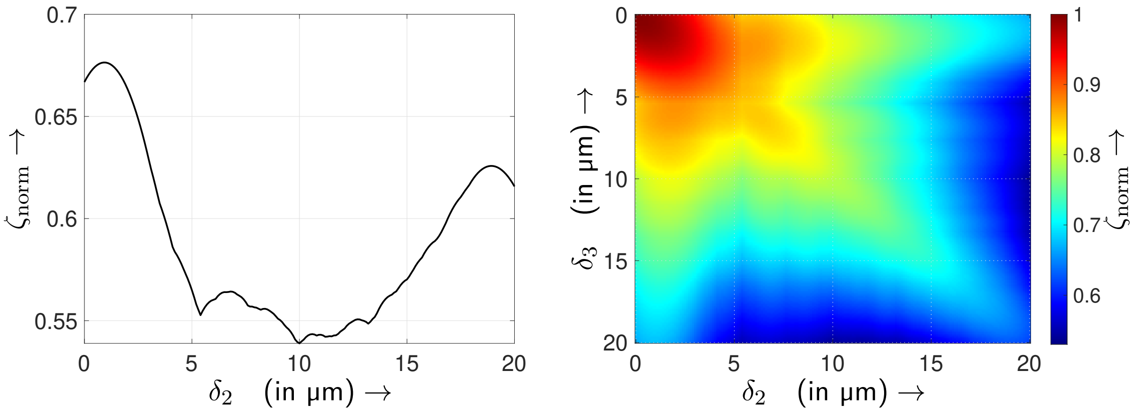

(a) Cross-section ($\delta_3 = 20$ µm) **(b)** Dependency on δ_2 and δ_3

Figure 3.28: Simulated normalized interference metric as a result of the 3x1 multiplexing process ($\delta_1 = 0$ µm)

values are in the region above 50% normalized interference, highlighting that even in the optimal configuration significant interference occurs. Our practical implementation of a (3×3) MIMO setup confirms this prediction and a reliable transmission was not feasible. It is worth noting that a working (3×1) multiple-input single-output setup for a short data segment has been demonstrated in [Schoe08]. However, this setup lacks the DEMUX structure, e.g. multi-mode couplers, to separate the MIMO signals and to detect all receive data at the same time. The required DEMUX structure would introduce additional attenuation, mode coupling and an increase in interference. So far, a fully operational (3×3) MIMO transmission with SMF to MMF splices with radial offset for mode-selective excitation and multi-mode couplers for MUX and DEMUX has not been realized.

Considerations for the Testbed Setup The measurement and simulation results highlight that the minimization of the mode cross-talk is essential for reducing the interference and simultaneously minimizing the BER in MIMO systems with IM/DD. Consequently, any unnecessary connector between multi-mode fibers and also splices should be avoided since any resulting fiber offset leads to mode coupling. In case of using a narrow-linewidth laser, such connections also add modal noise to the received signal. It is worth highlighting that modal noise and the interference term need to be clearly differentiated. Modal noise occurs due to spatial filtering in MMFs during propagation or detection and involves a narrow-linewidth laser so that a time-varying speckle pattern forms. In contrast, interference also occurs with a broad-linewidth laser and when mode coupling takes place even without any spatial filtering. The realization of higher-order MIMO systems, e.g. a (3×3) configuration, with IM/DD requires an improvement in the mode orthogonality during the mode-selective excitation, multiplexing and demultiplexing process. Despite components like phase plates or spatial light modulators that meet the high orthogonality requirements are available, short reach IM/DD systems require low-cost multiplexing components.

4 Multi-Mode Fiber MIMO Channel Description

This chapter characterizes optical multi-mode channels and discrete hardware components for MIMO applications with the focus on measurements. Firstly, a method is presented to determine the power coupling coefficients between mode groups in arbitrary multi-mode devices under test (DUTs) with a low-cost setup. Secondly, the time-variance and time-delay spread properties of a multi-mode fiber channel are analyzed under the influence of mechanical stress. The profound knowledge of the mode coupling and time-variance properties is vital for the design of a suitable transmission frame and the choice of signal processing strategies in the MIMO testbed.

4.1 Mode Group Power Coupling Analysis

It has been shown in Chap. 3.4 that in MIMO systems with IM/DD, mode cross-talk between signals leads to interference, impairing the overall system performance. Mode coupling itself is a process that takes place distributed along the fiber length due to fiber imperfections, e.g. impurities and bends of the fiber. In other optical components like spatial multiplexers and within connectors mode coupling occurs in an intensified way.

In this section, a method is presented that is able to determine the power coupling coefficients between mode groups for arbitrary testbed components with a low-cost setup. Previous studies have analyzed mode coupling by exciting an individual mode at the transmitter-side using e.g. a spatial light modulator and filtering a desired mode at the receiver [Berd82; Carp13; Carp16; Chen16a]. This work focuses on the analysis of power coupling between mode groups (rather than individual linearly polarized modes) in short reach and low-cost IM/DD systems. With the presented method, it is not necessary to exclusively excite a single mode group at the input of the DUT. It is based on multiple impulse response measurements with different excitation conditions. Furthermore, this method does not require a costly free-space setup.

In the next parts the measurement procedure, the coupling model as well as the mathematical steps to obtain the coupling coefficients are presented. Subsequently, the mode group power coupling matrices are measured for different DUTs at 1327 nm. As a proof of concept it is shown that also at 1508 nm operating wavelength with its significant chromatic dispersion, the power coupling coefficients can be obtained with the introduced method. The analyzed DUTs at 1327 nm involve different coupler types, including symmetric (SFC), asymmetric (AFC) and customized fusion couplers (CFC) as well as a polished coupler

(PC) and a mirror coupler (MC). The coupler types are discussed in Section 5.1.1. Based on the obtained coupling matrices, the simulated BER performances are compared, when the couplers are implemented as a mode multiplexing device in a (2×2) MIMO configuration, and the corresponding SMF to MMF launch conditions are optimized.

4.1.1 Measurement Procedure

The method for determining the mode group power coupling matrix is based on measuring the impulse responses of the DUT under different excitation conditions. Figure 4.1 shows the corresponding measurement setup. Here, a short optical pulse with a full width at half maximum of 25 ps is generated by a pulse generator driving a laser diode with a nonlinear absorption layer. Subsequently, an SMF is aligned with the radial eccentricity δ to an MMF so as to excite specific mode groups. The alignment can be carried out with a simple fusion splicer in manual mode. In this setup a hexapod device is used for a higher resolution (hexapod: 33 nm, fusion splicer: 100 nm) and to reduce hysteresis effects. In order to analyze the power of the mode groups, they are separated by a fiber of 1 km length due to their different group velocities. Therefore, the chromatic dispersion needs to be lower than the modal dispersion. In [Carp13; Carp16] it has been shown that coupling between mode groups along an MMF is very small. This statement is confirmed later in Section 4.1.3. At the receiver-side a sampling oscilloscope with a 40 GHz detector is used. Since the input impulse spectrum is not fully flat, the influence is eliminated by using signal deconvolution according to [Gans86].

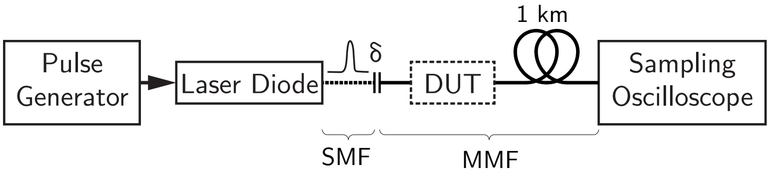

Figure 4.1: Measurement setup (δ represents the SMF to MMF radial offset realized by a hexapod alignment device)

An operating wavelength of 1327 nm is chosen since in this wavelength region the chromatic dispersion is low compared to other regions. With the occurring modal dispersion, optimal conditions for separating the mode groups on the time axis exist. The proposed method also works in the 1550 nm region with a spectrally narrow laser as it is confirmed in Section 4.1.4. However, this approach does not work in the 850 nm optical window as modal separation is prevented by the high chromatic dispersion.

Two series of measurements need to be conducted (without and with the DUT) for determining the incident and outgoing mode group specific powers. Multiple measurements with different excitation conditions are required within a series since this setup does not allow the launch of a single mode group. With just one measurement the underlying

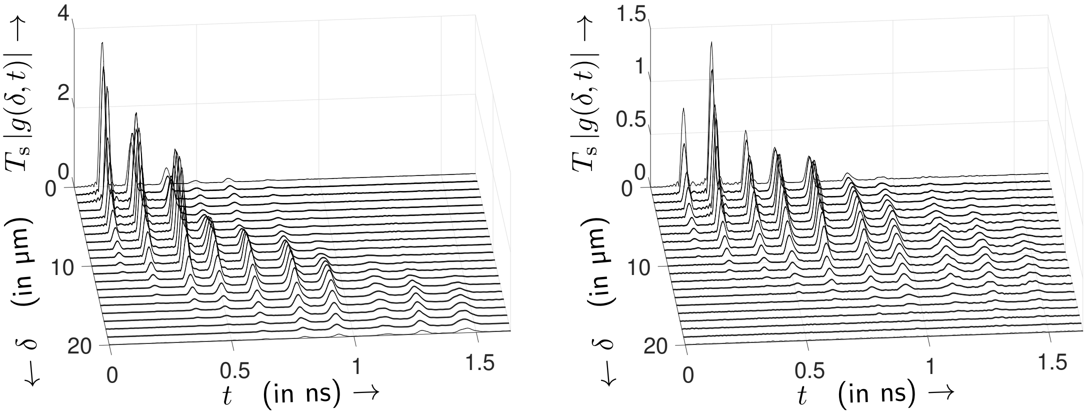

(a) Without DUT **(b)** With DUT

Figure 4.2: Measured electrical impulse responses scaling with $1/T_\mathrm{s} = 5$ GHz

mathematical problem is under-determined. Here, the eccentricity δ is varied in the range between 0 and 20 µm in increments of 1 µm. The resulting impulse responses at an operating wavelength of 1327 nm without and with an optical coupler chosen as the DUT are depicted in Fig. 4.2. Each peak represents a mode group. If an optical signal is transmitted through this channel, the area of the peak is proportional to the optical power of the received signal in that specific mode group. The proportionality factor cancels later in the system of equations, see Section 4.1.2, and hence in the procedure the areas for all peaks are automatically measured and associated to the corresponding mode groups. As shown by the measurement results, using $\delta = 0$ µm mainly the LP_{01} mode is excited, whereas higher δ values excite higher-order mode groups. Including the DUT and launching centric into the MMF shows that the second mode group has the highest power after the signal is transferred through the DUT, highlighting the mode coupling process.

4.1.2 Determining the Power Coupling Coefficients

Considering a DUT with J incident and I outgoing mode groups per fiber port, as highlighted in Fig. 4.3, each incident mode group carries the power $P_{\mathrm{s},j}$ with the input index $j = 1, \ldots, J$. Correspondingly, the power of the ith outgoing mode group is denoted by $P_{\mathrm{r},i}$, with $i = 1, \ldots, I$ being the output index. The incident powers $P_{\mathrm{s},j}$ and the outgoing powers $P_{\mathrm{r},i}$ can be determined by an impulse response measurement as described

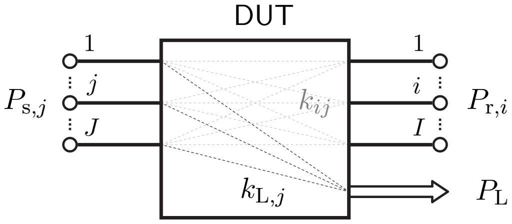

Figure 4.3: Mode group power coupling model

in Section 4.1.1. For the mth measurement, with $m = 1, \dots, M$, the power coupling is described as follows

$$P_{\mathrm{r},i}^{(m)} = \sum_{j=1}^{J} k_{ij}\, P_{\mathrm{s},j}^{(m)} \quad , \tag{4.1}$$

where k_{ij} denote the positive and real-valued optical power coupling coefficients to be determined. A portion of the power of the incident modes is lost in the DUT. The power losses are described as follows

$$P_{\mathrm{L}}^{(m)} = \sum_{j=1}^{J} k_{\mathrm{L},j}\, P_{\mathrm{s},j}^{(m)} \quad . \tag{4.2}$$

Here, the factor $k_{\mathrm{L},j}$ describes the portion of the jth incident mode group power that is lost during the transfer through the DUT. This power loss is given by

$$P_{\mathrm{L}}^{(m)} = \sum_{j=1}^{J} P_{\mathrm{s},j}^{(m)} - \sum_{i=1}^{I} P_{\mathrm{r},i}^{(m)} \quad , \tag{4.3}$$

implying that

$$k_{\mathrm{L},j} + \sum_{i=1}^{I} k_{ij} = 1 \qquad \forall j \;\; . \tag{4.4}$$

A system of equations in matrix notation for the mth measurement is formed. Therefore, matrix $\boldsymbol{S}_m$ is defined as follows

$$\boldsymbol{S}_m = \begin{pmatrix} \boldsymbol{p}_{\mathrm{s}}^{(m)} & \boldsymbol{0} & \cdots & \boldsymbol{0} \\ \boldsymbol{0} & \boldsymbol{p}_{\mathrm{s}}^{(m)} & \cdots & \boldsymbol{0} \\ \vdots & \vdots & \ddots & \vdots \\ \boldsymbol{0} & \boldsymbol{0} & \cdots & \boldsymbol{p}_{\mathrm{s}}^{(m)} \end{pmatrix} \quad , \tag{4.5}$$

with the vector

$$\boldsymbol{p}_{\mathrm{s}}^{(m)} = \begin{pmatrix} P_{\mathrm{s},1}^{(m)} & P_{\mathrm{s},2}^{(m)} & \cdots & P_{\mathrm{s},J}^{(m)} \end{pmatrix} \quad , \tag{4.6}$$

containing the measured powers of the incident mode groups. Symbol $\boldsymbol{0}$ denotes a zero vector. Also, an intermediate vector containing the coupling coefficients to the ith output is given by

$$\boldsymbol{k}_i = \begin{pmatrix} k_{i1} & k_{i2} & \cdots & k_{iJ} \end{pmatrix} \tag{4.7}$$

and is used to define the vector containing all mode group power coupling coefficients resulting in

$$\boldsymbol{k} = \begin{pmatrix} \boldsymbol{k}_1 & \boldsymbol{k}_2 & \cdots & \boldsymbol{k}_I & k_{\mathrm{L},1} & \cdots & k_{\mathrm{L},J} \end{pmatrix}^{\mathrm{T}} \ . \tag{4.8}$$

The vector containing the powers of the outgoing mode groups is described by

$$\boldsymbol{r}_m = \begin{pmatrix} P_{\mathrm{r},1}^{(m)} & P_{\mathrm{r},2}^{(m)} & \cdots & P_{\mathrm{r},I}^{(m)} & P_{\mathrm{L}}^{(m)} \end{pmatrix}^{\mathrm{T}} \ . \tag{4.9}$$

With this matrix and vectors, the system of equations is written in short form as follows

$$\boldsymbol{S}_m \cdot \boldsymbol{k} = \boldsymbol{r}_m \ , \tag{4.10}$$

where matrix $\boldsymbol{S}_m$ is of size $(I+1) \times J\,(I+1)$, vector $\boldsymbol{k}$ is of size $J\,(I+1) \times 1$ and vector $\boldsymbol{r}_m$ is of size $(I+1) \times 1$. In order to obtain an over-determined system, multiple measurements indexed with $m = 1, \ldots, M$ need to be conducted. The coupling coefficients are assumed to be identical for all measurements, and therefore the system of equations is composed as follows

$$\begin{pmatrix} \boldsymbol{S}_1 \\ \boldsymbol{S}_2 \\ \vdots \\ \boldsymbol{S}_M \end{pmatrix} \cdot \boldsymbol{k} = \begin{pmatrix} \boldsymbol{r}_1 \\ \boldsymbol{r}_2 \\ \vdots \\ \boldsymbol{r}_M \end{pmatrix} \ . \tag{4.11}$$

It is rewritten in short form as follows

$$\boldsymbol{S} \cdot \boldsymbol{k} = \boldsymbol{r} \tag{4.12}$$

and consists of $J\,(I+1)$ unknowns and $M\,(I+1)$ equations. Hence, $M > J$ needs to be respected, where each measurement needs a different set of input powers $P_{\mathrm{s},j}^{(m)}$ that are not linearly dependent between the measurements. For the least squares minimization of this problem the objective function is formulated as follows

$$\min_{\boldsymbol{k}} \left\{ \|\boldsymbol{S}\,\boldsymbol{k} - \boldsymbol{r}\|_2 \right\} \tag{4.13}$$

subject to the inequality constraint

$$\boldsymbol{k} \geq \boldsymbol{0} \tag{4.14}$$

and to the equality constraint

$$\underbrace{\begin{pmatrix} \boldsymbol{I}_J & \boldsymbol{I}_J & \cdots & \boldsymbol{I}_J \end{pmatrix}}_{J\,(I+1)} \boldsymbol{k} = \begin{pmatrix} 1 \\ 1 \\ \vdots \\ 1 \end{pmatrix} . \tag{4.15}$$

Symbol $\|\cdot\|_2$ denotes the Euclidean matrix norm and $\boldsymbol{I}_J$ is a $J \times J$ identity matrix. The equality constraint enforces the conservation of energy described in Eq. 4.4 and ensures in combination with the inequality constraint that all k_{ij} and loss coefficients $k_{\mathrm{L},j}$ are between zero and one. This constrained least squares optimization problem is solved with the interior-point algorithm in order to give an estimate of the coupling coefficient vector $\boldsymbol{k}$. For the sake of clarity the coupling coefficients are restructured into a coupling matrix as follows

$$\boldsymbol{K} = \begin{pmatrix} k_{11} & \cdots & k_{1J} \\ \vdots & \ddots & \vdots \\ k_{I1} & \cdots & k_{IJ} \end{pmatrix} . \tag{4.16}$$

By taking the measured input powers $P_{\mathrm{s},j}^{(m)}$ and the estimated power coupling coefficients k_{ij}, the powers of the outgoing mode groups can be simulated according to Eq. 4.1. The simulated output powers are denoted by $\widehat{P}_{\mathrm{r},i}^{(m)}$ and the measured powers by $P_{\mathrm{r},i}^{(m)}$. The quality of the estimated coupling matrices is computed using these power levels. Therefore, the normalized mean absolute error (NMAE) is taken, being defined as

$$E_{\mathrm{NMAE}} = \frac{1}{\sum\limits_{m=1}^{M} \sum\limits_{i=1}^{I} P_{\mathrm{r},i}^{(m)}} \cdot \sum_{m=1}^{M} \sum_{i=1}^{I} \left| P_{\mathrm{r},i}^{(m)} - \widehat{P}_{\mathrm{r},i}^{(m)} \right| . \tag{4.17}$$

4.1.3 Mode Group Power Coupling Results

Hereinafter, the power coupling matrices for a 1 km MMF and different coupler types as listed in Tab. 4.1 are measured for an operating wavelength of 1327 nm. Compared to the

Table 4.1: Analyzed coupler types

Coupler type	Abbreviation	Internal label	Operation mode
50/50 symmetric fusion coupler	SFC	MM1	MUX
20/80 asymmetric fusion coupler	AFC	MM3	MUX
Polished coupler	PC	MM4	MUX
Mirror coupler	MC	MM5	MUX
Customized fusion coupler for 10 µm	CFC10	xx31	both
Customized fusion coupler for 15 µm	CFC15	xx30	DEMUX

first publication [Sand18] several refinements in the measurement procedure are conducted. Firstly, the powers of the mode groups are evaluated by taking the area under the pulses of $g(\delta, t)$ instead of the amplitude multiplied with a constant pulse width, respecting different pulse shapes. Secondly, the measurement of the impulse responses is sped up to reduce long term time-variance effects. Furthermore, the equality constraint given by Eq. 4.15 is added in the optimization process to make sure Eq. 4.4 is met. Consequently, the coupling matrix quality in terms of NMAE is significantly improved.

The power coupling results are shown in Figs. 4.4–4.11 with their corresponding loss coefficients being listed in Tab. 4.2. Considering the coupling matrix of the 1 km MMF (OM4-grade fiber) shows that the majority of the incident power stays in the same mode group and only a small portion is coupled into the neighboring mode groups. Coupling into distant mode groups does not occur. This result confirms the coupling behavior of a similar 2 meter long fiber reported in [Carp13]. For the 1 km MMF a measurement is used, which could not be optimized since a 2 km fiber was shortened to 1 km with the cut-back method to avoid any additional connectors. Therefore, this measurement results in a relatively high NMAE. Here, the use of the 2 km fiber represents the measurement with DUT, and the use of the shortened 1 km fiber represents the measurement without DUT. A repetition of the measurement with optimizations requires a new fiber because of the applied cut-back method. In general, the losses in MMF propagation can be divided into different components: Absorption, scattering and bending losses. In particular, the latter component may lead to mode coupling where e.g. high-order modes can be coupled

Table 4.2: Mode group specific loss coefficients $k_{\mathrm{L},j}$

	j	1	2	3	4	5	6	7	8	9	10
1 km MMF	$k_{\mathrm{L},j}$	0.00	0.00	0.00	0.00	0.00	0.00	0.00	0.00	0.29	0.67
SFC	$k_{\mathrm{L},j}^{(1\rightarrow1)}$	0.98	0.80	0.73	0.18	0.96	0.03	0.35	1.00	0.66	0.73
	$k_{\mathrm{L},j}^{(2\rightarrow1)}$	0.05	0.09	0.42	0.18	0.98	0.00	0.35	0.99	0.90	0.26
AFC	$k_{\mathrm{L},j}^{(3\rightarrow1)}$	0.00	0.00	0.00	0.00	0.00	0.00	0.55	0.15	1.00	0.10
	$k_{\mathrm{L},j}^{(4\rightarrow1)}$	1.00	1.00	0.99	0.96	1.00	0.92	0.75	0.88	0.62	0.56
PC	$k_{\mathrm{L},j}^{(1\rightarrow1)}$	0.59	0.67	0.36	1.00	0.88	0.26	0.87	1.00	0.74	0.99
	$k_{\mathrm{L},j}^{(2\rightarrow1)}$	0.49	0.83	0.92	0.44	0.65	1.00	0.53	1.00	1.00	0.48
MC	$k_{\mathrm{L},j}^{(1\rightarrow1)}$	0.49	0.75	0.78	0.54	0.88	0.00	0.85	0.82	1.00	0.37
	$k_{\mathrm{L},j}^{(2\rightarrow1)}$	0.34	0.72	0.82	0.43	1.00	0.03	0.74	1.00	0.69	0.65
CFC10	$k_{\mathrm{L},j}^{(3\rightarrow1)}$	0.38	0.21	0.86	0.13	0.54	0.06	1.00	0.36	1.00	0.37
	$k_{\mathrm{L},j}^{(4\rightarrow1)}$	0.42	0.72	0.63	0.38	0.65	1.00	0.83	0.20	0.89	0.68
CFC10	$k_{\mathrm{L},j}^{(1\rightarrow3)}$	0.57	0.27	0.63	0.17	0.27	0.91	0.14	1.00	0.48	0.54
DEMUX	$k_{\mathrm{L},j}^{(1\rightarrow4)}$	0.41	0.66	0.58	1.00	0.75	0.42	0.86	1.00	1.00	0.56
CFC15	$k_{\mathrm{L},j}^{(1\rightarrow3)}$	0.32	0.46	0.51	0.90	0.64	0.81	1.00	1.00	1.00	1.00
DEMUX	$k_{\mathrm{L},j}^{(1\rightarrow4)}$	0.70	0.66	0.77	0.66	0.89	0.35	0.99	1.00	0.87	1.00

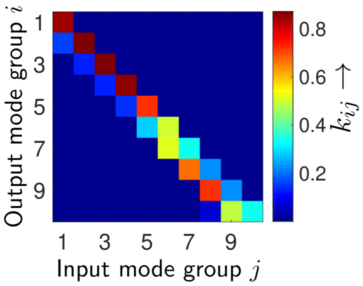

Figure 4.4: Estimated mode group power coupling matrix $\boldsymbol{K}$ of the 1 km MMF (NMAE: 15.80%)

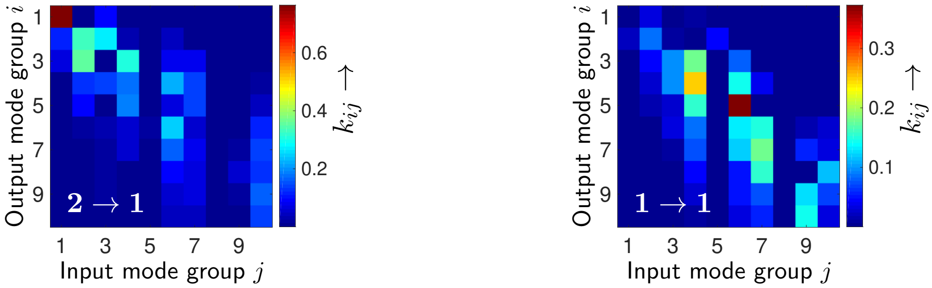

Figure 4.5: Estimated mode group power coupling matrices of the SFC in MUX operation (NMAE left: 2.27%, right: 4.04%; inset shows respective port numbers)

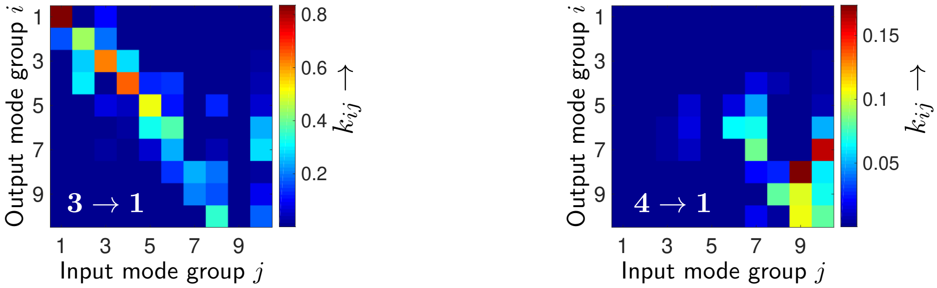

Figure 4.6: Estimated mode group power coupling matrices of the AFC in MUX operation (NMAE left: 5.75%, right: 8.21%; inset shows respective port numbers)

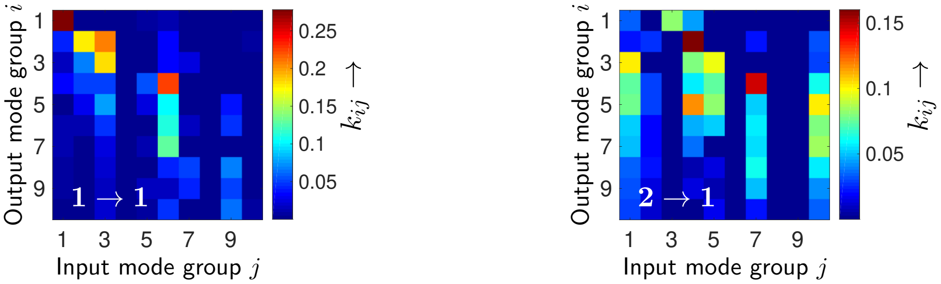

Figure 4.7: Estimated mode group power coupling matrices of the PC in MUX operation (NMAE left: 3.85%, right: 2.81%; inset shows respective port numbers)

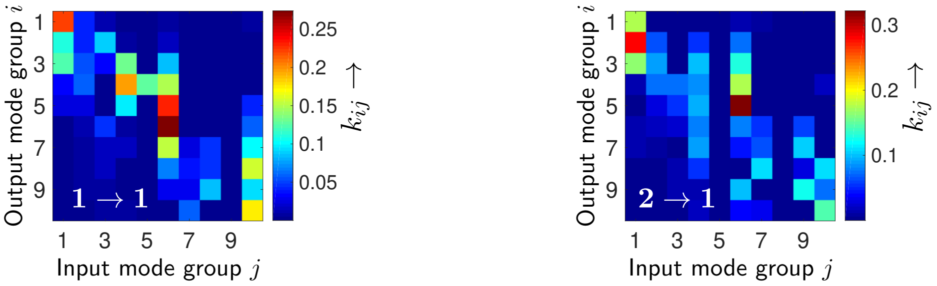

Figure 4.8: Estimated mode group power coupling matrices of the MC in MUX operation (NMAE left: 2.58%, right: 2.75%; inset shows respective port numbers)

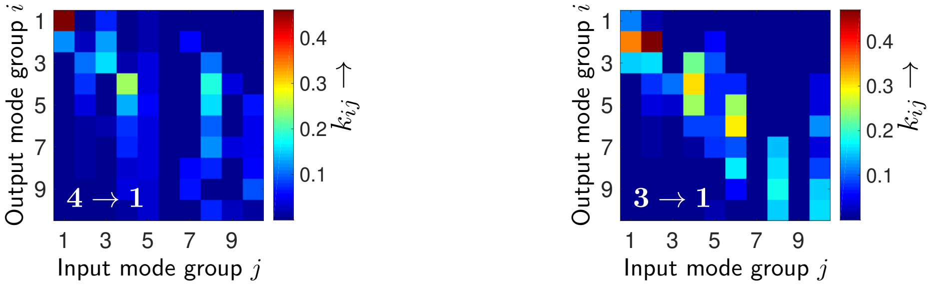

Figure 4.9: Estimated mode group power coupling matrices of the CFC10 in MUX operation (NMAE left: 2.45%, right: 2.32%; inset shows respective port numbers)

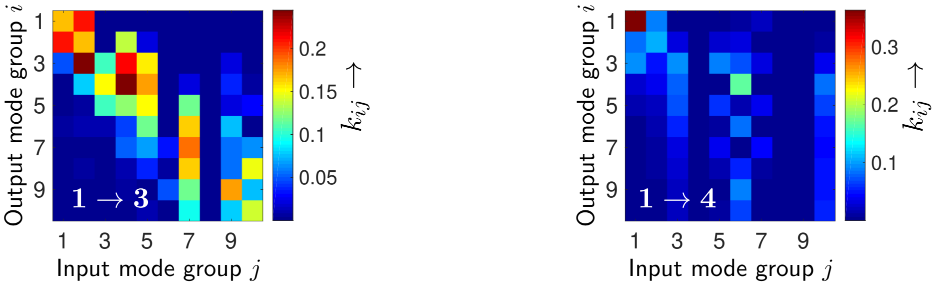

Figure 4.10: Estimated mode group power coupling matrices of the CFC10 in DEMUX operation (NMAE left: 3.35%, right: 3.22%; inset shows respective port numbers)

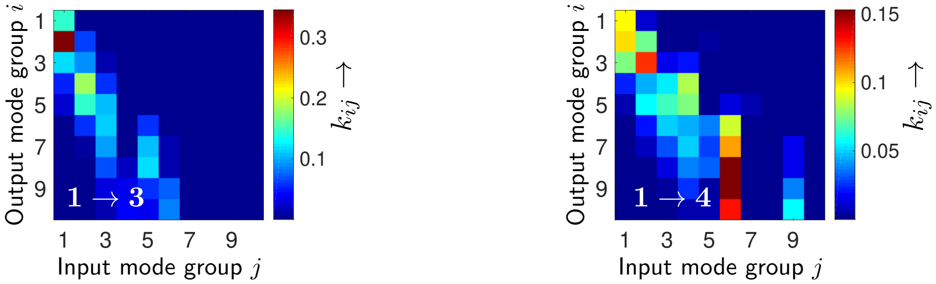

Figure 4.11: Estimated mode group power coupling matrices of the CFC15 coupler in DEMUX operation (NMAE left: 4.87%, right: 2.5%; inset shows respective port numbers)

into even higher ones that are not supported by the fiber. The obtained loss coefficients of groups 9 and 10 clearly show this effect. Mode groups 1–8 show no losses, which is reasonable within the margin of error.

Within any coupler device, we may realize that strong mode group power coupling takes place. For instance, in Fig. 4.10 path 1 → 3 input mode group 7 is spread to output mode groups 5–10. Please note, a path is considered as the transfer through a coupler device from the input to the output port, with the ports being denoted with Arabic numerals. Focusing on the coupling matrices of the SFC, the path 2 → 1 has a low loss when launching with the fundamental mode, whereas in the 1 → 1 path input mode groups 4 and 6 have a low loss. The AFC clearly shows a high degree of mode group selectivity between the two paths. In the 4 → 1 path only power from higher-order mode groups is transferred, exhibiting a relatively high attenuation. In contrast, the 3 → 1 path transfers low-order mode groups with a low loss. Some mode groups show a complete lossless transfer through the DUT. Considering the error margin described by the NMAE this optimization result is reasonable. Both matrices obtained for the MC and PC show significant mode coupling with a weak mode group maintenance. The coupling results of the SFC and CFC10 are principally similar since the fabrication technology is the same. They only differ in their degree of fusion, which is selected for the CFC10 such that the power being transferred through the cross-path is maximized when launching with 10 µm eccentricity. It is worth noting that the power coupling matrices of the CFC10 are not transpose symmetric in reverse operation when considering the MUX and DEMUX results. The CFC15 in DEMUX operation shows that incident low-order mode groups are mainly transferred to output 3 and high-order mode groups, specifically mode group 6, are transferred to output 4. Please consider that for some coupler types there are columns with very weak coupling, whereas the neighboring columns show strong coupling, e.g. compare SFC path 1 → 1 input mode group 8. This is unexpected and the source of this effect needs to be determined. In the simulation in Section 4.1.5, the matrices of the couplers in MUX operation depicted in the left column are used for the first MIMO input with its corresponding eccentricity δ_1, and likewise the matrices in the right column are used for the second MIMO input with its launch eccentricity δ_2. It is worth noting that the coupling results may vary at different wavelengths.

With these coupling results, the orthogonality as well as the mode group specific losses are visualized, and they are used to optimize the testbed configurations.

4.1.4 Coupling Analysis at 1508 nm

So far, measurements at 1327 nm operating wavelength were used since the minimal chromatic dispersion simplifies the time-separation of the mode groups. This is required in order to obtain the coupling coefficients with the presented method. This part shows that a sufficient mode group separation at 1508 nm is possible when using a narrow-linewidth DFB

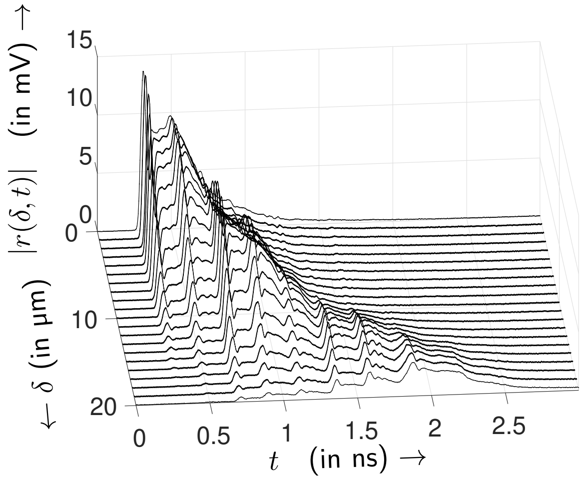

Figure 4.12: Measured electrical output signals without DUT for different launch eccentricities at 1508 nm

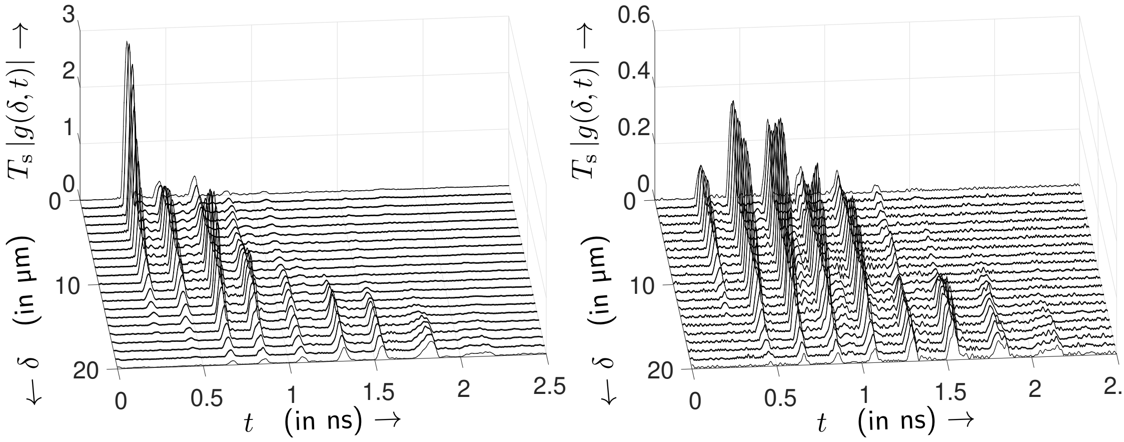

(a) Without DUT **(b)** With DUT (coupler ports 1 → 3)

Figure 4.13: Measured electrical impulse responses scaling with $1/T_\mathrm{s} = 5$ GHz operating at 1508 nm

laser. As a proof of concept, the CFC10 in DEMUX operation is analyzed. Figure 4.12 shows the measured output signals impaired by the wide shoulder of the input impulse and the occurring chromatic dispersion at this wavelength. The wide shoulder of the input impulse is necessary since the narrow-linewidth significantly limits the transmit power. With signal deconvolution the impulse responses of the channel with and without DUT are obtained. As shown by the results in Fig. 4.13, the mode groups can be clearly separated. This enables the use of the algorithm to obtain the mode group power coupling matrix, being shown in Fig. 4.14. The corresponding loss coefficients are listed in Tab. 4.3. Please note that at 1508 nm only 9 mode groups could be identified in the fiber compared to the 10 groups at 1327 nm. It is evident that the obtained matrix at 1508 nm differs from the results at 1327 nm presented in Fig. 4.10. However, the weak diagonal structure is similar at both wavelengths. The results highlight that the presented strategy to determine the mode group power coupling coefficients functions in the 1310 nm as well as in the 1550 nm wavelength window.

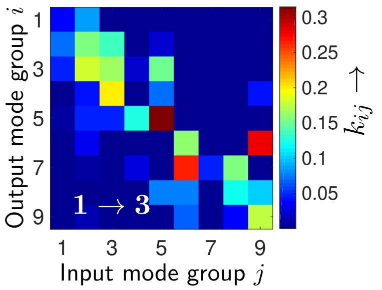

Figure 4.14: Estimated mode group power coupling matrix of the CFC10 in DEMUX operation at 1508 nm wavelength (NMAE: 4.37%)

Table 4.3: Mode group specific loss coefficients $k_{\mathrm{L},j}$

j	1	2	3	4	5	6	7	8	9
$k_{\mathrm{L},j}$	0.83	0.44	0.45	0.82	0.37	0.43	0.95	0.69	0.41

4.1.5 BER Performance Evaluation

A time-domain simulation is used to model impulse responses for an IM/DD transmission. This model integrates modal dispersion as well as chromatic dispersion approximated by a Gaussian pulse [Grim89, p. 82 ff.]. Thereby, the specific fiber parameters and operating wavelengths are taken into account. Modal coupling when launching from an SMF into an MMF with different eccentricities is integrated as well, compare Section 2.1.1. Also, arbitrary coupling matrices can be added at different locations in the setup so as to model different devices or integrate mode group specific attenuation of the fiber. A more detailed overview of the simulation tool is shown in [Bart15a; Sand18].

Subsequently, simulated and measured impulse responses for a SISO transmission through 1 km MMF with mode-selective launch are compared for verification purposes. The simulation uses the measured reference impulse as the input, and then calculates the corre-

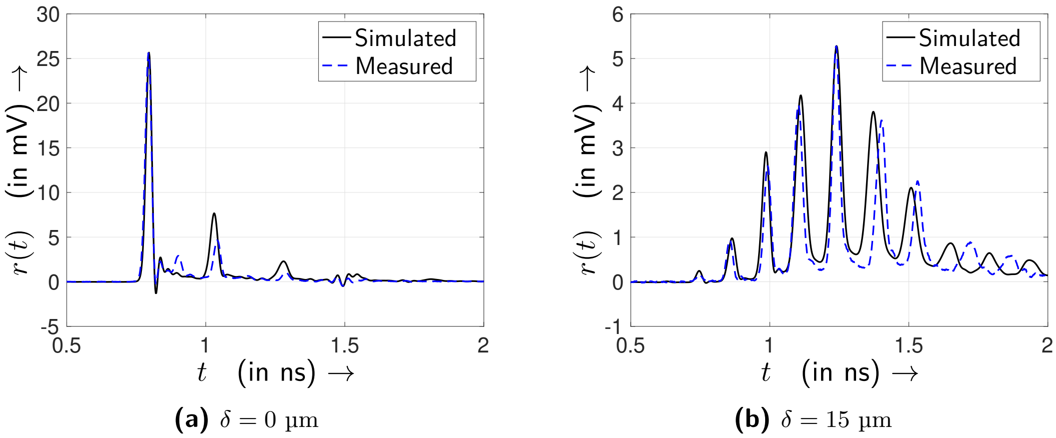

(a) $\delta = 0$ µm **(b)** $\delta = 15$ µm

Figure 4.15: Comparing the measured with the simulated SISO output signals launching with different offsets δ and considering the 1 km OM4-grade fiber

sponding output signal based on the measured fiber coupling matrix (compare Fig. 4.4) and dispersion parameters. Figure 4.15 shows the comparison for different SMF to MMF launch eccentricities. The simulation results exhibit a high similarity to the measurements.

By adding the obtained power coupling matrices to the impulse responses' simulation, an optical (2×2) MIMO system at 1327 nm operating wavelength is modeled as shown in Fig. 4.16. At the transmitter (Tx) the different coupler types in MUX operation are compared by including the corresponding matrices. The 1 km MMF channel model involves the obtained fiber coupling matrix and for the DEMUX process at the receiver-side the matrices for the CFC10 are used. The impulse responses are simulated for different SMF to MMF launch eccentricities δ_1 and δ_2, and based on these the BER is simulated, transmitting independent on-off keying signals at a rate of 5 Gbps at both MIMO inputs. The overall MIMO system is assumed to be linear and possible interference effects due to mode cross-talk are neglected, compare interference signal in Section 3.4.1. Perfect channel state information is assumed to be available at the receiver. The inter-symbol interferences are removed with a simple MIMO zero forcing equalizer. For comparison reasons, the SNR is defined in such a way that the effects of channel dispersion and attenuation are visible in the BER, see abscissa in Fig 4.18. In the SNR definition, σ_s^2 denotes the variance of the transmit symbols at each MIMO input, $1/T_\mathrm{s} = 5$ GHz is the symbol rate and N_0 defines the noise power spectral density of the additive and white Gaussian noise.

The BER performance results as a function of the launch eccentricities δ_1 and δ_2 comparing different coupler types at the transmitter-side for mode multiplexing are shown in Fig. 4.17. They highlight that the optimal operating point marked by the magenta dot depends on the used coupler. If a coupler name is followed by an asterisk (*) in Fig. 4.17, the outputs have been swapped for achieving the best BER performance. It is worth noting that choosing δ_1 or δ_2 to be zero is not necessarily the best option as shown by the AFC, MC and CFC10 results. In these cases, the fundamental mode excited by a centric launch is not optimally transferred through either transmission channel, and hence an eccentric launch increases the received power and/or the MIMO system orthogonality. Furthermore, the region of low BERs is relatively narrow such that deviations of 2 µm from the optimal operating point can lead to a tenfold increase in the BER. Therefore, the eccentricities need to be chosen carefully depending on the setup.

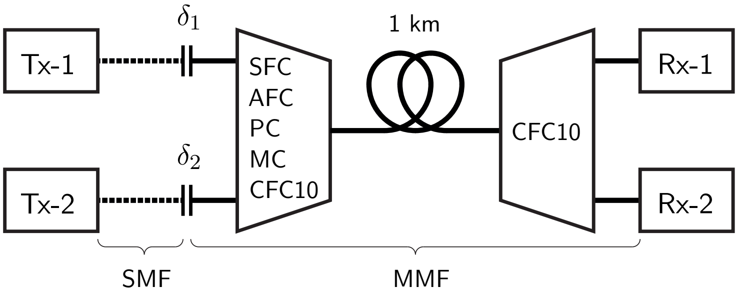

Figure 4.16: MIMO simulation setup

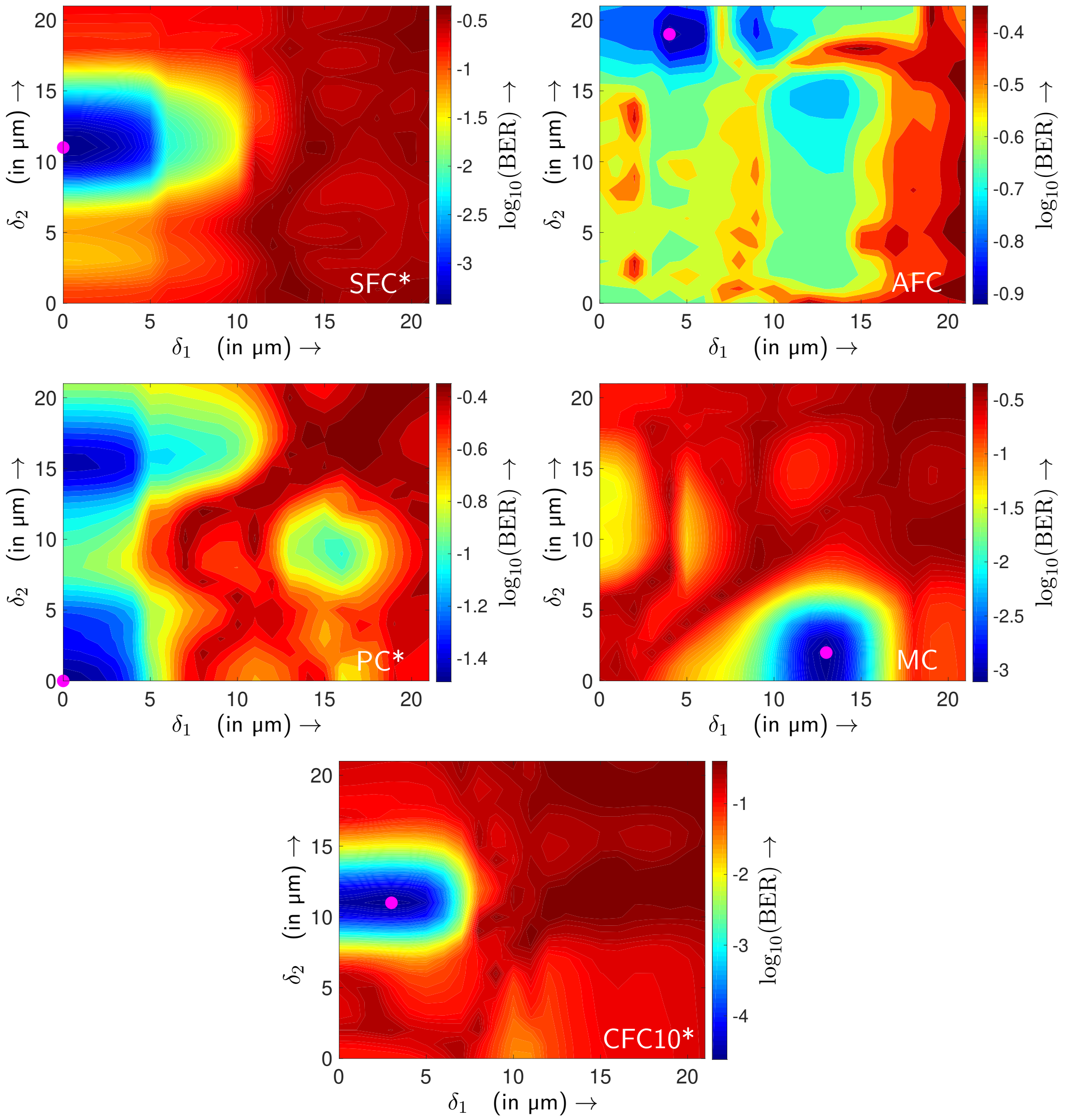

Figure 4.17: BER versus eccentricities δ_1 and δ_2 comparing different coupler types when transmitting with a symbol rate of 5 GHz at a fixed SNR of 40 dB

A comparison of the different coupler types for mode MUX in their optimal operating point in terms of the BER versus SNR is shown in Fig. 4.18. Here, the CFC10 shows the best results closely followed by the SFC and MC. Despite the high orthogonality of the AFC, it is impaired by significant losses of the path that transfers the high-order mode groups. This leads to a high imbalance of the MIMO layers' SNRs. Since the transmit power and the number of bits per symbol are symmetrically allocated to both MIMO inputs, the performance with the AFC turns out to be worst. In a real world scenario, mode cross-talk needs to be minimized in order to avoid interference effects.

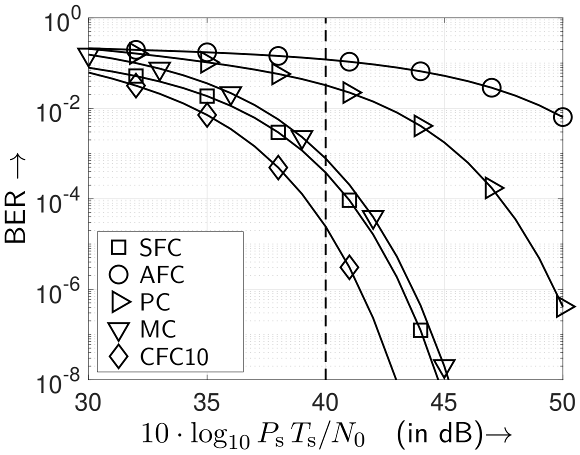

Figure 4.18: BER versus SNR comparing different coupler types at their optimal eccentricities (compare magenta dot in Fig. 4.17) when transmitting with a symbol rate of 5 GHz

4.2 Fiber Channel Time-Variance Characterization

Environmental influences like changes in temperature, pressure and humidity as well as vibration can introduce a time-variance to the channel. The knowledge of this time-variance is important for the design of the transmission parameters. This includes parameters like frame length, how often a channel estimation needs to be carried out and what type of equalization strategy should be applied. For instance, channels with a slow time-variation benefit from adaptive signal processing approaches. Considering a multi-mode system, the introduction of time-variance means that the phase of the fiber modes can change, and mode coupling can occur, e.g. leading to a varying speckle pattern in the received intensity profile.

Time-variance effects in multi-mode transmission under the influence of fiber vibration, temperature changes and different launch conditions have been discussed in the IEEE 802.3ae and IEEE 802.3aq standardization process for interoperability tests and to establish the worst case time-variance of the channel impulse response [Task05]. In a different study it has also been shown that in an MMF system with a centric launch condition, vibration has practically no effect on the system performance [Bole13]. An IM/DD transmission through an MMF channel of 1 km length is characterized in this section with mode-selective launching and vibration influences. The time duration in which the channel can be considered as time-invariant, i.e. coherence time, and the maximum transmission bandwidth where the channel is frequency-flat, i.e. coherence bandwidth, are the key parameters for such a characterization. In order to obtain these parameters, two different measurement approaches are used: The first analyzes the changes in the intensity profile with a camera at the end of the MMF channel and the second uses a faster repeated channel impulse response estimation. The latter gives the time-variant and frequency-selective impulse response, also known as the input delay spread function [Bell63]. With this function, the power delay profile and a corresponding energy time profile can be defined in order to extract the delay and time parameters, respectively [Rapp02; Gold05]. Based on the knowledge of these parameters, the transmitter and receiver structure can be designed accordingly. The results of this SISO experiment can be later transferred to MIMO systems.

The main focus of this analysis is the comparison of two different approaches for determining MMF channel parameters under mode-selective launching. Next to the camera measurements, repeated impulse response measurements are carried out for parameter estimation.

4.2.1 Intensity Profile Analysis

In this section, the changes of the intensity profile at the end-face of a 1 km OM4-grade MMF are measured using the setup depicted in Fig. 4.19. Here, a continuous wave laser source emits light into an SMF. By aligning the SMF with an eccentricity δ to an MMF a specific set of modes can be selectively excited. Subsequently, the MMF is arranged in 9 loops and is then twisted into an 8-shape, compare Fig. 4.19. This shape is then compressed and expanded by the fiber shaker in a sinusoidal motion with an adjustable vibration frequency. A 1 km MMF is used to emulate the channel, and finally the intensity pattern is captured in a video using a fiber end-face camera.

The measured intensity patterns at the fiber end-face, launching with $\delta = 20$ µm, are shown in Fig. 4.20. Two different laser types are used. The broad-linewidth Fabry-Pérot laser (spectral width 9 nm) shows an intensity pattern with practically no visible speckle pattern. In contrast, the DFB laser has a narrow spectral width, and hence shows a distinct speckle pattern. In order to study the time-variance of the captured video, a 10×10 pixel area is cut-out from the intensity ring. The value of each pixel represents the intensity denoted by $I(x, y, t)$, i.e. optical power per unit area, at the pixel location (x, y) and time t. Correspondingly, the measured voltage of the 10×10 pixel area A_i is calculated as follows

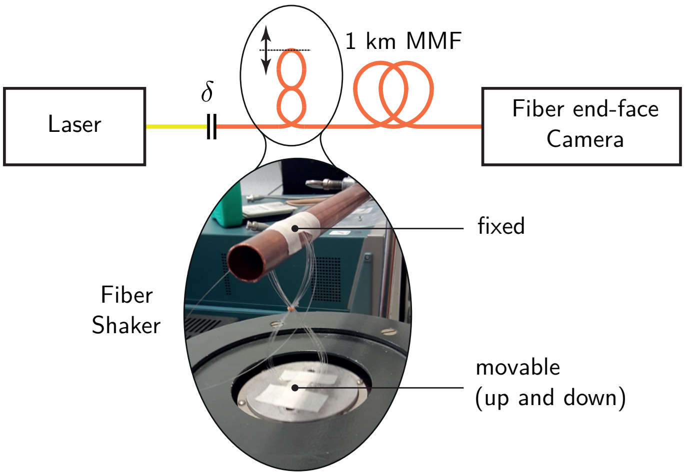

Figure 4.19: Intensity profile measurement setup with the fiber shaker

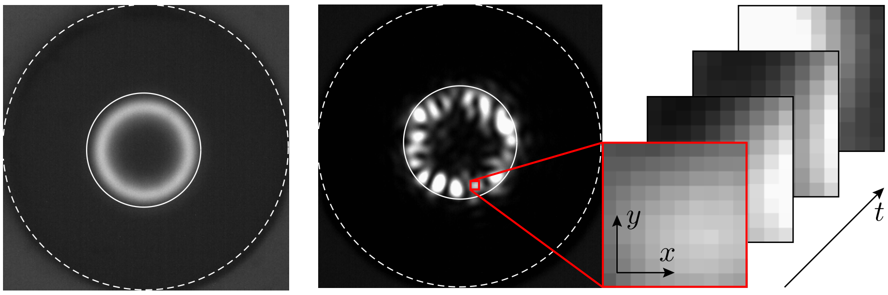

Figure 4.20: Measured intensity pattern and the 10×10 pixel segment cut-out at different time-instances (left: Fabry-Pérot laser 850 nm, right: DFB laser 779 nm); The dashed line represents the 125 µm cladding and the solid line represents the 50 µm core diameter

$$u_i(t) = F \iint\limits_{A_i} I(x, y, t)\,\mathrm{d}x\,\mathrm{d}y \ , \tag{4.18}$$

where F is the conversion factor of the camara's CCD matrix. Furthermore, i denotes the index of the investigated 10×10 pixel area on the fiber end-face. Consider the auto-correlation function (ACF) as defined by

$$\phi_{uu}^{(i)}(\Delta t) = \mathrm{E}\Big\{\widetilde{u}_i(t)\,\widetilde{u}_i(t+\Delta t)\Big\} \ , \tag{4.19}$$

where $\widetilde{u}_i(t)$ is the AC of the voltage signal $u_i(t)$ and $\mathrm{E}\{\,\cdot\,\}$ denotes the expectation functional. Taking the Fourier transform gives the measured PSD

$$\Phi_i(\nu) = \mathcal{F}\Big\{\phi_{uu}^{(i)}(\Delta t)\Big\} \ , \tag{4.20}$$

with ν being the frequency that is related to time, and hence it is termed Doppler. Please note that the DC is removed in the spectrum since we are mainly interested in the changes. The PSD is calculated for multiple 10×10 pixel areas indexed with $i = 1, \ldots, N$, which are located on the intensity ring, see red squares in Fig. 4.21. These PSDs are then averaged in order to extract the deterministic components, i.e. the vibration frequencies, by calculating

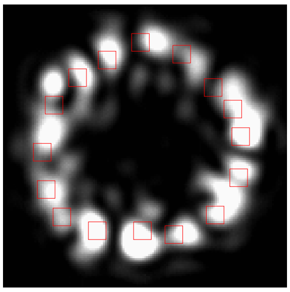

Figure 4.21: Selected 10×10 pixel areas A_i $(i = 1, \ldots, 16)$ framed by the red squares for the DFB laser

$$\Phi(\nu) = \frac{1}{N} \sum_{i=1}^{N} \Phi_i(\nu) \ . \tag{4.21}$$

Figure 4.22a shows the averaged PSD using the Fabry-Pérot laser and measuring with 33.68 FPS (frames per second). The spectrum shows the 10 Hz vibration frequency and the harmonic at 20 Hz, which is located at 14 Hz due to aliasing. Figure 4.22b highlights the PSD using the DFB laser and measuring at a rate of 81.56 FPS. Here, also the 10 Hz vibration frequency and harmonics at 20 Hz, 30 Hz and 40 Hz are visible. Harmonics at even higher frequencies could exist, but due to the limited frame rate they are not visible, or they are mirrored into the lower frequency region by the alias effect. Comparing the DC-free spectrum as shown in Figs. 4.22a and 4.22b to the DC amplitude shows that the DC amplitude is dominant. Thus, despite the introduced vibration, the channel can be considered as time-invariant in the measured time window of 5 s or 19 s, respectively.

Analyzing the overall optical power of the ring pattern inside a centric aligned ring mask, having an inner radius of 10 µm and an outer radius of 28 µm, the detected power can be considered as stable. This benefits from a segmented photo detection when looking at a spatial multiplexed transmission, see Section 5.2.

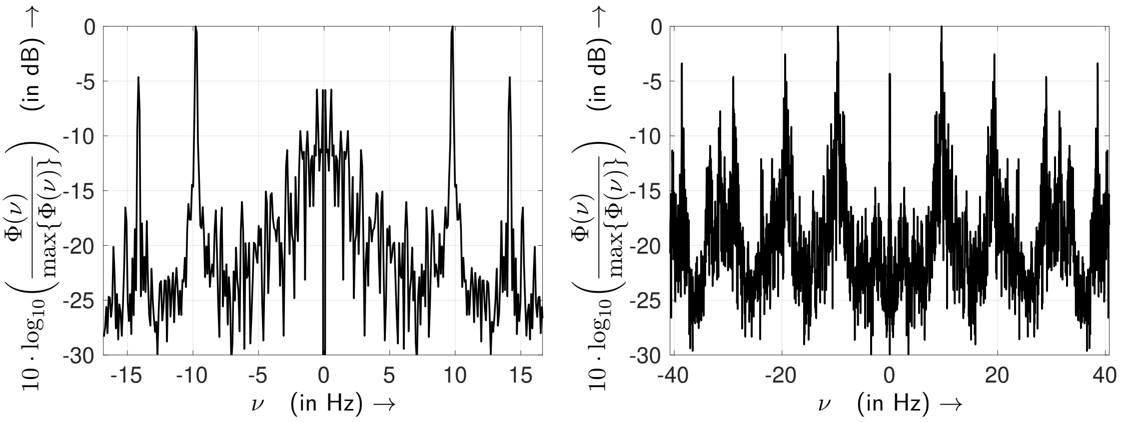

(a) Fabry-Pérot laser **(b)** DFB laser

Figure 4.22: Averaged PSD at a vibration frequency of 10 Hz

4.2.2 Input Delay Spread Function Measurement

Consider the transmission system model depicted in Fig. 4.23. The parameter τ represents the delay and t is the time variable. In this model signal $s(\tau)$ contains the binary training data in form of a pulse train. The input delay spread function $h(\tau, t)$ summarizes multiple filters as follows

$$h(\tau, t) = g_{\mathrm{s}}(\tau) * g(\tau, t) * g_{\mathrm{ef}}(\tau) \ , \tag{4.22}$$

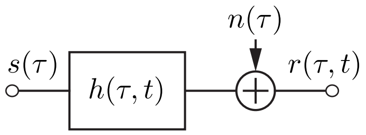

Figure 4.23: Equivalent system model for an IM/DD transmission

with $g_s(\tau)$ and $g_{ef}(\tau)$ being the transmitter-side rectangular pulse shaping and rectangular receive filter, respectively. The channel $g(\tau, t)$ is the equivalent baseband representation for the employed intensity modulation and direct detection transmission through the optical channel as shown in [Paul09; Fisc15] for an SMF transmission. Please note that the convolution operation in Eq. 4.22 is performed with respect to the delay variable τ. This linear description can be adapted to a multi-mode transmission as well, compare Section 3.3. This representation enables the use of a linear least squares channel estimation. Furthermore, the equivalent noise term is denoted by $n(\tau)$, and the receive signal is described by $r(\tau, t)$.

At the transmitter a binary training sequence of 512 bits length is repeatedly transmitted at a symbol-rate of $1/T_s = 5$ GHz using on-off keying modulation. Symbol-spaced sampling is applied to the received data, and then frame synchronization is used to locate the beginning of each training sequence. Finally, a least squares estimator is used to obtain the channel impulse response estimate $h(\tau, t)$. Taking the symbol-rate and the pilot sequence length into account, the channel state information is updated with the frequency of 9.766 MHz. This is much faster than the camera's maximum update frequency of 81.56 Hz. The update frequency of the channel estimation can be reduced by performing segmented acquisition with the oscilloscope. This is necessary in order to extract the relatively low vibration frequency and to account for the limited memory of the digital storage oscilloscope (DSO). The higher the vibration frequency, the lower is the corresponding displacement of the fiber shaker. Therefore, vibrations are only measured up to 30 Hz.

The testbed setup is shown in Fig. 4.24. A continuous wave DFB laser operating at 1537 nm feeds a Mach-Zehnder modulator (MZM) with a controlled polarization (Pctrl) in order to maximize the extinction ratio. With the MZM, the optical signal is modulated with the training data using on-off keying at 5 GHz. Subsequently, the intensity modulated data is transmitted through the channel. This channel is identical to the one of the camera measurements, and it also includes the fiber shaker, compare Fig. 4.19. At the receiver the

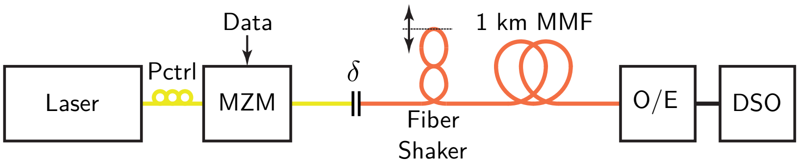

Figure 4.24: Input delay spread function measurement setup

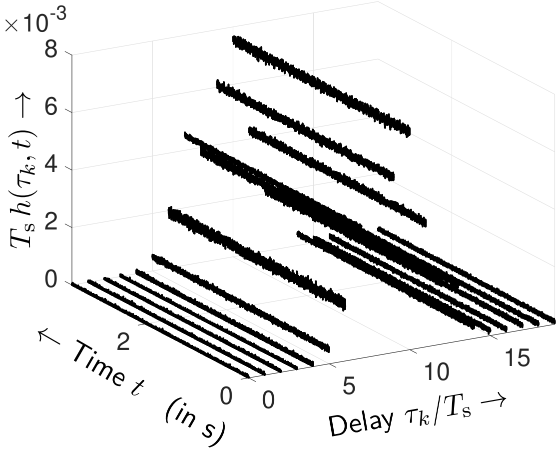

Figure 4.25: Input delay spread function when launching with $\delta = 15$ µm and vibrating with 10 Hz

O/E element converts the optical signal into the electrical domain, and finally the signal is captured with the DSO and is further processed offline.

An example of a measured input delay spread function is presented in Fig. 4.25 when launching with an SMF to MMF eccentricity δ of 15 µm and vibrating with 10 Hz. Here, the estimated channel taps are spaced by the symbol period T_s and are indexed with k. Please note that the input delay spread function is an energy signal in direction of the delay axis and a power signal in direction of the time axis. The dispersion introduced by the channel is clearly visible. Considering the impulse response along the time axis, it is apparent that the vibration has just a minor effect on the impulse response.

Power Delay Profile

In order to extract the delay specific parameters the power delay profile (PDP) is used [Rapp02]. The PDP $P(\tau)$ is defined as the average of the absolute squared input delay spread function over time as given by

$$P(\tau) \overset{\mathrm{def}}{=} \lim_{t_0 \to \infty} \frac{1}{t_0} \int\limits_0^{t_0} \underline{h}(\tau, t)\, \underline{h}^*(\tau, t)\, \mathrm{d}t \quad . \tag{4.23}$$

Please note that the input delay spread function is generally complex-valued. Comparing this expression with the definition of the ACF for a power signal

$$\underline{\phi}_{hh}(\tau, \Delta t) = \lim_{t_0 \to \infty} \frac{1}{t_0} \int\limits_0^{t_0} \underline{h}(\tau, t)\, \underline{h}^*(\tau, t + \Delta t)\, \mathrm{d}t \quad , \tag{4.24}$$

one can see that the PDP can be expressed by $P(\tau) = \underline{\phi}_{hh}(\tau, 0)$. Considering $\underline{h}(\tau, t)$ to be wide-sense stationary over time t, the ACF can be expressed as follows

$$\underline{\phi}_{hh}(\tau, \Delta t) = \mathrm{E}\{\underline{h}(\tau, t)\, \underline{h}^{*}(\tau, t + \Delta t)\} \ . \tag{4.25}$$

Please note that the ACF is the inverse Fourier transform of the PSD function $\Phi_{hh}(\tau, \nu)$ as given by

$$\underline{\phi}_{hh}(\tau, \Delta t) = \int\limits_{-\infty}^{+\infty} \Phi_{hh}(\tau, \nu)\, \mathrm{e}^{\mathrm{j}2\pi\, \Delta t\, \nu}\, \mathrm{d}\nu \ . \tag{4.26}$$

Since an ACF has a Hermitian symmetry by default, PSD functions are always real-valued. Substituting $\Delta t = 0$ shows that the power delay profile can also be obtained by integrating over the PSD, i.e. Delay-Doppler spread function.

The PDP of a signal received after transmitting a discrete unit impulse through the above input delay spread function is depicted in Fig. 4.26. Based on the PDP the following delay-related parameters can be calculated [Rapp02]: The mean excess delay $\bar{\tau}$ is a measure of latency and can be calculated by

$$\bar{\tau} = \frac{\sum\limits_{k=0}^{K-1} \tau_k\, P(\tau_k)}{\sum\limits_{k=0}^{K-1} P(\tau_k)} \ . \tag{4.27}$$

Please note that the mean excess delay shown in Fig. 4.26 is just a relative delay. The absolute delay, i.e. latency of the transmission, is higher since in the impulse response

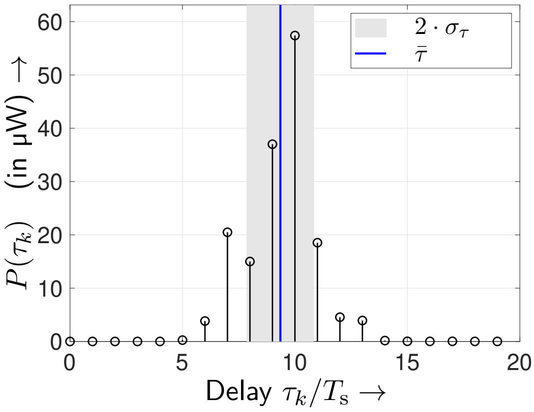

Figure 4.26: PDP launching with $\delta = 15$ µm and vibrating with 10 Hz

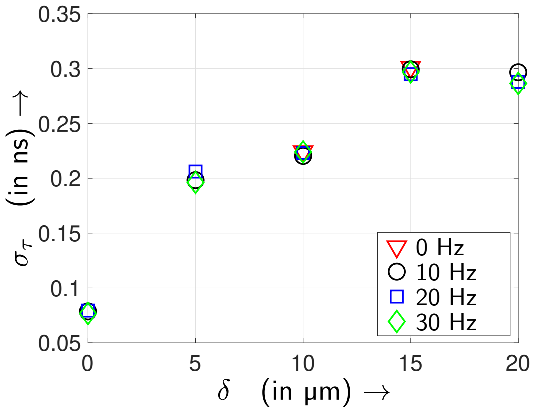

Figure 4.27: RMS delay spread versus launch eccentricity for different vibration frequencies

estimation the precursor zeros are neglected. The root mean square (RMS) delay spread

$$\sigma_\tau = \sqrt{\frac{\sum\limits_{k=0}^{K-1} \tau_k^2 \, P(\tau_k)}{\sum\limits_{k=0}^{K-1} P(\tau_k)} - \bar{\tau}^2} \tag{4.28}$$

is a measure of dispersion or how much inter-symbol interference is introduced by the channel.

The RMS delay spreads for different launch eccentricities and vibration frequencies are shown in Fig. 4.27. With increasing eccentricity δ the RMS delay spread increases as well. A centric launch excites mainly the fundamental mode. In contrast, launching with a high eccentricity δ excites multiple high-order mode groups separated by the modal dispersion. This leads to a high RMS delay spread value. A channel can be considered as flat-fading, if the symbol duration T_s is longer than $10 \cdot \sigma_\tau$, i.e. at a symbol-rate of $1/T_\mathrm{s} = 5$ GHz the 1 km MMF channel shows a frequency-selective behavior for all δ values. Thus, in such testbed configurations frequency-selective signal processing is required. Adding vibration to the fiber has practically no effect on the RMS delay spread, and therefore no coupling between mode groups takes place, confirming [Carp13; Bole13].

Energy Time Profile

In addition to the PDP, a time-related profile is defined in order to extract time-variance information. Since the impulse response in delay direction is an energy signal, the energy time profile (ETP) is defined. It is calculated by integrating the absolute squared input delay spread function over the delay as follows

$$E(t) = \int\limits_{-\infty}^{+\infty} \underline{h}(\tau, t) \, \underline{h}^*(\tau, t) \, \mathrm{d}\tau \quad . \tag{4.29}$$

Applying the Fourier transform to the ETP without DC gives the energy spectral density (ESD). Figure 4.28a shows the ESD when no vibration is applied to the fiber. In this spectrum no specific frequencies are dominant except for the ones around the DC. The effect of introducing a 10 Hz vibration is clearly visible in the ESD as highlighted in Fig. 4.28b. Here, the 10 Hz vibration and its harmonics at 20 Hz, 30 Hz and 40 Hz are clearly visible. In accordance with the camera measurements, the spectral amplitudes of the vibration frequencies are more than 13 dB lower when comparing to the DC value. Please note that the DC is removed in Fig. 4.28 for illustration purposes. Thus, the channel can be considered as time-invariant in the analyzed time span.

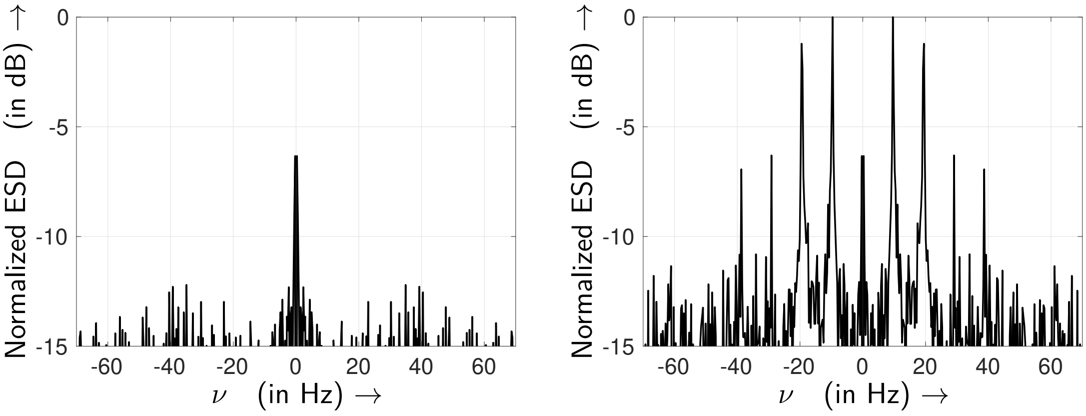

(a) No vibration **(b)** 10 Hz vibration

Figure 4.28: Energy spectral density launching with $\delta = 15$ µm

4.2.3 Signal Processing Considerations

Combining the results of the camera and impulse response measurements highlight that the SISO channel with mode-selective launch is time-invariant in the analyzed time span even under considerable vibration stress. Over an extended period of time the channel might show slow fading effects e.g. due to temperature changes. Therefore, designing an IM/DD transmission through such an MMF channel, adaptive signal processing is recommended. For example: An initial estimation of the channel impulse response can be carried out using training data. Subsequently, the channel impulse response can be adapted based on previous decisions, i.e. decision-aided channel estimation. Also, adaptive equalization with a data-aided initialization and later a decision-aided adaptation can be carried out as shown in [Ryf11; Font15]. The advantage is that after the initialization no further training data is required, and therefore this strategy better exploits the available channel capacity. Considering a MIMO configuration, this time-variance study has shown that coupling between mode groups does not occur under vibration stress. If a MIMO setup is designed to transmit different data streams on separate mode groups, these streams will not interfere under the influence of vibration. Thus, the time-invariant channel characteristic also applies to such MIMO configurations.

5 Testbed Results

In this chapter, different concepts for short reach MIMO transmissions with IM/DD are realized in a laboratory testbed and their benefits and drawbacks are discussed. This includes conventional offset SMF to MMF launches for mode-selective excitation, multi-mode couplers for MUX and DEMUX and an MMF channel. Furthermore, the concept of using multiple detector segments at the receiver for simultaneous spatial separation and optical electrical conversion is analyzed. Also, photonic lanterns in combination with a few-mode fiber channel are discussed. Finally, the suitability of different hardware components for their use in MIMO with IM/DD is summarized.

5.1 Multi-Mode Setup with Offset SMF to MMF Splices and Fiber Optical Couplers

The use of SMF to MMF splices, aligned with different radial offsets, allows the excitation of different modes. A corresponding schematic and bright-field microscope image of such a splice is shown in Fig. 5.1. It is clearly visible from the image that the physical dimensions do not allow the simultaneous alignment of two or more SMFs to an MMF since the 125 µm cladding diameter prevents this. In order to overcome this issue the modal excitation is carried out in two separate paths with different eccentricities and a multi-mode coupler subsequently combines the excited modes. This concept stands out due to its passive nature and simple manufacturing process using readily available components. It is worth noting that this multiplexing strategy has been applied in literature for MIMO with IM/DD [Schoe07; Step14].

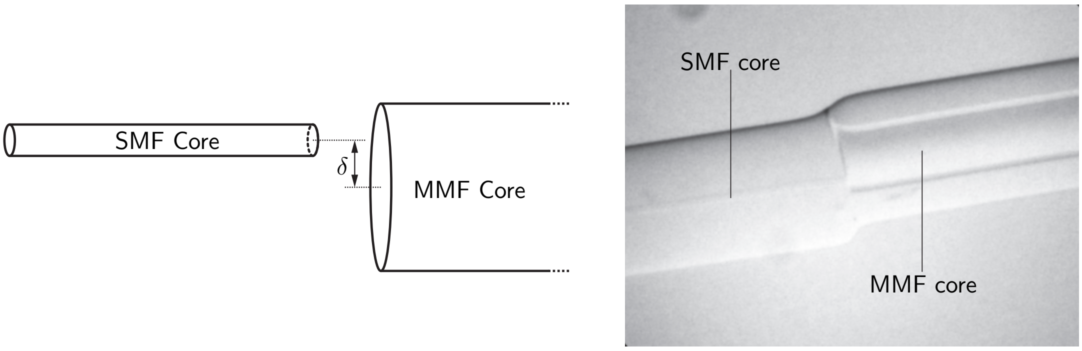

(a) Schematic with fiber cores only

(b) Microscope image using $\delta = 20$ µm

Figure 5.1: Offset SMF to MMF splice for mode-selective excitation using the eccentricity δ

As an example for the spatial diversity of this concept, the measured spatial intensity patterns of a centric launch, i.e. $\delta = 0$ µm, and a launch with the eccentricity of $\delta = 15$ µm are shown in Fig. 5.2. It is worth noting that for the 850 nm pattern a silicon-based fiber end-face camera and for the 1550 nm measurement a scanning procedure is utilized. The results clearly show that the spatial patterns are well-separated with some minor overlapping parts. Analytically calculating the modal power coupling coefficients with Eq. 2.11 in Chapter 2 shows, that launching with two different offsets the excitation of a perfect orthogonal set of modes is not viable. Thus, the parts of the MIMO input signals that are superimposed on the same mode are subject to interference as it is demonstrated in Section 3.4.4.

In order to combine the excited modes, different multi-mode coupler types can be used. They are analyzed in the subsequent section.

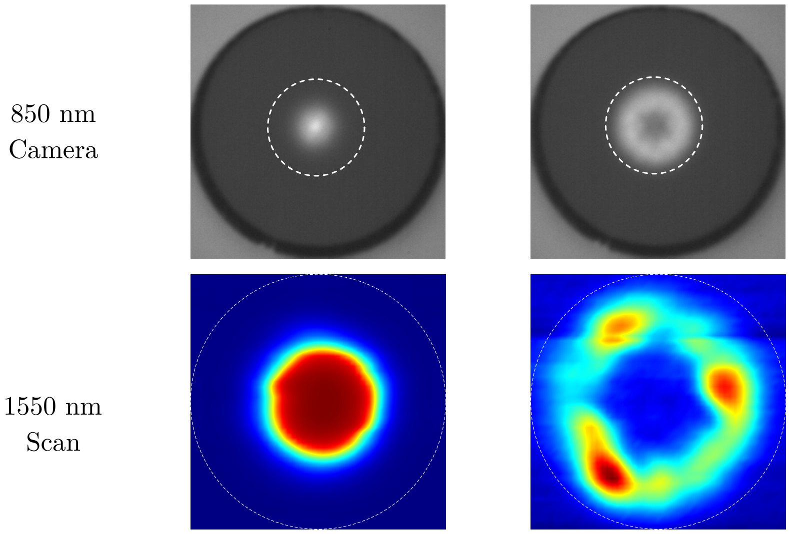

(a) $\delta = 0$ µm **(b)** $\delta = 15$ µm

Figure 5.2: Measured spatial intensity patterns for two launch eccentricities δ at different operating wavelengths and using Fabry-Pérot-type lasers; the dashed line represents the 50 µm MMF core diameter

5.1.1 Multi-Mode Coupler-Types

Optical couplers are passive components that are usually employed for splitting or combining SISO data in optical fibers. In contrast to this standard purpose, in this work different multi-mode couplers are analyzed with respect to their mode multiplexing and demultiplexing capabilities.

Fusion couplers are manufactured by aligning two waveguides with core and cladding next to each other, and then they are fused together by applying heat and pull tension, compare Fig. 5.3a. The degree of fusion and the length of the fused region are the interesting parameters to control the mode coupling properties. In general, fusion couplers are so-called

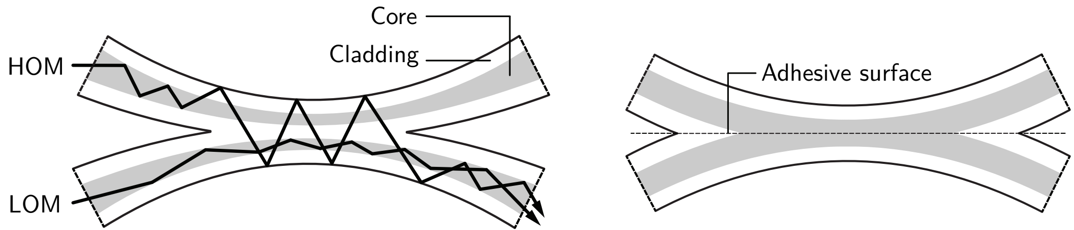

(a) Mode-selective fusion coupler with simplified operating principle

(b) Polished coupler

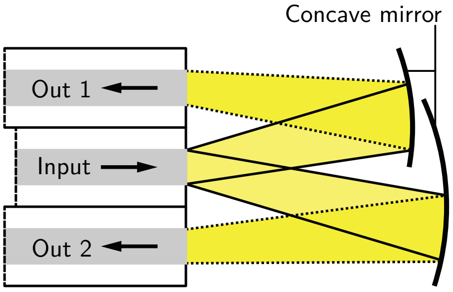

(c) Mirror coupler

Figure 5.3: Coupler types schematics

evanescent field couplers where high-order modes (HOMs) couple into the neighboring waveguide first. Therefore, a low degree of fusion is sufficient and such couplers are called asymmetric fusion couplers (AFC). The higher the degree of fusion of such couplers, the higher the tendency that also low-order modes (LOMs) couple into the neighboring waveguide. Couplers with a high degree of fusion are symmetric fusion couplers (SFC), and they split the incident power in all modes relatively symmetric to the two output ports, compare Section 4.1.3. Since an SFC splits all modes to both waveguides equally they are not suitable for mode demultiplexing.

Off-the-shelf AFCs have a high insertion loss when coupling from one waveguide to the other and SFCs have a low mode separability. Thus, a compromise of a customized fusion coupler (CFC) with a medium degree of fusion is of interest. This CFC aims at combining the best of both approaches, i.e. a low power asymmetry and a high mode separability. During the manufacturing process of a CFC, light is launched with an offset SMF to MMF splice with e.g. $\delta = 15$ µm into one waveguide and the fusion process is carried out until a transfer of light into the neighboring waveguide can be measured. In case of using 15 µm offset, the coupler is termed CFC15, and in case of 20 µm offset it is named CFC20.

Polished couplers are manufactured by aligning two fibers with a defined curvature and by abrasively removing parts of the fiber. This removal is done up to the core center such that the cores of the two waveguides are in direct contact and are merged into one fiber core of e.g. 50 µm diameter, see Fig. 5.3b. In this position the two waveguides are glued together.

The mirror coupler (MC) is a custom-made micro-optical device where two concave mirrors with different focal points are used to separate the signal into two waveguides or vice versa

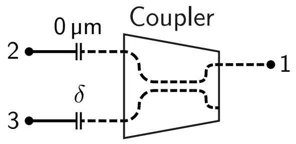

Figure 5.4: Measurement setup (solid lines: SMF, dashed lines MMF)

[Labs89, p. 136]. Its unique construction characteristic is that the second mirror is glued on top of the first mirror, compare schematic in Fig. 5.3c.

Hereinafter, the multi-mode coupler types are evaluated with respect to their transfer characteristics and fiber end-face intensity patterns under mode-selective launch conditions. The corresponding testbed is shown in Fig. 5.4. At input port 2 a centric SMF to MMF launch is used and at input port 3 an off-center launch with the eccentricity of δ is performed. The measured attenuation values and derived parameters are listed in Tab. 5.1. Herein, the coupling ratio a_{cr} is obtained from the insertion losses a_{12} and a_{13} and results in

$$a_{\mathrm{cr}}\,[\mathrm{dB}] = \Big|a_{13}\,[\mathrm{dB}] - a_{12}\,[\mathrm{dB}]\Big| \ , \tag{5.1}$$

showing that all coupler types except the AFC exhibit a relatively symmetric power coupling ratio. The excess loss describes the mean additional loss inside the coupler and is calculated by

$$a_{\mathrm{e}}\,[\mathrm{dB}] = -10 \cdot \log_{10} \frac{1/a_{12,} + 1/a_{13,}}{2} \ . \tag{5.2}$$

The in-fiber devices, i.e. SFC, AFC and PC, show the lowest excess losses, whereas the MC being a micro-optical device exhibits the highest excess loss of all coupler types.

In addition to the transfer characteristic, the end-face intensity patterns are measured under mode-selective launch conditions at 850 nm using a Fabry-Pérot laser. The resulting patterns are depicted in Fig. 5.5. Please consider that the launch eccentricities δ are empirically chosen with the aim to get a distinct dot and ring pattern. Nevertheless, a good insight into the modal structure can be obtained. When considering the low-order mode path with the center launch condition, the PC and AFC have a concentrated dot

Table 5.1: Measured attenuation and derived parameters under mode-selective launch conditions at 1535 nm

	SFC	AFC	PC	MC
a_{12} [dB]	1.4	0.2	2.9	3.2
a_{13} [dB]	3.4	8.0	3.6	4.6
δ [µm]	11	15	0	10
Excess loss a_{e} [dB]	2.3	2.5	3.2	3.8
Coupling ratio a_{cr} [dB]	2.0	7.8	0.7	1.4

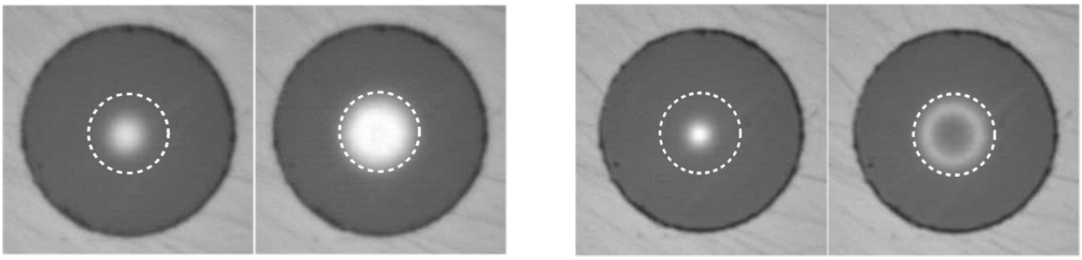

(a) SFC and $\delta = 11$ µm

(b) AFC and $\delta = 15$ µm

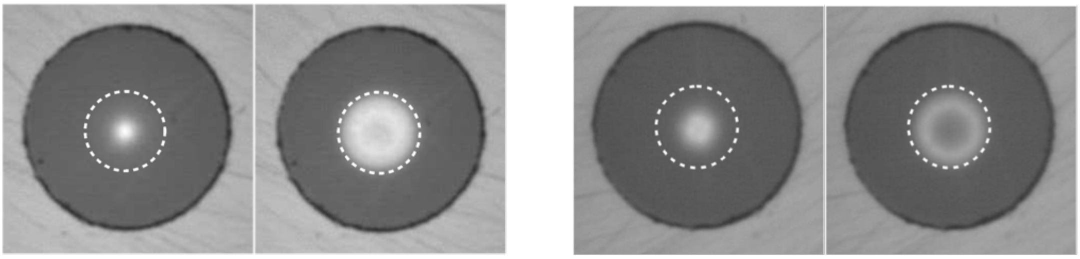

(c) PC and $\delta = 0$ µm

(d) MC and $\delta = 10$ µm

Figure 5.5: Measured intensity pattern comparing different coupler types (left pattern of the pairs: center launch condition; right pattern of the pairs: off-center launch condition δ); the dotted line represents the 50 µm core diameter

pattern, which is an indicator for a good mode maintenance. For the high-order mode path the AFC and MC show a distinct ring pattern. Overall the AFC shows a high mode separability with a small overlap of the two patterns. However, including the AFC in a MIMO setup, its very asymmetric insertion losses would clearly degrade the quality (i.e. SNR) of the MIMO layer where the data is transferred on the high-order modes.

5.1.2 Analysis of a (4x4) Configuration

Based on channel impulse response measurements and optical mode pattern analyses in a 2 km OM4-grade multi-mode fiber testbed, the feasibility to form a (4×4) MIMO configuration is studied. This analysis neglects possible interference of a real data transmission since both measurement principles employ averaging by default. Nevertheless, a good insight of the mode group structure is obtained from this study. The corresponding (4×4) testbed setup is depicted in Figs. 5.6 and 5.7. It makes use of two (2×4) fusion star couplers for mode multiplexing as well as demultiplexing. Internally, the (2×4) couplers are composed of concatenated (1×2) couplers.

The included picosecond laser generates short pulses with an FWHM of 25 picoseconds at an operating wavelength of 1326 nm. Four SMF to MMF splices with three different eccentricities ($\delta = 0,\ 10,\ 15$ µm) for mode-selective excitation have been analyzed. By changing the granularity of the eccentricities further optimizations are possible. Since this setup already exhibits a high insertion loss due to the concatenated couplers, eccentricities $\delta > 15$ µm are not viable. Subsequently, a (2×4) fusion coupler is utilized for multiplexing

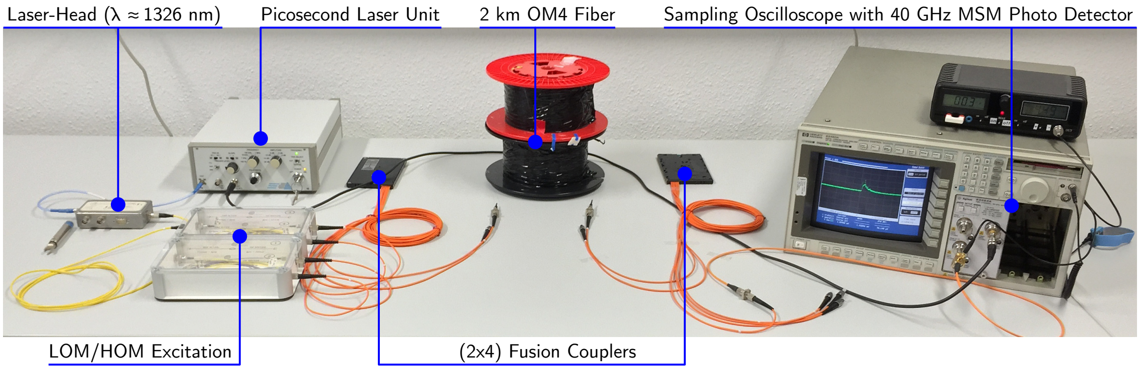

Figure 5.6: Testbed configuration

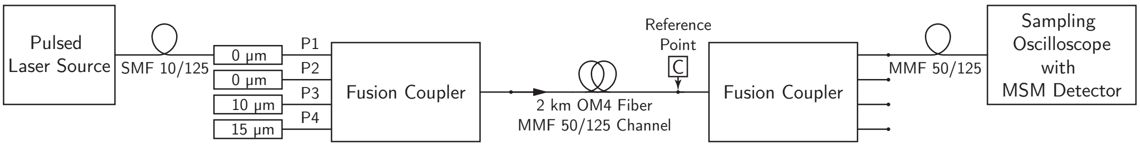

Figure 5.7: Measurement setup for determining the MIMO specific impulse responses

the different modes into the 2 km OM4 fiber channel and then another fusion coupler is placed in reverse operation for mode demultiplexing. The received signal is then measured with a sampling oscilloscope with a 40 GHz metal-semiconductor-metal (MSM) photo detector.

Port Selection

The first step in the port selection process is to decide, which coupler is used for mode multiplexing (input coupler) and which is used for mode demultiplexing (output coupler). Afterwards the input output configuration, where each of the four physical inputs of the input coupler needs to be connected to a specific splice with a certain eccentricity, has to be selected. Therefore, different criteria can be analyzed. The first criterion is the energy of the measured signals at reference point C (see Fig. 5.7), which is converted into input specific insertion losses. A second criterion is the mode separability, describing how the four different channels excite different modes or mode groups. For this purpose, the degree

Table 5.2: Port selection outcome and respective input specific insertion losses between the laser source and the reference point at $\lambda = 1326$ nm

Physical input port no.	Launch eccentricity δ	Input specific insertion losses
P1	0 µm	10.7 dB
P2	0 µm	10.2 dB
P3	10 µm	12.6 dB
P4	15 µm	15.7 dB

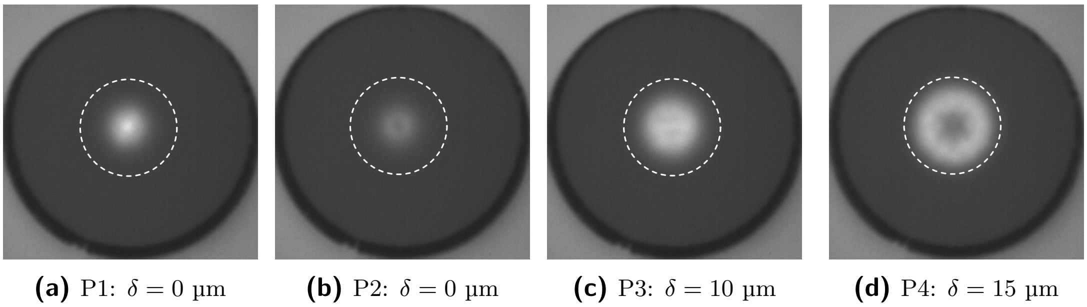
(a) P1: $\delta = 0$ µm **(b)** P2: $\delta = 0$ µm **(c)** P3: $\delta = 10$ µm **(d)** P4: $\delta = 15$ µm

Figure 5.8: Measured intensity pattern as a function of the light launch eccentricity δ at an operating wavelength of 850 nm; the dashed line represents the 50 µm core size

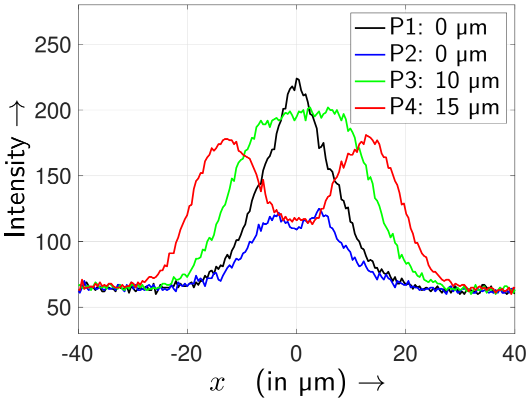

Figure 5.9: Cross-section of the measured mean power distribution (x is the coordinate in horizontal direction; intensity values are normalized and have 8-bit quantization)

of overlap in the spatial mean power distribution pattern, measured with a camera, is examined. In addition, the mode separability is resolved from the modal structure of the measured impulse responses. Combining low input specific insertion losses and a high mode separability are used for the manual decision-making. The outcome of the port selection process is shown in Tab. 5.2. With the selected port configuration, the obtained spatial power distribution patterns at the end of the 2 km OM4 fiber at the reference point C (see label in Fig. 5.7) are depicted in Fig. 5.8. The power distribution patterns show the spatial diversity while exciting different mode groups with different launch eccentricities. The cross-section depicted in Fig. 5.9 shows that the spatial separability of the signals launched at P1 (0 µm) and P4 (15 µm) is relatively high compared to the signals launched at other ports. In particular, the spatial power distributions of the signals launched at P2 and P3 are highly correlated.

Measuring the Impulse Responses

The specific impulse responses of the (4×4) optical MIMO system are measured with the conventional signal deconvolution approach for removing the influence of the picosecond input impulse on the measured output signal [Gans86; Sand15e]. Signal deconvolution is necessary since the spectrum of the picosecond impulse is not fully flat in the region

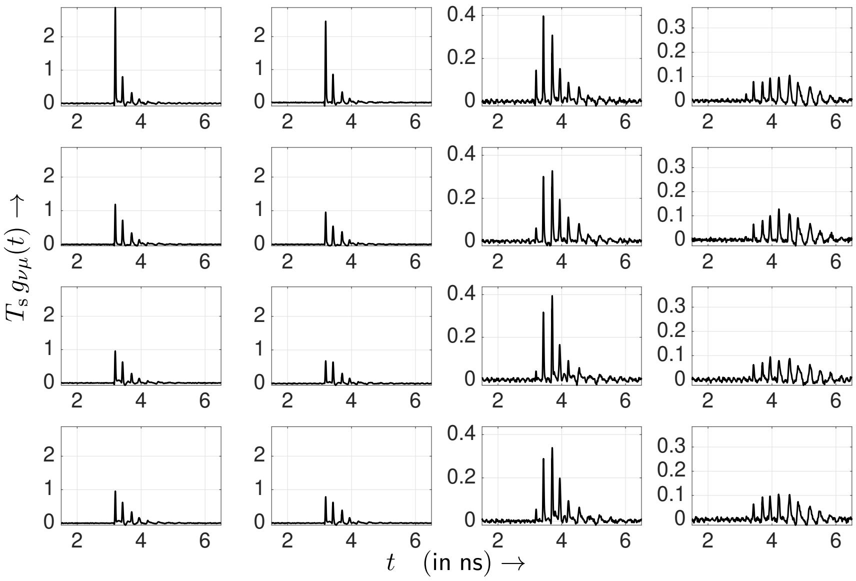

Figure 5.10: Measured electrical MIMO impulse responses with respect to the pulse frequency $f_T = 1/T_s = 625$ MHz at 1326 nm operating wavelength

of interest. The obtained impulse responses $g_{\nu\mu}(t)$ are presented in Fig. 5.10. Here, the mode group structure is clearly visible as a result of the occurring modal dispersion in the 2 km OM4 fiber. Each peak represents one mode group. In addition, the mode group structure is not distorted by the effect of chromatic dispersion since it is nearly zero at the used operating wavelength of 1326 nm. Column 1 and 2 of the impulse responses show the results when the SMF is aligned centric to the MMF. These responses show a high similarity to each other indicating a high correlation as a result of using the same launch eccentricity for both inputs. Column 3 displays the measured impulse responses when launching with 10 µm eccentricity and the fourth column indicates the impulse responses when launching with 15 µm offset. The different mode group structures of the four columns highlight that the mode-selective excitation and multiplexing process works as expected. In contrast, comparing the signals at the four output ports (i.e. comparing the rows) shows a high similarity of the signals. Since the utilized couplers are concatenated symmetric fusion couplers, it is evident that this coupler type is not suited fur the purpose of separating modes. The amplitudes of the pulses when launching with a high eccentricity are notably smaller compared to a centric launch position. This can be confirmed, if we consider the normalized energy of the underlying impulse responses defined as follows

$$E_{\nu\mu} = \frac{\int\limits_{-\infty}^{+\infty} |g_{\nu\mu}(t)|^2 \, \mathrm{d}t}{\int\limits_{-\infty}^{+\infty} |g_{11}(t)|^2 \, \mathrm{d}t} \,. \tag{5.3}$$

These obtained ratios are depicted in Fig. 5.11 and used for the channel mapping. This

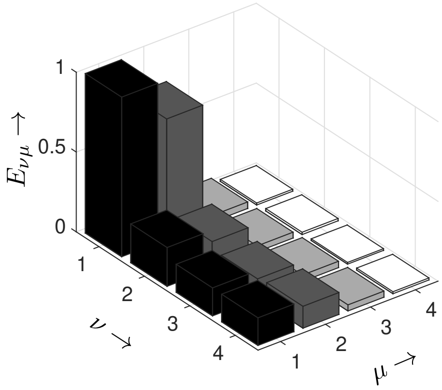

Figure 5.11: Normalized energy of the deconvolved MIMO impulse responses

means the physical input/output port combination, where the impulse response has the highest energy, is identified to be the first direct channel, i. e. $g_{11}(t)$. Then the remaining input/output port combination with the second-highest energy of the impulse response is chosen to be $g_{22}(t)$ etc. When the direct channels are known, i. e. $\nu = \mu$, the mapping of the other channels follows correspondingly. The results shown in Figs. 5.10 and 5.11 are already organized accordingly.

Performance Indicator based on Singular Values

For further performance evaluation a block-oriented MIMO description named spatio-temporal vector coding is applied [Rale98; Sand17c]. It is described by

$$\boldsymbol{u} = \boldsymbol{H} \cdot \boldsymbol{b} + \boldsymbol{n} \ , \tag{5.4}$$

where the transmitted signal vector $\boldsymbol{b}$ is mapped by the channel matrix $\boldsymbol{H}$ onto the received vector $\boldsymbol{u}$. The channel matrix itself is composed as follows

$$\boldsymbol{H} = \begin{bmatrix} \boldsymbol{H}_{11} & \dots & \boldsymbol{H}_{1n_{\mathrm{T}}} \\ \vdots & \ddots & \vdots \\ \boldsymbol{H}_{n_{\mathrm{R}}1} & \cdots & \boldsymbol{H}_{n_{\mathrm{R}}n_{\mathrm{T}}} \end{bmatrix} , \tag{5.5}$$

with $\boldsymbol{H}_{\nu\mu}$ being convolution matrices containing the cumulative channel impulse responses that are sampled with the pulse frequency $f_{\mathrm{T}} = 625$ MHz. The cumulative channel impulse responses contain the channels $g_{\nu\mu}(t)$ as well as the rectangular transmit and receive filter. Finally, the vector of the additive, white Gaussian noise is defined by $\boldsymbol{n}$. Singular-value decomposition (SVD) is applied as follows

$$\boldsymbol{H} = \boldsymbol{S} \cdot \boldsymbol{V} \cdot \boldsymbol{D}^{\mathsf{H}} \tag{5.6}$$

and the positive real-valued singular-values $\sqrt{\xi_{\ell,k}}$ of the channel matrix $\boldsymbol{H}$ are extracted from the diagonal of matrix $\boldsymbol{V}$ as follows

$$\sqrt{\xi_{\ell,k}} = \mathrm{diag}(\boldsymbol{V}) \ . \tag{5.7}$$

With SVD pre- and post-processing, the whole system is transferred into independent, non-interfering layers exhibiting unequal gains per layer as highlighted in Fig. 5.12. With the proposed system structure, the SVD-based equalization leads to a different number of MIMO layers ℓ (with $\ell = 1, 2, \ldots, L$) at the time k (with $k = 1, 2, \ldots, K$). Here it is worth noting that the number of parallel transmission layers L at the time slot k is limited by $\min(n_\mathrm{T}, n_\mathrm{R})$, and K defines the number of symbols per data block. The data symbol $c_{\ell,k}$ to be transmitted over the layer ℓ at the time k is now weighted by the corresponding singular-value $\sqrt{\xi_{\ell,k}}$ and further disturbed by the additive noise term $w_{\ell,k}$ [Ahre09a].

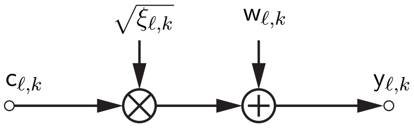

Figure 5.12: Resulting layer specific SVD-based broadband MIMO system model

Considering the measured impulse responses of the (4×4) system, the resulting singular values are presented in Fig. 5.13. They highlight, that the weighting factors drop in amplitude by a factor of 10 from the 1st to 2nd layer. This indicates a significant impairment of the transmission quality of higher-order layers in terms of SNR. Considering the singular values of the 4th layer reveals that they are more than a factor of 100 lower compared to the ones of the 1st layer. It has been shown in [Ahre14] that highly correlated MIMO channels lead to extreme differences between the singular values of the first and last layer. Highly correlated channels indicate that the different MIMO input signals often use the same modes for transmission. This indirect analysis suggests that mode cross-talk

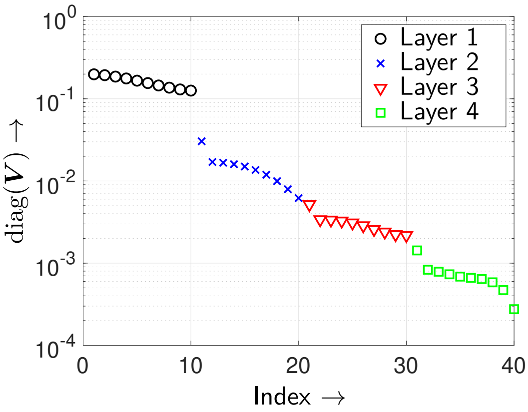

Figure 5.13: Singular values as layer specific weighting factors of the block oriented system ($K = 10$)

occurs in this (4×4) configuration, which leads to significant interference in a real world scenario.

The analysis in this section has confirmed that with the high attenuation of this testbed configuration and the high correlation between the MIMO channels, i.e. high mode cross-talk, a (4×4) transmission based on offset SMF to MMF excitation and fusion couplers is not feasible. As suggested in Section 3.4, low-cost multiplexing components that exhibit a high mode orthogonality need to be found in order to reliably run high-order MIMO systems.

5.1.3 BER Performance of a (2x2) Configuration

In order to evaluate the BER performance of a (2×2) MIMO setup based on SMF to MMF offset splices and couplers, the testbed configuration in Fig. 5.14 is implemented (compare Section 3.4.3). A Fabry-Pérot and a DFB laser, both operating at 1550 nm, are used to compare a narrow- with a broad-linewidth source. The use of just one laser saves costs and ensures that both MIMO input sequences are transmitted in the same frequency range. Since the included Mach-Zehnder modulator is highly polarization dependent, it is preceded by a polarization controller. Subsequently, the modulated signal is split into two paths. The centric launch path, exhibiting a lower attenuation, is delayed by $\Delta\tau = 819.2$ ns to guarantee uncorrelated data patterns at the MIMO inputs. In this (2×2) MIMO setup the transmitted data consists of two concatenated sequences, which are repeatedly transmitted, each having a length of $\Delta\tau$. Thus, for different symbol rates the sequence length needs to be adapted according to Tab. 5.3. The chosen pseudo random binary sequences (PRBSs) are concatenated by a ’0’ bit to ensure that the numbers of ’0’ and ’1’ bits are identical. Furthermore, the two sequences are generated with different primitive generator polynomials and initialization vectors. Mode-selective excitation is carried out with a centric launch and an offset launch with $\delta = 15$ µm. Afterwards the signals are multiplexed with a customized fusion coupler, transmitted through an OM4-grade MMF channel and demultiplexed with another customized fusion coupler. Channel lengths of 0 (back-to-back), 100, 250, 350 and 1000 m are analyzed. Finally, the received signals are directly detected and the sampled data of the DSO is stored for offline signal processing.

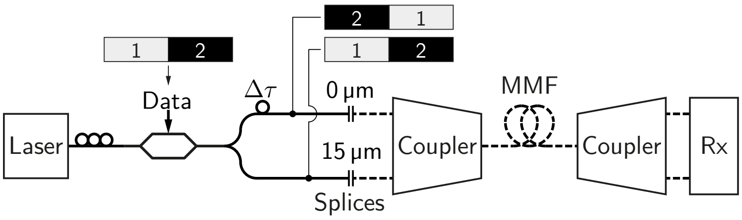

Figure 5.14: Coupler-based MIMO testbed configuration (solid line: SMF, dashed line: MMF)

Table 5.3: Sequence type choice in dependency on the symbol rate for each MIMO input to match the delay $\Delta\tau = 819.2$ ns

Symbol rate f_T	Sequence type	Sequence length
1.25 GHz	PRBS $2^{10} - 1$ and '0' bit	1024 bits
2.5 GHz	PRBS $2^{11} - 1$ and '0' bit	2048 bits
5 GHz	PRBS $2^{12} - 1$ and '0' bit	4096 bits
6.875 GHz	shortened PRBS $2^{13} - 1$	5632 bits

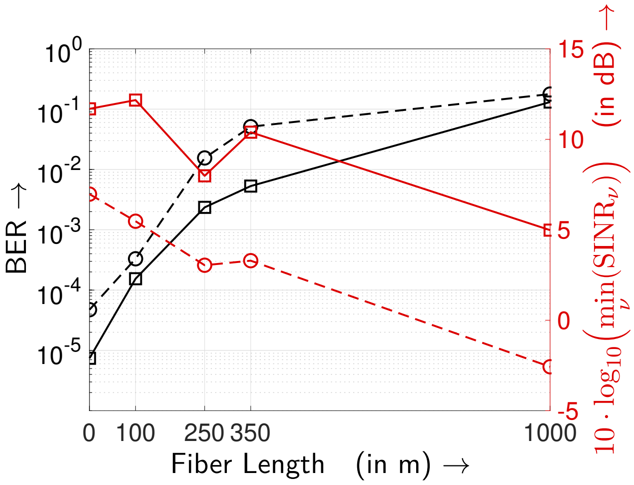

Figure 5.15: Measured BER and SINR versus MMF length analyzing the (2×2) coupler setup at $f_\mathrm{T} = 6.875$ GHz (solid lines: DFB laser, dashed lines: FP laser)

A pilot-based least squares algorithm is used to estimate the frequency-selective MIMO channel taps, and a decision feedback equalizer is applied to remove their influence on the receive signal. The first symbols of the PRBSs are used for the pilot tones, e.g. 800 symbols for a data-rate of $f_\mathrm{T} = 6.875$ GHz. Please note, that for the BER analysis at least 150 frames (depending on the data rate) have been analyzed in order to be able to confidently measure BER levels as low as 10^{-4}.

Firstly, a symbol rate of $f_\mathrm{T} = 6.875$ GHz is analyzed, resulting in a total uncoded bit rate of $R_\mathrm{b} = 13.75$ Gbps ($R_\mathrm{b}/\mathrm{Gbps} = n_\mathrm{T} \cdot f_\mathrm{T}/\mathrm{GHz}$). At this rate the BER performance and the SINR values are compared for different fiber lengths in Fig. 5.15. The results show a decrease in SINR with an increase in fiber length. This is a combined result of an increase in attenuation for higher fiber lengths and an increase in interference. Considering the BER results they highlight that a reliable transmission up to 100 m of MMF is feasible with appropriate channel coding. The DFB laser shows a superior BER performance compared to the FP laser. This is caused by its higher optical power and its lower spectral width, reducing the chromatic dispersion.

Table 5.4 lists the achieved bit rates for different fiber lengths and the two laser types. For each fiber length symbol rates of 1.25, 2.5, 5 and 6.875 GHz have been tested. The results

Table 5.4: Maximum bit rates R_b with a BER $< 10^{-3}$ achieved for a fixed fiber length using the coupler setup

Laser	Length/m	$\max\{R_\mathrm{b}\}$/Gbps	BER
FP	0	13.75	$< 10^{-4}$
	100	13.75	$3.3 \cdot 10^{-4}$
	250	5*	$< 10^{-4}$
	350	5	$< 10^{-4}$
	1000	2.5	$6.2 \cdot 10^{-4}$
DFB	0	13.75	$< 10^{-4}$
	100	13.75	$1.5 \cdot 10^{-4}$
	250	10	$< 10^{-4}$
	350	10	$< 10^{-4}$
	1000	2.5	$7.3 \cdot 10^{-4}$

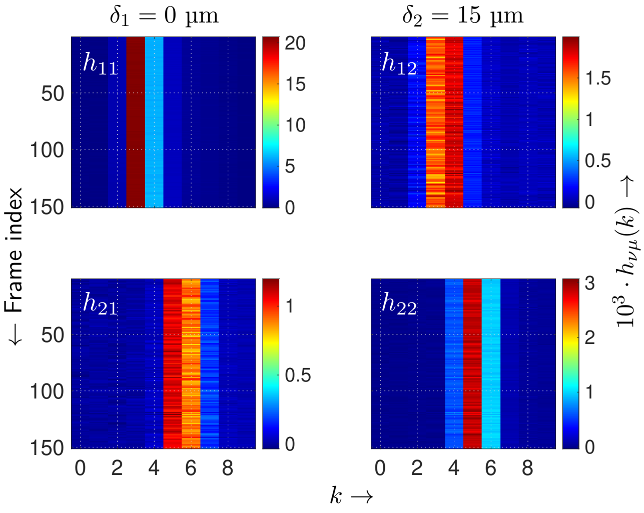

Figure 5.16: Estimated (2×2) MIMO channel taps $h_{\nu\mu}(k)$ for 150 transmission frames (DFB laser, $f_\mathrm{T} = 5$ GHz, 350 m MMF channel, frame length: 4096 symbols)

highlight that the DFB laser's performance is slightly superior, specifically for fiber lengths of 250 and 350 m.

In addition to the BER results, an example of the channel estimation output for 150 frames is presented in Fig. 5.16. In this experiment a DFB laser, a 350 m MMF fiber channel and a symbol rate of 5 GHz are considered. The signal transmitted via the centric launch on low-order modes is quite well separated at the receiver-side by the customized fusion coupler. In contrast, the signal launched with 15 µm offset is carried on high-order modes, which are evenly split by the demultiplexing coupler. This is the outcome of the electrical field of HOMs being mainly guided at the edge of the fiber core, and hence HOMs are more prone to couple into the opposing path when considering the implemented weakly fused multi-mode coupler. In terms of dispersion, two to three significant symbol-spaced channel

---

*With zero forcing equalizer and T/2-spaced processing taps are visible at this rate and channel length. Moreover, the estimation result shows that the channel impulse response is quite stable within the 150 frames. This implies, that just one initial channel estimation is sufficient and minor adaptations could be made with a decision-based adaptive channel estimator or equalizer.

5.2 Multi-Segment Detection

Multi-segment photo detectors can be directly attached to the multi-mode fiber channel at the receiver side, and they are able to combine the demultiplexing as well as optical-electrical conversion process in a single low-cost device. As previously shown in Fig. 5.2, a centric and an offset SMF to MMF launch lead to a dot and ring intensity pattern, respectively. The idea is to independently detect these patterns by having electrically independent detector segments whose geometry is adapted to the respective mode pattern. Hereinafter, these detectors are analyzed with respect to their channel impulse responses, bandwidth characteristics and BER performances in a (2×2) MIMO setup.

5.2.1 Chip Characterization

The multi-segment photo detectors manufactured by Vienna University of Technology in 2009 [Silv10] are characterized by measuring their responsivities in dependency on the fiber alignment. Therefore, an SMF with a 4.4 µm core diameter is placed over the silicon-based chip at a distance of 10 to 20 µm, as illustrated in Fig. 5.17a. Considering the beam divergence based on the fiber's numerical aperture of 0.13 and the 800 nm operating wavelength, the light field diameter on the chip is 7.6 to 10.2 µm, respectively. An exact alignment is achieved by inserting the fiber into a rigid cannula, which itself is fixed on a 6-axis precision alignment system, being henceforth referred to as Hexapod. The setup with the detector located on the circuit board is shown in Fig. 5.17b. In this contribution different chip types are analyzed. The first type uses two detection segments, a circular area

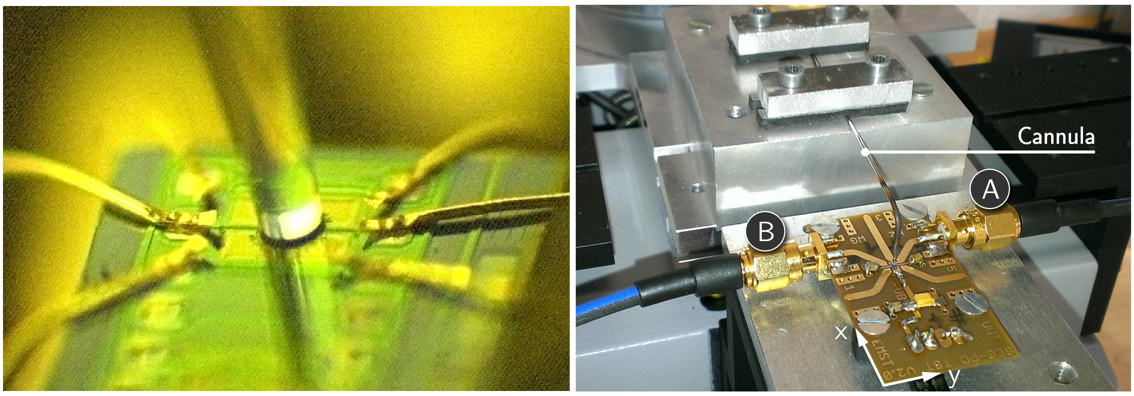

(a) SMF placed over the chip **(b)** Hexapod setup

Figure 5.17: SMF alignment on the two-segment detector

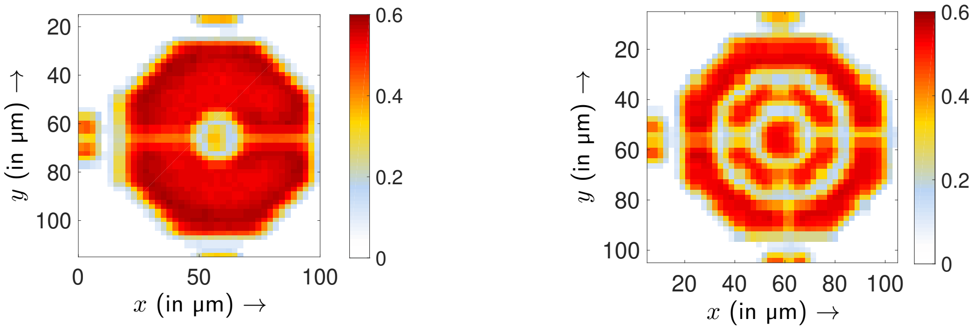

Figure 5.18: Responsivity distributions in A/W of the two-segment detector (left) and the three-segment detector (right) at 850 nm operating wavelength

in the chip center and an outer ring, whereas the second type uses three detection segments with an additional inner ring, as illustrated in Tab. 5.5. Bonding wires interconnect the chip with the circuit board in order to provide external access via SMA connectors. The port labeled with A is connected to the centric circular area and port B to the outer ring. Considering the three-segment detector, port C is connected to the inner ring.

In this testbed configuration the chips are scanned in 1 µm incremental steps to determine the local responsivities. The results in Fig. 5.18 show a homogeneous responsivity distribution within the detection segments with a peak photo current of 0.6 A/W incident light power, being a typical value for silicon PIN photo diodes when operating at 850 nm wavelength. It can also be seen that the small bridging lines, which connect the circular area and the inner ring to their respective bonding pads show some responsivity themselves.

Table 5.5: Measured 3 dB bandwidths of the two detector types

DUT	Segment Part	Port	Bandwidth in GHz
two-segment det.	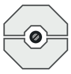	A	0.438
	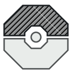	B	0.801
		B	0.813
three-segment detector		A	0.732
		B	0.708
		B	0.703
		C	0.488
		C	0.503

It is worth noting that the air gaps between the segments reduce the overall detection efficiency.

The impulse response measurement method utilizing a 25 ps FWHM pulse and signal deconvolution is applied [Gans86; Sand15e]. Based on the measured impulse responses, the corresponding transfer function is used to determine the bandwidth of the individual detector's segments. Therefore, the SMF is positioned over the segment of interest when measuring its bandwidth. The 3 dB bandwidth results are summarized in Tab. 5.5 for the two detector types and their different segment parts. The measured bandwidths are relatively low, which is presumably a result of the large detector size, resulting in undesired capacitances.

5.2.2 Packaging and MIMO Impulse Responses

In order to guarantee reproducible measurements and a transportable MIMO detection system, a 50/125 graded-index (GI) fiber is permanently attached to the detector by using UV-curable adhesive for fixation. The fiber is aligned with the Hexapod such that the measured photo current of the centric circular area is maximized and the cross-talk to the outer-ring is minimal. Subsequently, the fiber is lifted, the adhesive is applied, and finally the fiber is re-aligned. However, the re-alignment process is time limited since the small UV portion of the microscope illumination starts curing the adhesive. This packaging process step is crucial because residual fiber misalignment may also lead to cross-talk. As an additional safety measure, 3D printed strain relief elements are utilized. After the MMF fixation, the setup is packaged in a metal housing as illustrated in Fig. 5.19 to protect the detector from extraneous light and to make it transportable.

The two-segment detector is used to form a (2×2) MIMO system as shown in Fig. 5.20. In this system, SMF to MMF splices aligned with different radial offsets δ are used for mode-selective excitation. A mode-selective fusion coupler is included for mode multiplexing, and then the signals are transferred through a 1 km GI 50/125 channel. Finally, the two-segment

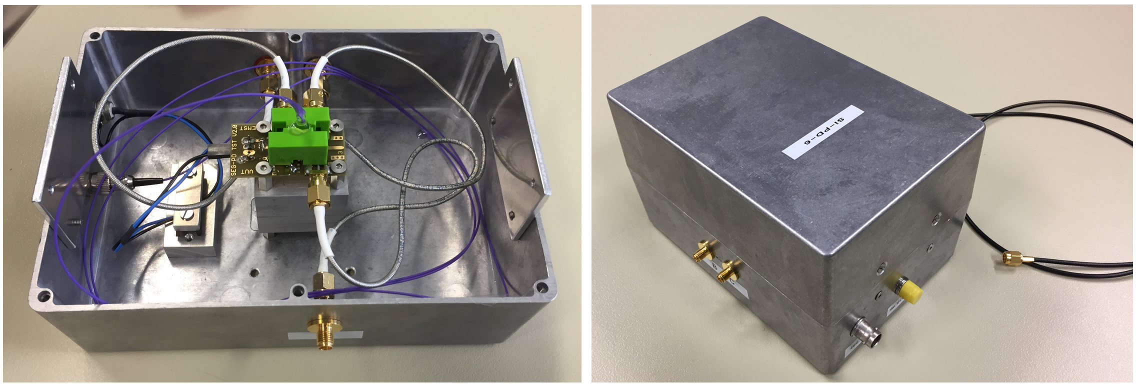

Figure 5.19: Multi-segment photo detector packaging (3 detection segments)

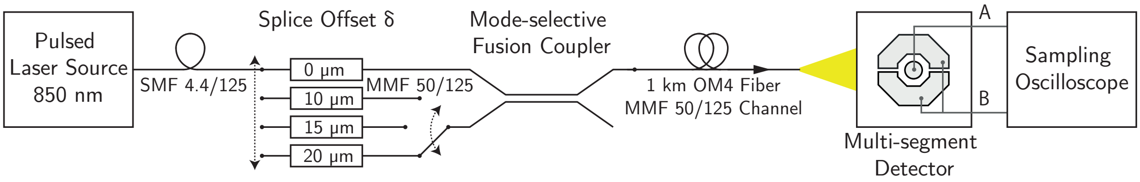

Figure 5.20: Testbed configuration for determining the MIMO specific impulse responses

detector is used for mode demultiplexing as well as for the optical-electrical conversion process. The MIMO transmission system characteristics are obtained by measuring the impulse responses at 850 nm. For the offset launch condition different radial eccentricities, i.e. 10, 15 and 20 µm, are studied. Figure 5.21 shows the measured MIMO impulse responses using the two-segment detector. Comparing the impulse responses when launching with $\delta = 0$ µm shows significant cross-talk to the outer ring segment B. The centric launch condition mainly excites the LP_{01} mode, which has a mode field diameter of approximately 11.6 µm at 850 nm in the 50/125 GI fiber with a numerical aperture of 0.2. Taking the beam divergence between the MMF and detector into account, it is still expected that the detected energy is concentrated in the inner circular segment A, which has a diameter of approximately 10.1 µm. However, a slight misalignment during the adhesive curing process can lead to such cross-talk effects. An optimization of the housing technology may reduce this cross-talk. Another source is the electrical cross-talk in the detector itself. Comparing the high-order mode excitation paths, the highest signal-to-interference ratio is achieved at $\delta = 15$ µm.

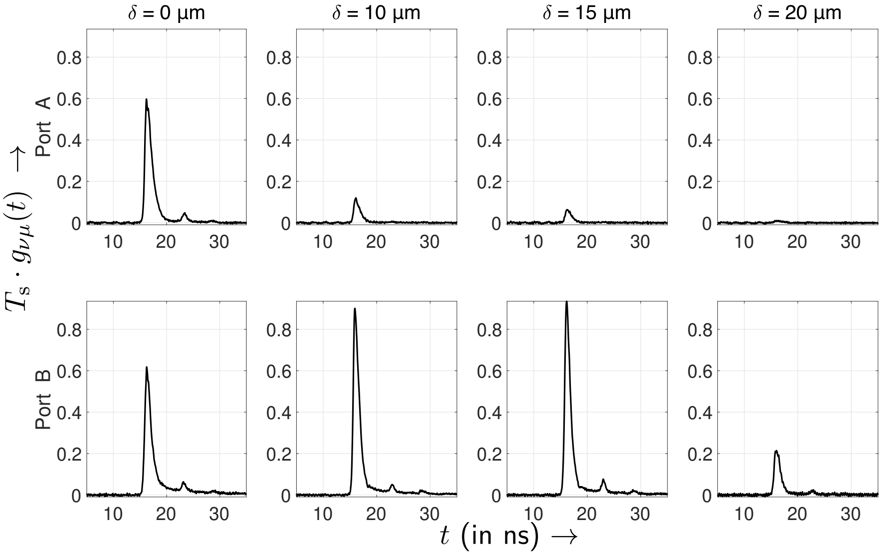

Figure 5.21: Measured electrical MIMO impulse responses using the two-segment detector when comparing different launch eccentricities δ and detector outputs (Port A or B) at 850 nm operating wavelength with respect to the pulse frequency $f_\mathrm{T} = 1/T_\mathrm{s} = 625$ MHz

5.2.3 BER Performance Analysis

In addition to the impulse response evaluation, an end-to-end transmission testbed is realized as shown in Fig. 5.22. A 780 nm DFB laser source launches light into a 4.4 µm diameter SMF, which is split into the two MIMO input paths. Here, the modulation of the PRBS data of length $2^{15}-1$ preceded by polarization control and the offset SMF to MMF launch is carried out. Both paths are combined by a customized fusion coupler and then the signals are transmitted through the MMF channel of either 500 m or 0 m (back-to-back) length. Subsequently, the 2-segment detector is used to separate the MIMO signals. It is followed by a bias-tee to remove the DC and ensure compatibility with the 28 dB amplifier. Finally, the signals are sampled at 40 GSps and stored for offline signal processing.

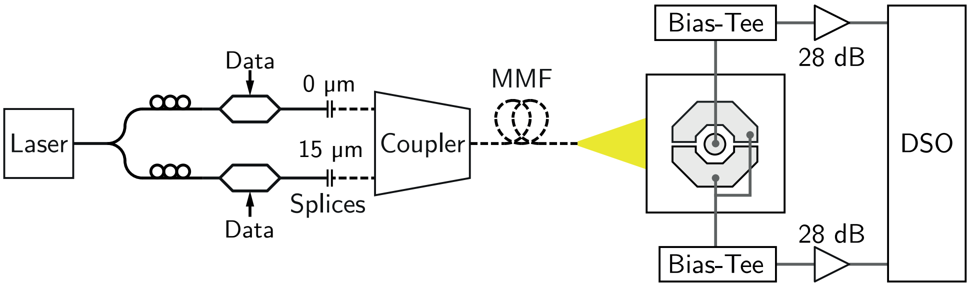

Figure 5.22: MIMO testbed configuration incorporating multi-segment photo detection

The measured MIMO signals at a symbol rate of $f_\mathrm{T} = 2.5$ GHz are shown in Fig. 5.23 for a channel length of 500 m. Herein, the measured signals are compared to an ensemble averaged version, which is obtained by repeating the same PRBS frame and calculating the ensemble average over all frames. Both measured signals overlap quite well, highlighting that interference due to mode cross-talk in the fiber is minimal. However, the transmitted rectangular signals are received highly dispersed due to the bandwidth limitations of the multi-segment detector. Furthermore, the observed noise levels are relatively low compared

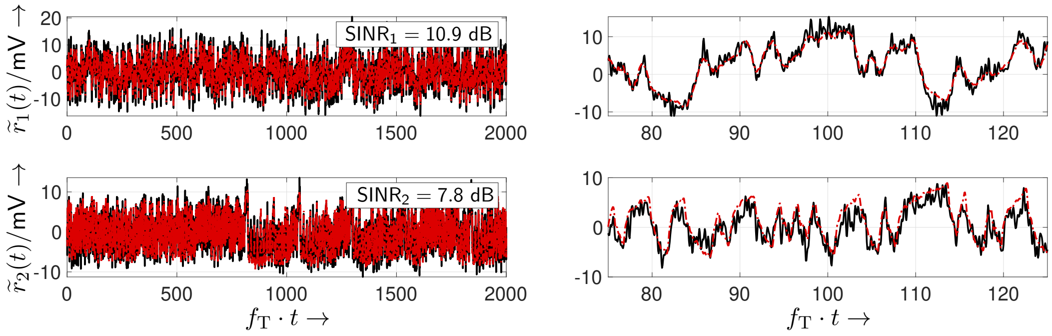

(a) 2000 symbols (b) 50 symbols

Figure 5.23: Measured MIMO receive signals of the (2×2) setup with multi-segment detection using a DFB laser and transmitting at $f_\mathrm{T} = 2.5$ GHz over 500 m MMF (red dashed lines: ensemble average, black solid lines: without ensemble averaging)

Table 5.6: Bit-error rate performance with the multi-segment detector setup

f_T/GHz	R_b/Gbps	Length/m	BER
0.625	1.25	0	$< 10^{-4}$
		500	$< 10^{-4}$
1.25	2.5	0	$< 10^{-4}$
		500	$< 10^{-4}$
2.5	5	0	$< 10^{-4}$
		500	$1.9 \cdot 10^{-3}$
5	10	0	$9.5 \cdot 10^{-3}$
		500	0.32

to the pure coupler-based setup, highlighting that this specific receiver structure adds low electronic noise.

In terms of signal processing, T/2-spaced sampling gave the best results when considering the BER performance. A corresponding least squares channel estimator and a frequency-selective zero forcing MIMO equalizer are implemented. The achieved BER performance results for different symbol rates and fiber lengths are listed in Tab. 5.6. Focussing on the transmission over 500 m MMF shows that the feasible symbol rate with a low BER is limited to 1.25 GHz. This is a result of the high dispersion due to the detector's bandwidth limitation in combination with the high chromatic dispersion at 780 nm operating wavelength. The back-to-back results (0 m MMF channel) confirm the bandwidth limitations since at 5 GHz already a significant BER increase is evident. In comparison, the pure coupler-based setup with a conventional receiver easily achieves 6.875 GHz with no significant impairment, compare Tab. 5.4.

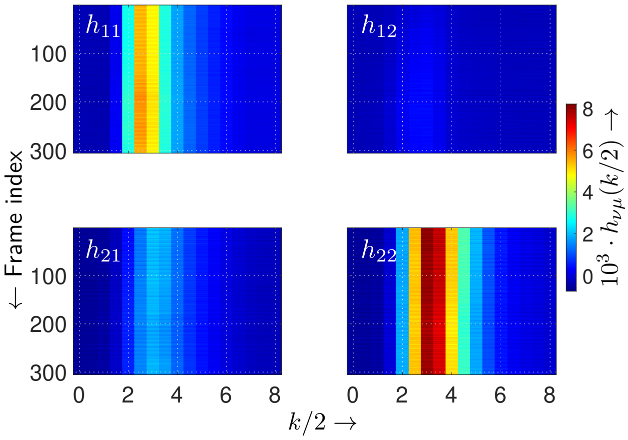

Figure 5.24: Estimated (2×2) MIMO impulse responses for multiple transmission frames employing a 2-segment detector ($f_\mathrm{T} = 2.5$ GHz, 500 m MMF channel, frame length: 4096 symbols, T/2-spaced sampling)

A repeated channel estimation for a shorter frame length of 4096 symbols is used to analyze the MIMO channel time-variance. At 2.5 GHz symbol rate each frame is separated by 1.6384 µs. The obtained results in Fig. 5.24 highlight that the channel remains constant over the analyzed 300 frames, i.e. a time-span of roughly 0.5 ms. Since the channel is just slowly changing over time, decision-aided adaptive signal processing approaches could better exploit the available channel capacity.

Finally, the estimated MIMO channel impulse response of the multi-segment detection setup is compared to the one of the purely coupler-based setup with a conventional detector. In order to focus on the demultiplexing and detection concepts, the channel influences are minimized by choosing the back-to-back channel. This also removes the different dispersive natures of the operating wavelengths out of the equation. Furthermore, the amplitudes of the estimated channel taps are normalized to the maximum tap for each individual impulse response giving $h^{\mathrm{n}}_{\nu\mu}(k/2)$ for this comparison. The comparison is shown in Fig. 5.25. Considering the conventional detection concept shows that 3 to 4 significant taps are present, whereas the multi-segment detector shows a much higher level of dispersion with its 4 to 5 main taps and long tail of smaller amplitude taps. This confirms the bandwidth limitations of the multi-segment detection setup.

All in all, the multi-segment detection concept, which combines the demultiplexing and detection process in a single low-cost device, has proven to be a good alternative to conventional concepts. It needs to be mentioned that modal noise needs to be taken into account with this concept since the electric field is split between different detection areas. However, a radial-symmetric design as used with the implemented detectors reduces model noise, compare Section 2.1.2. In the measured receive signals, no significant modal noise could be observed. If the bandwidth limitations of multi-segment detectors can be

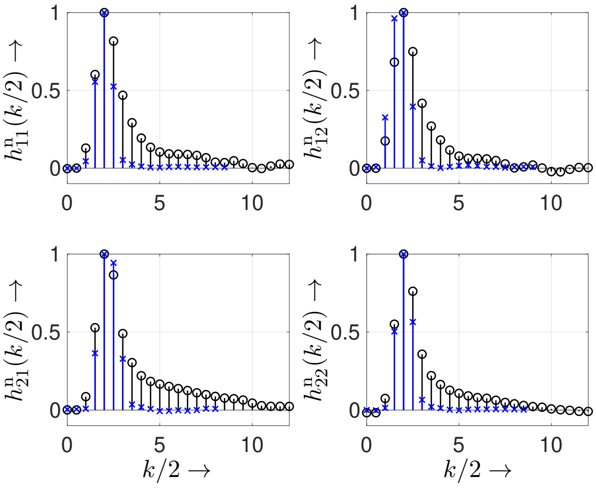

Figure 5.25: Normalized estimated channel impulse responses comparing the coupler setup with conventional detection (blue markers) and the multi-segment detection setup (black markers) at $f_{\mathrm{T}} = 2.5$ GHz using the back-to-back channel

overcome in the future, it will be the preferred low-cost detection method for incoherent MIMO applications.

5.3 Few-Mode Setup with Photonic Lanterns

Photonic lanterns (PLs) are devices that transfer the signals carried in the incident LP_{01} modes of the SMFs to specific modes of the outgoing few-mode fibers and vice versa to realize mode-multiplexing and -demultiplexing, respectively. The corresponding transmission model of a MIMO system based on PLs is visualized in Fig. 5.26. Ideally, each SMF input should excite just one mode in the FMF. In order to achieve this, the phases of the incident electrical fields in the SMFs need to have a specific phase relation to each other, so that their superposition at the end of the taper matches the amplitude and phase relation of the mode to be excited in the FMF. In practice, it is difficult to control the exact phase relations, and also effects like laser phase noise need to be taken into account. In general, two methods to construct PLs can be differentiated:

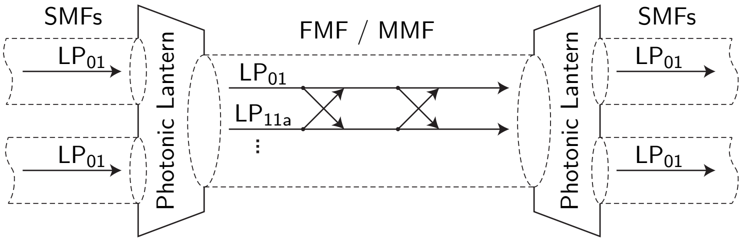

Figure 5.26: Multi-mode MIMO transmission model using photonic lanterns for mode combining and splitting

All-fiber Photonic Lantern With this method, a bundle of SMF ends with core and cladding is put into a capillary with a low refractive index. This capillary is then adiabatically tapered to the desired diameter of the output few-mode fiber. The capillary is the resulting cladding of the FMF, and the SMFs' claddings merge into the new FMF core [Leon14].

Photonic Integrated Circuits type Photonic Lantern This implementation is based on a photonic integrated circuit (PIC) to realize the SMF to FMF transfer. Here, the structure to transfer multiple SMF inputs to an FMF output is inscribed in a glass substrate [Thom11].

In our testbed one PL of each type is available with 6 SMF inputs and a 6-mode graded-index fiber output. In addition, a 6-mode graded-index fiber of 1 km length is used as a channel. Firstly, the insertion losses of the PLs for the MUX process are evaluated, and their results are shown in Tab. 5.7. Since an ideal adiabatic taper can be assumed

Table 5.7: Insertion loss measurements when launching from different SMF inputs through the all-fiber and PIC type 6-port PLs compared to a 2-port fusion coupler-based setup

SMF input port	1	2	3	4	5	6
All-fiber PL insertion loss [dB]	6.7	6.7	4.2	4.1	7.0	4.1
PIC type PL insertion loss [dB]	1.7	2.2	1.5	2.2	2.0	1.7
Fusion coupler insertion loss [dB]	0.1	8.1	–	–	–	–

as lossless it was expected that the all-fiber PL has a lower insertion loss than the PIC type PL. However, the measured results show an opposite loss characteristic. The high loss of the all-fiber PL is caused by splicing the tapered end of the PL, which is essentially a step-index fiber, to the graded-index 6-mode fiber. Here, the mode field diameters at the taper end are different for each mode, and they do not exactly match the mode field diameter of the 6-mode fiber [Phot14]. Also, it is worth noting that for the minimization of the mode dependent losses in a PL setup the number of input and output SMFs should be the same as the number of guided modes in the few-mode fiber. However, this means that strong mode coupling would occur in the FMF, which leads to significant interference in an IM/DD system as it is shown in Section 3.4.2. The insertion loss differences of the PL-based setups are relatively small when comparing to the differences of an optical MIMO system based on offset SMF to MMF splices and fusion couplers as shown in the same table [Sand16a]. Extending a fusion coupler-based system to 6 ports requires the concatenation of multiple 2-port systems, which is accompanied by a significant insertion loss increase. Thus, for its 6 ports, the PL can be considered as a low loss multiplexing and demultiplexing device.

Considering the modal behavior, the desired conception of a PL is that it transfers the signals from each SMF to a discrete mode in the FMF, see Fig. 5.27. However, the specific phase relations of the input signals required to achieve this are difficult to realize. As confirmed by the measured intensity patterns in Fig. 5.28, a real PL excites a combination of modes, which are superimposed in the FMF. The measured patterns (a) and (e) show that the shape of an LP_{11} mode is majorly involved, in pattern (b) the LP_{02} is included, and pattern (c) shows the LP_{01} mode. In addition to the mode cross-talk introduced by

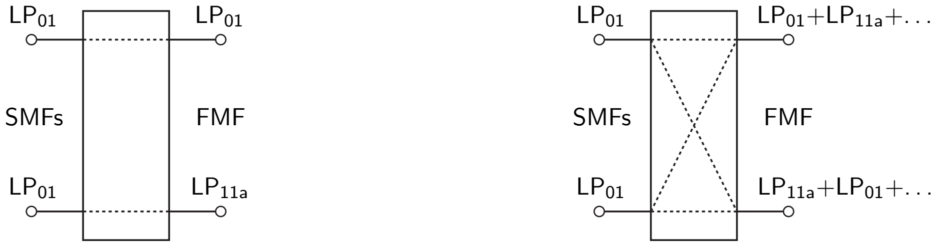

(a) Desired characteristic **(b)** Real characteristic

Figure 5.27: Spatial mode transformation of photonic lanterns

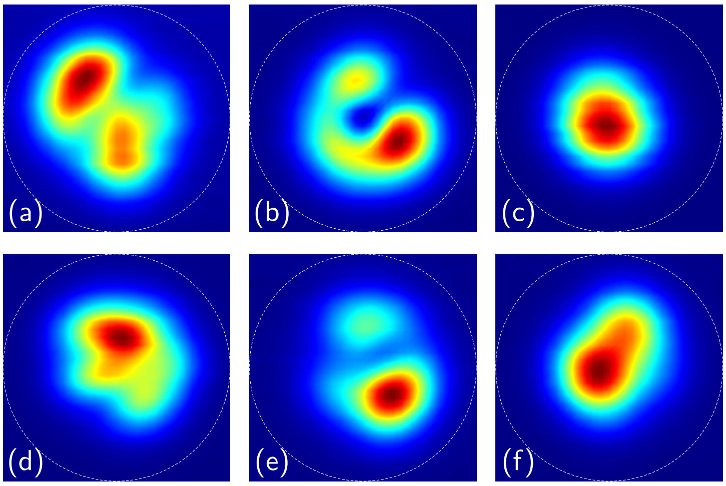

Figure 5.28: Measured spatial intensity patterns at the few-mode fiber output of the all-fiber PL launching at different SMF input ports; the dotted line represents the 30 µm FMF core diameter ($\lambda = 1550$ nm, Fabry-Pérot laser)

the PLs in the MUX and DEMUX process, mode mixing during the transmission through the FMF occurs.

The high level of mode cross-talk that is presented in the measured spatial intensity patterns is confirmed in a (2×2) testbed setup through a 6-mode fiber of 1 km length, compare Fig. 3.24 in Section 3.4.3. The high interference is independent of the port choice. Thus, the MIMO receive signals exhibit a low SINR such that a reliable transmission with an uncoded BER $< 10^{-3}$ is not viable in an IM/DD setup.

In addition, a (3×3) MIMO setup with a 1 km 6-mode fiber channel and a DFB laser source is constructed for validation purposes as shown in Fig. 5.29. The analyzed symbol rate is 2.5 GHz, and the frame length is 1024 symbols per MIMO input. In the testbed configuration the first MIMO input is delayed by two transmission frames, i.e. $2\Delta\tau = 819.2$ ns, and the second input is delayed by one transmission frame, i.e. $\Delta\tau = 409.6$ ns, guaranteeing independent MIMO input signals. Since the PLs have 6 inputs or outputs, respectively, different port configurations have been tested. None of the configurations allows for an almost error-free transmission. The measured receive signals are depicted in Fig. 5.30. They show that without averaging, the high level envelope is subject to significant interference similar to the (2×2) configuration results shown in Fig. 3.24. In the ensemble averaged data the interference term is eliminated. Thus, if the black curve (without averaging) is

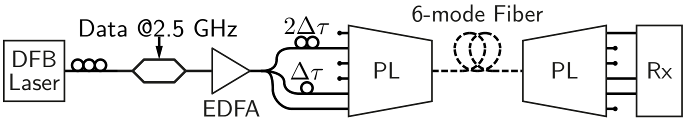

Figure 5.29: (3×3) photonic lantern testbed configuration (solid line: SMF, dashed line: 6-mode fiber)

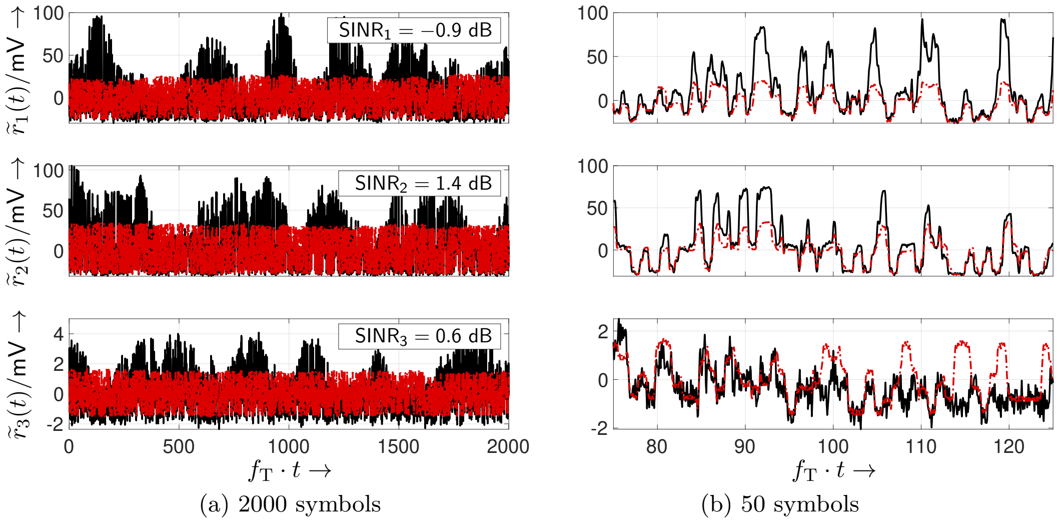

(a) 2000 symbols (b) 50 symbols

Figure 5.30: Measured MIMO receive signals of the (3×3) PL setup using a DFB laser and transmitting at $f_\text{T} = 2.5$ GHz (red dashed lines: ensemble average, black solid lines: without ensemble averaging)

above the red curve (with ensemble averaging), mainly constructive interference occurs. In the opposite case mainly destructive interference is present. It is also visible that the interference changes quickly within one frame. The high interference is reflected in the low SINR values. Since an EDFA is used in the setup, electronic noise is not the limiting factor. A least-squares estimator with T/2-spaced sampling is applied to obtain the channel impulse response. It is repeatedly measured for multiple transmission frames, and the result is given in Fig. 5.31. The estimation is based on the assumption that the overall

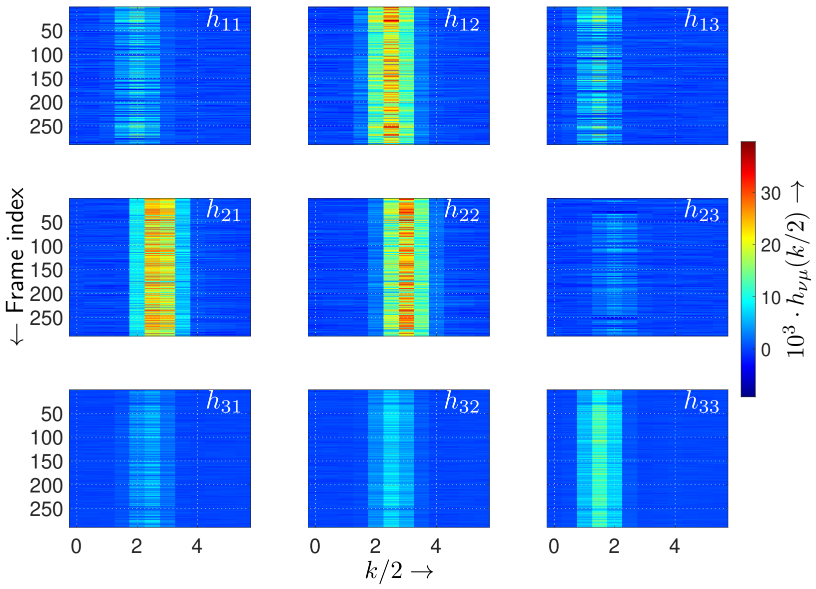

Figure 5.31: Estimated (3×3) MIMO impulse responses for multiple transmission frames with the photonic lantern setup ($f_\text{T} = 2.5$ GHz, 1 km 6-mode fiber channel, frame length: 1024 symbols, T/2-spaced sampling)

system is linear. This is not the case due to the significant interferences. The rapid changes of the significant tap amplitudes reflect the changes in interference from one frame to the next one. With ensemble averaging the overall transmission is error-free. Without averaging the high interference level results in BERs above 10%.

All in all, the analyzed (2×2) and (3×3) PL configurations are impaired by significant mode cross-talk due to their low mode orthogonality. This results in severe interference affecting the system. In this state the photonic lantern configuration is not viable for MIMO with IM/DD. An approach to optimize the mode-selectivity of PLs exists by using dissimilar fiber core geometries in the capillary, which leads to an elliptical core fiber at the end of the taper [Sai17]. A reported MIMO transmission experiment suggests that the BER performance with mode-selective PLs is still limited by remaining cross-talk between the mode groups in the MUX and DEMUX process [Liu17].

5.4 Hardware Component Discussion for MIMO Systems with IM/DD

In order to realize MIMO, different concepts involving various hardware components exist. This section summarizes the pros and cons of these components for their use in low-cost MIMO with IM/DD. In addition to the components used throughout the thesis, other hardware devices that are often related to MIMO are included in this overview.

SMF to MMF splice with radial offset This component is able to transform the LP_{01} mode of an SMF to different modes in an MMF or FMF in dependency on the radial alignment. It is very low-cost, has a low insertion loss and is a passive device. However, the excitation of an individual mode is not possible with this approach. Furthermore, using different radial alignments, e.g. centric and 20 µm offset, still leads to a significant overlap of the excited modes. This results in interference when these modes are combined and limits this mode excitation approach to low-order MIMO systems. For the realization of higher-order MIMO systems (e.g. 3×3) with this concept, the mode orthogonality needs to be improved. In addition to the parallel alignment with radial offset, the use of different angles between the SMF and MMF adds a degree of freedom for optimizing the mode orthogonality.

MMF Coupler Couplers exist in different variants, e.g. fusion, polished and mirror couplers, and they can be utilized for mode multiplexing as well as demultiplexing. Their properties can be highly adjusted in the manufacturing process, and they have the benefit of being mostly low-cost passive components. The insertion loss of couplers highly depends on the transfer path and the set of incident modes. A disadvantage is that significant coupling between modes of different groups is introduced by the coupler, compare Section 4.1. The ideal behavior would be that an incident mode is coupled to exactly just one desired output mode in all transfer paths. In order to implement couplers for demultiplexing, they need to have a high mode-selectivity. For instance: incident low-order modes are only transferred to the first output port and high-order modes mainly to the second output port. Therefore, off-the-shelf asymmetric fusion couplers are a possible solution, but custom manufactured fusion couplers with a medium degree of fusion are the preferred solution, see Section 4.1. It needs to be considered that for higher-order MIMO systems, couplers need to be concatenated, which adds significant attenuation and mode coupling.

Multi-Segment Detector Such a detector is a low-cost component that integrates mode DEMUX and optical-electrical conversion in a single step. Its drawback is the low electrical bandwidth due to the large area detector segments. Furthermore, modal noise needs to be considered when a narrow-linewidth laser is used. If the bandwidth limitation can be overcome in the future, segmented photo detection is a promising candidate for geometrically demultiplexing modes in IM/DD systems.

Photonic Lantern This device enables the mode transformation and multiplexing or demultiplexing process in a single step. It transfers the fundamental mode from the incident SMFs to specific sets of modes in an FMF and vice versa. This concept is also suited for coherent detection mechanisms since the MIMO output ports are SMFs that only carry the LP_{01} mode. Photonic lanterns are passive components, and they benefit from their low insertion loss specifically for high-order MIMO systems. The drawback is that individual modes cannot be easily excited and the manufacturing process is relatively complex. The testbed results confirmed the low mode-selectivity. This leads to significant interference and makes this MIMO concept unfeasible for IM/DD systems in this state. A photonic lantern configuration with a high mode-selectivity, where each SMF input excites a dedicated mode group and vice versa, could be a potential candidate for IM/DD systems [Sai17; Liu17].

Mode Filter One application of mode filters is the extraction of a desired set of modes after a demultiplexer that is non mode-selective (e.g. a 50:50 coupler with a high degree of fusion). However, such filters are accompanied by a loss of information, which is not desirable. Therefore, it is favorable to use mode-selective demultiplexers instead. Mode filters can be realized by spatial filtering. In the simplest case this can be an MMF to SMF transition with specific alignments. Another concept is the use of a partially coated fiber end-face with a thin layer of reflective material (e.g. gold). With spatial filters, modal noise needs to be considered, specifically when narrow line-width lasers are deployed. A way to reduce the influence of modal noise is to use a radial symmetric filter design. Besides spatial filtering, fiber bending is an option to remove high-order modes from a fiber. Therefore, the fiber can be simply coiled around a cylindrical object with a small diameter.

Phase Plate This glass-based device enables the transformation of modes by spatially controlling the phase to match the desired pattern of the mode to be excited [Thor94]. Its major advantage is the ability to excite individual modes. However, it is costly, bulky and mechanically susceptible since it requires a free-spaced setup with beam splitters, collimator lenses and so forth. Therefore, this concept is not an option for low-cost IM/DD systems.

Spatial Light Modulator (SLM) The concept of SLMs is similar to the one of phase plates with the difference, that they allow to programmatically adjust the spatial phase pattern with a liquid crystal on silicon [Fran12]. This reconfigurability and the ability to excite individual modes are the pros. The cons are the same as for phase plates, and therefore this device type is not feasible for low-cost IM/DD applications. It is also worth noting that SLMs are sensitive to polarization.

Multi-plane Light Conversion (MPLC) In principle, MPLC manipulates the spatial phase of multiple SMF inputs at the same time with reflective phase plates [Mori10]. The setup is arranged as a multi-pass cavity where the light's phase is manipulated multiple times by the phase plate to achieve the desired modal phase pattern. The advantage over the above described phase plate and SLM components is that it does not require beam splitters, and hence benefits from a lower insertion loss. Thus, MPLC combines a high mode-selectivity with a low insertion loss. Record-breaking spectral efficiencies of 202 bit/s/Hz realizing a 45 modes dual polarization transmission through a single MMF core (i.e. 90×90 MIMO configuration) have been achieved in [Ryf18] with MPLC multiplexers. However, its costly free-space setup yet prevents a widespread implementation in IM/DD setups.

6 Closing Remarks

In this work concepts for low-cost and short reach optical SDM systems have been investigated to further increase the channel capacity of multi-mode waveguides. In such systems, different fiber modes are used to generate spatial diversity, and the MIMO technique, which is well-known from wireless communications, is adapted to fiber-optic transmission.

In order to understand the transmission characteristics of an optical MIMO system with IM/DD, a corresponding model has been developed. Inherently, the detection process can be represented by a square-law process. With the model, it has been shown that in low mode-cross talk scenarios, the equivalent baseband system can be considered as linear. This implies that linear signal processing strategies can be applied. On the other hand, if high mode cross-talk is present, significant interference prevents a reliable transmission. Consequently, the conceptual design of such a system needs to focus on the minimization of mode cross-talk. In this respect, different hardware concepts for mode-selective excitation, mode MUX and DEMUX have been studied. It has been shown that a system based on SMF to MMF launches with different eccentric alignments is limited to a (2×2) configuration when considering an OM4-grade MMF with 50 µm core diameter. In a corresponding (3×3) configuration the low mode orthogonality leads to significant interference. It has further been shown that a concept based on photonic lanterns for mode MUX and DEMUX as well as an FMF channel is impaired by significant interference as well. With the analyzed photonic lanterns, individual modes cannot be excited such that parts of the data streams are multiplexed to the same modes. Thus, these photonic lanterns are not suited for MIMO with IM/DD. Multi-segment photo detectors have shown to be a promising approach by combining the DEMUX and optical to electrical conversion process in a single low-cost device. They could be further improved, if their bandwidth limitations can be overcome, and the detector material is changed to support the 1550 nm wavelength window.

A time variance analysis has determined that a MIMO system with IM/DD can be considered as time-invariant in a time-frame of at least three seconds, when assuming that the data streams are transmitted on separate mode groups. This applies even under considerable vibration stress. Furthermore, a method which is able to calculate the power coupling coefficients between mode groups for any device under test has been presented. It is based on multiple impulse response measurements, and in contrast to existing methods, it does not require the excitation of individual modes. Therefore, it can be realized with inexpensive hardware. The power coupling coefficients for different multi-mode coupler types have been determined. It has been evaluated that customized fusion couplers are well-suited for mode separation at the DEMUX. These customized fusion couplers are manufactured to exhibit the best compromise between a low loss, like symmetric fusion couplers, and a high mode separability, like asymmetric fusion couplers. This has been achieved by choosing a degree of fusion, which is in-between these two types. Off-the-shelf symmetric fusion couplers are not suited for mode separation. Furthermore, it has been confirmed that coupling between distant mode groups in an OM4-grade fiber of 1 km length does not occur. A small portion can be coupled into the neighboring groups. Therefore, mode groups can be practically exploited as separate and non-interfering transmission channels, i.e. termed mode group division multiplexing. In theory, the 10 propagating mode gorups in an OM4-grade fiber at 1550 nm could enable a (10×10) configuration. However, higher order groups contain a higher number of individual modes and since strong mode-mixing within a group occurs, the receiver needs to extract all modes of a group individually. Consequently, this process increases in cost for higher order groups.

In order to further improve optical MIMO with IM/DD, devices for mode multiplexing and demultiplexing need to be developed that exhibit a high mode orthogonality on one hand and are low-cost on the other hand. Once such devices are available, the use of mode groups as separate transmission channels, as it has been shown with multi-plane light conversion experiments by other research groups, seems to be the most promising approach. The benefit is that cross-talk between mode groups is minimal and therefore no MIMO signal processing is required, which further reduces cost. With this strategy, each mode group can be viewed as an individual SISO transmission channel, and conventional MMFs can still be used.

Appendices

A Derivations

In this part of the Appendix, mathematical derivations are made, which are too long to include in the main chapters of this thesis.

A.1 MMSE-DFE Backward Filter Coefficients Optimization

In order to find the optimal backward filter coefficients, the trace of the error auto-correlation matrix needs to be minimized as follows

$$\min_{\boldsymbol{B}_{\mathrm{M}},\kappa} \operatorname{tr}(\boldsymbol{R}_{ee}) \ . \tag{A.1}$$

It is assumed that only previous decisions are used for the feedback, i.e. $\boldsymbol{B}_0 = \boldsymbol{I}_{n_{\mathrm{T}}}$. For the minimization the backward filter matrix is partitioned as follows

$$\boldsymbol{B}_{\mathrm{M}} = \begin{pmatrix} \underbrace{\boldsymbol{0}_{n_{\mathrm{T}} \times n_{\mathrm{T}}\,\kappa} \quad \boldsymbol{I}_{n_{\mathrm{T}}}}_{\boldsymbol{X}^{\mathsf{H}}} & \underbrace{\boldsymbol{B}_1 \quad \dots \quad \boldsymbol{B}_{L_{\mathrm{b}}-1}}_{\boldsymbol{Y}} \end{pmatrix} \ , \tag{A.2}$$

where $\boldsymbol{X}^{\mathsf{H}}$ of size $n_{\mathrm{T}} \times n_{\mathrm{T}}\,(\kappa+1)$ describes the delay κ as well as the zeroth backward filter matrix and matrix $\boldsymbol{Y}$ of size $n_{\mathrm{T}} \times n_{\mathrm{T}}\,(L_{\mathrm{b}}-1)$ includes the backward filter coefficients that need to be optimized. Accordingly, matrix $\boldsymbol{R}$ is also partitioned into submatrices as follows

$$\boldsymbol{R} = \begin{pmatrix} \boldsymbol{R}_{11} & \boldsymbol{R}_{12} \\ \boldsymbol{R}_{21} & \boldsymbol{R}_{22} \end{pmatrix} \ , \tag{A.3}$$

with $\boldsymbol{R}_{11}$ being of size $n_{\mathrm{T}}\,(\kappa+1) \times n_{\mathrm{T}}\,(\kappa+1)$ and matrix $\boldsymbol{R}_{12}$ being of size $n_{\mathrm{T}}\,(\kappa+1) \times n_{\mathrm{T}}\,(L_{\mathrm{b}}-1)$. With the partitioning of $\boldsymbol{R}$ and $\boldsymbol{B}_{\mathrm{M}}$, the error auto-correlation matrix is rewritten as follows

$$\boldsymbol{R}_{ee} = \begin{pmatrix} \boldsymbol{X}^{\mathsf{H}} & \boldsymbol{Y} \end{pmatrix} \begin{pmatrix} \boldsymbol{R}_{11} & \boldsymbol{R}_{12} \\ \boldsymbol{R}_{21} & \boldsymbol{R}_{22} \end{pmatrix}^{-1} \begin{pmatrix} \boldsymbol{X} \\ \boldsymbol{Y}^{\mathsf{H}} \end{pmatrix} \ . \tag{A.4}$$

With using block matrix inversion [Pete12, p. 46] and after some manipulations we get

$$\begin{aligned} \boldsymbol{R}_{ee} &= \boldsymbol{X}^{\mathsf{H}} \boldsymbol{R}_{11}^{-1} \boldsymbol{X} + \boldsymbol{X}^{\mathsf{H}} \boldsymbol{R}_{11}^{-1} \boldsymbol{R}_{12} \boldsymbol{S} \boldsymbol{R}_{21} \boldsymbol{R}_{11}^{-1} \boldsymbol{X} - \boldsymbol{Y} \boldsymbol{S} \boldsymbol{R}_{21} \boldsymbol{R}_{11}^{-1} \boldsymbol{X} \dots \\ &\dots - \boldsymbol{X}^{\mathsf{H}} \boldsymbol{R}_{11}^{-1} \boldsymbol{R}_{12} \boldsymbol{S} \boldsymbol{Y}^{\mathsf{H}} + \boldsymbol{Y} \boldsymbol{S} \boldsymbol{Y}^{\mathsf{H}} \ , \end{aligned} \tag{A.5}$$

with

$$\boldsymbol{S} = \left(\boldsymbol{R}_{22} - \boldsymbol{R}_{21} \boldsymbol{R}_{11}^{-1} \boldsymbol{R}_{12} \right)^{-1} \ . \tag{A.6}$$

Rewriting all terms that are not dependent on $\boldsymbol{Y}$ with $\boldsymbol{P}, \boldsymbol{M}$ and $\boldsymbol{N}$ leads to

$$\boldsymbol{R}_{ee} = \boldsymbol{P} - \boldsymbol{Y} \boldsymbol{M} - \boldsymbol{N} \boldsymbol{Y}^{\mathsf{H}} + \boldsymbol{Y} \boldsymbol{S} \boldsymbol{Y}^{\mathsf{H}} \ . \tag{A.7}$$

In order to minimize the MSE, the partial derivative of the error auto-correlation matrix trace with respect to the matrix $\boldsymbol{Y}^{\mathsf{H}}$ is calculated as follows

$$\frac{\partial \operatorname{tr}(\boldsymbol{R}_{ee})}{\partial \boldsymbol{Y}^{\mathsf{H}}} = \underbrace{\frac{\partial \operatorname{tr}(\boldsymbol{P})}{\partial \boldsymbol{Y}^{\mathsf{H}}} - \frac{\partial \operatorname{tr}(\boldsymbol{Y} \boldsymbol{M})}{\partial \boldsymbol{Y}^{\mathsf{H}}}}_{\boldsymbol{0}} - \frac{\partial \operatorname{tr}\left(\boldsymbol{N} \boldsymbol{Y}^{\mathsf{H}}\right)}{\partial \boldsymbol{Y}^{\mathsf{H}}} + \frac{\partial \operatorname{tr}\left(\boldsymbol{Y} \boldsymbol{S} \boldsymbol{Y}^{\mathsf{H}}\right)}{\partial \boldsymbol{Y}^{\mathsf{H}}} \ . \tag{A.8}$$

Please note that $\operatorname{tr}(\boldsymbol{A} + \boldsymbol{B}) = \operatorname{tr}(\boldsymbol{A}) + \operatorname{tr}(\boldsymbol{B})$, if $\boldsymbol{A}$ and $\boldsymbol{B}$ are square. Consequently, the result is set to the zero matrix and calculates to [Pete12]

$$\frac{\partial \operatorname{tr}(\boldsymbol{R}_{ee})}{\partial \boldsymbol{Y}^{\mathsf{H}}} = -\boldsymbol{N} + \boldsymbol{Y}_{\text{opt}} \boldsymbol{S} = \boldsymbol{0} \ . \tag{A.9}$$

Back-substituting $\boldsymbol{N}$ yields

$$\boldsymbol{Y}_{\text{opt}} \boldsymbol{S} = \boldsymbol{X}^{\mathsf{H}} \boldsymbol{R}_{11}^{-1} \boldsymbol{R}_{12} \boldsymbol{S} \qquad \Big/ \cdot \boldsymbol{S}^{-1} \ , \tag{A.10}$$

and therefore

$$\boldsymbol{Y}_{\text{opt}} = \boldsymbol{X}^{\mathsf{H}} \boldsymbol{R}_{11}^{-1} \boldsymbol{R}_{12} \ . \tag{A.11}$$

With this result, the optimal backward filter matrix is given by

$$\boldsymbol{B}_{\text{M,opt}} = \left(\boldsymbol{X}^{\mathsf{H}}, \quad \boldsymbol{Y}_{\text{opt}} \right) = \left(\boldsymbol{X}^{\mathsf{H}}, \quad \boldsymbol{X}^{\mathsf{H}} \boldsymbol{R}_{11}^{-1} \boldsymbol{R}_{12} \right) \tag{A.12}$$

and is simplified as follows, compare Equation 17 in [Al-D00]

$$\boldsymbol{B}_{\mathrm{M,opt}} = \boldsymbol{X}^{\mathsf{H}} \cdot \left(\boldsymbol{I}_{n_{\mathrm{T}}(\kappa+1)} \, , \quad \boldsymbol{R}_{11}^{-1} \, \boldsymbol{R}_{12} \right) \ . \tag{A.13}$$

The remaining error auto-correlation matrix is calculated by inserting $\boldsymbol{Y}_{\mathrm{opt}}$ in Eq. A.5 resulting in

$$\boldsymbol{R}_{ee,\mathrm{min}} = \boldsymbol{X}^{\mathsf{H}} \, \boldsymbol{R}_{11}^{-1} \, \boldsymbol{X} \ . \tag{A.14}$$

A.2 Equivalence of the Analytic and Real-valued Bandpass Signal

In this part, it is shown that the analytic signal expression

$$\underline{x}^{+}(t) = s(t) \exp(\mathrm{j}\omega_{\mathrm{c}} t) * \underline{g}_{\mathrm{o}}^{+}(t) \tag{A.15}$$

corresponds to the following real-valued bandpass representation

$$x(t) = s(t) \cos(\omega_{\mathrm{c}} t) * g_{\mathrm{o}}(t) \ . \tag{A.16}$$

The relation between an analytic and real-valued signal is defined by [Kamm04, p. 24]

$$\underline{x}^{+}(t) = x(t) + \mathrm{j}\mathcal{H}\{x(t)\} \ . \tag{A.17}$$

Thus, taking the real part of the analytic signal $\underline{x}^{+}(t)$ gives the real-valued bandpass signal $x(t)$ resulting in

$$\begin{aligned} x(t) =& \mathrm{Re}\Big\{ s(t) \exp(\mathrm{j}\omega_{\mathrm{c}} t) * \underline{g}_{\mathrm{o}}^{+}(t) \Big\} \\ =& \mathrm{Re}\Big\{ \Big[s(t)\cos(\omega_{\mathrm{c}} t) + \mathrm{j} s(t) \sin(\omega_{\mathrm{c}} t) \Big] * \Big[\mathrm{Re}\Big\{ \underline{g}_{\mathrm{o}}^{+}(t) \Big\} + \mathrm{j}\mathrm{Im}\Big\{ \underline{g}_{\mathrm{o}}^{+}(t) \Big\} \Big] \Big\} \\ =& \mathrm{Re}\Big\{ \Big[s(t)\cos(\omega_{\mathrm{c}} t) + \mathrm{j} s(t) \sin(\omega_{\mathrm{c}} t) \Big] * \Big[g_{\mathrm{o}}'(t) + \mathrm{j}\mathcal{H}\{ g_{\mathrm{o}}'(t) \} \Big] \Big\} \\ =& s(t)\cos(\omega_{\mathrm{c}} t) * g_{\mathrm{o}}'(t) - s(t)\sin(\omega_{\mathrm{c}} t) * \mathcal{H}\{ g_{\mathrm{o}}'(t) \} \ . \end{aligned} \tag{A.18}$$

Since the Hilbert transform is essentially a convolution with $1/(\pi t)$, and convolution is commutative as well as associative, we can write

$$x(t) = s(t)\cos(\omega_{\mathrm{c}} t) * g_{\mathrm{o}}'(t) - \mathcal{H}\{ s(t) \sin(\omega_{\mathrm{c}} t) \} * g_{\mathrm{o}}'(t) \ . \tag{A.19}$$

Using Bedrosian's theorem [King09, p. 184], the Hilbert transform only needs to be applied to the sinusoidal signal as follows

$$x(t) = s(t)\cos(\omega_{\mathrm{c}} t) * g_{\mathrm{o}}'(t) - s(t)\, \mathcal{H}\{ \sin(\omega_{\mathrm{c}} t) \} * g_{\mathrm{o}}'(t) \ . \tag{A.20}$$

With the relation $\mathcal{H}\{\sin(\omega_\mathrm{c}t)\} = -\cos(\omega_\mathrm{c}t)$, the real-valued bandpass signal is given by

$$x(t) = s(t)\cos(\omega_\mathrm{c}t) * \underbrace{2\,g_\mathrm{o}'(t)}_{g_\mathrm{o}(t)} \quad . \tag{A.21}$$

By assigning the factor two in this way, the following relation is obtained

$$g_\mathrm{o}(t) = 2\,g_\mathrm{o}'(t) = 2\,\mathrm{Re}\Big\{\underline{g}_\mathrm{o}^{+}(t)\Big\} \quad . \tag{A.22}$$

A.3 Inverse Fourier Transform of a Complex Exponential Function with Quadratic Argument

The factor of the analytic bandpass SMF transfer function with the quadratic phase component is given by

$$\underline{A}(\omega) = \exp\left(-\mathrm{j}L\frac{\beta_2}{2}\left(\omega - \omega_\mathrm{c}\right)^2\right) \quad . \tag{A.23}$$

Applying binomial expansion and separating the resulting parts, the transfer function is rewritten as follows

$$\underline{A}(\omega) = \exp\left(-\mathrm{j}L\frac{\beta_2}{2}\omega^2\right)\,\exp(\mathrm{j}L\beta_2\omega_\mathrm{c}\omega)\,\underbrace{\exp\left(-\mathrm{j}L\frac{\beta_2}{2}\omega_\mathrm{c}^2\right)}_{\underline{A}\,=\,\mathrm{const.}} \quad . \tag{A.24}$$

With this separation, the inverse Fourier transform is obtained as follows

$$\begin{array}{l} \underline{A}(\omega) = \underline{A}\,\exp\left(-\mathrm{j}L\frac{\beta_2}{2}\omega^2\right)\,\exp(\mathrm{j}L\beta_2\omega_\mathrm{c}\omega) \\ \begin{array}{c}\bullet\\ |\\ \circ\end{array} \\ \underline{a}(t) = \underline{A}\cdot\mathcal{F}^{-1}\left\{\exp\left(-\mathrm{j}L\frac{\beta_2}{2}\omega^2\right)\right\} * \mathcal{F}^{-1}\{\exp(\mathrm{j}L\beta_2\omega_\mathrm{c}\omega)\} \quad . \end{array} \tag{A.25}$$

The second term is a time shift and results in

$$\mathcal{F}^{-1}\{\exp(\mathrm{j}L\beta_2\omega_\mathrm{c}\omega)\} = \delta(t + L\beta_2\omega_\mathrm{c}) \quad . \tag{A.26}$$

In order to obtain the inverse Fourier transform of the first term, two cases need to be differentiated. Therefore, the following transformation pairs are utilized [Beve16]

$$\begin{array}{lcll} \exp\left(-\mathrm{j}kt^2\right) & \circ\!\!-\!\!\bullet & \sqrt{\frac{\pi}{k}}\,\exp\left(\mathrm{j}\left(\frac{\pi^2 f^2}{k} - \frac{\pi}{4}\right)\right) \;, & \text{if} \quad k > 0 \\ \exp\left(-\mathrm{j}kt^2\right) & \circ\!\!-\!\!\bullet & \sqrt{\frac{\pi}{|k|}}\,\exp\left(-\mathrm{j}\left(\frac{\pi^2 f^2}{|k|} - \frac{\pi}{4}\right)\right) \;, & \text{if} \quad k < 0 \;. \end{array} \tag{A.27}$$

The first pair is used for constellations, where $\beta_2 < 0$, e.g. a conventional fiber at 1550 nm operating wavelength. In contrast, the latter transformation pair applies, if $\beta_2 > 0$, e.g. a conventional fiber at 850 nm. After some equation expansions and further manipulations we get

$$\mathcal{F}^{-1}\left\{\exp\left(-\mathrm{j}L\frac{\beta_2}{2}\omega^2\right)\right\} = \begin{cases} \dfrac{1}{\sqrt{-2\pi L\beta_2}} \cdot \exp\left[\mathrm{j}\left(\dfrac{t^2}{2L\beta_2} + \dfrac{\pi}{4}\right)\right] \;, & \text{if} \quad \beta_2 < 0 \\ \dfrac{1}{\sqrt{2\pi L\beta_2}} \cdot \exp\left[-\mathrm{j}\left(\dfrac{t^2}{-2L\beta_2} + \dfrac{\pi}{4}\right)\right] \;, & \text{if} \quad \beta_2 > 0 \;. \end{cases} \tag{A.28}$$

Both expressions can be summarized using the absolute value function and the sign function $\mathrm{sgn}(\,\cdot\,)$ as follows

$$\mathcal{F}^{-1}\left\{\exp\left(-\mathrm{j}L\frac{\beta_2}{2}\omega^2\right)\right\} = \frac{1}{\sqrt{2\pi L|\beta_2|}} \cdot \exp\left[-\mathrm{j}\,\mathrm{sgn}(\beta_2)\left(\frac{\pi}{4} - \frac{t^2}{2L|\beta_2|}\right)\right] \quad \text{for } \beta_2 \in \mathbb{R} \;. \tag{A.29}$$

By inserting Eqs. A.26 and A.28 in Eq. A.25, one part of the analytic bandpass impulse response for the SMF channel is given by

$$\underline{a}(t) = \begin{cases} \dfrac{1}{\sqrt{-2\pi L\beta_2}} \cdot \exp\left(\mathrm{j}\left(\dfrac{t^2}{2L\beta_2} + \omega_\mathrm{c}t + \dfrac{\pi}{4}\right)\right) \;, & \text{if } \beta_2 < 0 \\ \dfrac{1}{\sqrt{2\pi L\beta_2}} \cdot \exp\left(-\mathrm{j}\left(-\dfrac{t^2}{2L\beta_2} - \omega_\mathrm{c}t + \dfrac{\pi}{4}\right)\right) \;, & \text{if } \beta_2 > 0 \;. \end{cases} \tag{A.30}$$

A unified expression of the analytic channel impulse response could be written as follows

$$\begin{aligned} &\underline{A}(\omega) = \exp\left(-\mathrm{j}L\frac{\beta_2}{2}\left(\omega - \omega_\mathrm{c}\right)^2\right) \\ &\begin{array}{c}\bullet\\ |\\ \circ\end{array} \\ &\underline{a}(t) = \frac{1}{\sqrt{2\pi L\,|\beta_2|}} \cdot \exp\left(\mathrm{j}\left[\mathrm{sgn}(\beta_2)\left(\frac{t^2}{2L\,|\beta_2|} - \frac{\pi}{4}\right) + \omega_\mathrm{c}t\right]\right) \qquad \forall\, \beta_2 \in \mathbb{R} \;. \end{aligned} \tag{A.31}$$

A.4 Inverse Fourier Transform of the Heaviside Step Function

In order to perform the inverse Fourier transform, let us redefine the Heaviside step function with the sign function as follows

$$1(\omega) = \frac{1}{2}\left(\mathrm{sgn}(\omega) + 1\right) \;. \tag{A.32}$$

The following Fourier transform pairs are used [Howe01, pp. 682–683]:

$$\begin{aligned} \frac{1}{t} \quad &\circ\!\!-\!\!\bullet \quad -\mathrm{j}\pi\,\mathrm{sgn}(\omega) \\ \delta(t) \quad &\circ\!\!-\!\!\bullet \quad 1 \end{aligned} \tag{A.33}$$

By rewriting the first pair as follows

$$\mathcal{F}^{-1}\{\mathrm{sgn}(\omega)\} = \frac{j}{\pi t} \tag{A.34}$$

and considering the linearity property, the inverse Fourier transform of the Heaviside step function is given by

$$\mathcal{F}^{-1}\{1(\omega)\} = \frac{1}{2}\left(\mathrm{j}\frac{1}{\pi t} + \delta(t)\right). \tag{A.35}$$

Please note that the convolution of a signal with $1/(\pi t)$ equals the Hilbert transform of that signal.

A.5 Hilbert Transform of a Sine Function with Quadratic Argument

In order to obtain the Hilbert transform of the chirp signal

$$x(t) = \sin\Big(At^2 + Bt + C\Big) \qquad \text{with } A < 0 \text{ and } B > 0 \ , \tag{A.36}$$

having a quadratic function in its argument, the relation between the signal and its analytic representation $\underline{x}^+(t)$ is used

$$\underline{x}^+(t) = x(t) + \mathrm{j}\mathcal{H}\{x(t)\} \ . \tag{A.37}$$

The analytic signal has by definition non-zero components only at positive frequencies. Firstly, let us consider the generalized form of a chirp signal as defined by

$$x(t) = \sin\left(\int \omega(\tau)\,\mathrm{d}\tau\right) \ , \tag{A.38}$$

where $\omega(t)$ is the virtual instantaneous frequency course given by

$$\omega(t) = \frac{\mathrm{d}}{\mathrm{d}t}(At^2 + Bt + C) = 2At + B \ , \tag{A.39}$$

being zero at

$$\omega(-B/(2A)) = 0 \ . \tag{A.40}$$

By the definition of an analytic signal, only positive frequencies are considered, and hence the absolute value function is employed. Thus, the following two cases need to be distinguished

$$|\omega(t)| = \begin{cases} 2At + B \ , & \text{if } t < -\frac{B}{2A} \\ -(2At+B) \ , & \text{if } t > -\frac{B}{2A} \ . \end{cases} \tag{A.41}$$

Please note that A is negative. This frequency course is illustrated in Fig. A.1 and highlights the use of only positive frequencies in the analytic signal. By rewriting Eq. A.37, the Hilbert transform is obtained as follows

$$\mathcal{H}\{x(t)\} = \frac{1}{\mathrm{j}} \Big(\underline{x}^{+}(t) - x(t) \Big) \ . \tag{A.42}$$

Inserting the exponential form of $x(t)$ we get

$$\mathcal{H}\{x(t)\} = \frac{1}{\mathrm{j}} \underline{x}^{+}(t) + \frac{1}{2} \exp\Big(\mathrm{j}(At^2 + Bt + C)\Big) - \frac{1}{2} \exp\Big(-\mathrm{j}(At^2 + Bt + C)\Big) \ . \tag{A.43}$$

The spectrum of the analytic signal has no Hermitian symmetry since it only consists of positive frequency parts. Therefore, $\underline{x}^{+}(t) \in \mathbb{C}$ so that it is defined as follows

$$\underline{x}^{+}(t) = |\underline{x}^{+}(t)| \exp\Big(\mathrm{j}\varphi(t)\Big) \ . \tag{A.44}$$

From Fig A.1, we can conclude that

$$\varphi(t) = \begin{cases} At^2 + Bt + C \ , & \text{if } t < -\frac{B}{2A} \\ -(At^2 + Bt + C) \ , & \text{if } t > -\frac{B}{2A} \ . \end{cases} \tag{A.45}$$

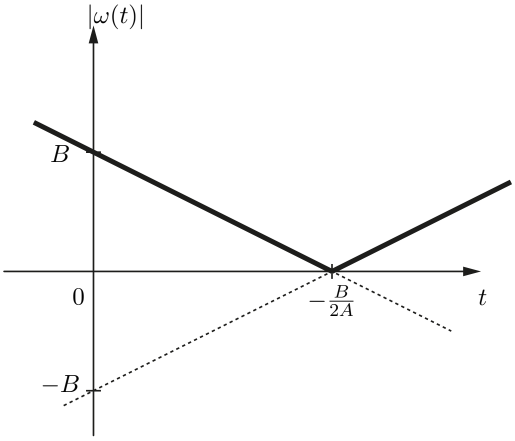

Figure A.1: Instantaneous angular frequency graph of the analytic signal

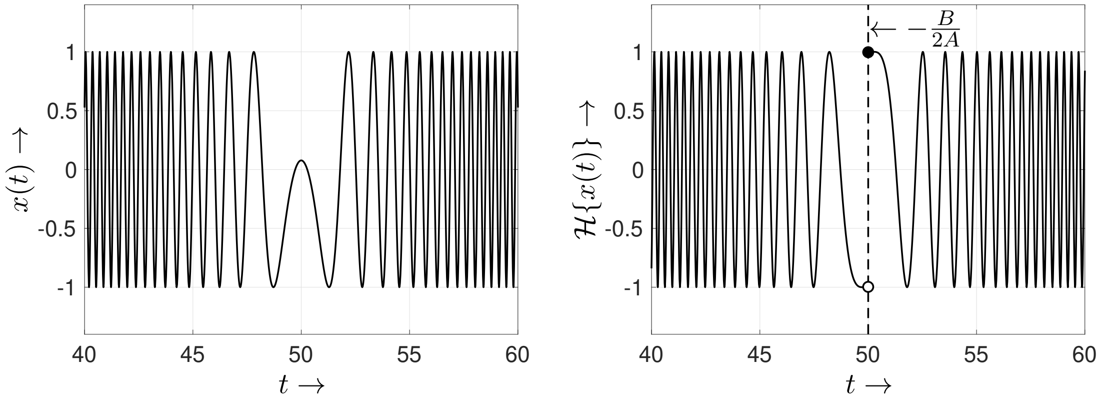

Figure A.2: Chirp signal and its Hilbert transform for $A = -1$, $B = 100$ and $C = \pi/4$

Considering that the amplitude of $x(t)$ is constant, $|\underline{x}^{+}(t)|$ needs to be constant as well. With this knowledge, the analytic signal is described as follows

$$\underline{x}^{+}(t) = \begin{cases} \underline{c}_1 \exp\Big(j\big(At^2 + Bt + C\big)\Big) \ , & \text{if } t < -\frac{B}{2A} \\ \underline{c}_2 \exp\Big(-j\big(At^2 + Bt + C\big)\Big) \ , & \text{if } t > -\frac{B}{2A} \ . \end{cases} \tag{A.46}$$

Considering the two cases and that the result of the Hilbert transform is real-valued, the constants yield $\underline{c}_1 = -j$ and $\underline{c}_2 = j$ and the Hilbert transform results in

$$\mathcal{H}\{x(t)\} = \begin{cases} -\cos\big(At^2 + Bt + C\big) \ , & \text{if} \quad t < -\frac{B}{2A} \\ +\cos\big(At^2 + Bt + C\big) \ , & \text{if} \quad t \geq -\frac{B}{2A} \ . \end{cases} \tag{A.47}$$

The graphs of the original function and its Hilbert transform are illustrated in Fig. A.2. Since the frequency course is not differentiable at $t = -B/(2A)$, the resulting Hilbert transform of $x(t)$ shows a discontinuity at this time instance.

In addition to the Hilbert transform of the chirped sine function, the same method can be applied to obtain the Hilbert transform of a chirped cosine function, resulting in

$$\mathcal{H}\Big\{\cos\Big(At^2 + Bt + C\Big)\Big\} = \begin{cases} +\sin\big(At^2 + Bt + C\big) \ , & \text{if} \quad t < -\frac{B}{2A} \\ -\sin\big(At^2 + Bt + C\big) \ , & \text{if} \quad t \geq -\frac{B}{2A} \ . \end{cases} \tag{A.48}$$

valid for $A < 0$ and $B > 0$. Applying the Hilbert transform twice yields

$$\mathcal{H}\Big\{\mathcal{H}\Big\{\sin\Big(At^2 + Bt + C\Big)\Big\}\Big\} = -\sin\Big(At^2 + Bt + C\Big) \tag{A.49}$$

for all cases, which shows that the inversion property of the Hilbert transform defined by $\mathcal{H}\{\mathcal{H}\{x(t)\}\} = -x(t)$ applies [King09, p. 148].

Acknowledgment I would like to thank the user “mateC” at `dsp.stackexchange.com` for his/her support related to this Hilbert transform problem [Mate18].

Bibliography

[Agil01] Agilent Technologies. *Accurate Characterization of Source Spectra Using an Optical Spectrum Analyzer - Application Note 1550-5*. 2001.

[Agra01] G. Agrawal. *Nonlinear Fiber Optics*. Optics and Photonics. Elsevier Science, 2001.
ISBN: 9780080479743.

[Agra02] G. P. Agrawal. *Fiber-Optic Communication Systems*. Third. John Wiley & Sons, Inc., 2002.
ISBN: 0-471-21571-6.

[Agra10] G. P. Agrawal. *Fiber-Optic Communication Systems*. Fourth. John Wiley & Sons, Inc., 2010.
ISBN: 978-0-470-50511-3.

[Ahre09a] A. Ahrens and C. Benavente-Peces. "Modulation-Mode and Power Assignment in SVD-assisted Broadband MIMO Systems". In: *International Conference on Wireless Information Networks and Systems (WINSYS)*. Milan (Italy), July 2009, pp. 83–88.
DOI: `10.5220/0002165700830088`.

[Ahre14] A. Ahrens, S. Schröder, and S. Lochmann. "Modal and Chromatic Dispersion Analysis Within a Measured 1,4 km MIMO Multimode Channel". In: *E-Business and Telecommunications: International Joint Conference, ICETE 2013, Reykjavik, Iceland, July 29-31, 2013, Revised Selected Papers*. Ed. by M. S. Obaidat and J. Filipe. Berlin, Heidelberg: Springer Berlin Heidelberg, 2014, pp. 183–196.
ISBN: 978-3-662-44788-8.
DOI: `10.1007/978-3-662-44788-8_11`.

[Al-D00] N. Al-Dhahir and A. H. Sayed. "The finite-length multi-input multi-output MMSE-DFE". In: *IEEE Transactions on Signal Processing* 48.10 (Oct. 2000), pp. 2921–2936. ISSN: 1053-587X.
DOI: `10.1109/78.869048`.

[Bala00] J. Balakrishnan, H. Viswanathan, and C. Johnson. "Decision Device Optimization for Soft Decision Feedback Equalization". In: 2000.

[Bart15a] P. Bartmann, A. Ahrens, and S. Lochmann. "Iterative time domain simulation of optical MIMO channels". In: *Advances in Wireless and Optical Communications (RTUWO), 2015*. Nov. 2015, pp. 38–41.
DOI: `10.1109/RTUWO.2015.7365715`.

[Bell63] P. Bello. "Characterization of Randomly Time-Variant Linear Channels". In: *IEEE Transactions on Communications Systems* 11.4 (Dec. 1963), pp. 360–393.
ISSN: 0096-1965.
DOI: `10.1109/TCOM.1963.1088793`.

[Beny17] K. Benyahya et al. “5Tb/s transmission over 2.2 km of multimode OM2 fiber with direct detection thanks to wavelength and mode group multiplexing”. In: *Optical Fiber Communication Conference*. Optical Society of America, 2017. DOI: 10.1364/OFC.2017.M2D.2.

[Beny18] K. Benyahya et al. “High-Speed Bi-Directional Transmission Over Multimode Fiber Link in IM/DD Systems”. In: *Journal of Lightwave Technology* 36.18 (Sept. 2018), pp. 4174–4180. ISSN: 0733-8724. DOI: 10.1109/JLT.2018.2858151.

[Beny18a] K. Benyahya et al. “200Gb/s Transmission Over 20km of FMF Fiber Using Mode Group Multiplexing and Direct Detection”. In: *2018 European Conference on Optical Communication (ECOC)*. 2018, pp. 1–3.

[Berd82] S. Berdagué and P. Facq. “Mode division multiplexing in optical fibers”. In: *Applied Optics* 21.11 (June 1982), pp. 1950–1955. DOI: 10.1364/AO.21.001950.

[Beve16] P. J. Bevelacqua. *The Fourier Transform*. http://www.thefouriertransform.com/pairs/complexGaussian.php. Accessed: 2016-12-08. 2016.

[Bikh09] N. W. Bikhazi, M. A. Jensen, and A. L. Anderson. “MIMO signaling over the MMF optical broadcast channel with square-law detection”. In: *IEEE Transactions on Communications* 57.3 (Mar. 2009), pp. 614–617. ISSN: 1558-0857. DOI: 10.1109/TCOMM.2009.03.070029.

[Bole13] A. Boletti et al. “Robustness to mechanical perturbations of center-launching technique for transparent board-to-board and data server interconnects”. In: *Optics Express* 21.10 (May 2013), pp. 12410–12418. DOI: 10.1364/OE.21.012410.

[Bron05] I. N. Bronstein et al. *Taschenbuch der Mathematik*. Vol. 6. Verlag Harri Deutsch, 2005. ISBN: 3-8171-2006-0.

[Carp12] J. Carpenter and T. D. Wilkinson. “Characterization of Multimode Fiber by Selective Mode Excitation”. In: *Journal of Lightwave Technology* 30.10 (May 2012), pp. 1386–1392. ISSN: 0733-8724. DOI: 10.1109/JLT.2012.2189756.

[Carp13] J. Carpenter, B. J. Eggleton, and J. Schröder. “110x110 optical mode transfer matrix inversion”. In: *39th European Conference and Exhibition on Optical Communication (ECOC)*. Sept. 2013, pp. 1–3. DOI: 10.1049/cp.2013.1506.

[Carp16] J. Carpenter, B. J. Eggleton, and J. Schröder. “Complete spatiotemporal characterization and optical transfer matrix inversion of a 420 mode fiber”. In: *Optics Letters* 41.23 (Dec. 2016), pp. 5580–5583. DOI: 10.1364/OL.41.005580.

[Chen12] J. Cheng et al. “Time-domain multimode dispersion measurement in a higher-order-mode fiber”. In: *Optics Letters* 37.3 (Feb. 2012), pp. 347–349. DOI: 10.1364/OL.37.000347.

[Chen16a] H. Chen, N. K. Fontaine, and R. Ryf. “Transfer matrix characterization of 10-mode mode-selective spatial multiplexers”. In: *IEEE Photonics Society Summer Topical Meeting Series (SUM)*. July 2016, pp. 51–52. DOI: `10.1109/PHOSST.2016.7548733`.

[Cisc20] Cisco. *Cisco Annual Internet Report (2018–2023) — White paper*. Online. Accessed: 2021-08-09. 2020. URL: `https://www.cisco.com/c/en/us/solutions/collateral/executive-perspectives/annual-internet-report/white-paper-c11-741490.html`.

[Coom14] W. Coomans et al. “XG-FAST: Towards 10 Gb/s copper access”. In: *IEEE Globecom Workshops (GC Wkshps)*. 2014, pp. 630–635. DOI: `10.1109/GLOCOMW.2014.7063503`.

[Davi09] M. Davies et al. “Polynomial Matrix QR Decomposition and Iterative Decoding of Frequency Selective MIMO Channels”. In: *IEEE Wireless Communications and Networking Conference*. 2009, pp. 1–6. DOI: `10.1109/WCNC.2009.4917911`.

[Elli16] A. D. Ellis et al. “Communication networks beyond the capacity crunch”. In: *Philosophical Transactions of the Royal Society A: Mathematical, Physical and Engineering Sciences* 374 (Mar. 2016). DOI: `10.1098/rsta.2015.0191`.

[Ette75] W. van Etten. “An Optimum Linear Receiver for Multiple Channel Digital Transmission Systems”. In: *IEEE Transactions on Communications* 23.8 (1975), pp. 828–834.

[Fisc15] R. F. H. Fischer and S. Hassanpour. “Equalization in Fiber-Optic Transmission Systems: Theoretical Limits and Lattice-Reduction-Aided Techniques”. In: *Proceedings of 16th ITG Symposium: Photonic Networks*. May 2015, pp. 1–8.

[Font15] N. K. Fontaine et al. “30x30 MIMO transmission over 15 spatial modes”. In: *Optical Fiber Communications Conference and Exhibition (OFC)*. Mar. 2015, pp. 1–3.

[Fost10] J. A. Foster et al. “An Algorithm for Calculating the QR and Singular Value Decompositions of Polynomial Matrices”. In: *IEEE Transactions on Signal Processing* 58.3 (Mar. 2010), pp. 1263–1274. ISSN: 1053-587X. DOI: `10.1109/TSP.2009.2034325`.

[Fran12] B. Franz and H. Bülow. “Experimental Evaluation of Principal Mode Groups as High-Speed Transmission Channels in Spatial Multiplex Systems”. In: *IEEE Photonics Technology Letters* 24.16 (Aug. 2012), pp. 1363–1365. ISSN: 1041-1135. DOI: `10.1109/LPT.2012.2202224`.

[G652] International Telecommunication Union. *Characteristics of a single-mode optical fibre and cable*. Recommendation ITU-T G.652 (11/2016). Nov. 2016.

[Gall84] P. Gallion and G. Debarge. “Quantum phase noise and field correlation in single frequency semiconductor laser systems”. In: *IEEE Journal of Quantum Electronics* 20.4 (Apr. 1984), pp. 343–349. ISSN: 1558-1713. DOI: `10.1109/JQE.1984.1072399`.

[Gans86] W. L. Gans. "Calibration and Error Analysis of a Picosecond Pulse Waveform Measurement System at NBS". In: *Proceedings of the IEEE* 74.1 (Jan. 1986), pp. 86–90. ISSN: 0018-9219.
DOI: `10.1109/PROC.1986.13408`.

[Gatt19] A. Gatto et al. "Discrete Multitone Modulation for Short-Reach Mode Division Multiplexing Transmission". In: *Journal of Lightwave Technology* 37.20 (2019), pp. 5185–5192.
DOI: `10.1109/JLT.2019.2929829`.

[Gold05] A. Goldsmith. *Wireless Communications.* New York, USA: Cambridge University Press, 2005.
ISBN: 0521837162.
DOI: `10.1017/CBO9780511841224`.

[Gree07] M. Greenberg, M. Nazarathy, and M. Orenstein. "Data Parallelization by Optical MIMO Transmission Over Multimode Fiber With Intermodal Coupling". In: *Journal of Lightwave Technology* 25.6 (June 2007), pp. 1503–1514. ISSN: 1558-2213.
DOI: `10.1109/JLT.2007.896812`.

[Grim89] E. Grimm and W. Nowak. *Lichtwellenleitertechnik.* Dr. Alfred Hüthig Verlag, 1989.

[Ho13] K.-P. Ho and J. Kahn. "Mode Coupling and its Impact on Spatially Multiplexed Systems". In: *Optical Fiber Telecommunications VIB - Systems and Networks.* Ed. by I. P. Kaminow, T. Li, and A. E. Willner. Boston: Academic Press, 2013. Chap. 11, pp. 491–568.
DOI: `10.1016/B978-0-12-396960-6.00011-0`.

[Howe01] K. B. Howell. *Principles of Fourier Analysis.* Textbooks in Mathematics. CRC Press, 2001.
ISBN: 0-8493-8275-0.

[ITU20] I. T. U. (ITU). *Measuring digital development — Facts and figures 2020.* Geneva, 2020.
ISBN: 978-92-61-32511-4.

[Kamm04] K.-D. Kammeyer. *Nachrichtenübertragung.* Stuttgart, Leipzig, Wiesbaden: B. G. Teubner, 2004.

[King09] F. W. King. *Hilbert Transforms Volume 1.* Encyclopedia of Mthematics and its Aplications. Cambridge University Press, 2009.
ISBN: 9781107089792.

[Koeb11] C. Koebele et al. "Two mode transmission at 2x100Gb/s, over 40km-long prototype few-mode fiber, using LCOS-based programmable mode multiplexer and demultiplexer". In: *Optics Express* 19.17 (Aug. 2011), pp. 16593–16600.
DOI: `10.1364/OE.19.016593`.

[Kowa12] M. Kowalczyk. "Incoherent optical MIMO transmission over multimode fibers". In: *Proceedings of SPIE, Photonics Applications in Astronomy, Communications, Industry, and High-Energy Physics Experiments.* Vol. 8454. 2012.
DOI: `10.1117/12.2000140`.

[Labr14] G. Labroille et al. “Efficient and mode selective spatial mode multiplexer based on multi-plane light conversion”. In: *IEEE Photonics Conference*. 2014, pp. 518–519.
DOI: 10.1109/IPCon.2014.6995478.

[Labr15] G. Labroille et al. “30 Gbit/s transmission over 1 km of conventional multimode fiber using mode group multiplexing with OOK modulation and direct detection”. In: *European Conference on Optical Communication (ECOC)*. Sept. 2015, pp. 1–3.
DOI: 10.1109/ECOC.2015.7341786.

[Labs89] J. Labs. *Verbindungstechnik für Lichtwellenleiter*. VEB Verlag Technik Berlin, 1989.
ISBN: 3-341-00444-0.

[Leon14] S. G. Leon-Saval et al. “Mode-selective photonic lanterns for space-division multiplexing”. In: *Optics Express* 22.1 (Jan. 2014), pp. 1036–1044.
DOI: 10.1364/OE.22.001036.

[Li20] J. Li et al. “Terabit Mode Division Multiplexing Discrete Multitone Signal Transmission Over OM2 Multimode Fiber”. In: *IEEE Journal of Selected Topics in Quantum Electronics* 26.4 (2020), pp. 1–8.
DOI: 10.1109/JSTQE.2020.2985278.

[Liu17] H. Liu et al. “3×10 Gb/s mode group-multiplexed transmission over a 20 km few-mode fiber using photonic lanterns”. In: *Optical Fiber Communications Conference and Exhibition (OFC)*. 2017, pp. 1–3.
DOI: 10.1364/OFC.2017.M2D.5.

[Male99] A. Maleki-Tehrani, B. Hassibi, and J. M. Cioffi. “Adaptive equalization of multiple-input multiple-output (MIMO) frequency selective channels”. In: *Conference Record of the Thirty-Third Asilomar Conference on Signals, Systems, and Computers (Cat. No.CH37020)*. Vol. 1. 1999, pp. 547–551.
DOI: 10.1109/ACSSC.1999.832390.

[Mate18] mateC. *Hilbert Transform of a sine Function with Quadratic Argument*. Online. Accessed: 2018-12-06. Dec. 2018.
URL: https://dsp.stackexchange.com/questions/53925/hilbert-transform-of-a-sine-function-with-quadratic-argument-sinat2-bt/53949#53949.

[Mori10] J.-F. Morizur et al. “Programmable unitary spatial mode manipulation”. In: *J. Opt. Soc. Am. A* 27.11 (Nov. 2010), pp. 2524–2531.
DOI: 10.1364/JOSAA.27.002524.

[Mori13] T. Mori et al. “Wideband WDM coherent optical MIMO transmission over 50 µm-core GI-MMF using selective mode excitation technique”. In: *Optical Fiber Technology* 19.6, Part A (2013), pp. 658–664. ISSN: 1068-5200.
DOI: https://doi.org/10.1016/j.yofte.2013.10.007.

[Nguy10] P. T. Nguyen. “Investigation of spectral characteristics of solitary diode lasers with integrated grating resonator”. Dissertation. TU Berlin, 2010.

[Pate01] K. M. Patel and S. E. Ralph. “Improved multimode link bandwidth using spatial diversity in signal reception”. In: *Technical Digest. Summaries of papers presented at the Conference on Lasers and Electro-Optics. Postconference Technical Digest (IEEE Cat. No.01CH37170)*. May 2001, p. 416.
DOI: `10.1109/CLEO.2001.947989`.

[Paul09] H. Paul and K.-D. Kammeyer. “Equivalent Baseband Channels of Systems Using Envelope Detection”. In: *AEU International Journal of Electronics and Communications* 63.7 (July 2009), pp. 533–540.
DOI: `10.1016/j.aeue.2009.01.010`.

[Pete12] K. B. Petersen and M. S. Pedersen. *The Matrix Cookbook*. Nov. 2012.
URL: `http://www2.imm.dtu.dk/pubdb/p.php?3274`.

[Phot14] P. Photonics. *Fiber Space (De)Multiplexer based on Photonic Lantern – Technical Brief 8*. Online. 2014.
URL: `http://www.phoenixphotonics.com/website/technology/documents/PhotonicLantern0414_v1.pdf`.

[Rade20] G. Rademacher et al. “1.01 Peta-bit/s C+L-band transmission over a 15-mode fiber”. In: *European Conference on Optical Communications (ECOC)*. 2020, pp. 1–4.
DOI: `10.1109/ECOC48923.2020.9333321`.

[Rale98] G. G. Raleigh and J. M. Cioffi. “Spatio-Temporal Coding for Wireless Communication”. In: *IEEE Transactions on Communications* 46.3 (Mar. 1998), pp. 357–366. ISSN: 0090-6778.
DOI: `10.1109/26.662641`.

[Rame81] O.-G. Ramer. “Single-Mode Fiber-To-Channel Waveguide Coupling”. In: *Journal of Optical Communications* 2.4 (July 1981), pp. 122–127.
DOI: `10.1515/JOC.1981.2.4.122`.

[Rao20] R. Rao. “Optical communication systems serve as the backbone of today’s technologies”. In: *MRS Bulletin* 45.12 (2020), pp. 1056–1057.
DOI: `10.1557/mrs.2020.319`.

[Rapp02] T. S. Rappaport. *Wireless Communications: Principles and Practice*. Prentice Hall communications engineering and emerging technologies series. Prentice Hall PTR, 2002.
ISBN: 9780130422323.

[Rath17] R. Rath et al. “Tomlinson–Harashima Precoding For Dispersion Uncompensated PAM-4 Transmission With Direct-Detection”. In: *Journal of Lightwave Technology* 35.18 (Sept. 2017), pp. 3909–3917. ISSN: 0733-8724.
DOI: `10.1109/JLT.2017.2724032`.

[Ryf11] R. Ryf et al. “Space-division multiplexing over 10 km of three-mode fiber using coherent 6x6 MIMO processing”. In: *Optical Fiber Communication Conference/National Fiber Optic Engineers Conference 2011*. Optical Society of America, 2011.
DOI: `10.1364/OFC.2011.PDPB10`.

[Ryf18] R. Ryf et al. “High-Spectral-Efficiency Mode-Multiplexed Transmission Over Graded-Index Multimode Fiber”. In: *2018 European Conference on Optical Communication (ECOC)*. 2018, pp. 1–3.
DOI: `10.1109/ECOC.2018.8535536`.

[Sai17] X. Sai et al. “Elliptical-core Mode-selective Photonic Lanterns for MIMO-free Mode Division Multiplexing Systems”. In: *Conference on Lasers and Electro-Optics*. Optical Society of America, 2017.
DOI: 10.1364/CLEO_AT.2017.JW2A.68.

[Sale85] B. E. A. Saleh and R. M. Abdula. “Optical interference and pulse propagation in multimode fibers”. In: *Fiber and Integrated Optics* 5.2 (1985), pp. 161–201.
DOI: 10.1080/01468038508242751.

[Sale91] B. E. A. Saleh and M. C. Teich. *Fundamentals of Photonics*. First. John Wiley & Sons, Inc., 1991.

[Sand14] A. Sandmann, A. Ahrens, and S. Lochmann. “Experimental Description of Multimode MIMO Channels utilizing Optical Couplers”. In: *15. ITG-Symposium on Photonic Networks*. Leipzig (Germany): VDE VERLAG GmbH, May 2014, pp. 125–130.
ISBN: 978-3-8007-3604-1.

[Sand15e] A. Sandmann, A. Ahrens, and S. Lochmann. “Zero-Forcing Equalisation of Measured Optical Multimode MIMO Channels”. In: *E-Business and Telecommunications: 11th International Joint Conference, ICETE 2014, Vienna, Austria, August 28-30, 2014*. Ed. by S. M. Obaidat, A. Holzinger, and J. Filipe. Communications in Computer and Information Science. Cham: Springer International Publishing, Dec. 2015, pp. 115–130.
ISBN: 978-3-319-25915-4.
DOI: 10.1007/978-3-319-25915-4_7.

[Sand16] A. Sandmann, A. Ahrens, and S. Lochmann. “Experimental Evaluation of a (4x4) Multi-Mode MIMO System Utilizing Customized Optical Fusion Couplers”. In: *17. ITG-Symposium on Photonic Networks*. Leipzig (Germany): VDE VERLAG GmbH, May 2016, pp. 101–105.
ISBN: 978-3-8007-4219-6.

[Sand16a] A. Sandmann et al. “MIMO Signal Processing in Optical Multi-Mode Fiber Transmission using Photonic Lanterns”. In: *11th International Conference on Mathematics in Signal Processing*. Birmingham (United Kingdom), Dec. 2016.

[Sand17] A. Sandmann et al. “Experimental Multi-Mode MIMO System Evaluation using Segmented Photo Detection”. In: *18. ITG-Symposium on Photonic Networks*. Leipzig (Germany): VDE VERLAG GmbH, May 2017, pp. 94–97.
ISBN: 978-3-8007-4427-5.

[Sand17c] A. Sandmann, A. Ahrens, and S. Lochmann. “Evaluation of Polynomial Matrix SVD-based Broadband MIMO Equalization in an Optical Multi-Mode Testbed”. In: *Advances in Wireless and Optical Communications (RTUWO)*. Riga (Latvia), Nov. 2017, pp. 1–11.
DOI: 10.1109/RTUWO.2017.8228495.

[Sand18] A. Sandmann et al. “Mode Group Power Coupling Analysis for Short Reach Space Division Multiplexing”. In: *19. ITG-Symposium on Photonic Networks*. Leipzig (Germany): VDE VERLAG GmbH, June 2018, pp. 77–82.
ISBN: 978-3-8007-4684-2.
URL: https://www.vde-verlag.de/proceedings-de/454684012.html.

[Sand19] A. Sandmann et al. “Performance evaluation of mode group power coupling for short reach SDM”. In: *Optical Fiber Technology - Journal - Elsevier* 48 (2019), pp. 22–27. ISSN: 1068-5200.
DOI: `10.1016/j.yofte.2018.12.010`.

[Sand19a] A. Sandmann, A. Ahrens, and S. Lochmann. “Characterization of Mechanically Stressed Multi-Mode Fiber Channels”. In: *International Interdisciplinary PhD Workshop (IIPhDW)*. May 2019, pp. 101–105.
DOI: `10.1109/IIPHDW.2019.8755413`.

[Sand20] A. Sandmann et al. “Baseband linearity and interference effects in intensity modulated and direct detected optical MIMO systems”. In: *Optical Fiber Technology - Journal - Elsevier* 60 (2020). ISSN: 1068-5200.
DOI: `10.1016/j.yofte.2020.102329`.

[Schoe06] S. Schöllmann and W. Rosenkranz. “Experimental Verification of Mode Group Diversity Multiplexing over GI-POF at 21.4 Gb/s without Equalization”. In: *Plastic Optical Fiber (POF) Conference*. 2006, pp. 408–413.

[Schoe07] S. Schöllmann and W. Rosenkranz. “Experimental Equalization of Crosstalk in a 2 x 2 MIMO System Based on Mode Group Diversity Multiplexing in MMF Systems @ 10.7 Gb/s”. In: *33rd European Conference and Ehxibition on Optical Communication (ECOC)*. Sept. 2007, pp. 1–2.
DOI: `10.1049/ic:20070268`.

[Schoe07a] S. Schöllmann, S. Soneff, and W. Rosenkranz. “10.7 Gb/s Over 300 m GI-MMF Using a 2x2 MIMO System Based on Mode Group Diversity Multiplexing”. In: *OFC/NFOEC 2007 - 2007 Conference on Optical Fiber Communication and the National Fiber Optic Engineers Conference*. Mar. 2007, pp. 1–3.
DOI: `10.1109/OFC.2007.4348820`.

[Schoe08] S. Schöllmann, N. Schrammar, and W. Rosenkranz. “Experimental Realisation of 3 x 3 MIMO System with Mode Group Diversity Multiplexing Limited by Modal Noise”. In: *Optical Fiber Communication Conference/National Fiber Optic Engineers Conference (OFC/NFOEC)*. Feb. 2008, pp. 1–3.
DOI: `10.1109/OFC.2008.4528224`.

[Schoe09] S. Schöllmann. “Optimierung des Bandbreiten-Längenproduktes optischer MMF-Übertragungssysteme durch Anwendung der MIMO-Technik”. Dissertation. Kiel University, June 2009.

[Silv10] M. Silva-Lopez et al. “Segmented Photo-Detection for a MIMO Multi-Mode Fiber Transmission System”. In: *Journal of Optical Communications* 31.1 (Mar. 2010), pp. 10–13. ISSN: 0173-4911.
DOI: `10.1515/JOC.2010.31.1.10`.

[Simo16] C. Simonneau et al. “4x50Gb/s transmission over 4.4 km of multimode OM2 fiber with direct detection using mode group multiplexing”. In: *Optical Fiber Communication Conference*. Optical Society of America, 2016.
DOI: `10.1364/OFC.2016.Tu2J.3`.

[Stee13] R. Steed. “Derivations of the Phase Noise Spectra of Lasers and of Lasers Passing Through Interferometers”. Jan. 2013.

[Step14] G. Stepniak. “Dispersion-supported direct-detection mode group division multiplexing using commercial multimode fiber couplers”. In: *Optics Letters* 39.7 (Apr. 2014), pp. 1815–1818.
DOI: `10.1364/OL.39.001815`.

[Stua00] H. R. Stuart. “Dispersive Multiplexing in Multimode Optical Fiber”. In: *Science* 289.5477 (2000), pp. 281–283. ISSN: 0036-8075.
DOI: `10.1126/science.289.5477.281`.

[Task05] D. Cunningham et al. *802.3aq Task Force - 10GBASE-LRM Interoperability Report*. Presentation (Online). Accessed 10.03.2021. Nov. 2005.
URL: `https://www.ieee802.org/3/aq/public/nov05/mcvey_1_1105.pdf`.

[Teic16] W. G. Teich et al. “Equalization for Fiber-Optic Transmission Systems: Low-Complexity Iterative Implementations”. In: *Proceedings of Photonic Networks; 17. ITG-Symposium*. May 2016, pp. 1–8.

[Thom11] R. R. Thomson et al. “Ultrafast laser inscription of an integrated photonic lantern”. In: *Optics Express* 19.6 (Mar. 2011), pp. 5698–5705.
DOI: `10.1364/OE.19.005698`.

[Thor94] W. Q. Thornburg, B. J. Corrado, and X. D. Zhu. “Selective launching of higher-order modes into an optical fiber with an optical phase shifter”. In: *Optics Letters* 19.7 (Apr. 1994), pp. 454–456.
DOI: `10.1364/OL.19.000454`.

[Unge93] H.-G. Unger. *Optische Nachrichtentechnik - Band 1: Optische Wellenleiter*. Hüthig Verlag, 1993.
ISBN: 3-7785-2261-2.

[Wang92] J. Wang and K. Petermann. “Small signal analysis for dispersive optical fiber communication systems”. In: *Journal of Lightwave Technology* 10.1 (Jan. 1992), pp. 96–100. ISSN: 0733-8724.
DOI: `10.1109/50.108743`.

[Weik07] O. Weikert and U. Zölzer. “Efficient MIMO Channel Estimation With Optimal Training Sequences”. In: *Proceedings of 1st Workshop on Commercial MIMO-Components and -Systems (CMCS 2007)*. Duisburg (Germany), Sept. 2007.

[Wild15] J. Wilde et al. “Selective higher order fiber mode excitation using a monolithic setup of a phase plate at a fiber facet”. In: *Proceedings of SPIE*. Vol. 9343. 2015.
DOI: `10.1117/12.2078933`.

[Will20] A. E. Willner, ed. *Optical Fiber Telecommunications VII*. Academic Press, 2020.
ISBN: 978-0-12-816502-7.
DOI: `https://doi.org/10.1016/B978-0-12-816502-7.00031-2`.

[Winz13] P. J. Winzer, R. Ryf, and S. Randel. “Spatial Multiplexing Using Multiple-Input Multiple-Output Signal Processing”. In: *Optical Fiber Telecommunications VIB - Systems and Networks*. Ed. by I. P. Kaminow, T. Li, and A. E. Willner. Boston: Academic Press, 2013. Chap. 10, pp. 433–490.
DOI: `10.1016/B978-0-12-396960-6.00010-9`.

[Winz18] P. J. Winzer, D. T. Neilson, and A. R. Chraplyvy. “Fiber-optic transmission and networking: the previous 20 and the next 20 years”. In: *Optics Express* 26.18 (Sept. 2018), pp. 24190–24239.
DOI: `10.1364/OE.26.024190`.

[Yari89] A. Yariv. *Quantum Electronics*. Third. John Wiley and Sons, 1989.
ISBN: 0-471-60997-8.

[Zou20] D. Zou et al. “Single λ 500-Gbit/s PAM Signal Transmission for Data Center Interconnect Utilizing Mode Division Multiplexing”. In: *Optical Fiber Communication Conference (OFC)*. 2020.
DOI: `10.1364/OFC.2020.W1D.6`.

Liste der Veröffentlichungen des Autors

Veröffentlichungen, die Teil der Dissertationsschrift sind

Nachfolgend sind die Veröffentlichungen des Doktoranden aufgelistet, aus denen Teile in der Dissertation verwendet wurden. Die entsprechenden Stellen sind im Kapitel 1.3 auf Seite 21 aufgeführt. Da diese Veröffentlichungen Gemeinschaftsarbeiten mehrerer Autoren sind, ist die Höhe des Eigenanteils des Doktoranden in den Tabellen angegeben.

Beiträge in Fachzeitschriften

“Baseband linearity and interference effects in intensity modulated and direct detected optical MIMO systems”. In: *Optical Fiber Technology - Journal - Elsevier* 60 (2020). ISSN: 1068-5200.
DOI: 10.1016/j.yofte.2020.102329

Autoren: A. Sandmann, A. Ahrens, S. Lochmann und S. Pachnicke

Konzeptionierung	Planung	Durchführung	Manuskripterstellung
hoch	hoch	hoch	hoch

“Performance evaluation of mode group power coupling for short reach SDM”. In: *Optical Fiber Technology - Journal - Elsevier* 48 (2019), S. 22–27. ISSN: 1068-5200.
DOI: 10.1016/j.yofte.2018.12.010

Autoren: A. Sandmann, A. Ahrens, S. Lochmann und S. Pachnicke

Konzeptionierung	Planung	Durchführung	Manuskripterstellung
hoch	hoch	hoch	hoch

Konferenzbeiträge

“Characterization of Mechanically Stressed Multi-Mode Fiber Channels”. In: *International Interdisciplinary PhD Workshop (IIPhDW)*. Mai 2019, S. 101–105.
DOI: 10.1109/IIPHDW.2019.8755413

Autoren: A. Sandmann, A. Ahrens und S. Lochmann

Konzeptionierung	Planung	Durchführung	Manuskripterstellung
hoch	hoch	mittel	hoch

“Mode Group Power Coupling Analysis for Short Reach Space Division Multiplexing”. In: *19. ITG-Symposium on Photonic Networks*. Leipzig (Germany): VDE VERLAG GmbH, Juni 2018, S. 77–82.
ISBN: 978-3-8007-4684-2.
URL: https://www.vde-verlag.de/proceedings-de/454684012.html

Autoren: A. Sandmann, A. Ahrens, S. Lochmann und S. Pachnicke

Konzeptionierung	Planung	Durchführung	Manuskripterstellung
hoch	hoch	hoch	hoch

“Evaluation of Polynomial Matrix SVD-based Broadband MIMO Equalization in an Optical Multi-Mode Testbed”. In: *Advances in Wireless and Optical Communications (RTUWO)*. Riga (Latvia), Nov. 2017, S. 1–11.
DOI: 10.1109/RTUWO.2017.8228495

Autoren: A. Sandmann, A. Ahrens und S. Lochmann

Konzeptionierung	Planung	Durchführung	Manuskripterstellung
hoch	hoch	hoch	hoch

“Experimental Multi-Mode MIMO System Evaluation using Segmented Photo Detection”. In: *18. ITG-Symposium on Photonic Networks*. Leipzig (Germany): VDE VERLAG GmbH, Mai 2017, S. 94–97.
ISBN: 978-3-8007-4427-5

Autoren: A. Sandmann, A. Ahrens, S. Lochmann, W. Rosenkranz und H. Zimmermann

Konzeptionierung	Planung	Durchführung	Manuskripterstellung
niedrig	niedrig	mittel	hoch

“MIMO Signal Processing in Optical Multi-Mode Fiber Transmission using Photonic Lanterns”. In: *11th International Conference on Mathematics in Signal Processing*. Birmingham (United Kingdom), Dez. 2016

Autoren: A. Sandmann, M. Götten, A. Ahrens und S. Lochmann

Konzeptionierung	Planung	Durchführung	Manuskripterstellung
mittel	hoch	hoch	hoch

“Experimental Evaluation of a (4x4) Multi-Mode MIMO System Utilizing Customized Optical Fusion Couplers”. In: *17. ITG-Symposium on Photonic Networks*. Leipzig (Germany): VDE VERLAG GmbH, Mai 2016, S. 101–105.
ISBN: 978-3-8007-4219-6

Autoren: A. Sandmann, A. Ahrens und S. Lochmann

Konzeptionierung	Planung	Durchführung	Manuskripterstellung
mittel	hoch	hoch	hoch

"Experimental Description of Multimode MIMO Channels utilizing Optical Couplers". In: *15. ITG-Symposium on Photonic Networks*. Leipzig (Germany): VDE VERLAG GmbH, Mai 2014, S. 125–130.
ISBN: 978-3-8007-3604-1

Autoren: A. Sandmann, A. Ahrens und S. Lochmann

Konzeptionierung	Planung	Durchführung	Manuskripterstellung
mittel	mittel	mittel	mittel

Weitere Publikationen

Buchbeiträge

A. Ahrens, A. Sandmann und S. Lochmann. "Optical MIMO Transmission Focusing on Photonic Lanterns and Optical Couplers". In: *E-Business and Telecommunications*. Hrsg. von M. S. Obaidat und E. Cabello. Springer International Publishing, 2019, S. 104–122.
ISBN: 978-3-030-11039-0.
DOI: 10.1007/978-3-030-11039-0_6

A. Sandmann, A. Ahrens, S. Lochmann und P. Bartmann. "Mode Excitation and Multiplexing for MIMO Systems Focusing on Digital Mirror Devices". In: *E-Business and Telecommunications: 13th International Joint Conference, ICETE 2016, Lisbon, Portugal, July 26-28, 2016*. Hrsg. von M. S. Obaidat. Cham: Springer International Publishing, Okt. 2017, S. 161–176.
ISBN: 978-3-319-67876-4.
DOI: 10.1007/978-3-319-67876-4_8

A. Sandmann, A. Ahrens und S. Lochmann. "Zero-Forcing Equalisation of Measured Optical Multimode MIMO Channels". In: *E-Business and Telecommunications: 11th International Joint Conference, ICETE 2014, Vienna, Austria, August 28-30, 2014*. Hrsg. von S. M. Obaidat, A. Holzinger und J. Filipe. Communications in Computer and Information Science. Cham: Springer International Publishing, Dez. 2015, S. 115–130.
ISBN: 978-3-319-25915-4.
DOI: 10.1007/978-3-319-25915-4_7

Beiträge in Fachzeitschriften

Z. Wang, A. Sandmann, J. McWhirter und A. Ahrens. "Decoupling of Broadband Optical MIMO Systems Using the Multiple Shift SBR2 Algorithm". In: *International Journal of Advances in Telecommunications, Electrotechnics, Signals and Systems* 6.1 (2017), S. 30–37. ISSN: 1805-5443.
DOI: 10.11601/ijates.v6i1.207

A. Ahrens, A. Sandmann, K. Bremer, B. Roth und S. Lochmann. “Improving Optical Fiber Sensing by MIMO Signal Processing”. In: *Informatics, Control, Measurement in Economy and Environment Protection (IAPGOŚ)* 6.3 (Aug. 2016). Scientific Conference WD2016, S. 51–55. ISSN: 2083-0157.
DOI: 10.5604/20830157.1212268

A. Sandmann, A. Ahrens und S. Lochmann. “Modulation-Mode and Power Assignment in SVD-Assisted Broadband MIMO Systems using Polynomial Matrix Factorization”. In: *Przeglad Elektrotechniczny* 04/2015 (Apr. 2015), S. 10–13. ISSN: 0033-2097.
DOI: 10.15199/48.2015.04.03

KONFERENZBEITRÄGE

2018

E. Auer, A. Ahrens, A. Sandmann und C. Benavente-Peces. “Influence of uncertainty and numerical errors in the context of MIMO systems”. In: *8th International Workshop on Reliable Engineering Computing (REC)*. University of Liverpool. Liverpool (UK), Juli 2018.
URL: http://rec2018.uk/papers/REC2018-16_E.%20Auer,%20C.%20Benavente-Peces,%20A.%20Ahrens__Influence%20of%20Uncertainty%20and%20Numerical%20Errors%20in%20the%20Context%20of%20MIMO%20Systems.pdf

2017

A. Ahrens, A. Sandmann, E. Auer und S. Lochmann. “Optimal Power Allocation in Zero-Forcing Assisted PMSVD-based Optical MIMO Systems”. In: *Sensor Signal Processing for Defence Conference (SSPD)*. London (United Kingdom), Dez. 2017, S. 1–5.
DOI: 10.1109/SSPD.2017.8233253

A. Sandmann, A. Ahrens und S. Lochmann. “Successive Interference Cancellation in Spatially Multiplexed Fiber-optic Transmission”. In: *Advances in Wireless and Optical Communications (RTUWO)*. Riga (Latvia), Nov. 2017, S. 91–95.
DOI: 10.1109/RTUWO.2017.8228512

M. Götten, S. Lochmann, A. Sandmann und A. Ahrens. “Mode Coupling Analysis in Optical MIMO Systems”. In: *8th International Symposium on AUTOMATIC CONTROL (AUTSYM)*. Wismar (Germany), Sep. 2017

A. Ahrens, A. Sandmann und S. Lochmann. “Optical MIMO Multi-mode Fiber Transmission using Photonic Lanterns”. In: *Proceedings of the 14th International Joint Conference on e-Business and Telecommunications - Volume 5: OPTICS, (ICETE 2017)*. INSTICC. Madrid (Spain): SciTePress, Juli 2017, S. 24–31.
ISBN: 978-989-758-258-5.
DOI: 10.5220/0006394800240031

2016

A. Ahrens, A. Sandmann und S. Lochmann. “Iteratively Detected and SVD-assisted MIMO-BICM Multi-Mode Transmission Schemes using Optical Couplers”. In: *11th International Conference on Mathematics in Signal Processing*. Birmingham (United Kingdom), Dez. 2016

Z. Wang, A. Sandmann, J. G. McWhirter und A. Ahrens. “Multiple Shift SBR2 Algorithm for Calculating the SVD of Broadband Optical MIMO Systems”. In: *39th International Conference on Telecommunications and Signal Processing (TSP)*. Vienna (Austria), Juni 2016, S. 433–436.
DOI: `10.1109/TSP.2016.7760914`

2015

A. Ahrens, A. Sandmann, S. Lochmann und Z. Wang. “Decomposition of Optical MIMO Systems using Polynomial Matrix Factorization”. In: *2nd IET International Conference on Intelligent Signal Processing (ISP)*. London (United Kingdom): Institution of Engineering und Technology, Dez. 2015.
DOI: `10.1049/cp.2015.1758`

A. Sandmann, A. Ahrens und S. Lochmann. “Power Allocation in PMSVD-based Optical MIMO Systems”. In: *Advances in Wireless and Optical Communications (RTUWO)*. Riga (Latvia), Nov. 2015, S. 108–111.
ISBN: 978-1-4673-7432-3.
DOI: `10.1109/RTUWO.2015.7365729`

A. Ahrens, A. Sandmann, K. Bremer, B. Roth und S. Lochmann. “Optical Fibre Sensors based on Multi-Mode fibres and MIMO Signal Processing: An experimental Approach”. In: *24th International Conference on Optical Fibre Sensors (OFS24)*. Hrsg. von H. J. Kalinowski, J. L. Fabris und W. J. Bock. Bd. 9634. Curitiba (Brazil), Sep. 2015.
DOI: `10.1117/12.2195114`

A. Sandmann, A. Ahrens und S. Lochmann. “Performance Analysis of Polynomial Matrix SVD-based Broadband MIMO Systems”. In: *Sensor Signal Processing for Defence Conference (SSPD)*. Edinburgh (United Kingdom), Sep. 2015, S. 50–54.
DOI: `10.1109/SSPD.2015.7288517`

A. Sandmann, A. Ahrens und S. Lochmann. “Resource Allocation in SVD-Assisted Optical MIMO Systems using Polynomial Matrix Factorization”. In: *16. ITG-Symposium on Photonic Networks*. Leipzig (Germany): VDE VERLAG GmbH, Mai 2015, S. 128–134.
ISBN: 978-3-8007-3938-7

A. Sandmann, A. Ahrens und S. Lochmann. “Resource Allocation in SVD-Assisted Broadband MIMO Systems using Polynomial Matrix Factorization”. In: *Proceedings of the 5th International Conference on Pervasive and Embedded Computing and Communication Systems - Volume 1: AMC, (PECCS 2015).* Angers (France), Feb. 2015, S. 317–324.
ISBN: 978-989-758-084-0.
DOI: 10.5220/0005265403170324

2014

A. Sandmann, A. Ahrens und S. Lochmann. “Modulation-Mode and Power Assignment in Optical MIMO Systems using Polynomial Matrix Factorization”. In: *10th International Conference on Mathematics in Signal Processing.* Birmingham (United Kingdom), Dez. 2014

A. Sandmann, A. Ahrens und S. Lochmann. “Modulation-Mode and Power Assignment in SVD-Assisted Broadband MIMO Systems using Polynomial Matrix Factorization”. In: *XI Symposium of Magnetic Measurements.* Czarny Las, Czestochowa (Poland), Okt. 2014

A. Sandmann, A. Ahrens und S. Lochmann. “Time Domain Description of Optical MIMO Channels”. In: *7th International Symposium on AUTOMATIC CONTROL (AUTSYM).* Wismar (Germany), Sep. 2014

A. Sandmann, A. Ahrens und S. Lochmann. “Equalisation of Measured Optical MIMO Channels”. In: *5th International Conference on Optical Communication Systems (OPTICS).* Vienna (Austria): Science und Technology Publications, Lda., Aug. 2014, S. 37–44.
ISBN: 978-989-758-044-4.
DOI: 10.5220/0005019600370044

A. Sandmann, A. Ahrens und S. Lochmann. “Zero–Forcing Equalisation of Estimated Optical MIMO Channels”. In: *Baltic Young PhD Conference.* Riga (Latvia): Universität Rostock, Wissenschaftsverbund IuK, Juli 2014, S. 73–86

2013

A. Sandmann, A. Ahrens und S. Lochmann. “Signal Deconvolution of Measured Optical MIMO-Channels”. In: *XV International PhD Workshop OWD.* Wisła, Poland, Okt. 2013, S. 278–283.
ISBN: 978-83-935427-2-7

Erklärung zur Arbeit

Hiermit erkläre ich, dass diese Abhandlung, abgesehen von der Beratung durch meinen Betreuer, Herrn Prof. Dr.-Ing. Stephan Pachnicke, nach Inhalt und Form die eigene Arbeit ist. Zudem hat diese Arbeit weder im Ganzen noch zum Teil einer anderen Stelle im Rahmen eines Prüfungsverfahrens vorgelegen. Des Weiteren wurde diese Arbeit im Ganzen nicht veröffentlicht und auch nicht zur Veröffentlichung eingereicht. Teile dieser Arbeit wurden in Fachzeitschriften und im Rahmen von Fachkonferenzen in Proceedings veröffentlicht. Die entsprechenden Abschnitte mit den Verweisen auf die dazugehörigen Publikationen sind im Kapitel 1.3 auf Seite 21 gekennzeichnet. Diese Arbeit ist unter Einhaltung der Regeln guter wissenschaftlicher Praxis der Deutschen Forschungsgemeinschaft entstanden. Außerdem erkläre ich, dass mir kein akademischer Grad entzogen wurde.

Ort, Datum	Unterschrift